

The NEXT path to neutrino inverse hierarchy

DOCTORADO EN FÍSICA

Javier Muñoz Vidal

Director: Juan José Gómez Cadenas

Tutor: José Díaz Medina



VNIVERSITAT
DE VALÈNCIA

Departamento de Física Atómica, Molecular y Nuclear

Abril de 2018

The work in this thesis has been carried out at the *Instituto de Física Corpuscular* (IFIC), affiliated with the Universitat de València and CSIC.

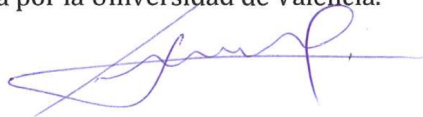
© Javier Muñoz Vidal, April 2018

INFORME DEL DIRECTOR

Juan José Gómez Cadenas, profesor de Ikerbaske – Donostia International Physics Center, como director de tesis del estudiante **Javier Muñoz Vidal**,

CERTIFICA:

Que los trabajos aquí detallados han sido realizados por el estudiante en el Instituto de Física Corpuscular bajo su dirección y que el presente texto constituye el trabajo de tesis doctoral por la que el estudiante opta al grado de Doctor en Física por la Universidad de Valencia.

A handwritten signature in blue ink, appearing to be 'Juan José Gómez Cadenas', written over a horizontal line.

Paterna, a 26 de Abril de 2018.

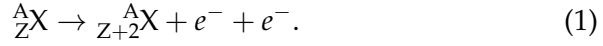
Resumen

De todas las partículas que componen el universo, quizás la más común de ellas sea también la más misteriosa, el neutrino. Ahora mismo miles de millones de estas partículas nos atraviesan sin percibirlo, y detectar una sola de ellas necesita de enormes detectores enterrados a gran profundidad. Postuladas por primera vez por Wolfgang Pauli en 1930, fueron bautizadas en 1934 como "pequeños neutrones" por Enrico Fermi, aludiendo a dos de sus principales características: su pequeña masa y su ausencia de carga eléctrica. A mediados de los años 70, los neutrinos fueron incluidos en el Modelo Estándar bajo las premisas de: carecer de masa y carga eléctrica, experimentar únicamente la fuerza nuclear débil, ser los neutrinos distintos de sus antipartículas y la existencia de 3 familias con números leptónicos conservados por separado.

Sin embargo, los experimentos de oscilaciones de neutrinos llevados a cabo durante las últimas décadas han demostrado que los neutrinos tienen masa y se mezclan, abriendo un nuevo campo en la física más allá del Modelo Estándar. Una de las maneras de acomodar estas masas en la teoría es que los neutrinos podrían ser partículas de Majorana, es decir, idénticas a sus antipartículas, al contrario que el resto de fermiones, y violar la conservación del número leptónico. De ser así, los neutrinos pudieran tener relación con la asimetría materia - antimateria del universo via leptogénesis, así como ser una elegante explicación de la pequeñez de su masa a través del mecanismo "see-saw". Ante esta situación, es fácil entender que los neutrinos sean en la actualidad uno de los campos de moda de la investigación en física a nivel mundial y multitud de experimentos traten de arrojar luz sobre su naturaleza.

El método más sensible para establecer la naturaleza de los neutri-

nos es la búsqueda de una hipotética y extremadamente rara transición nuclear llamada desintegración doble beta sin emisión de neutrinos ($0\nu\beta\beta$) en el que un núcleo de número atómico Z y número másico A se transforma en su isóbaro de número atómico $Z + 2$ emitiendo únicamente dos electrones:



Aunque la versión del proceso que incluye emisión de neutrinos ha sido observada y medida en varios isótopos, la versión sin neutrinos del proceso aún no lo ha sido a día de hoy. El mecanismo físico más simple que lo describe es el intercambio virtual de un neutrino ligero de tipo Majorana, de manera que toda la energía disponible en la desintegración ($Q_{\beta\beta}$) se reparta entre los dos electrones emitidos. Precisamente ésta, sería la señal característica del proceso y por tanto el objetivo de todo experimento que pretenda encontrarlo. La semivida de este proceso viene dada por:

$$(T_{1/2}^{0\nu})^{-1} = G^{0\nu} |M^{0\nu}|^2 \left(\frac{m_{\beta\beta}}{m_e} \right)^2 \quad (2)$$

donde $G^{0\nu}$ es una integral de espacio de fases, $M^{0\nu}$ es el elemento de matriz nuclear del proceso, m_e es la masa del electrón y $m_{\beta\beta}$ es la llamada masa Majorana efectiva del neutrino:

$$m_{\beta\beta} \equiv \left| \sum_{i=1}^3 U_{ei}^2 m_i \right|, \quad (3)$$

donde U_{ei} son los elementos de la primera fila de la matriz de mezcla de neutrinos y m_i son los autoestados de masa. Por tanto, la observación del proceso llevaría implícita una medida indirecta de la masa de los neutrinos.

Los experimentos actuales han seguido distintas aproximaciones tecnológicas buscando la mejor resolución energética y la menor actividad de ruido posible que maximicen su sensibilidad. Para comparar el potencial de los distintos detectores, se hace uso de la sensibilidad a $m_{\beta\beta}$ que viene dada por:

$$\mathcal{S}(m_{\beta\beta}) \propto \sqrt{1/\varepsilon} \left(\frac{b \Delta E}{M t} \right)^{1/4}, \quad (4)$$

donde ε es la eficiencia de detección del experimento, M es la masa de isótopo $0\nu\beta\beta$ usada en el experimento, t es el tiempo de medida, ΔE es la resolución energética del detector y b es la tasa de ruido del experimento en la ventana de energía de interés (ROI) (expresada, normalmente, en cuentas por keV, kilogramo de fuente y año).

Las técnicas más prometedoras son los bolómetros, las TPCs, los semiconductores y los centelleadores. Precisamente, a este último tipo pertenece Kamland-ZEN, experimento japonés que haciendo uso de ^{136}Xe disuelto en centelleador líquido, ha establecido el límite más estricto hasta la fecha a la semi-vida de la desintegración $0\nu\beta\beta$ de 1.07×10^{26} años, con un rango de masa efectiva del neutrino Majorana entre 61 - 165 meV [1]. Es importante recalcar aquí lo realmente improbable que es el proceso, con una semi-vida 17 órdenes de magnitud mayor que la propia edad del universo y que convierte su búsqueda en un gran desafío físico y tecnológico.

La colaboración NEXT propone el detector *NEXT-100* para la búsqueda de desintegraciones $0\nu\beta\beta$, cuya sensibilidad es el objeto de estudio de esta tesis. Se trata de una TPC electroluminiscente capaz de albergar 100 kg de gas xenón a 15 bares de presión enriquecido al 91% en ^{136}Xe , que será operada en el Laboratorio Subterráneo de Canfranc. El gas xenón es un medio ideal pues presenta una serie de características fundamentales para la búsqueda de desintegraciones $\beta\beta$ como son el que se pueda enriquecer fácilmente en su isótopo ^{136}Xe , la facilidad para limpiarlo de impurezas, que presente señales de ionización y centelleo, que su resolución energética intrínseca sea mejor del 0.5% (FWHM a 2.5 MeV) y finalmente que su modo de desintegración $2\nu\beta\beta$ sea lento.

En NEXT-100 cada uno de los planos está dedicado y optimizado para una función distinta. Los electrones de la desintegración $\beta\beta$ ionizan y hacen centellear al xenón a la par. La luz de centelleo es leída por los PMTs de gran tamaño del cátodo para dar una medida del comienzo del evento (t_0). Los electrones de ionización derivan hacia el ánodo bajo la acción de un campo eléctrico moderado (300 - 500 V cm^{-1}) donde son acelerados por un campo mucho más intenso. Esta aceleración genera luz de electroluminiscencia o centelleo secundario de forma proporcional al número de electrones que llegan. Esta luz es leída desde el cátodo para proporcionar la medida de la energía total depositada en el detector. Por su parte el ánodo, instrumentado con

SiPMs equiespaciados 1 cm entre ellos, es el encargado de reconstruir la topología de las señales registradas a través de la lectura de esta misma luz de electroluminiscencia.

De esta forma, la señal de dos electrones con origen en un mismo vértice y energía total depositada igual a $^{136}\text{Xe } Q_{\beta\beta}$ (2458 keV) correspondiente a la señal $0\nu\beta\beta$ tiene una morfología muy característica que es reconstruida por ambos planos de nuestro detector. Por un lado, el ánodo proporciona una reconstrucción topológica en forma de una única deposición de energía en forma de traza alargada, con una densidad de energía depositada por unidad de espacio recorrido constante, y que presenta áreas de alta deposición energética en sus dos extremos debido a los picos de Bragg. La reconstrucción topológica viene afectada principalmente por la difusión de los electrones de ionización a lo largo de su viaje hasta el cátodo, la difusión de la luz de electroluminiscencia, y de la separación existente entre los sensores. La resolución espacial esperada es de 10 mm en las componentes transversales y de 5 mm en la longitudinal. Por otro lado, el cátodo proporciona una medida de la energía total depositada en el volumen activo del detector que en el caso de nuestra señal será de 2458 keV con una resolución estimada del 0.7% FWHM.

Cualquier evento registrado en el detector capaz de imitar la impronta dejada por la señal se considera un evento de ruido y como hemos visto anteriormente, su minimización es clave para maximizar la sensibilidad del detector. La identificación y evaluación de todos ellos bajo distintas circunstancias supone el principal objetivo de esta tesis. En NEXT-100 las principales fuentes de ruido son:

- La *radioactividad natural* presente en todos los componentes del detector. Es la fuente de ruido más común. Especialmente dañinos son los isótopos ^{208}Tl y ^{214}Bi presentes en las cadenas de desintegración del torio y del uranio respectivamente, cuyas gammas de desexcitación poseen una energía cercana a $Q_{\beta\beta}$ y que eventualmente pueden presentar una topología similar a la de la señal. La selección de componentes de una radiopureza extrema es por lo tanto esencial en la fabricación de los detectores.
- El *radón* es también un producto intermedio de las cadenas de desintegración, cuyo isótopo ^{222}Rn con origen en el uranio y

vida media de 3.8 días es especialmente perjudicial. Hay varios mecanismos por los cuales el radón puede producir eventos de ruido: desde el aire del laboratorio, a la contaminación intrínseca que puede presentar el xenón, así como al *degassing* de los materiales del detector cercanos al volumen activo. Para la mitigación de este tipo de ruido el LSC ha comprado un sistema que reduce en 4 órdenes de magnitud la presencia de radón en el aire del laboratorio; y eventualmente, en caso de ser necesario, pueden instalarse en el sistema de gas trampas de radón que filtren el xenón del detector.

- Los *muones cosmogénicos*. Un flujo de $3 \times 10^{-6} \text{ cm}^{-2}\text{s}^{-1}$ ha sido medido en el Hall A del LSC, con una energía estimada teóricamente de entre 220 y 245 GeV con altos grados de incertidumbre. El paso de muones por el detector crea una serie de núcleos inestables y de neutrones que generan cascadas electromagnéticas capaces de generar eventos de ruido. Inicialmente, un sistema de centelleadores rodeando el detector puede detectar el paso de los mismos, y aplicando un tiempo muerto tras su paso eliminar el correspondiente ruido. Una segunda contribución de los muones viene de la activación del xenón por neutrones secundarios. La desintegración beta del ^{137}Xe con un valor de Q de 4173 keV, en la práctica introduce un número de eventos en nuestra región de interés, que a la postre no pueden ser vetados y deben ser tenidos en cuenta en los cálculos de ruido del detector.
- Los *neutrones* son partículas muy penetrantes capaces de activar distintos isótopos en las componentes del detector o generar alfas y protones que acaban generando gammas energéticas que pueden producir eventos de ruido. En el caso del LSC, el mayor porcentaje de neutrones tiene su origen en la contaminación de uranio y torio de las rocas que conforman las paredes del laboratorio y el flujo total medido es de $\phi_{\text{Hall A}} = 1.38 \pm 0.14 \times 10^{-5} \text{ cm}^{-2} \text{ s}^{-1}$. Como los muones, los neutrones también pueden generar ruido a través de la activación del xenón. Por suerte, los neutrones son fáciles de vetar. Existen placas comerciales de polietileno dopado con boro al 5% de 20 cm de espesor que los reduce en 3 órdenes de magnitud lo que con-

vierte su contribución en despreciable.

Parte del objetivo de esta tesis consiste en la simulación y evaluación de la eficiencia de señal, la actividad de ruido esperada de cada una de las fuentes y con estos datos, estimar la sensibilidad del detector. La simulación realizada es de tipo Monte Carlo y está basada en GEANT4. El análisis consiste en la aplicación secuencial de una serie de algoritmos y cortes encargados de identificar y cuantificar cuantos eventos de señal y de cada tipo de ruido poseen la energía y el patrón característico de las desintegraciones $0\nu\beta\beta$. Los resultados obtenidos se resumen en una eficiencia de señal del 32% y un ruido total esperado de $< 4.22 \times 10^{-4}$ cts keV⁻¹ kg⁻¹ yr⁻¹, siendo la mayor contribución la radioactividad natural presente en ambos planos de sensores del detector. Gracias a estos valores, la sensibilidad de NEXT-100 tras 5 años de toma de datos asciende a una $T_{1/2}^{0\nu} = 9.85 \times 10^{25}$ años al 90% CL, que se corresponde a una masa del neutrino de Majorana de 57 - 161 meV en función del elemento de matriz nuclear (NME) empleado, obteniendo los mejores límites de sensibilidad publicados hasta la fecha.

Los últimos estudios realizados dentro de la colaboración permiten una evolución del detector NEXT-100 a una versión que denominamos *alta definición* que mejora las prestaciones del detector y la respuesta del análisis. Las principales mejoras y sus consecuencias son:

- *Alta resolución espacial.* La adición de ciertos gases como el CO₂ o el He al xenón permite la reducción de la difusión transversal y longitudinal a valores alrededor de 2 mm/sqrt(m), a la par que se mantiene la producción de luz. En la práctica esto supone poder "ver" los eventos del detector en alta definición lo que propicia una mejor discriminación del ruido en base a su patrón topológico.
- *Alta resolución energética.* Las últimas medidas de resolución energética hechas en NEW para eventos puntuales es ya del 0.5%, y esperamos poder extender dicha resolución a eventos más extensos en el corto plazo. La mejora permite una reducción lineal del ruido procedente del ²⁰⁸Tl y del ¹³⁷Xe, y en un factor aún mayor del ²¹⁴Bi.

- *Deep Neural Networks*. Los estudios preliminares llevados a cabo por la colaboración en el uso de DNNs para la discriminación topológica de los eventos presentan ya una mejora sensible respecto al análisis estándar, y cabe destacar el amplio margen de mejora existente en el uso de estas novedosas técnicas.

La combinación de estas tres mejoras supone una reducción de la tasa de ruido esperada a un nivel de 6.82×10^{-5} cts keV⁻¹ kg⁻¹ yr⁻¹ con una eficiencia de señal del 29%. El valor actualizado de sensibilidad al 90% CL tras 5 años de toma de datos es de $T_{1/2}^{0\nu} = 1.48 \times 10^{26}$ años y una masa del neutrino de Majorana de 47 - 131 meV. El número total de cuentas de ruido tras 5 años es de 0.6, lo que en la práctica convierte a NEXT-100 alta definición en un detector libre de ruido y que por lo tanto puede ser escalado a la tonelada para poder barrer todo el rango de masas correspondiente a la jerarquía inversa (20 - 50 meV).

La extrapolación de la tecnología de la alta definición a un detector de una tonelada de xenón ha sido evaluada de forma somera en el presente estudio. Aún con ciertas licencias en el diseño del futuro detector, una estimación del ruido esperado arroja una actividad de 7.89×10^{-6} cts keV⁻¹ kg⁻¹ yr⁻¹. Una figura tan baja de ruido permite que el incremento de masa de isótopo del nuevo detector tenga un reflejo casi lineal en la sensibilidad del detector, siendo la nueva sensibilidad tras 5 años de toma de datos de $T_{1/2}^{0\nu} = 1.34 \times 10^{27}$ años al 90% CL y una masa del neutrino Majorana de 12 - 33 meV, barriendo por completo el rango de masas de la jerarquía inversa.

Por último cabe destacar los esfuerzos de la colaboración en la búsqueda de la identificación del ión de bario (Ba⁺⁺) que se genera tras la desintegración $\beta\beta$ del xenón usando una técnica de microscopía de super-resolución sensible a una sola molécula (SMFI) usada ampliamente en bio-química. En la práctica supondría la eliminación de toda fuente de ruido a excepción de la desintegración $2\nu\beta\beta$. Este escenario permitiría reducir la actividad de ruido del detector a un valor residual de $\sim 5 \times 10^{-9}$ cts keV⁻¹ kg⁻¹ yr⁻¹ a la par que permitiría incrementar la eficiencia de detección de señal al 56%. La sensibilidad que se alcanzaría en este caso tras 5 años de toma de datos sería de $T_{1/2}^{0\nu} = 3.21 \times 10^{27}$ años al 90% CL y una masa del neutrino Majorana de 10 - 28 meV, con una mejora lineal de la sensibilidad $T_{1/2}^{0\nu}$ con la exposición.

En el hipotético caso de que la masa de los neutrinos siguiera la jerarquía normal en vez de la inversa, la tecnología necesaria para explorar las masas del neutrino de Majorana correspondientes (~ 1 meV) deberá contemplar inexorablemente el "*barium tagging*".

Agradecimientos

Me gustaría empezar dando las gracias a Juanjo. Los que le conocemos, sabemos de su entusiasmo por todo lo que hace. En mi caso, ha sabido transmitirme su pasión por la física y por la investigación. Pasión que ahora comparto con él, y que me ha hecho dedicar el poco tiempo libre del que he dispuesto a lo largo de estos últimos años a NEXT. Desde que le conozco, ha sido siempre un amigo, una especie de hermano mayor con el que he podido hablar de las cosas importantes de la vida, y eso ... no tiene precio.

Me gustaría agradecer también a mis más íntimos colaboradores en todos los estudios que he realizado: Justo, Paola y Miquel. No sería justo si no admitiera que sin su ayuda esta tesis no sería hoy una realidad. Cada uno a su manera y en su momento han sabido escucharme y explicarme, trabajar codo con codo, siempre de forma honesta, paciente y con una sonrisa. Mis más sentidas gracias.

También quiero agradecer al resto de gente que me he encontrado en el IFIC a lo largo de todos los años. A riesgo de olvidarme de alguno de ellos, me gustaría nombrar a Alex, Ánder, Andrew, Anselmo, Carmen, David, Francesc, Igor, Japepe, Jose, Jose María, Josh, Lorena, Luis, Michel, Nadia, Neus, Pau, Pepe, Raphaël, Ryan y Toni. A pesar de mi presencia intermitente, todos y cada uno de ellos me han hecho sentir uno más del equipo. La diferencia de edad no ayudaba, lo sé, pero me habéis hecho sentir más joven de lo que soy ... ¿Cómo no estaros agradecidos?

No puedo dejar de nombrar a mis hermanas y padres. Sin su cariño, su esfuerzo, su dedicación y fomento de la curiosidad, indudablemente no sería quien soy, no hubiera podido tener la formación que hoy tengo,

y no podría de ninguna forma haber realizado el presente doctorado. Eternamente agradecido.

No puedo olvidarme de mis amigos. Siempre han mostrado interés por ese *hobby* de Javi tan raro, al que tanto tiempo dedica. Más de uno me ha animado a no tirar la toalla en los momentos difíciles que han habido en el camino. Gracias por estar ahí siempre.

Y por último, mi familia. Chelo, mi esposa, doctora consorte desde el lado oscuro del trabajo diario de la casa y de los niños. A ella le debo todo lo que sé de física, y mis dos tesoros, Paula y Pablo. ¿Cómo no quererla? Paula me enseña que la belleza está en el interior. Y Pablo, mi pequeño, mi luchador, mi campeón, mi cruz, mi vida ... sin vosotros, nada tiene sentido.

A todos, GRACIAS.

Valencia, Abril de 2018

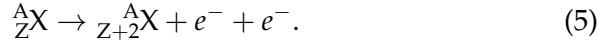
Summary

From all the particles conforming the universe, the most common and perhaps the most mysterious ones are neutrinos. Right now billions of these particles are passing through us without perceiving them, and detecting them requires huge detectors buried deep underground. First postulated by Wolfgang Pauli in 1930, they were named in 1934 as "small neutrons" by Enrico Fermi, alluding to two of their main characteristics: their small mass and their absence of electric charge. In the mid-70s, neutrinos were included in the Standard Model (SM) of particle physics under the premises of: lack of mass and electric charge, only affected by the nuclear weak force, the existence of 3 families with separately preserved leptonic numbers and to be neutrinos distinct from their antiparticles.

However, experiments of neutrino oscillations carried out during the last few decades have shown that neutrinos have mass and mix, opening up a new field of physics beyond the SM. One way to accommodate these masses in the theory is that neutrinos could be Majorana particles that is, identical to their own antiparticles, as opposed to the rest of fermions, and violate the conservation of leptonic numbers. If so, neutrinos could have relationship with the cosmic asymmetry of matter - antimatter via leptogenesis, and could be an elegant explanation of the smallness of their masses through the "see-saw" mechanism. Faced with this situation, it is easy to understand that nowadays neutrinos are a fashionable field of research, and many experiments worldwide try to shed light on their nature.

The most sensitive method to establish the nature of neutrinos is the search for a hypothetical and extremely rare nuclear transition called double beta decay without emission of neutrinos ($0\nu\beta\beta$) in which a nucleus with atomic number Z and mass number A decays to

a nucleus with atomic number $Z + 2$ emitting two electrons only:



Although the version of the process with neutrinos emission $2\nu\beta\beta$ has been observed and measured in several isotopes, the version without neutrinos has not been observed yet. The simplest physical mechanism describing the process is the virtual exchange of a Majorana neutrino, so that all the available energy in the decay ($Q_{\beta\beta}$) is shared between the two electrons emitted. The imprint left by these electrons in the detector is the key signal of the process and therefore, the goal of any experiment aimed to its search. The half-life of this process is given by:

$$(T_{1/2}^{0\nu})^{-1} = G^{0\nu} |M^{0\nu}|^2 \left(\frac{m_{\beta\beta}}{m_e}\right)^2 \quad (6)$$

where $G^{0\nu}$ is a phase-space factor, $M^{0\nu}$ is the nuclear matrix element of the transition, m_e is the electron mass and $m_{\beta\beta}$ is the effective Majorana mass of the electron neutrino given by:

$$m_{\beta\beta} \equiv \left| \sum_{i=1}^3 U_{ei}^2 m_i \right|, \quad (7)$$

where U_{ei} are the elements of the first row of the neutrino mixing matrix and m_i are the neutrino mass eigenstates. So from previous equation, the observation of the process will entail an indirect measurement of neutrino masses.

Current experiments of $\beta\beta$ -decay searches have followed different technological approaches, looking for the best energy resolution and the lowest possible background activity to maximize their sensitivity. To compare the potential of the different detectors, the sensitivity to $m_{\beta\beta}$ is used. It is given by:

$$\mathcal{S}(m_{\beta\beta}) \propto \sqrt{1/\varepsilon} \left(\frac{b \Delta E}{M t}\right)^{1/4}, \quad (8)$$

where ε is the detection efficiency of the experiment, M is the $0\nu\beta\beta$ isotope mass used in the experiment, t is the time of data taking, ΔE is the energy resolution of the detector and b is the background rate in

the energy window of interest (ROI) normally expressed in counts per keV, kilogram of source and year.

Among the most promising technologies are bolometers, TPCs, semiconductors and scintillators. Precisely to this last type belongs Kamland-ZEN, a Japanese experiment that making use of ^{136}Xe dissolved in liquid scintillator has established the highest limit to the decay half-life $T_{1/2}^{0\nu\beta\beta} = 1.07 \times 10^{26}$ years. It is worth to note here how unlikely the process is, with a half-life 17 orders of magnitude greater than the age of the universe itself, which makes its search a major technological and physical challenge.

The NEXT collaboration proposes a detector called *NEXT-100* for the search of $0\nu\beta\beta$ decays, whose sensitivity is the object of study of this thesis. It is an electroluminescent TPC containing 100 kg of xenon gas at 15 bar enriched at 91% for ^{136}Xe , that will be operated at Canfranc Underground Laboratory. Xenon gas is an ideal medium as it presents a series of key characteristics for the search of $\beta\beta$ decays such as easy enrichment in ^{136}Xe isotope, easy cleaning of impurities, presence of ionization and scintillation signals, intrinsic energy resolution better than 0.5% (FWHM at 2.5 MeV) and a very slow $2\nu\beta\beta$ decay mode.

NEXT-100 sensor planes are dedicated and optimized for different functions. Electrons from the $\beta\beta$ -decay ionize and scintillate xenon at the same time. The scintillation light is read by the large size PMTs of the cathode to give a measure of the beginning of the event (t_0). Ionization electrons drift towards the anode by the action of a moderate electric field (300 - 500 V cm $^{-1}$) where they are accelerated by the effect of a stronger electric field. This acceleration generates electroluminescence light or secondary scintillation proportional to the number of arriving electrons. This new light is also read from the cathode to provide the measure of the total energy deposited in the detector. On the other side, the anode instrumented with SiPMs equispaced 1 cm between them, reconstructs the topology of registered events through the reading of the same electroluminescence light.

This way, the signal of two-electrons originated from a single vertex with total deposited energy of ^{136}Xe $Q_{\beta\beta}$ (2458 keV) corresponding to the $0\nu\beta\beta$ signal present a very characteristic morphology when being reconstructed by the detector. On one side, the anode provides the topological reconstruction of a single energy deposition in the

form of a long track, with a constant density of energy deposition per unit of space, which presents areas of high energy deposition at both extremes due to the Bragg peaks. The topological reconstruction is mainly affected by the diffusion of ionization electrons along the drift, the diffusion of electroluminescence light, and the sensors pitch. The expected spatial resolution is 10 and 5 mm for transverse and longitudinal components respectively. On the other side, the cathode provides a measure of the total energy deposited on the active volume which in case of our signal, it will be 2458 keV with an estimated energy resolution of 0.7% FWHM.

Any event recorded in the detector capable of imitating the imprint left by the $0\nu\beta\beta$ signal is considered a background event and, as seen above, its minimization is key to maximize the sensitivity of the detector. The identification and evaluation of all of them under different circumstances is the main objective of this thesis. The main background sources for NEXT-100 are:

- *Natural radioactivity* present in all components and materials of the detector. It's the most common source of background for these type of experiments. Especially damaging for NEXT-100 are the isotopes ^{208}Tl and ^{214}Bi from the thorium and uranium decay chains respectively, whose de-excitation gammas possess an energy close to $Q_{\beta\beta}$ and which may eventually present a topology similar to that of the signal. The selection of extremely radiopure components is therefore essential in the manufacture of rare-event searching detectors like ours.
- *Radon* is also an intermediate product of the natural decay chains whose isotope ^{222}Rn , with origin in the uranium and half-life of 3.8 years is particularly harmful. There are several mechanisms by which radon can produce background events: from laboratory air, from the pollution that can present xenon, and from the degassing of detector materials close the active volume. To mitigate these backgrounds, the LSC has purchased a system that reduces by 4 orders of magnitude the presence of radon in laboratory air; and eventually, if needed, radon traps to filter the xenon could be installed in the gas system.

- *Cosmogenic muons.* A flux of $3 \times 10^{-6} \text{ cm}^{-2}\text{s}^{-1}$ has been measured in LSC Hall A, with a theoretically estimated energy between 220 and 245 GeV with high uncertainty. The muon passage through the detector creates a series of unstable nuclei and neutrons that generate electromagnetic cascades capable of generating background events. Initially, a scintillators system surrounding the detector is able to detect their passage, and by applying a dead time after the muon tag, discard the corresponding background. A second muon contribution comes from the xenon activation by secondary neutrons. The beta decay of ^{137}Xe with a Q-value of 4173 keV introduces a number of events in our energy region of interest, which ultimately cannot be vetoed and must be taken into account in the detector background budget.
- *Neutrons* are very penetrating particles capable of activating different isotopes in detector components or generating alphas and protons that can end up generating energetic gammas that finally can lead to background events. In the LSC, the highest percentage of neutrons originates from uranium and thorium contamination of lab rocks and the total measured flux is $\phi_{\text{HallA}} = 1.38 \pm 0.14 \times 10^{-5} \text{ cm}^{-2} \text{ s}^{-1}$. Like muons, neutrons can also generate background through xenon activation. Luckily, neutrons are easily vetoed. There are commercial slabs of 20 cm thickness of boron-doped at 5% polyethylene, which reduce neutron flux by 3 orders of magnitude making their contribution to the background budget negligible.

Part of the aim of this thesis is to simulate and evaluate the signal efficiency, the expected background activity from each source and type, and using this data, estimate the sensitivity of the detector. Simulations are Monte Carlo type, and they are based on GEANT4. The analysis consists of the sequential application of a series of algorithms and cut-offs to quantify the fraction of signal events and all kind of backgrounds that possess the energy and topologic pattern of the $0\nu\beta\beta$ decays. The main results obtained are summarized in a signal efficiency of 32% and a total expected background level of $< 4.22 \times 10^{-4} \text{ cts keV}^{-1} \text{ kg}^{-1} \text{ yr}^{-1}$, being the largest contribution the natural radioactivity present in both measurement planes. Thanks to

these values, the NEXT-100 sensitivity after 5 years of data taking is $T_{1/2}^{0\nu} = 9.85 \times 10^{25}$ years at 90% CL, which corresponds to an effective mass of Majorana neutrinos of 57 - 161 meV depending on the nuclear matrix element (NME) used; yielding the best sensitivity limits published to date.

Latest studies carried out within the collaboration allow an evolution of NEXT-100 detector to a *high-definition* version that improves the performance of the detector and the analysis response. The main improvements and their consequences are:

- *High spatial resolution.* The addition of certain gases to xenon such as the CO₂ or He allows the reduction of transversal and longitudinal diffusions to levels around 2 mm / sqrt(m) while maintaining the light yield. In practice, this improvement allows "to see" events in the detector in high-definition, what leads to better background discrimination based on their topological signature.
- *High energy resolution.* The latest energy resolution measurements made in NEW for single-point events have reached a 0.5%, and we expect to be able to extend this resolution to larger events in the short term. This improvement allows for a linear reduction ²⁰⁸Tl and ¹³⁷Xe backgrounds, and in a higher factor for ²¹⁴Bi.
- *Deep Neural Networks.* Preliminary studies carried out by the collaboration in the use of DNNs for topological discrimination of events have already shown a noticeable improvement over the standard analysis. It must be noted that there is a considerable room for improvement in the use of these novel techniques.

The combination of these three improvements supposes a reduction of the expected background rate to 6.82×10^{-5} cts keV⁻¹ kg⁻¹ yr⁻¹ with a signal efficiency of 29%. The updated value of sensitivity at 90% CL after 5 years of data taking is $T_{1/2}^{0\nu} = 1.48 \times 10^{26}$ years and an effective mass of Majorana neutrinos of 47 - 131 meV. The total number of background counts expected after 5 years is 0.6, what makes NEXT-100 high definition a background-free detector and therefore it can be scaled to the ton to be able to cover the full mass range corresponding to the inverse hierarchy (20 - 50 meV).

The extrapolation of the NEXT high-definition technology to a tonne detector has been succinctly evaluated in present study. Although with some licenses in the future detector design, an estimate of the expected background rate yields an activity of 7.89×10^{-6} cts $\text{keV}^{-1} \text{kg}^{-1} \text{yr}^{-1}$. Such a low background figure allows a quasi-linear improvement of detector sensitivity with the increase of the isotope mass, yielding a new sensitivity after 5 years of data taking of $T_{1/2}^{0\nu} = 1.34 \times 10^{27}$ years at 90% CL and an effective mass of Majorana neutrino of 12 - 33 meV and thus, completely covering the mass range of the inverse hierarchy.

Finally, it is worth highlighting the efforts of the collaboration in the search for a method to identify the barium ions (Ba^{++}) generated after xenon decays using single molecule fluorescence imaging technique widely used in bio-chemistry. In practice, it would suppose the elimination of all background types but $2\nu\beta\beta$ decays. This new scenario would imply the reduction of background rate to a residual level of $\sim 5 \times 10^{-9}$ cts $\text{keV}^{-1} \text{kg}^{-1} \text{yr}^{-1}$ and at the same time, it would allow to increase the signal detection efficiency to 56%. After 5 years of data taking the reached sensitivity would be $T_{1/2}^{0\nu} = 3.21 \times 10^{27}$ years at 90% CL and an effective mass of Majorana neutrinos of 10 - 28 meV, with a linear improvement of the $T_{1/2}^{0\nu}$ sensitivity with the exposure.

In the hypothetical case that neutrino masses followed the normal hierarchy rather than the inverse, the technologies needed to cover the corresponding range of masses (~ 1 meV) must inexorably contemplate the "barium tagging".

Contents

Resumen	i
Agradecimientos	ix
Summary	xi
1 The nature of neutrinos	1
1.1 A Brief History of Neutrinos	1
1.2 Neutrinos in the Standard Model	5
1.3 Massive Neutrinos	9
1.3.1 Experimental Neutrino Mass Measurement . . .	12
1.3.2 Dirac vs Majorana Neutrinos	17
2 Neutrinoless double beta decay	21
2.1 Double Beta Decay	21
2.2 Neutrinoless Double Beta Decay	23
2.3 Design of Double Beta Decay Experiments	26
2.4 Current Experiments	32
2.4.1 Bolometer Detectors – CUORE	32
2.4.2 Time Projection Chambers – EXO	34
2.4.3 Semiconductors – GERDA, MAJORANA	37
2.4.4 Scintillators – KamLAND-Zen, SNO+	39
2.4.5 Other Experiments	42
3 The NEXT Experiment	45
3.1 Xenon Gas as Source and Detector Medium	46
3.2 The SOFT Concept	56
3.3 Detectors	57

3.3.1	R&D Prototypes	59
3.3.2	NEXT NEW	64
3.3.3	NEXT-100	78
4	NEXT $0\nu\beta\beta$ Backgrounds	83
4.1	Natural Decay Series	85
4.2	Radon	91
4.3	Muons and Neutrons	96
4.4	Negligible Backgrounds	103
5	Detector Simulation	107
5.1	Geant4 and Nexus	107
5.2	Simulation Modes	111
5.3	Validation	112
5.3.1	Data vs Parameterized Simulation	112
5.3.2	Full vs Parameterized Simulations	113
5.4	NEXT-100 Simulation	120
6	Classical Analysis	127
6.1	Analysis Description	127
6.1.1	Energy and Position Smearing	128
6.1.2	Topology	130
6.1.3	ROI	136
6.1.4	Summary	137
6.2	Parameterized and Fast Modes comparison	139
6.3	NEXT-100 Background Model	141
6.3.1	Natural Decay Chains	141
6.3.2	Radon	143
6.3.3	Muons and Neutrons	145
6.3.4	Summary	153
6.4	NEXT-100 Sensitivity	154
6.4.1	Sensitivity Procedure	154
6.4.2	Sensitivity Results	158
7	NEXT High Definition	161
7.1	High Spatial Resolution	161
7.2	Deep Neural Networks	166
7.2.1	Deep Learning	167

7.2.2	DNNs and NEXT-100	168
7.3	High Energy Resolution	171
7.4	NEXT100-HD Sensitivity	172
8	Towards The Inverted Hierarchy	177
8.1	NEXT-Ton	177
8.2	Barium Tagging	179
	Bibliography	187

The nature of neutrinos

1.1 A Brief History of Neutrinos

The existence of neutrinos was first proposed by W. Pauli in December 1930 in the famous letter addressed to participants of a nuclear conference in Tübingen [2] as a *desperate remedy* to preserve the principle of energy conservation in β -decays.

At that time protons and electrons were considered elementary particles and nuclei were considered bound states of protons and electrons. In this framework, there was a fundamental problem with β decays. The emission of a single e^- with a fixed kinetic energy $Q = (M_{A,Z} - M_{A,Z+1}) - m_e$ was expected but experiments, however, showed a continuous β spectrum with end-point energy equal to Q .

There was a belief that continuous β -spectra could be explained by the energy loss of electrons in the target. However, in 1927 Ellis and Wooster performed a calorimetric β -decay experiment [3] that proved that the energy detected in the β -decay was smaller than the total released energy.

Pauli was the first to understand that under the condition of energy-momentum conservation the only possibility to explain the continuous β -spectra was to assume the existence of a new neutral particle which was emitted in β -decays alongside the electron and couldn't be detected by detectors of the time. This way, if the β -decay is a three-body process $(A, Z) \rightarrow (A, Z + 1) + e^- + "n"$, the released energy is shared between the electron and the new neutral particle, and a continuous electron spectrum could be observed. Pauli called this new particle "the neutron" and according to his theory it had spin 1/2 and a very light mass. He worried that he might have postulated a particle which could never be detected.

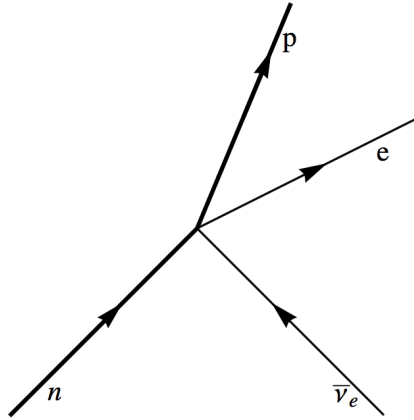


Figure 1.1: Fermi four-fermion coupling responsible for β -decay.

The next fundamental contribution to the development of the idea of the neutrino was made in the thirties. In 1934 E. Fermi [4] built the first theory of the β -decay of nuclei depicted in Figure 1.1, based on Pauli's assumptions and called the light and neutral Pauli particle *the neutrino* (from neutral and small in Italian). In 1937 Italian physicist E. Majorana [5] proposed a new theory for particles without electric charge and spin equal to $1/2$ (which today are called Majorana particles) in which particles and antiparticles are identical. One of the most important open issues of modern neutrino physics is if the neutrino is a truly neutral Majorana particle or a Dirac particle with a lepton number.

Physicists in the thirties and the forties started to think about possible experiments to detect the elusive particle. An early estimate of the neutrino absorption length in solid matter by Bethe and Pearls [6] gave a result larger than 10^{14} km (very close to the current value) which, due to the limited technology available at the time, made a direct detection unfeasible, and made them conclude that "*it is absolutely impossible to observe processes of this kind*".

The first method of neutrino detection was proposed by B. Pontecorvo in 1946 [7]. He wrote "*The object of this note is to show that*

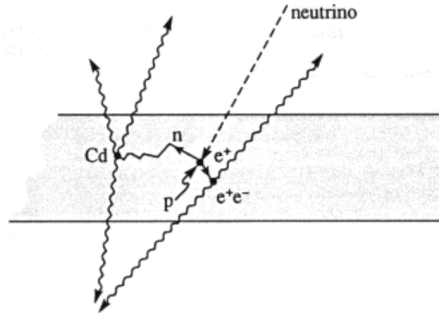
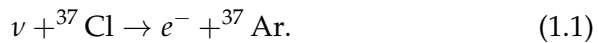


Figure 1.2: Detection technique in the Reines-Cowan experiment.

the experimental observation of an inverse β process produced by neutrino is not out of the question with the modern experimental facilities, and to suggest a method which might make an experimental observation feasible". Pontecorvo proposed radiochemical methods of neutrino detection. He considered the Cl-Ar reaction (eq. 1.1) as an appropriate candidate for neutrino detection. After irradiation of a target (containing ^{37}Cl) by neutrinos for a relatively long time a few radioactive atoms of ^{37}Ar could be produced. As argon is a noble gas, atoms of ^{37}Ar can be easily extracted from the target and can be placed into a proportional counter in which their decay will be detected.



In 1953-1959 physicists Fred Reines and Clyde Cowan designed the first experiment [8] that proved the existence of neutrinos through the observation of the process



They used the Savannah River reactor as $\bar{\nu}_e$ source, and steel and plastic tanks filled with liquid scintillator ($1.4 \cdot 10^3$ liters of CdCl_2) as target. They were able to detect neutrinos thanks to the clean signal given by the positron and neutron in delayed coincidence depicted in Figure 1.2. This experiment not only led to the discovery of anti-neutrinos, but introduced a detection technique that is still being used

today in state-of-the-art reactor neutrino experiments, that continue to make discoveries in neutrino physics. In 1995 F. Reines was awarded with the Nobel Prize for the first detection of the neutrino.

Pontecorvo's radiochemical method of neutrino detection was used by R. Davis and collaborators [9] in the first experiment in which solar neutrinos were detected, and he was awarded with the Nobel Prize in 2002 for their detection.

Soon after anti-neutrinos were discovered, it was realized that they come in flavours. The muon had been discovered in cosmic rays much earlier, but it took a long time to understand that this particle was the heavier version of the electron, and that the process analogous to β decay involving muons was pion decay

$$\pi^- \rightarrow \mu^- + \bar{\nu}_\mu \quad (1.3)$$

In 1962, the Brookhaven neutrino experiment [10] was the first experiment dealing with accelerator neutrinos originating from decays of pions, kaons and muons. Lederman, Schwartz and Steinberger created the first neutrino beam mimicking what happens in cosmic rays. A boosted photon beam hits a target producing pions and other hadrons that decay into neutrinos and other particles. A neutrino detector is located behind the shield. A neutrino event is identified by the appearance of a muon in the detector.

The Brookhaven experiment led to the discovery of the second neutrino: It proved that ν_e and ν_μ are different particles, and it established the pair (ν_μ, μ) as the second family of leptons accompanying the first family (ν_e, e) . Again, this was such a great idea that it became the so-called conventional accelerator neutrino beam, and we are still making discoveries with modern versions of it.

The results of the Brookhaven and other experiments suggested that the total electron and muon lepton numbers L_e and L_μ , which are called flavor lepton numbers, were conserved:

$$\sum_i L_e^{(i)} = \text{const}; \quad \sum_i L_\mu^{(i)} = \text{const} \quad (1.4)$$

Finally, the third type of neutrino ν_τ , the partner of the τ -lepton, was observed in 2000 in an experiment performed by the DONUT

Collaboration at Fermilab [11]. In this experiment the production of τ was observed in the process

$$\nu_\tau + (A, Z) \rightarrow \tau + \dots \quad (1.5)$$

The reader interested in this topic may consult the paper "Neutrino. The history of a unique particle" by S. M. Bilenky [12], that has been used as a guide for this section.

1.2 Neutrinos in the Standard Model

The Standard Model of particle physics was developed in the mid 1970s. Over the past 35 years, it has been an extremely successful theory of electromagnetic, weak, and strong nuclear interactions; providing an excellent description of most of the phenomena of particle physics. But there are still some missing pieces in it, many of them related with neutrinos and their intrinsic characteristics.

At the time the Standard Model (figure 1.3) was constructed, it was assumed that:

- Neutrinos had exactly zero mass.
- There were exactly three neutrinos, one for each of the three charged leptons, and lepton number was conserved separately for each of the three lepton families (e, ν_e) , (μ, ν_μ) , (τ, ν_τ) .
- Neutrinos and antineutrinos were distinct.
- All neutrinos were left-handed, and all antineutrinos were right-handed.
- Neutrinos had no color or electromagnetic charge, and hence they only feel the weak force.

With hindsight, the problems with the neutrino picture in the Standard Model were already visible before the model was even built. The results from Ray Davis' chlorine-37 solar neutrino experiment [9] showed that the electron-neutrino flux from the Sun was only about 1/3 of that expected from the predictions of the Standard Solar Model. Although these results were not taken too seriously, due to the lack

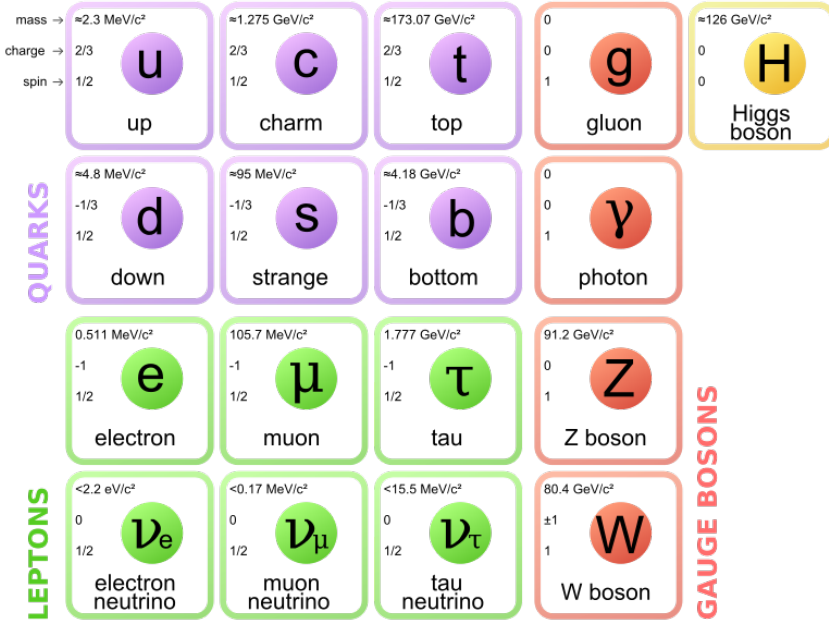


Figure 1.3: Particle content of the Standard Model. Notice the mass scale of neutrinos compared with that of other fundamental particles. Reproduced from [13].

of confidence at the time on the Standard Solar Model; following experiments confirmed the reality of the deficit.

At the end of the eighties the solar neutrino experiment Kamiokande-II [14] only observed $46(\pm 13)\%$ of the predicted flux of high energy neutrinos (>9.3 MeV), via the recoil electrons from the elastic $\nu + e \rightarrow \nu + e$ scattering reaction from the decay

$${}^8\text{B} \rightarrow {}^8\text{Be} + e^+ + \nu_e \quad (1.6)$$

while at the beginning of the nineties, two new solar neutrino experiments based on Gallium: GALLEX [15] and SAGE [16] were performed with similar conclusion. In these experiments, like in Davis' experiment, ν_e 's were detected via the observation of radioactive ${}^{71}\text{Ge}$ atoms produced in the process

$$\nu_e + {}^{71}\text{Ga} \rightarrow e^- + {}^{71}\text{Ge} \quad (1.7)$$

The event rates measured by these experiments were $62(\pm 10)\%$ of the predicted flux for energies >0.233 MeV.

Therefore, by the mid-1990s, the *solar neutrino problem* had become a real issue. All the experiments were seeing a deficit of detected neutrinos, but these were not constant but a function of neutrino energy. The fact that different experiments sensitive to the same neutrinos saw similar deficits revealed that the differences were likely to be real. In this landscape, the hypothesis of neutrino oscillations first pointed out by Bruno Pontecorvo in 1957 [17] arising from a mixture between the flavour and mass eigenstates of neutrinos, became the easiest explanation for these results.

In 1998, the situation with neutrino oscillations drastically changed. The Super-Kamiokande atmospheric neutrino experiment [18] observed a significant up-down asymmetry of the high-energy muon events. A striking feature of these results was the zenith angle distribution for muon-neutrinos, as shown in Figure 1.4. Neutrinos produced in the Earth atmosphere and coming from above travel distances ranging from about 20 km to 500 km. Neutrinos arriving at the detector from below pass through the Earth and travel distances ranging from 500 km to about 12 000 km. The number of up-going high-energy muon neutrinos was about two times smaller than the number of down-going high-energy muon neutrinos. Thus, it was proved that the number of observed muon neutrinos depends on the distance which neutrinos passed from a production point in the atmosphere to the detector.

In 2002 the SNO solar neutrino experiment [19] observed the disappearance of solar ν_e . In this experiment high-energy solar neutrinos from ${}^8\text{B}$ -decay were detected through the observation of CC and NC reactions. The detection of solar neutrinos through the observation of the CC reaction allows one to determine the flux of solar ν_e on the earth, while the detection of solar neutrinos through the observation of the NC reaction allows one to determine the flux of all flavor neutrinos (ν_e , ν_μ and ν_τ). The flux of solar ν_e observed was approximately three times smaller than the flux of ν_e , ν_μ and ν_τ together. Thus, it was proved that solar ν_e 's on the way from the sun to the earth were transferred to ν_μ and ν_τ .

In 2002-2004 the KamLAND reactor neutrino experiment [20] observed evidence of oscillations of ν_e . In this experiment ν_e 's from 55

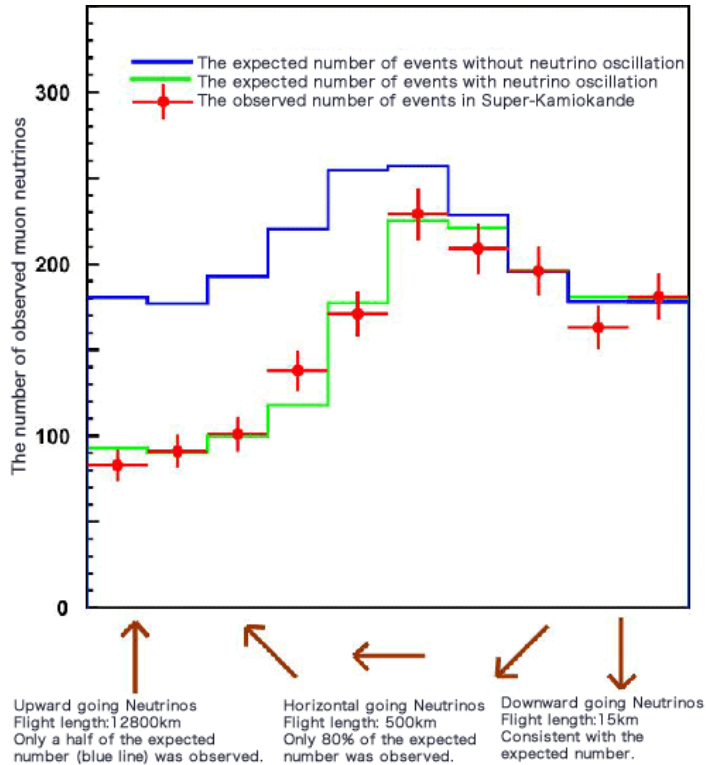


Figure 1.4: From [18]: Super-K observed and predicted number with and without oscillations of muon neutrinos vs zenith angle. The difference between data and expectations without oscillations (red line) increases with the distance travelled.

reactors at an average distance of about 170 km from the large KamLAND detector were recorded. It was found that the total number of $\bar{\nu}_e$ events was about 0.6 of the number of the expected events.

Finally neutrino oscillations from any kind of source (solar, atmospheric and reactor) had been proven and precisely measured. The Standard Model requires massless neutrinos in its basic formulation, but the theory of neutrino oscillations implies massive neutrinos, opening up a new field of physics beyond the Standard Model.

1.3 Massive Neutrinos

Neutrino oscillations rely on the quantum-mechanical idea of mixed states. Although the neutrino is in a well-defined flavour state when it is produced (defined by the charged lepton with which it was associated), and it is in a well-defined flavour state when it interacts, it is not in a well-defined flavour state when it travels between the two. The property that is well-defined as the neutrino travels is its mass, and as there are three different types of neutrino, there will be three distinct mass states. Different masses imply different speeds, therefore when the neutrino has traveled some distance, the proportions of each mass eigenstate have changed, and the probability of being a certain flavour has also changed.

The mathematics of oscillation is essentially identical to the mathematics of rotation. A flavour state can be expressed mathematically as a combination of the three mass eigenstates:

$$| \nu_\alpha \rangle = \sum_i U_{\alpha i}^* | \nu_i \rangle \quad (1.8)$$

where $| \nu_\alpha \rangle$ is a neutrino with flavour $\alpha = e$ (electron), μ (muon) or τ (tau), and $| \nu_i \rangle$ is a neutrino with definite mass m_i ($i = 1, 2, 3$). $U_{\alpha i}$ represents the αi entry of the Pontecorvo-Maki-Nakagawa-Sakata (PMNS) lepton mixing matrix:

$$U = \begin{pmatrix} U_{e1} & U_{e2} & U_{e3} \\ U_{\mu1} & U_{\mu2} & U_{\mu3} \\ U_{\tau1} & U_{\tau2} & U_{\tau3} \end{pmatrix} \quad (1.9)$$

If this matrix were the identity matrix, then the flavour eigenstates would be the same as the mass eigenstates. However, the experimental

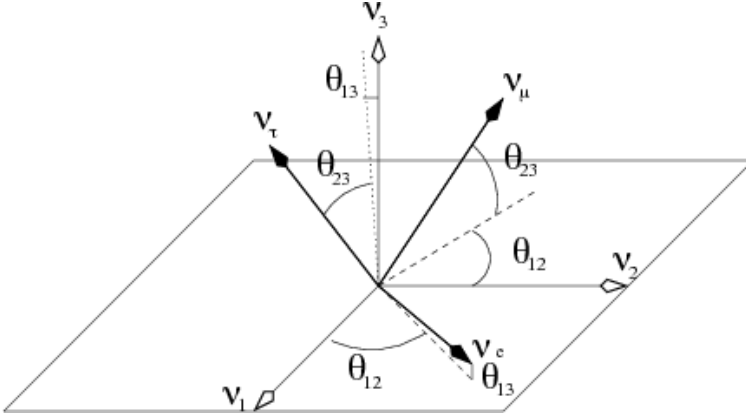


Figure 1.5: Representation of the three mass eigenstates and the three flavour eigenstates, with all the mixing angles playing the game.

data show that this is not the case. When the standard three neutrino theory is considered, the standard parametrization of the matrix is

$$U = \begin{pmatrix} c_{12}c_{13}e^{i\alpha_1/2} & s_{12}c_{13} & s_{13}e^{-i\delta} \\ -s_{12}c_{23} - c_{12}s_{23}s_{13}e^{i\delta} & (c_{12}c_{23} - s_{12}s_{23}s_{13}e^{i\delta})e^{i\alpha_2/2} & s_{23}c_{13} \\ s_{12}s_{23} - c_{12}c_{23}e^{i\delta} & -c_{12}s_{23} - s_{12}c_{23}s_{13}e^{i\delta} & c_{23}c_{13} \end{pmatrix} \quad (1.10)$$

where α_1 and α_2 are the two Majorana phases which exist only if neutrinos are Majorana particles. The phases α_1 and α_2 together with the phase factor δ are different from zero only if neutrinos violate CP symmetry, that is a difference between $P(\nu_\alpha \rightarrow \nu_\beta) \neq P(\bar{\nu}_\alpha \rightarrow \bar{\nu}_\beta)$, for $\alpha \neq \beta$. The parameter c_{ij} means $\cos\theta_{ij}$ and s_{ij} means $\sin\theta_{ij}$, where θ_{ij} is the mixing angle between neutrino masses as described in Figure 1.5.

The Simplest Oscillation Scenario

Although neutrino oscillations imply massive neutrinos, oscillation experiments are only sensitive to the differences between the squared neutrino masses:

$$\Delta m_{ij}^2 = m_i^2 - m_j^2 \quad (1.11)$$

and not to the absolute mass scale.

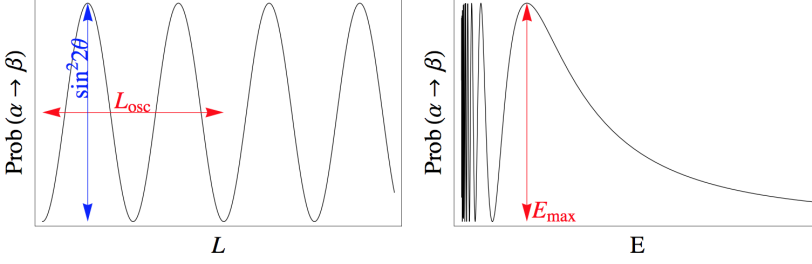


Figure 1.6: Left: two-family appearance oscillation probability as a function of the baseline of L at fixed neutrino energy. Right: same probability shown as a function of the neutrino energy for fixed baseline.

In the simplest case of two-family mixing in vacuum, the mixing matrix depends on just one mixing angle:

$$V_{\text{PMNS}} = \begin{pmatrix} \cos \theta & \sin \theta \\ -\sin \theta & \cos \theta \end{pmatrix} \quad (1.12)$$

and there is only one mass square difference Δm^2 . The oscillation probability for both neutrinos and antineutrinos, becomes the well-known expression:

$$P(\nu_\alpha \rightarrow \nu_\beta) = \sin^2 2\theta \sin^2 \left(1.27 \frac{\Delta m^2 (\text{eV}^2) L (\text{Km})}{E_\nu (\text{GeV})} \right), \quad \alpha \neq \beta \quad (1.13)$$

of a sinusoidal function with a period determined by the oscillation length:

$$L_{\text{osc}} (\text{km}) = 2\pi \frac{E_\nu (\text{GeV})}{1.27 \Delta m^2 (\text{eV}^2)}, \quad (1.14)$$

proportional to the neutrino energy and inversely proportional to the neutrino mass square difference. The amplitude of the oscillation is determined by the mixing angle. It is maximal for $\sin^2 2\theta = 1$ or $\theta = \pi/4$. The oscillation probability as a function of the baseline is shown on the left plot of Fig 1.6.

In many neutrino oscillation experiments the baseline is not varied but the oscillation probability can be measured as a function of the

neutrino energy. This is shown on the right plot of Fig 1.6. In this case, the position of the first maximum contains information on the mass splitting:

$$E_{\max} (\text{GeV}) = 1.27 \frac{\Delta m^2 (\text{eV}^2) L (\text{Km})}{\pi/2}, \quad (1.15)$$

An optimal experiment that intends to measure both the mixing and the mass splitting requires running at $E/L \sim \Delta m^2$.

Current knowledge

Global analyses of the existing neutrino oscillation data [21] have determined with relatively good precision (at the few percent level) the value of the three mixing angles: the *solar* angle $\theta_{12} \simeq 34^\circ$, the *atmospheric* angle $\theta_{23} \simeq 42^\circ$ and the *reactor* angle $\theta_{13} \simeq 9^\circ$; each named according to its main measurement channel. Experiments using solar and reactor neutrinos have measured one mass difference, the so-called *solar mass splitting*: $\Delta m_{\text{sol}}^2 \simeq 7.5 \times 10^{-5} \text{ eV}^2$. Atmospheric and accelerator-based oscillation experiments have measured another mass difference, the *atmospheric mass splitting*: $\Delta m_{\text{atm}}^2 \simeq 2.5 \times 10^{-3} \text{ eV}^2 \gg \Delta m_{\text{sol}}^2$. These results cannot differentiate between two possibilities for the neutrino mass ordering, usually referred to as *normal* and *inverted* orderings. In the former, Δm_{sol}^2 is the difference between the squared masses of the two lightest mass states, while in the latter it corresponds to the difference between the two heaviest states. This is illustrated in Figure 1.7. Notice that the states have been numbered in such a way that $\Delta m_{\text{sol}}^2 \equiv \Delta m_{21}^2$ is always greater than zero, whereas Δm_{atm}^2 is a positive quantity in the normal ordering ($\Delta m_{\text{atm}}^2 \equiv \Delta m_{31}^2 > 0$) and a negative one in the inverted ordering ($\Delta m_{\text{atm}}^2 \equiv \Delta m_{32}^2 < 0$). Our present knowledge of neutrino masses and mixings provided by neutrino oscillation data is summarized in Table 1.1.

Besides the CP-violation phase and the neutrino mass ordering, another piece of information remains to be known: the absolute value of the lightest neutrino mass which will be discussed in next section.

1.3.1 Experimental Neutrino Mass Measurement

Neutrino oscillation experiments only provide information about relative differences between the mass eigenstates, not the absolute mass

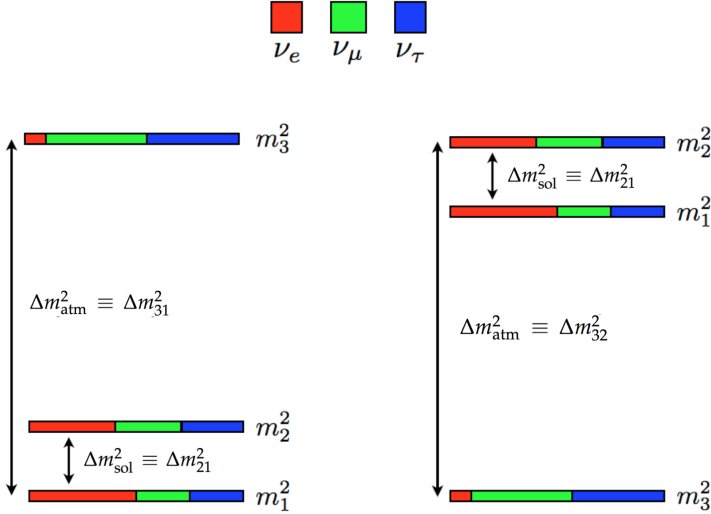


Figure 1.7: Current knowledge of neutrino masses and mixings from neutrino oscillation experiments. Left and right panels show, respectively, the normal and inverted mass orderings. Neutrino masses increase from bottom to top. The electron, muon and tau flavour contents of each neutrino mass eigenstate are shown via the red, green and blue fractions, respectively.

Table 1.1: Neutrino mixing parameters according to the most recent global oscillation analysis [21]. Note that $\Delta m_{3i}^2 \equiv \Delta m_{31}^2$ for the normal ordering and $\Delta m_{3i}^2 \equiv \Delta m_{32}^2$ for the inverted one.

Parameter	Normal ordering		Inverted ordering	
	best fit $\pm 1\sigma$	3σ range	best fit $\pm 1\sigma$	3σ range
θ_{12} ($^\circ$)	$33.56^{+0.77}_{-0.75}$	[31.38, 35.99]	$33.56^{+0.77}_{-0.75}$	[31.38, 35.99]
θ_{23} ($^\circ$)	$41.6^{+1.5}_{-1.2}$	[38.4, 52.8]	$50.0^{+1.1}_{-1.4}$	[38.8, 53.1]
θ_{13} ($^\circ$)	$8.46^{+0.15}_{-0.15}$	[7.99, 8.90]	$8.49^{+0.15}_{-0.15}$	[8.03, 8.93]
δ_{CP} ($^\circ$)	261^{+51}_{-59}	[0, 360]	277^{+40}_{-46}	[145, 391]
Δm_{21}^2 (10^{-5} eV 2)	$7.50^{+0.19}_{-0.17}$	[7.03, 8.09]	$7.50^{+0.19}_{-0.17}$	[7.03, 8.09]
Δm_{3i}^2 (10^{-3} eV 2)	$2.524^{+0.039}_{-0.040}$	[2.407, 2.643]	$-2.514^{+0.038}_{-0.041}$	[-2.635, -2.399]

values. The absolute scale of neutrino masses is very important for understanding the evolution and the structure formation of the universe as well as for nuclear and particle physics beyond the Standard Model. Complementary to deducing constraints on the sum of all neutrino masses from cosmological observations, two different methods to determine the neutrino mass scale in the laboratory are pursued: the search for neutrinoless double β -decay (see § 2) and the direct neutrino mass search by investigating single β -decays or electron captures.

Measurement with β decay

Ideally, the simplest way to measure the absolute neutrino mass is to look at the energy spectrum of the electron emitted by a β decay source, also called the *Kurie plot* (Figure 1.8). In beta decay, an electron and an anti-neutrino are emitted, with the total transition energy (Q_β) being distributed between their kinetic energies, the electron mass and the electron anti-neutrino mass. The difference between the maximum energy released by the β particle and the Q_β value can provide an estimation of the effective electron neutrino mass (m_β). However, this measurement is very challenging due to the small mass of the neutrino, smaller than 1 eV [22].

Different experiments have employed this technique, most of them using tritium as the source ($Q_\beta = 18570$ eV). The Troitsk experiment [23] and the Mainz experiment [24], established an upper limit for the electron neutrino mass of 2.5 eV and 2.3 eV respectively, giving a combined limit of 2 eV [25]. In the forthcoming years, the KATRIN experiment [26] is expected to improve the current limit by almost an order of magnitude thanks to better statistics, energy resolution and background rejection. It will reach a sensitivity to the electron neutrino mass of 0.30 eV with 3 sigma significance and 0.35 eV with 5 sigma significance.

Measurement with Cosmology

Neutrinos are the second largest population of particles in the Universe, behind photons. Therefore, massive neutrinos would have had an impact on the rate of expansion and the growth of perturbations [27], producing a measurable effect in the Universe's structure.

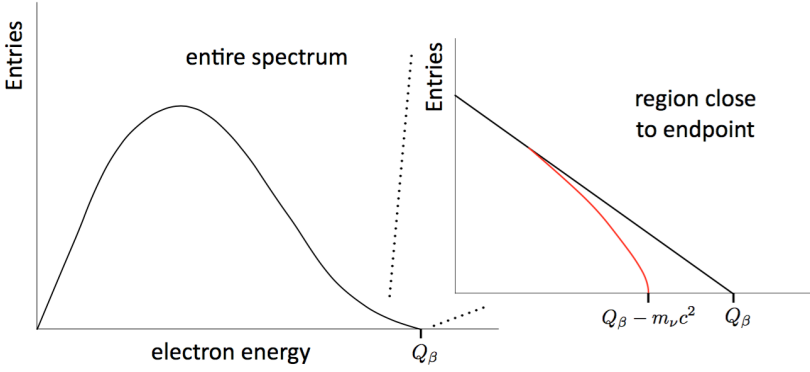


Figure 1.8: Energy spectrum of beta decay showing the endpoint region. The black line corresponds to zero neutrino mass and the red line to finite neutrino mass.

Cosmological observations can probe the sum of the neutrino masses,

$$\sum_{\nu} m_{\nu} \equiv m_1 + m_2 + m_3 \quad (1.16)$$

The study of the distribution of galaxies in the Universe and supernovae, combined with the Cosmic Microwave Background (CMB) data of WMAP experiment [28] provide an upper limit for the sum of all neutrino masses. Depending on the model complexity and the input data used one obtains [29] $\sum_{\nu} m_{\nu} < (0.3 - 1.3) \text{ eV}$ (at 95% CL). In 2015 the Planck collaboration published their most recent constraints on $\sum_{\nu} m_{\nu}$ [30]. In combination with supernovae and Baryon Acoustic Oscillations (BAO) data lowers the limit to:

$$\sum_{\nu} m_{\nu} < 0.23 \text{ eV (95% CL)} \quad (1.17)$$

Although preliminary, it is worth to mention here the recently published measurement of $\sum_{\nu} m_{\nu} = 0.11 \pm 0.03 \text{ eV}$ by the Sloan Digital Sky Survey (SDSS) [31].

The relationship between $\sum m_{\nu}$ and the lightest neutrino mass m_{light} (m_1 in the case of normal ordering, or m_3 in the case of inverted)

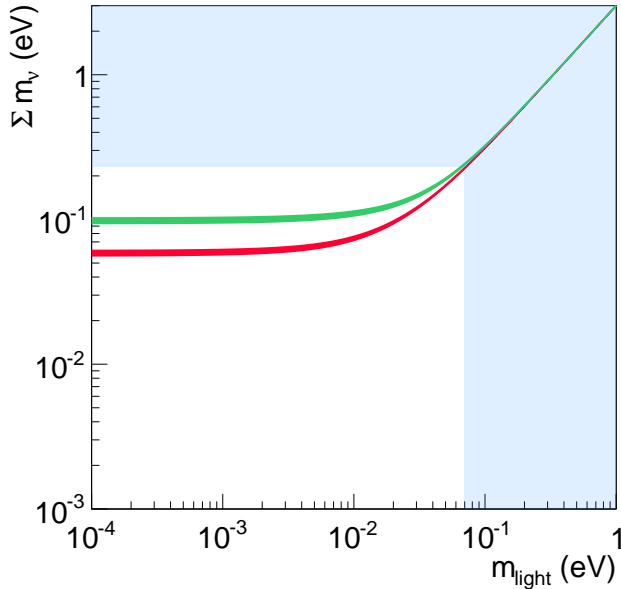


Figure 1.9: Constraints on the lightest neutrino mass m_{light} coming from cosmology. The red and green bands correspond to the allowed regions of the normal and inverted orderings, respectively. The $\sum m_\nu$ upper bound, by the Planck Collaboration [30], translates into an upper limit on m_{light} shown via the vertical band in the same panel.

is shown in Figure 1.9. The red and green bands correspond to the normal and inverted orderings. The width of the bands is given by the 3σ ranges in the mass oscillation parameters Δm_{sol}^2 and Δm_{atm}^2 shown in Table 1.1. The horizontal blue band in the graph is the upper limit on $\sum m_\nu$ quoted above (eq. 1.17). In the quasi-degenerate regime of neutrino masses corresponding to that upper bound, $m_{\text{light}} \simeq \sum m_\nu / 3 \leq 0.07$ eV at 95% CL, as shown by the vertical band in the graph.

In light of these results, neutrino masses are at least 6 orders of magnitude smaller compared to those from charged leptons and quarks. It is natural to suppose that the remarkable smallness of neutrino masses is related to the existence of a new fundamental mass scale in particle physics, and thus to new physics beyond the Standard Model.

1.3.2 Dirac vs Majorana Neutrinos

Neutrinos were introduced in the Standard Model (SM) of particle physics as massless particles; however, experimental observations, as the ones described in § 1.2, require the SM to be modified in order to include a neutrino mass term.

In the Standard Model, fermion masses result from the Yukawa interactions with the Higgs field. These interactions involve both left and right-handed fermions. However, only left-handed neutrinos have been observed experimentally, so neutrinos may have another source of mass, which must be included in the SM. Theory allows two possibilities of neutrino mass terms: Dirac and Majorana.

A Dirac neutrino mass can be generated with the same Higgs mechanism that gives masses to quarks and charged leptons, with the only introduction in the SM of right-handed components $\nu_{\alpha R}$ of the neutrino fields ($\alpha = e, \mu, \tau$) [32,33].

$$\nu_L = \begin{pmatrix} \nu_{eL} \\ \nu_{\mu L} \\ \nu_{\tau L} \end{pmatrix} \quad \nu_R = \begin{pmatrix} \nu_{eR} \\ \nu_{\mu R} \\ \nu_{\tau R} \end{pmatrix} \quad (1.18)$$

This model is usually called the "*minimally extended Standard Model*". These right-handed neutrino fields are called *sterile* [33] because they do not participate in weak, strong or electromagnetic interactions, their only interaction being gravitational. On the other hand, the normal left-handed neutrino fields that participate in weak interactions are usually called *active*.

However, despite being similar mechanisms, it is known that the masses of neutrinos are much smaller than those of charged leptons and quarks, and this mechanism gives no explanation of the very small values of the neutrino Yukawa couplings that are needed, making the explanation of neutrino masses with a Dirac mass term alone unsatisfactory.

The second way in which a neutrino mass term can be added to the SM Lagrangian was first proposed by Ettore Majorana [5], who realized that for neutral particles one can remove two of the four degrees of freedom in a massive spinor field by imposing the following condition:

$$\nu^c = \nu, \quad (1.19)$$

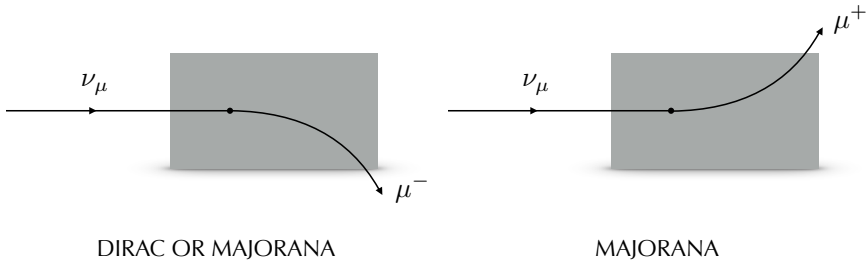


Figure 1.10: Scattering experiment to probe neutrino nature: a muon-neutrino beam is sent to a large magnetised detector. The observation of wrong-sign muons would be a signature of Majorana neutrinos.

where ν^c is the charge-conjugate of ν . This condition implies that there is only one field to describe neutrino and antineutrino states. Decomposing both sides of Eq. (1.19) into their chiral components, it can be shown that

$$\nu_R = (\nu_L)^c, \quad (1.20)$$

showing that the positive-chirality component of the Majorana neutrino field ν_R is not independent of, but obtained from its negative-chirality counterpart ν_L .

The Majorana mass terms coming from this new mechanism convert particles into their own antiparticles, thus violating the SM total lepton number $L \equiv L_e + L_\mu + L_\tau$ by two units ($|\Delta L| = 2$). Such mass terms are forbidden for all electrically charged fermions because of charge conservation, and therefore they are only possible for neutrinos.

Consequently, in the case of Majorana neutrinos, the detection of "wrong signed" neutrinos in a scattering experiment like the one shown in Fig. 1.10 would be possible, and therefore a clear evidence of their Majorana nature. Unfortunately, if this were the case, the production rate of wrong-sign muons would be suppressed by m_ν/E in amplitude, making it virtually impossible to detect. For example, for $m_\nu \sim 1$ eV and $E \sim 1$ GeV, the cross-section for the process would be, roughly, 10^{-18} times the usual charged-current neutrino cross-section [33].

The see-saw Mechanism

The seesaw mechanism is a generic model used to understand the tiny sizes of observed neutrino masses compared to those of quarks and charged leptons which are millions of times heavier, as depicted in Figure 1.3. The simplest version of the mechanism (*see-saw* Type 1) predicts the existence of a light left-handed neutrino state (m_1) for each one of the neutrino flavors, and the corresponding very heavy right-handed neutrino states (m_2), which have yet to be observed [34–37]. According to this model [32], the masses are of the order of

$$m_1 \simeq \frac{m_D^2}{m_R} ; \quad m_2 \simeq m_R \quad (1.21)$$

This assumption indicates that the light neutrino of mass m_1 would be the main components of the left-handed neutrinos already observed, while a very heavy neutrino of mass m_2 forms the right-handed neutrinos, not observed because of the extremely high energies needed to produce them, close to the grand unification energy [32]. The fact that a greater m_1 implies a lower m_2 and vice versa, gives name to the mechanism.

The missing antimatter

Current cosmological models of the universe predict that matter and antimatter had to be equally abundant at the beginning, and neutrino mass nature could contribute to explain current matter predominance.

A possible explanation of current baryon asymmetry is that matter and antimatter are essentially separated into different, widely separated regions of the universe. From a distance, antimatter atoms are indistinguishable from matter atoms; both produce light (photons) in the same way. But along the boundary between matter and antimatter regions, annihilation (and the subsequent production of gamma radiation) would occur. How easy such a boundary would be to detect would depend on its distance and the density of matter and antimatter. Such boundaries, if they exist, would likely lie in deep intergalactic space. The density of matter in intergalactic space is reasonably well established at about one atom per cubic metre [38]. Assuming this is a typical density near a boundary, the gamma ray luminosity of

the boundary interaction zone can be calculated. No such zones have been detected, so it is now deemed unlikely that any region within the observable universe is dominated by antimatter.

In conclusion, current asymmetry between matter and antimatter was not an initial condition and must have been generated dynamically in the early universe through processes which are known generically as *baryogenesis*. The amount of CP violation in the quark sector (first observed in 1964 by the Fitch-Cronin experiment [39] with neutral kaons, which resulted in the 1980 Nobel Prize in physics) does not appear to be sufficient to quantitatively account for the observed level of baryon asymmetry. Another contribution to baryogenesis could come from lepton asymmetry, known as *leptogenesis* [40, 41], possible if neutrinos are Majorana particles. The discovery of CP violation in the lepton sector via neutrino oscillations on the one hand, and the establishment of a Majorana nature for neutrinos on the other, would undoubtedly strengthen the case for leptogenesis as a source of the baryon asymmetry of the universe.

Neutrinoless double beta decay



The discovery of neutrinoless double beta decay would represent a major breakthrough in particle physics. A single and unequivocal observation of the decay would prove the Majorana nature of neutrinos, required by many theoretical models of the universe; it would imply the violation of total lepton number; it would reveal the neutrino mass ordering; and finally it would give a measurement of neutrinos absolute mass. All this makes the search of the utmost importance in current particle physics, and makes it challenging at the extreme. All this has inspired many groups of physicists around the world to develop different strategies and implement different detectors to search for this rare phenomenon.

2.1 Double Beta Decay

Double beta decay ($\beta\beta$) is a very rare nuclear transition in which a nucleus with Z protons decays into a nucleus with $Z + 2$ protons and the same mass number A . The ordinary decay mode in which two electrons plus two antineutrinos are produced:

$$(Z, A) \rightarrow (Z + 2, A) + 2 e^- + 2 \bar{\nu}_e. \quad (2.1)$$

was first observed in 1987 [42] in ^{82}Se with a time-projection chamber, and its half-life around 1.1×10^{20} years made it the rarest natural decay process ever observed directly in the laboratory. Such a long half-life makes the single β decay of most of the nuclides an extremely intense source of background for $2\nu\beta\beta$ detection; therefore, only when it is forbidden or highly suppressed (as in the case shown in Figure 2.1), $2\nu\beta\beta$ detection becomes feasible. Such a condition is fulfilled by 35 naturally-occurring isotopes, and twelve of them (see Table 2.1) have

Table 2.1: Weighted-average half-life values for two-neutrino double beta decay ($2\nu\beta\beta$) from the best direct measurements [43].

Isotope	$T_{1/2}^{2\nu}$ (10^{21} yr)	Experiment
^{48}Ca	$0.064^{+0.007}_{-0.006} \pm^{+0.012}_{-0.009}$	NEMO-3 [44]
^{76}Ge	1.926 ± 0.094	GERDA [43]
^{82}Kr	$9.2^{+5.5}_{-2.6} \pm 1.3$	BAKSAN [43]
^{82}Se	$0.096 \pm 0.003 \pm 0.010$	NEMO-3 [43]
^{96}Zr	$0.0235 \pm 0.0014 \pm 0.0016$	NEMO-3 [43]
^{100}Mo	0.00693 ± 0.00004	NEMO-3 [43]
^{116}Cd	$0.028 \pm 0.001 \pm 0.003$	NEMO-3 [43]
^{128}Te	7200 ± 400	geochemical [43]
^{130}Te	$0.82 \pm 0.02 \pm 0.06$	CUORE-0 [45]
^{136}Xe	$2.165 \pm 0.016 \pm 0.059$	EXO-200 [46]
^{150}Nd	$0.00911^{+0.00025}_{-0.00022} \pm 0.00063$	NEMO-3 [43]
^{238}U	2.0 ± 0.6	radiochemical [43]

been measured to date, with typical life-times of the order of 10^{18} – 10^{21} years.

The neutrinoless decay mode ($0\nu\beta\beta$),

$$(Z, A) \rightarrow (Z + 2, A) + 2 e^-, \quad (2.2)$$

was proposed by Wendell H. Furry in 1939 [47] as a method to test Majorana’s theory [5] applied to neutrinos. In contrast to the two-neutrino mode, the neutrinoless mode violates total lepton number conservation, and is, therefore, forbidden in the Standard Model of particle physics. Its existence is linked to that of Majorana neutrinos. No convincing experimental evidence of the decay exists to date.

In both decay modes the nuclear recoil is negligible, so the emitted leptons carry essentially all the available energy. Therefore, in the $0\nu\beta\beta$ mode, the spectrum for the sum of the kinetic energies of the emitted electrons is a mono-energetic line at $Q_{\beta\beta}$, the Q value of the reaction, defined as the mass difference between the parent and daughter nuclides:

$$Q_{\beta\beta} \equiv M(A, Z) - M(A, Z + 2). \quad (2.3)$$

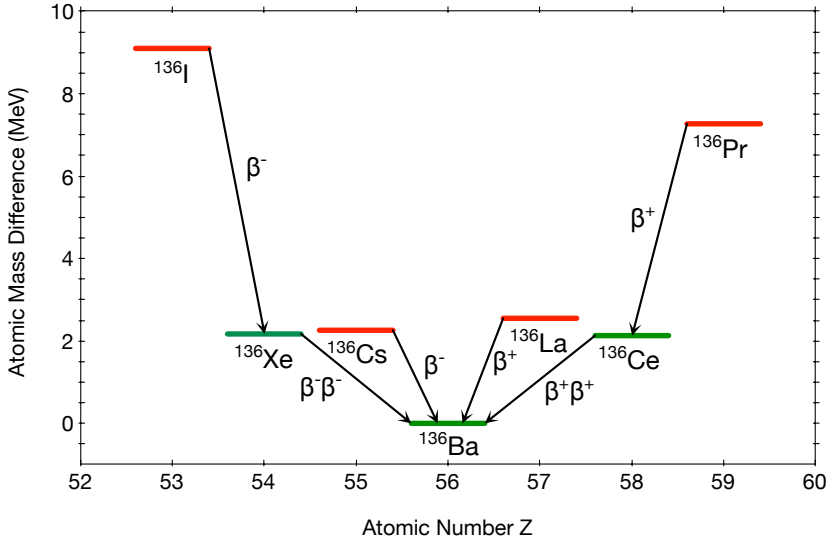


Figure 2.1: Atomic masses of isotopes with $A = 136$ given as differences with respect to the most bound isotope, ^{136}Ba . The red levels indicate odd-odd nuclides, whereas the green indicate even-even ones. The arrows show the type of nuclear transition connecting the levels. $\beta\beta$ (either plus or minus) transitions are possible because the intermediate state ($\Delta Z = \pm 1$) is less bound, forbidding the β decay.

In the case of the $2\nu\beta\beta$ -decay mode, the spectrum is continuous, extending from 0 to $Q_{\beta\beta}$ and peaking below $Q_{\beta\beta}/2$ as shown in Figure 2.2.

2.2 Neutrinoless Double Beta Decay

Neutrinoless double beta decay in its simplest mechanism, can arise from a diagram (see Figure 2.3 - Right) in which the parent nucleus emits a pair of virtual W bosons, and then these exchange a Majorana neutrino to produce the outgoing electrons. The probability of this disintegration depends on the neutrino mass. The inverse of the lifetime for the $0\nu\beta\beta$ process, if mediated by light Majorana neutrino

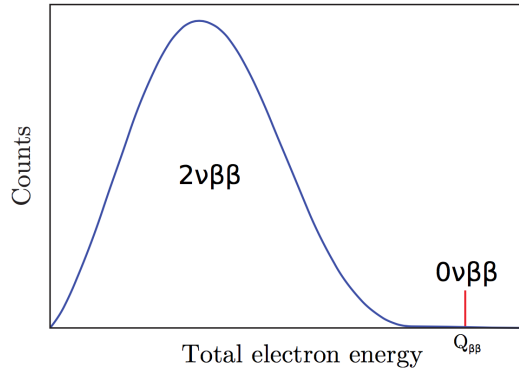


Figure 2.2: Spectra for the sum of the kinetic energies of the two emitted electrons for $2\nu\beta\beta$ and $0\nu\beta\beta$ decay modes. The amplitudes are arbitrary.

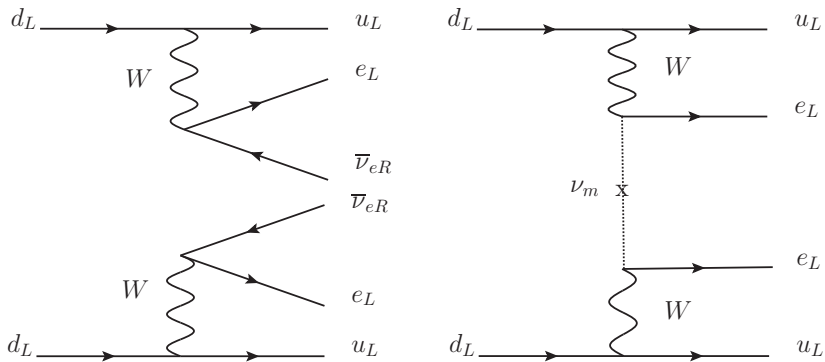


Figure 2.3: Feynman diagram for the $2\nu\beta\beta$ (left) and the $0\nu\beta\beta$ (right) decay modes.

exchange, can be expressed by [48]

$$(T_{1/2}^{0\nu})^{-1} = G^{0\nu} |M^{0\nu}|^2 \left(\frac{m_{\beta\beta}}{m_e} \right)^2 \quad (2.4)$$

where $G^{0\nu}$ is a phase-space factor for the emission of two electrons that depends on the transition Q value of the decay and on the nuclear Z of the parent nucleus, that can be analytically calculated very accurately [49,50]; $M^{0\nu}$ is the nuclear matrix element (NME) of the transition, which has to be evaluated theoretically with considerable uncertainty using nuclear models like the Interacting Shell Model (ISM) [51], Quasiparticle Random Phase Approximation (QRPA) [52,53], Interacting Boson Model (IBM-2) [54], Energy Density Functional Method (EDF) [55,56], etc.; and $m_{\beta\beta}$ is the *effective Majorana mass* of the electron neutrino given by

$$m_{\beta\beta} = \left| \sum_i U_{ei}^2 m_i \right| \quad (2.5)$$

where m_i are the neutrino mass eigenstates and U_{ei} are elements of the neutrino mixing matrix 1.10.

From Eq. 2.4 the value of the effective neutrino Majorana mass, $m_{\beta\beta}$, can be inferred from a non-zero $0\nu\beta\beta$ -rate measurement, providing direct information about the absolute neutrino mass scale, although with some nuclear physics uncertainties mainly arising from the calculation of $M^{0\nu}$. Conversely, if a given experiment does not observe the $0\nu\beta\beta$ process, the result can be interpreted in terms of an upper bound on $m_{\beta\beta}$.

The relationship between $m_{\beta\beta}$ and the actual neutrino masses m_i is affected by the uncertainties in the measured oscillation parameters, the unknown neutrino mass ordering (normal or inverted) and the unknown phases in the neutrino mixing matrix (both Dirac and Majorana). For example, the relationship between $m_{\beta\beta}$ and the lightest neutrino mass m_{light} , is shown in Figure 2.4. The width of the two bands is due to the unknown CP violation phases and the uncertainties in the measured oscillation parameters (3σ ranges quoted in Table 1.1). Figure 2.4 also shows the upper bound on m_{light} from cosmology discussed in § 1.3.1 ($m_{\text{light}} < 0.07$ eV), and an upper bound on $m_{\beta\beta}$ from $0\nu\beta\beta$ -decay searches ($m_{\beta\beta} < 200$ meV) [57,58].

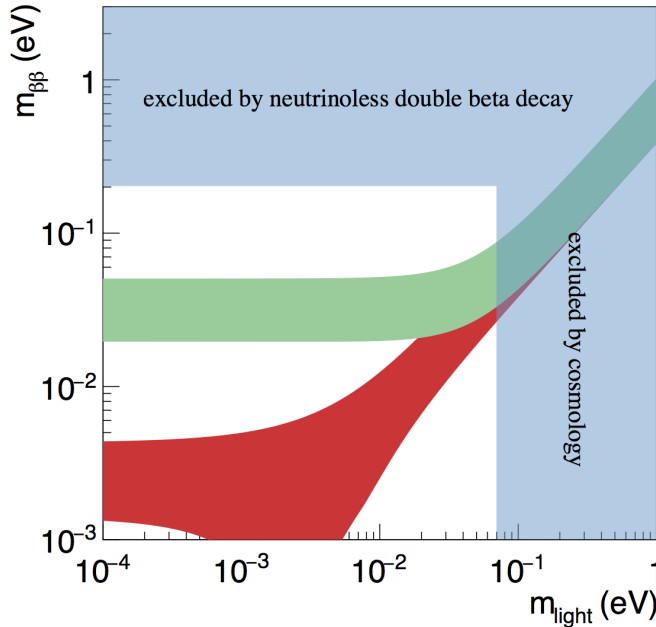


Figure 2.4: The effective neutrino Majorana mass, $m_{\beta\beta}$, as a function of the lightest neutrino mass, m_{light} . The green band corresponds to the inverted ordering of neutrino masses ($m_{\text{light}} \equiv m_3$), while the red band corresponds to the normal ordering ($m_{\text{light}} \equiv m_1$). The vertically-excluded region comes from cosmological bounds, the horizontal one from $0\nu\beta\beta$ constraints.

2.3 Design of Double Beta Decay Experiments

The design of a detector capable of identifying efficiently and unambiguously the rare $\beta\beta$ decays, represents a considerable experimental challenge. To begin with, one needs a large mass of the $\beta\beta$ isotope to probe in a reasonable time the extremely long lifetimes predicted for the process, and estimated using Eq. (2.4) in the order of 10^{26} to 10^{27} years (for a Majorana neutrino mass of 50 meV).

The main goal of basically all double beta decay experiments is to measure the total energy of the radiation emitted by a $\beta\beta$ source. In a neutrinoless double beta decay, the sum of the energies of the two

emitted electrons is constant and equal to the mass difference between the parent and the daughter atoms ($Q_{\beta\beta}$) as depicted in Fig. 2.2. Any experiment hoping to measure the $0\nu\beta\beta$ half-life must be able to count the number of events at this energy due to $0\nu\beta\beta$. However, due to the finite energy resolution of any detector, $0\nu\beta\beta$ events spread over an energy range centered around $Q_{\beta\beta}$, typically following a Gaussian distribution. Other processes occurring in the detector can fall within that energy window, becoming a background and compromising drastically the sensitivity of the experiment.

The background processes that can mimic a $0\nu\beta\beta$ -decay signal in a detector are abundant. To begin with, the experiments have to deal with the intrinsic background from the standard two-neutrino double beta decay, which can only be distinguished from the signal by measuring the energy of the emitted electrons, since the neutrinos go undetected. Good energy resolution is, therefore, essential to prevent the $2\nu\beta\beta$ spectrum tail from spreading over the $0\nu\beta\beta$ peak. However, this *energy signature* is not enough per se, since the continuous energy spectrum arising from natural radioactivity can easily overwhelm the signal peak, so careful selection of radiopure materials is crucial.

In order to evaluate the potential or quality of a $\beta\beta$ decay experiment, the sensitivity to $m_{\beta\beta}$ is used. This sensitivity, which will be described in detail in § 6.4.1, is proportional to:

$$S(m_{\beta\beta}) \propto \sqrt{1/\varepsilon} \left(\frac{B \Delta E}{M t} \right)^{1/4} \quad (2.6)$$

where M is the isotope mass, t is the running time of the detector, ΔE is the energy resolution, B is the background rate in the energy region of interest, and ε is the detection efficiency. This sensitivity can be directly translated to a sensitivity in terms of $T_{1/2}^{0\nu}$ half-life with (eq. 2.4).

Let's take a deeper look to the key parameters involved in $\beta\beta$ decay experiments.

Isotope

The selection of the isotope in $\beta\beta$ decay experiments is crucial, as it is responsible for many relevant aspects of them. We know from Eq. (2.4) that the half-life of the $0\nu\beta\beta$ process depends on $|M^{0\nu}|$, with small

differences between different isotopes; and depends on the phase-space factor $G^{0\nu}$, which varies as $Q_{\beta\beta}^5$ [49]. So isotopes with large $Q_{\beta\beta}$ values are strongly favored. Another advantage of using isotopes with high Q value comes from the fact that the higher the energy, the lower the amount of backgrounds coming from natural radioactivity. For this reason, only isotopes with $Q_{\beta\beta} > 2$ MeV have usually been considered for $0\nu\beta\beta$ -decay searches.

Another aspect to be considered is the two-neutrino decay mode, that in case of being relatively fast, can represent a considerable background, especially for experiments with energy resolution worse than 3–4% FWHM at the Q value. Moreover this is a background that can perfectly mimic the topology of the $0\nu\beta\beta$ signal which makes it very undesirable.

Finally, more general considerations such as the procurement cost, the possibility of enriching the element in the desired isotope, and the ease of handling; must be considered.

Energy Resolution

High energy resolution is a necessary condition (but not sufficient) for an ultimate $0\nu\beta\beta$ decay experiment: it is the only protection against the intrinsic $2\nu\beta\beta$ background, and improves the signal-to-noise ratio in the region of interest around $Q_{\beta\beta}$ as illustrated in Figure 2.5 where the energy region of interest around the Q value is represented for three Monte Carlo experiments with the same signal and background, but different energy resolution.

In conclusion, the better the energy resolution, the greater the *discovery potential* of an experiment given certain conditions of signal and background. Therefore, the experimental techniques with modest or poor energy resolution have to compensate this deficiency by reaching lower background rates and higher exposures.

Low Background

The natural radioactivity of detector components is usually the main background source in $0\nu\beta\beta$ -decay experiments. Particularly pernicious are ^{208}Tl and ^{214}Bi decay products of the Thorium and Uranium series respectively, present at some level in all materials, so all $0\nu\beta\beta$ -

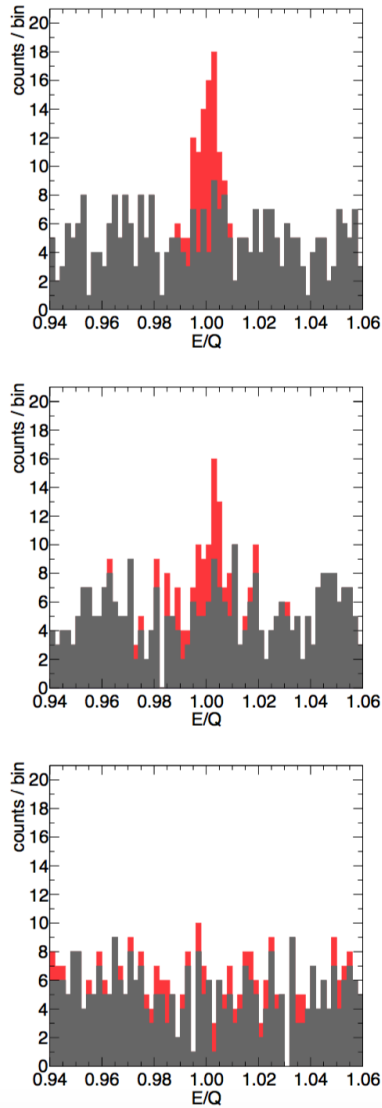


Figure 2.5: From [59]: signal and background (red and grey stacked histograms, respectively) in the region of interest around $Q_{\beta\beta}$ for three Monte Carlo experiments with the same signal strength (50 counts) and background rate (1 count/keV), but different energy resolution (top: 1% FWHM; centre: 3.5% FWHM; bottom: 10% FWHM). The signal is distributed normally around $Q_{\beta\beta}$, while the background is assumed flat.

decay experiments must follow an extensive selection campaign looking for extremely *radiopure* materials.

Radon, another intermediate decay product of the uranium and thorium series, is also a concern for most experiments as it has radioactive isotopes: ^{220}Rn and ^{222}Rn . Being a noble gas, radon is chemically not very reactive and can diffuse easily through many materials, infiltrating into the active region of the detectors. Radon progenies, also radioactive, tend to be charged and adhere to surfaces or dust particles. The impact of radon can be mitigated by flushing the detector surroundings with pure nitrogen or by installing radon traps in the laboratory air circulation systems.

In addition to backgrounds coming from radioactive impurities in detector components, there are external backgrounds originating outside the detector. Natural radioactivity in the rock of the underground caverns results in a gamma-ray and neutron flux that can interact in the detector producing background. These can be suppressed by placing the detector in a shielding system typically made of dense and radiopure material such as lead, copper and even water.

Finally, backgrounds with origin in the radiation from the atmosphere and outer space must be considered. These cosmic muons and neutrons are mitigated by placing the detector in underground facilities that reduce the flux at Earth's surface by several orders of magnitude. Several facilities are currently available to host physics experiments around the world [60].

Besides the passive background reduction techniques mentioned above, most experiments use now *active* methods for the discrimination of signal and background: reconstruction of the event topology, pulse-shape discrimination, combination of detection signatures, etc. A unique possibility offered by xenon-based experiments is that all backgrounds except the two-neutrino decay mode could be effectively removed by identification of the daughter barium ion using techniques such as atomic laser resonant spectroscopy [61], that would imply in practice a background-free experiment.

All relevant background sources are deeply described and quantified in Chapter § 4.

Detection Efficiency

Neutrinoless double beta decay is extremely rare, if existent at all. A high detection efficiency is, therefore, an important requirement for a $\beta\beta$ experiment, as clearly stated by Eqs. (2.6) and (6.13). To obtain the same increase in $m_{\beta\beta}$ sensitivity attained by doubling the efficiency, the mass would have to be increased by a factor of 4, assuming the same background. In general, the simpler the detection scheme, the higher the detection efficiency. For instance, pure calorimetric approaches such as germanium diodes or bolometers have detection efficiencies in excess of 80%. This is to be contrasted with experiments performing, for example, particle tracking, which will typically result in significant efficiency loss. Homogeneous detectors, where the source material is the detection medium, provide in principle higher efficiency than the separate-source approach for a number of reasons, including geometric acceptance or absorption in the $\beta\beta$ source. That being said, some homogeneous detectors may use part of the mass close to the detector boundaries for self-shielding against external backgrounds, paying for it with efficiency loss.

Exposure

Thousands of kilograms of $\beta\beta$ source will be needed to explore the extremely long $0\nu\beta\beta$ half-lives corresponding to the inverted hierarchy of neutrino masses. Most collaborations searching for $0\nu\beta\beta$ decay are planning future tonne-scale versions of their experiments. However, not all the technologies are equally suitable for that purpose. The scalability of each experimental technique will be, therefore, one of the key points.

Large-scale production of the $\beta\beta$ isotopes will represent a technical and logistic challenge, as they are quite rare on Earth. Moreover the isotopic abundance of them is around or below 10%, requiring isotopic enrichment in order to obtain large, concentrated masses. In fact, this has been so far the driving cost in the procurement of the isotopes.

The most cost-effective enrichment technology is centrifugal separation [62–64], but it is only possible for elements with a stable gas compound. Affordable enrichment of large quantities of those species with no gas compound, such as ^{48}Ca or ^{150}Nd , is not possible at present.

Centrifugation of xenon, being a noble gas, is, of course, simpler (and hence cheaper) than that of metalloids such as germanium. Therefore, from this point of view, ^{136}Xe would be a particularly favourable isotope to use for a tonne-scale experiment.

2.4 Current Experiments

As we have seen in the previous section § 2.3, there are several key topics that must be considered in every $\beta\beta$ decay experiment: isotope selection, energy resolution, low background, high efficiency, exposure and scalability. Around the world, different experimental detection approaches have been carried out in order to get the best possible combination of all of them that could lead to a positive $0\nu\beta\beta$ detection. Table 2.2 summarizes the best current limits for $0\nu\beta\beta$ decays.

In the following sub-sections different techniques and the leading experiment implementing them, are presented.

2.4.1 Bolometer Detectors – CUORE

A bolometer consists of an absorptive element, such as a thin layer of metal, connected to a thermal reservoir (a body of constant temperature) through a thermal link. The result is that any radiation impinging on the absorptive element raises its temperature above that of the reservoir such that the greater the absorbed energy, the higher the temperature. The temperature change can be measured directly with an attached resistive thermometer, or the resistance of the absorptive element itself can be used as a thermometer. These devices can be operated at cryogenic temperatures, enabling significantly greater sensitivity.

The *Cryogenic Underground Observatory for Rare Events* (CUORE) will search for the $0\nu\beta\beta$ decay of ^{130}Te using TeO_2 crystal bolometers [66]. When these crystals are cooled to 10 mK, their heat capacity becomes so small that the energy deposited by interacting particles is measurable as a rise in temperature. The crystals, therefore, function as highly sensitive calorimeters. This technique was used for the first time in $0\nu\beta\beta$ -decay searches by the MiDBD [67] experiment in 2003, using ^{130}Te . Cuoricino (2003-2008) [68] and its successor, CUORE-0 (2013-2015) [69] although they did not observe $0\nu\beta\beta$ decay in ^{130}Te , set

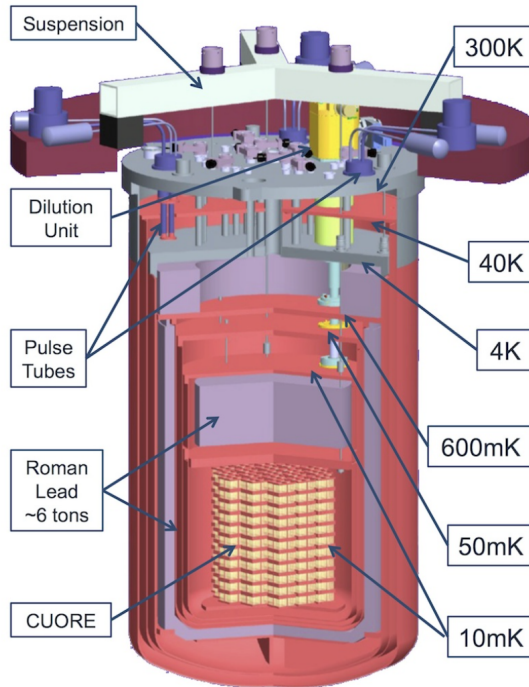


Figure 2.6: Cutaway view of the CUORE bolometers inside the cryostat, consisting of six nested copper vessels at 300 K (outer vacuum chamber), 40 K, 4 K (inner vacuum chamber), 0.6 K (still), 0.05 K (heat exchanger), and 0.01 K (mixing chamber). Several layers of radiopure lead shield the bolometers from external radiation. Reproduced from Artusa et al. (2014) [66].

the most stringent limit to date on its half-life: 4.0×10^{24} years at 90% C.L..

CUORE, currently under construction at the Laboratori Nazionali del Gran Sasso (Italy), is the latest evolution of a series of TeO_2 detectors, and it will be the largest bolometric experiment ever built. The detector consists of 988 TeO_2 bolometers for a total mass of 741 kg (206 kg of ^{130}Te), arranged in 19 vertical towers held by a copper frame. The towers will be housed in a cryostat composed of six nested

copper vessels (see Figure 2.6). Two cold lead shields will shield the bolometers from radiation originating in the cryostat, and this will be shielded by a 73-tonne octagonal external shield designed to screen the detector from environmental γ rays and neutrons. To cool these detectors, the CUORE cryostat creates the coldest cubic meter in the known universe [70].

CUORE aims at improving the sensitivity of CUORE-0, its predecessor, reaching a half-life of 9×10^{25} years at 90% C.L. with five years of live time [71]; by operating a larger, cleaner, better-shielded detector with enhanced energy resolution. The expected energy resolution (FWHM) of the CUORE crystals is 5 keV (0.2%) at the Q value of ^{130}Te (2528 keV) [66]. To reduce background activity, it has pursued two major complementary lines: the reduction of surface contamination and the selection of extremely radiopure construction materials. The goal is achieving a background rate in the region of interest not higher than 10^{-2} cts $\text{keV}^{-1} \text{kg}^{-1} \text{yr}^{-1}$ [72].

2.4.2 Time Projection Chambers – EXO

The "Time projection chamber" (TPC) is a type of particle detector that uses a combination of electric and magnetic fields, together with a sensitive volume of gas or liquid, to perform a three-dimensional reconstruction of a particle trajectory and its interactions. The original TPC was invented by David R. Nygren at Lawrence Berkeley Laboratory in the late 1970s [73]. This technology offers the possibility of measuring the scintillation and the ionization of particle interactions. The ability of use the same media as both source and detector gives compactness, scalability and could also give good energy resolution depending on the readout technique.

Xenon appears as a promising gas to be used in TPCs for $\beta\beta$ -decay searches. ^{136}Xe has a natural abundance of 9% and can be enriched by centrifugation at a reasonable cost and easily purified. This and the absence of other long-lived radioactive isotopes make xenon a perfect candidate. In addition, its $Q_{\beta\beta}$ (2458 keV) is high enough to avoid most of the natural radioactive background. Both liquid state, using cryogenics, and gas state are used experimentally.

The *Enriched Xenon Observatory* (EXO) is an experimental program searching for neutrinoless double beta decay using ^{136}Xe . The first

Table 2.2: Best present limits on $0\nu\beta\beta$ decay at 90% C.L. from [65].

Isotope	$Q_{\beta\beta}$ (keV)	$T_{1/2}$ (y)	$\langle m_\nu \rangle$ (eV)	Experiment
^{48}Ca	4267.98	$> 5.8 \cdot 10^{22}$	$< 3.1 - 15.4$	CANDLES
^{76}Ge	2039.00	$> 5.2 \cdot 10^{25}$	$< 0.15 - 0.39$	GERDA I + II
^{82}Se	2997.9	$> 3.6 \cdot 10^{23}$	$< 1 - 2.4$	NEMO-3
^{96}Zr	3355.85	$> 9.2 \cdot 10^{21}$	$< 3.6 - 10.4$	NEMO-3
^{100}Mo	3034.40	$> 1.1 \cdot 10^{24}$	$< 0.33 - 0.62$	NEMO-3
^{116}Cd	2813.50	$> 1.9 \cdot 10^{23}$	$< 1 - 1.8$	AURORA
^{128}Te	866.6	$> 1.5 \cdot 10^{24}$	2.3 – 4.6	Geochem. exp.
^{130}Te	2527.52	$> 4 \cdot 10^{24}$	$< 0.26 - 0.97$	CUORICINO + CUORE0
^{136}Xe	2457.83	$> 1.07 \cdot 10^{26}$	$< 0.06 - 0.17$	KamLAND-Zen
^{150}Nd	3371.38	$> 2 \cdot 10^{22}$	$< 1.6 - 5.3$	NEMO-3

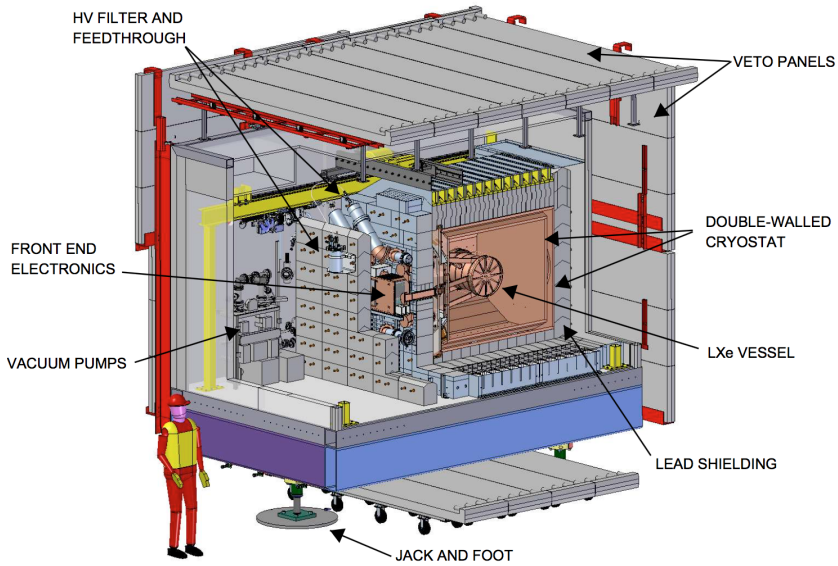


Figure 2.7: Drawing of the EXO-200 detector, cryostat and shielding. Reproduced from Auger et al. (2012) [74].

phase of the experiment: EXO-200, is a cylindrical TPC, about 40 cm in diameter and 44 cm in length, with two drift regions separated in the centre by a transparent cathode. The TPC measures the 3D coordinates and energy of ionization deposits in the LXe by simultaneously collecting the scintillation light and the charge. Charge deposits spatially separated by about 1 cm or more are individually observed with a position accuracy of a few millimetres. The xenon, enriched to 80.6% in ^{136}Xe , is held inside a thin copper vessel immersed in a cryofluid that also shields the detector from external radioactive backgrounds. Further shielding is provided by at least 25 cm of lead in all directions. The entire assembly is housed in a clean-room located underground at Waste Isolation Pilot Plant (WIPP) in New Mexico, USA. Four of the six sides of the clean-room are instrumented with plastic scintillator panels recording the passage of cosmic ray muons. Figure 2.7 shows the overall detector and shielding arrangement.

EXO-200 has been running since 2011, and it has published the first experimental measurement of the $^{136}\text{Xe } 2\nu\beta\beta$ [46,75]. It also set a limit on the $^{136}\text{Xe } 0\nu\beta\beta$ of 1.1×10^{25} yr with 100 kg · yr of exposure (corresponding to an upper limit on the Majorana neutrino mass of 190 - 450 meV), reaching 3.0% (FWHM) energy resolution at $Q_{\beta\beta}$ and $1.7 \pm 0.2 \times 10^{-3}$ cts keV $^{-1}$ kg $^{-1}$ yr $^{-1}$ in the $0\nu\beta\beta \pm 2\sigma$ ROI [57]. It has also set the first limits in $^{134}\text{Xe } \beta\beta$ decay searches to $T_{1/2}^{2\nu} > 8.7 \times 10^{20}$ yr and $T_{1/2}^{0\nu} > 1.1 \times 10^{23}$ yr at 90% C.L. [76].

Building on the success of EXO-200, the EXO Collaboration has started the R&D work for a future multi-tonne liquid xenon experiment called nEXO [77]. The detector would be placed in a large water shield instead of the lead shield used for EXO-200 and a deeper site would be chosen to reduce the cosmogenic neutron backgrounds. They will try to "tag" the barium daughter ion produced by the $^{136}\text{Xe } 0\nu\beta\beta$ decay, in order to eliminate all backgrounds except those coming from $2\nu\beta\beta$ decays.

A TPC filled with gaseous ^{136}Xe is the technical approach selected also by the NEXT collaboration. As it is the main subject of the present thesis, it will be described in depth in the following chapter § 3.

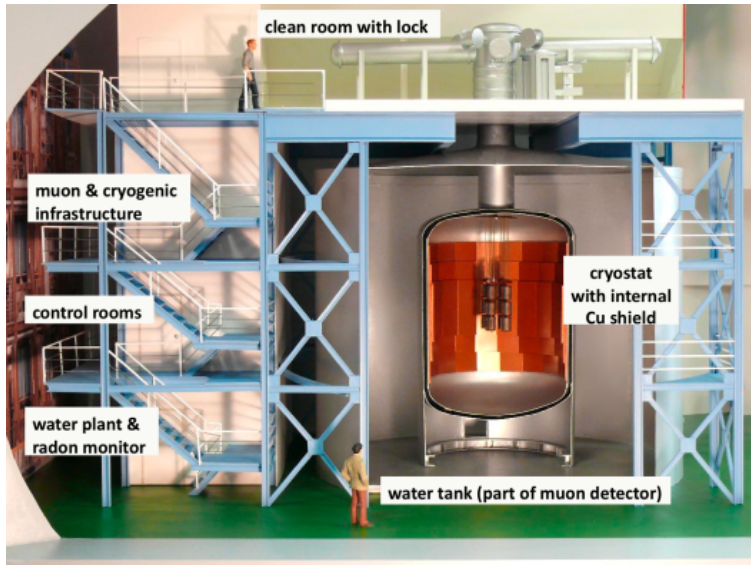


Figure 2.8: Artist's view (HPGe strings not to scale) of the GERDA detector at LNGS. Reproduced from Macolino (2013) [79].

2.4.3 Semiconductors – GERDA, MAJORANA

The GERmanium Detector Array (GERDA) experiment, located in Hall A of the Laboratori Nazionali del Gran Sasso (LNGS), consists of a large mass of germanium crystals isotopically enriched to $\sim 86\%$ in ^{76}Ge and simultaneously operated as source and detectors for $0\nu\beta\beta$ decay [78]. The detectors are arranged in strings and mounted in low-mass copper holders with ultra-low radioactivity. The strings are suspended inside a vacuum-insulated stainless steel cryostat of 4.2 m diameter and 8.9 m height filled with 70 tons of liquid argon (LAr), acting as cooling medium and shielding from external radiation. A 590 m^3 water tank surrounds the LAr cryostat and provides further shielding from external γ s and neutrons. It is instrumented with 66 PMTs for the detection of Cherenkov light induced by cosmic muons and operated in conjunction with scintillator panels located on the top of the experiment. See Figure 2.8.

GERDA Phase-I has been running from 2011 to 2013 giving $21.6\text{ kg}\cdot\text{yr}$ total exposure and was upgraded in 2015 to Phase-II, doubling

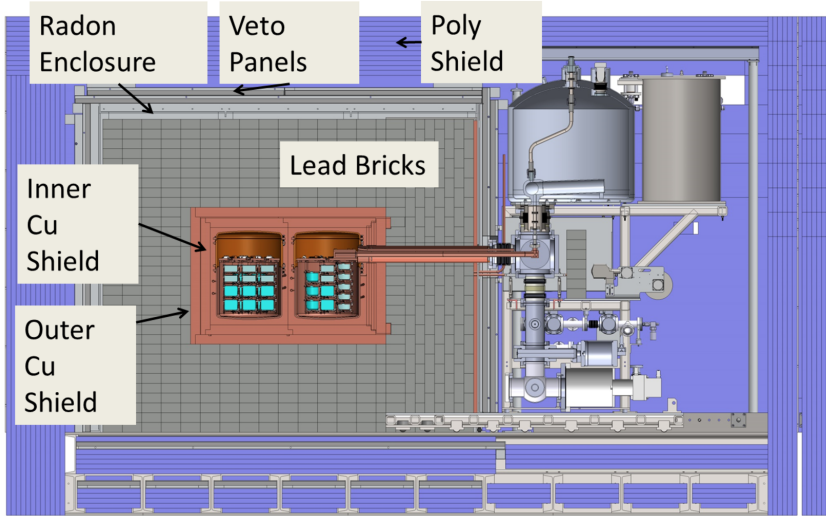


Figure 2.9: MAJORANA Demonstrator with both active and passive shielding in place [83].

the exposure. Phase-I achieved 10^{-2} cts $\text{keV}^{-1} \text{kg}^{-1} \text{yr}^{-1}$ background events and a exposure-averaged energy resolution of 0.1 - 0.2% FWHM at $Q_{\beta\beta}$ (2019.00 keV). No signal was observed and a lower limit for the half-life of neutrinoless double beta decay of ^{76}Ge , $T_{1/2}^{0\nu} > 2.1 \times 10^{25} \text{yr}$ at 90% C.L. [80], was set. The background index goal for Phase-II is 10^{-3} cts $\text{keV}^{-1} \text{kg}^{-1} \text{yr}^{-1}$ aiming for a sensitivity increase of a factor of 10, reaching to $T_{1/2}^{0\nu} > 5.3 \times 10^{25} \text{yr}$ at 90% C.L [81].

For the very long term, it is foreseen a third phase of the experiment with about 1 tonne of ^{76}Ge together with further reduction of background. Such an effort would be feasible only in a world-wide collaboration with the MAJORANA project [82], which is following a more classical approach than GERDA in the design of a germanium-based experiment.

The MAJORANA Collaboration is building a prototype to demonstrate the feasibility to achieve a background rate at or below one count per tonne-year in the 4 keV region of interest (ROI) around the 2039 keV $Q_{\beta\beta}$ for ^{76}Ge $0\nu\beta\beta$ decay. The demonstrator consists of a modular setup composed of enriched and natural germanium detectors, surrounded by two cryostats built on ultra-pure electroformed

copper. The baseline plan calls for 30 kg of the detectors to be built from Ge material enriched to 86% in isotope 76 and 10 kg fabricated from natural Ge. Starting from the innermost cavity, the cryostats are surrounded by an inner layer of electroformed copper, an outer layer of oxygen-free copper, high-purity lead, an active muon veto, polyethylene, and borated polyethylene; all of them enclosed in a radon exclusion box (See Figure 2.9). The entire experiment is located in a clean room at the Sanford Underground Research Facility (SURF) in South Dakota, USA.

With $3.03 \text{ kg} \cdot \text{yr}$ exposure, MAJORANA Demonstrator has set a limit of $T_{1/2}^{0\nu} \text{ } ^{76}\text{Ge} > 3.7 \times 10^{24} \text{ yr}$ and reached $23_{-10}^{+13} \text{ counts}/(\text{ROI} \cdot t \cdot \text{year})$ in a 3.1 keV ROI [82,83].

2.4.4 Scintillators – KamLAND-Zen, SNO+

Luminescent materials can absorb energy from the interacting particles, re-emitting light proportionally to the absorbed energy (scintillation), thus light detectors provide a way of measuring deposited energy. Liquid scintillator detectors have been used for neutrino physics due to their well known performance and their prominent large mass. Some experiments have upgraded the oscillation experiments of the last decade to detectors for $0\nu\beta\beta$ searches or as a multipurpose detectors. This is exactly the case of KamLAND-Zen and SNO+.

The KamLAND-Zen experiment is a modification of the neutrino KamLAND detector [84] carried out in summer of 2011, located at the Kamioka Observatory, Japan. It uses enriched Xe dissolved in liquid scintillator, a technique first proposed by R. Raghavan in 1994 [85]. The detector, shown in Figure 2.10, is composed of two concentric transparent balloons. The inner one, 3.08 m diameter and fabricated from transparent thick nylon film, contains 13 tons of ^{136}Xe -loaded liquid scintillator enriched up to 90.93% in ^{136}Xe , corresponding to approximately 350 kg of desired isotope. The outer balloon, 13 m in diameter, contains 1 kilotonne of pure liquid scintillator, and serves as an active shield for external gamma background as well as a detector for internal radiation from the inner balloon. An oil buffer between the outer balloon and an 18 m diameter spherical stainless-steel containment tank shields the detector from external radiation. Scintillation light is recorded by 1325 17-inch and 554 20-inch photomultiplier

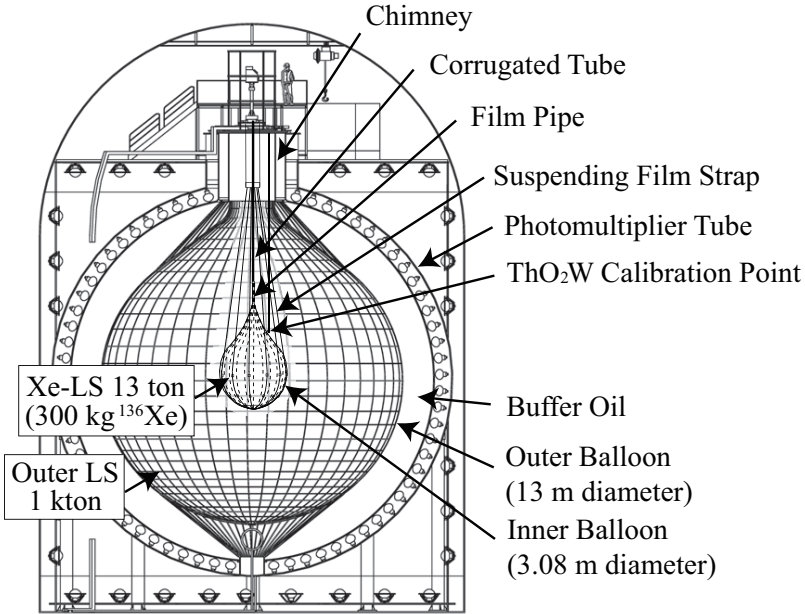


Figure 2.10: Schematic drawing of the KamLAND-Zen detector. Reproduced from Gando et al. (2012) [86].

tubes mounted on the stainless-steel tank, providing 34% solid-angle coverage. The containment tank is surrounded by a 3.2-kton water-Cherenkov outer detector for cosmic-ray muon identification [86].

KamLAND-Zen started collecting data in 2011. The second phase of data taking was carried out from December 2013 to October 2015 (534.5 days), after the purification to reduce the dominant $^{110}\text{Ag}^m$ background identified by first phase data. The background was reduced by more than a factor of 10 by purification of the liquid scintillator and xenon gas. By combining the first and second phase data it has made a preliminary measurement of $^{136}\text{Xe } T_{1/2}^{2\nu} = 2.21 \times 10^{21} \text{ yr}$ and set a preliminary limit of $^{136}\text{Xe } T_{1/2}^{0\nu} > 1.07 \times 10^{26} \text{ yr}$, corresponding to an effective Majorana neutrino mass $m_{\beta\beta} < (61 - 165) \text{ meV}$ [1], which represents the best limit to date.

SNO+, the follow-up of the *Sudbury Neutrino Observatory* (SNO) [87], is a multipurpose liquid scintillator experiment housed in SNO-LAB (Ontario, Canada), whose first goal is the search for $0\nu\beta\beta$ decays

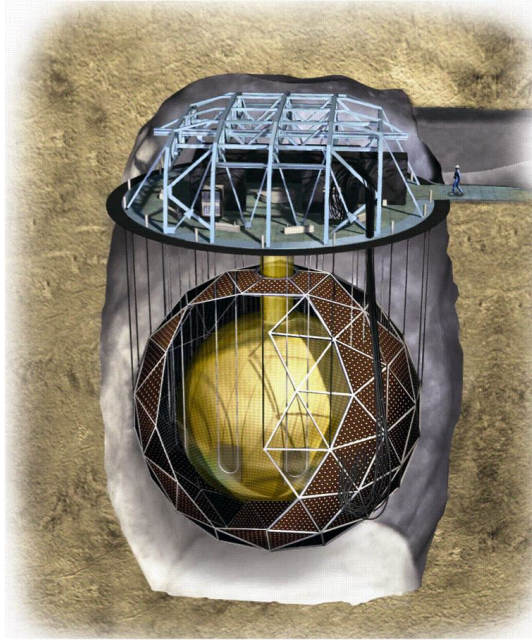


Figure 2.11: Artistic view of the SNO+ detector showing the acrylic vessel and the support structure of the photomultiplier tubes. Reproduced from Biller (2014) [88].

of ^{130}Te . The isotope (at natural abundance of 30.08%) will be loaded into the liquid scintillator in the form of telluric acid, corresponding to 780 kg of ^{130}Te . The detector, shown in Figure 2.11, reuses many of the components of its predecessor, replacing the original heavy water by 780 tonne of liquid scintillator. The detector consists of a 12 m diameter acrylic vessel surrounded by about 9500 8-in photomultiplier tubes that provide a 54% effective photocathode coverage. The acrylic vessel is immersed in a bath of ultra pure water that fills the remaining extent of the underground cavern, attenuating the background from external media such as the PMTs and surrounding rock. To keep it in place, a hold-down rope net has been installed over the detector and anchored to the cavity floor.

The SNO+ phase I is foreseen for late 2018 and will last about 5 years. The energy resolution is expected to be 10.5% FWHM at the $Q_{\beta\beta}$ value of ^{130}Te with a background level of 13.4 counts/year in the

ROI. After phase I, it aims to reach a sensitivity of $T_{1/2}^{0\nu} > 2 \times 10^{26}$ yr at 90% C.L., corresponding to an effective Majorana neutrino mass $m_{\beta\beta} < (40 - 90)$ meV [89].

2.4.5 Other Experiments

Neutrinoless double beta decay is an exciting physics topic and double beta decay searches keep on playing a unique role in neutrino physics. We have presented in previous sub-sections the main experimental approaches for the quest, and the main detectors making use of them. But these are not the only ones; plenty of them are currently being run or are planned to start in forthcoming years.

We would like to mention several other experiments, either for using designs similar to NEXT (i. e. PANDAX or AXEL), or for performing a topological reconstruction like NEXT does (Super-NEMO).

1. SuperNemo [90] is the new installation of the NEMO detector series. Its main difference with respect to other experimental approaches is the separation of the target (the $\beta\beta$ emitter) and the detector medium, which allows for the possibility to explore and measure different isotopes with the same detector. The detector is split in up to 20 modules (6.2 m long, 4.1 m high and 2.1 m wide). Each one consists of a thin source foil in the centre, surrounded on both sides by a tracker (inner) and a calorimeter (outer). The tracking is performed with Geiger-mode multi-wire drift-chamber cells under a magnetic field, allowing for particle identification and therefore helping with background suppression. To measure the event energy it uses plastic scintillators coupled to PMTs modules (14% FWHM energy resolution in NEMO-3 [91]). The collaboration has run the NEMO-3 demonstrator from 2003 to 2011 at Laboratoire Souterrain de Modane (LSM) measuring several isotopes. Currently the first Super-NEMO module is under-construction with ^{82}Se as the source. The expected performance is $T_{1/2}^{0\nu}(^{82}\text{Se}) \sim 10^{26}$ yr for 500 kg · yr exposure, with 4% FWHM energy resolution at 3 MeV and 5×10^{-5} cts $\text{keV}^{-1} \text{kg}^{-1} \text{yr}^{-1}$ around $Q_{\beta\beta}$ [92].
2. PandaX [93] is designed to build and operate a ton-scale liquid xenon experiment to search for elusive dark matter particles and

$0\nu\beta\beta$ decays. It will use a two-phase (liquid and gas) Time Projection Chamber (TPC) detector, and micromegas in the readout plane. It is located at China Jinping Underground Laboratory (CJPL), which is one of the deepest underground labs in the world. It is currently building a 20 kg scale prototype.

3. Axel [94] is developing an electroluminescent time projection chamber filled with high pressure xenon gas. They are developing a readout scheme where the light-emitting region is divided into cells and emitted light is detected by UV-sensitive SiPMs. They have constructed a small prototype detector using 64 SiPMs filled with 4 bar xenon gas, reaching an energy resolution of about 3% FWHM at 122 keV (from a ^{57}Co gamma-ray source). They expect further improvements by using new VUV-sensitive photosensors.

The NEXT Experiment 3

In chapter § 2.4 we have presented different technical approaches and the more relevant detectors facing the search for $0\nu\beta\beta$ decays. However, most of the existing techniques may not be suitable for exploring the neutrino-mass region corresponding to the inverse hierarchy; either because of the difficulty of reaching large detector masses, or due to their intrinsic poor energy resolution or limited background-rejection capabilities.

In contrast, we present in this chapter the approach followed by the NEXT¹ collaboration, that is: an electroluminescent high-pressure gas Time Projection Chamber (TPC) filled with xenon gas enriched in its ^{136}Xe isotope that will take advantage of the new "Separated and Optimized Functions TPC" (SOFT) technology. It is located at Laboratorio Subterráneo de Canfranc (LSC) [95] which is carved into the rock at 850 meters deep below the Tobazo Mountain, on the Spanish side of the Pyrenees. The following sections outline the different aspects of this approach.

It is worth noting that using xenon gas detectors for $0\nu\beta\beta$ decay searches is actually an old idea. In the late 1980s, the Milano experiment [96] at LNGS, made use of a multi-wire proportional chamber filled with xenon gas enriched on ^{136}Xe . Other pioneering experiment was the Gotthard TPC [97, 98] built by a Caltech-PSI-Neuchâtel collaboration and operated at the St. Gotthard road tunnel (Switzerland) in the 1990s. This TPC demonstrated the effectiveness of tracking in xenon to discriminate signal from background.

¹The acronym stands for Neutrino Experiment with a Xenon TPC

3.1 Xenon Gas as Source and Detector Medium

All radiation detectors are based on the same fundamental principle: the transfer of part or all of the radiation energy to the detector mass, where it is converted into some other form more adequate for human perception or electronic processing. The relative ease with which noble gases can be cleaned of impurities as well as the availability of both scintillation and ionization signals when using these materials as detection media have meant that these gases have been extensively used in medical imaging, dark matter detection, X-ray astronomy, and for the observation of double beta decay [99–102].

Xenon, both as a gas and liquid, is of special interest for $0\nu\beta\beta$ decay searches thanks to the existence of the ^{136}Xe isotope which can decay via the double beta mechanism. ^{136}Xe constitutes only 8.86% of natural xenon, but the enrichment process is relatively simple and cheap compared to that of other $\beta\beta$ isotopes. Moreover, the two-neutrino decay mode of ^{136}Xe is slow: $T_{1/2}^{2\nu}(^{136}\text{Xe}) = 2.2 \times 10^{21}$ years [46, 86], and hence the experimental requirement for energy resolution is less severe than for other $\beta\beta$ sources. Finally, in its gaseous phase, xenon can provide very good energy resolution, better, in principle, than 0.5% FWHM at the Q value of ^{136}Xe [103].

In summary Xe gas is an ideal medium for $\beta\beta$ decay searches due to:

- ^{136}Xe isotope can decay $\beta\beta$.
- Slow ^{136}Xe $2\nu\beta\beta$ mode.
- Availability of scintillation and Ionization signals.
- Energy resolution better than 0.5% FWHM.
- Simple and cheap enrichment process of ^{136}Xe .
- Easy cleaning of impurities.

Relevant ^{136}Xe properties related with $\beta\beta$ -decays according to (2.4) are listed in Table 3.1.

Relative atomic mass	135.907219(8) [104]
Q value $^{136}\text{Xe} \rightarrow ^{136}\text{Ba}$	2457.83(37) keV [105] 2458.7(6) keV [106] 2458.1(3) keV (average)
$G^{0\nu}$ (10^{-15} year $^{-1}$)	14.58 [49] 14.54 [50] 14.56 (average)
$0\nu\beta\beta$ decay NME	2.19 (ISM) [51] 2.46 (QRPA-Tu) [52] 2.91 (QRPA-Jy) [53] 3.05 (IBM-2) [54] 4.24 (EDF) [56] 4.20 - 4.77 (EDF) [55]

Table 3.1: Properties of ^{136}Xe relevant to $0\nu\beta\beta$ decay searches: relative atomic mass, Q value of the decay (i.e. mass difference between the parent and daughter atoms), phase-space factor ($G^{0\nu}$) and nuclear matrix element (NME). The figures in parentheses after the first two quantities give the 1σ experimental uncertainty in the last digits. The uncertainties on the $G^{0\nu}$ calculations (originating from the uncertainties on the Q value and the nuclear radius) are of the order of 5–10% [49]. The quoted nuclear matrix elements (NME) are the most recent calculations for $0\nu\beta\beta$ decay to the ground state mediated by light-neutrino exchange (all of them calculated with the free-nucleon value of the axial-vector coupling constant $g_A \simeq 1.26$) in four different nuclear-theory frameworks: ISM, QRPA (from Tübingen and Jyväskylä), IBM-2, and EDF.

Primary Signals in Xenon: Scintillation and Ionization

The energy released by the β particles in the $\beta\beta$ process is divided into excitation and ionization of xenon atoms. In general, both types of information together can be used to acquire information on the identity, energy and kinematics of the ionizing radiation. The first process is a resonant reaction in which atomic electrons are promoted to higher energy levels:



Upon de-excitation, electrons emit photons corresponding to their typical emission spectrum, with a peak at 172 nm (in the UV region).

If the energy transferred by the β particle is above a certain threshold, an electron can be extracted and the atom can suffer ionization, thus resulting in the creation of an electron-ion pair:



Both cases are described via Platzman's equation [107]:

$$E_\beta = \langle E_i \rangle N_i + \langle E_{sci} \rangle N_{sci} + \langle \epsilon \rangle N_i \quad (3.3)$$

where E_β is the energy absorbed by the gas, N_i is the number of electron-ion pairs ultimately produced with an average energy expenditure $\langle E_i \rangle$, N_{sci} is the number of atoms excited at an average energy expenditure $\langle E_{sci} \rangle$, and $\langle \epsilon \rangle$ is the average kinetic energy of sub-excitation electrons, with energy lower than the first excited level, which ultimately is released as heat.

In absence of an electric field, all electrons and ions liberated would eventually recombine generating more scintillation light and killing the origin of the ionization signal. The presence of intense electric fields in the detector, as the ones used in NEXT detectors (300-600 V/cm), prevents this recombination and allows the recording of ionization electrons.

The ionization and scintillation amplitudes are usually expressed in terms of the average energies required to produce respectively, an electron-ion pair: W_i (so-called ionization W), and a scintillation photon: W_{sci} (so-called scintillation W). From Equation (3.3), W_i and

W_{sci} can be written as

$$W_i \equiv \frac{E_\beta}{N_i} = \langle E_i \rangle + \langle E_{sci} \rangle \frac{N_{sci}}{N_i} + \langle \epsilon \rangle \quad (3.4)$$

$$W_{sci} \equiv \frac{E_\beta}{N_{sci}} = \langle E_i \rangle \frac{N_i}{N_{sci}} + \langle E_{sci} \rangle + \langle \epsilon \rangle \frac{N_i}{N_{sci}} \quad (3.5)$$

In the particular case of our interest, ^{136}Xe has a $W_i = 21.9$ eV [108] for the gaseous phase, and $W_i = 15.6$ eV [109] for the liquid phase; while the available energy from its $0\nu\beta\beta$ decay is $Q_{\beta\beta} = 2.458 \times 10^6$ eV; so the average number of primary ionization electrons is equal to:

$$Gas \ ^{136}\text{Xe} \ \bar{N}_i = \frac{Q_{\beta\beta}}{W_i} = \frac{2.458 \text{ MeV}}{21.9 \text{ eV}} = 112 \ 237 \ \text{electrons} \quad (3.6)$$

$$Liq. \ ^{136}\text{Xe} \ \bar{N}_i = \frac{Q_{\beta\beta}}{W_i} = \frac{2.458 \text{ MeV}}{15.6 \text{ eV}} = 157 \ 564 \ \text{electrons} \quad (3.7)$$

It is worth noting that xenon has the smallest W_i value, hence the largest ionization yield, of all noble gases.

On the other hand, the scintillation spectrum is the result of a complex system of discrete atomic lines and continuous bands originating from many excited states, and from various collision and transfer processes [110, 111]. It extends from the infrared to the far ultraviolet and, at atmospheric pressure and above, the vacuum-ultraviolet (VUV, 20-200 nm) emission dominates the spectrum. Several measurements of W_{sci} for xenon gas are available in the literature [112–114], but to date, none of them appear compatible with theoretical predictions and they present sensible discrepancies among each other.

The NEXT collaboration published [115] a value of *Gas* $W_{sci} = 39.2 \pm 3.2$ eV based on measurements of the ratio of excited to ionized atoms produced in the xenon gas by alpha particles in the NEXT-DEMO detector. Aprile et al. published in [111] a value of *Liq* $W_{sci} = 13.8$ eV. According to these values, the average numbers of primary scintillation photons for both states are equal to:

$$Gas \ ^{136}\text{Xe} \ \bar{N}_{sci} = \frac{Q_{\beta\beta}}{W_{sci}} = \frac{2.458 \text{ MeV}}{39.2 \text{ eV}} = 62 \ 704 \ \text{primary photons} \quad (3.8)$$

$$Liq \ ^{136}\text{Xe} \ \bar{N}_{sci} = \frac{Q_{\beta\beta}}{W_{sci}} = \frac{2.458 \text{ MeV}}{13.8 \text{ eV}} = 178 \ 116 \ \text{primary photons} \quad (3.9)$$

Detection of the Ionization and Scintillation Signals

The detection of the ionization signal generally involves the transport of the ionization pairs through the gas under the influence of an external electric field. In this process, known as *drift*, the electrons and ions liberated by ionizing radiation are accelerated along the electric-field lines in opposite directions towards, respectively, the anode and cathode. The acceleration is intermittently interrupted by collisions with the gas atoms, limiting the maximum average velocity attainable by the drifting charges. For sufficiently low fields, the *drift velocity* of electrons, v_d , is proportional to the field strength. At high fields, the drift velocity saturates, becoming independent of the field. The drift velocity of ions is several orders of magnitude smaller than that of the electrons.

During the drift, due to the collisions with gas atoms, ionization charges deviate from the trajectories defined by the field lines spreading gaussianly in both the longitudinal and transverse directions. This *diffusion* limits the intrinsic position resolution of gaseous detectors. The magnitude of the spread is proportional to the drift time, t_d :

$$\sigma_L = \sqrt{D_L t_d}, \quad \sigma_T = \sqrt{D_T t_d}, \quad (3.10)$$

where D_L and D_T are, respectively, the longitudinal and transverse diffusion coefficients of the gas.

Electron *attachment* to electronegative impurities dissolved in the gas may lead to a significant decrease of the ionization signal during drift. This effect can be described, in general, by an exponential distribution:

$$N(t_d) = N(0) \exp(-t_d/\tau), \quad (3.11)$$

where N is the number of drifting electrons, which is a function of the drift time, t_d , and τ is the *electron lifetime* in the gas, which becomes shorter with higher concentration of impurities. Sufficiently long electron lifetimes can be achieved by circulating the gas continuously through appropriate filters of impurities.

In most applications, the total ionization charge collected is too low to be distinguished by the electronics or leads to a poor signal-to-noise ratio. In these cases, the primary-electron signal can be amplified using electric fields of higher intensity than those typically applied for the

drift. If the amplification field is such that the electrons gain energy above the excitation threshold of the gas but below the ionization threshold, they will excite gas atoms along their path. These will decay later, emitting light known as *electroluminescence* (EL) or secondary scintillation. In this way, each primary ionization electron produces a measurable, proportional optical signal (see Figure 3.1). If the amplification field is intense enough for the electrons to gain energy above the ionization threshold, they will produce new electron-ion pairs while drifting. The secondary ionization electrons can also gain energy from the field and ionize further atoms. Eventually, a *charge avalanche* is generated, resulting in an electron yield orders of magnitude higher than the number of primary ionization electrons. This charge signal is then large enough to be picked up by the electronics with a good signal-to-noise ratio.

NEXT detectors make use of an amplification able to generate EL light but no secondary ionization. The absolute electroluminescence gain η , under a uniform and constant \bar{E}/p , defined as the number of scintillation photons produced by a single ionization electron, is given by [116]:

$$\eta = 140 \cdot (E/p - 0.83) \cdot p \cdot \Delta x \text{ (UV photons/e}^{-}\text{)} \quad (3.12)$$

where E/p is given in $\text{kV cm}^{-1} \text{ bar}^{-1}$, p in bar, and the separation Δx between the meshes generating the secondary drift field in cm.

The VUV scintillation photons emitted by noble gases are difficult to detect because they are strongly absorbed by most materials. Therefore, the VUV light is usually shifted to the visible or near-visible band using photo-fluorescent coatings deposited onto the surfaces exposed to the gas volume. At these wavelengths, the efficiency of photosensors (devices that transform an optical signal into an electric current through the photoelectric effect) is optimal, and highly transparent or reflective materials are available. Popular wavelength shifting (WLS) substances used in xenon detectors are p-terphenyl (TPH) and tetraphenyl butadiene (TPB) [111].

Intrinsic Energy Resolution of Xenon Gas

The ionization signal is a good measure of the energy deposited in the medium, given that W_i is almost independent of the type and kinetic

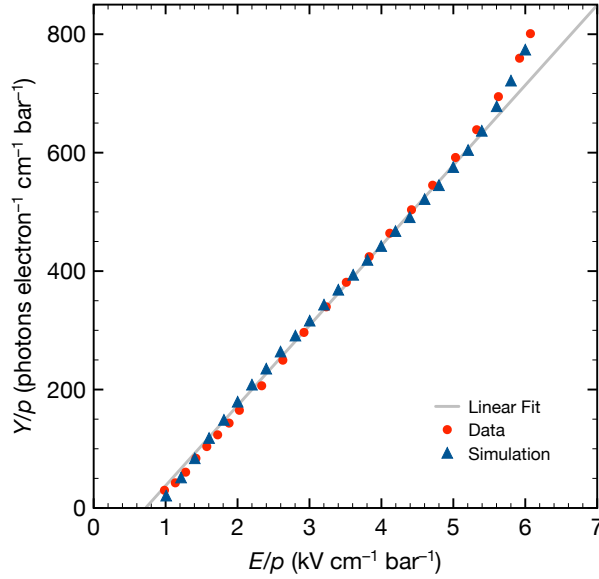


Figure 3.1: Reduced electroluminescence yield (Y/p) of gaseous xenon as a function of the reduced electric field, E/p . The results of Garfield / Magboltz microscopic simulations [108] are compared to the experimental measurements by Monteiro et al. (2007) [117]. A linear fit to the simulation data points is also shown. The EL yield is linearly proportional to the reduced electric field above a threshold of $0.83 \text{ kV cm}^{-1} \text{ bar}^{-1}$ and up to approximately $5.5 \text{ kV cm}^{-1} \text{ bar}^{-1}$, where secondary-ionization effects become visible. Figure redrawn from Oliveira et al. (2011) [108].

energy of the ionizing radiation. Nevertheless, stochastic fluctuations in the number of electron-ion pairs produced limit the energy resolution that can be achieved in a gaseous detector. If each ionization could be considered independent of the others, the fluctuations would then be described by a Poisson distribution with variance

$$\sigma_i^2 = N_i \quad (3.13)$$

where N_i is the mean number of electron-ion pairs produced for a given deposited energy. However, Ugo Fano demonstrated [118] that the processes leading to the creation of ionization pairs are not independent, and that, in general, the associated fluctuations can be described by the variance

$$\sigma_i^2 = F N_i, \quad (3.14)$$

where the number F , known as *Fano factor*, depends on the detection medium. The ultimate energy resolution (FWHM) achievable with an ionization detector (often called *intrinsic resolution* or *Fano limit*) is, therefore, given by

$$\delta E / E = 2.35 \sqrt{F N_i} W_i / E = 2.35 \sqrt{F W_i / E} \quad (3.15)$$

where $E = N_i W_i$ is the total energy deposited by radiation.

The Fano factor of noble gases is well understood, and it is typically less than 1. For pure gaseous xenon (GXe), at densities up to the High Pressure Gas Xenon (HPXe) threshold: $\rho \approx 0.025 \text{ g/cm}^3$, various experimental measurements [119–121] report that:

$$F_{GXe} = 0.15 \pm 0.02 \quad (3.16)$$

On the other hand, this value is extremely small compared with the one of liquid xenon (LXe) [122]:

$$F_{LXe} \approx 20 \quad (3.17)$$

and therefore from 3.15, the intrinsic energy resolution is much better in HPXe detectors than in LXe ones:

$$(\delta E / E)_{Gas \text{ } ^{136}\text{Xe}} = 2.35 \sqrt{0.15 \cdot 21.9 / Q_{\beta\beta}} = 0.38\% \text{ FWHM} \quad (3.18)$$

$$(\delta E/E)_{Liq\ ^{136}\text{Xe}} = 2.35 \sqrt{20 \cdot 15.6 / Q_{\beta\beta}} = 2.65\% \text{ FWHM} \quad (3.19)$$

Bolotnikov and Ramsey reported [123] the dependence with the density of the energy resolution obtained in a xenon gas detector by measuring the ionization signal generated by 662-keV gamma rays from ^{137}Cs (see Figure 3.2). For the density range between 0.12 and 0.6 g/cm^3 , they measured an approximately-constant resolution, $\delta E/E = 0.6\%$ FWHM at 662 keV, a value close to the Fano limit. For xenon densities above 0.55 g/cm^3 , however, the energy resolution quickly deteriorated, approaching the typical values measured for liquid xenon. It has been suggested [103, 111] that this behavior may be due to the appearance of globs of liquid xenon coexisting with the gas as density increases. Below the apparent density threshold at 0.55 g/cm^3 , the liquid phase fraction would be insufficient to contribute measurably to the processes introducing anomalous fluctuations. With increasing density, the liquid phase fraction would grow, and so would the impact of anomalous fluctuations related to recombination, reaching a maximum at the density of the liquid phase.

In practice, however, all detectors are affected by losses, noise and fluctuations that may worsen the intrinsic energy resolution of the gas; and they need to be evaluated to compute the global energy resolution. It seems reasonable to assume that any possible fluctuations associated with the signal s_i are uncorrelated with those intrinsic to the ionization process, described by Eq. (3.14). In that case both variances can be added in quadrature, and the overall variance of the detection process can be written as

$$\sigma_E^2 = \sigma_i^2 + \sigma_G^2 = F N_i + G N_i = (F + G) N_i, \quad (3.20)$$

where G is defined as the variance of signal s_i . Therefore, the energy resolution (FWHM) of a gaseous detector, including the effect of fluctuations in the detection, is given by

$$\delta E/E = 2.35 \sqrt{(F + G) W_i / E}. \quad (3.21)$$

It is worth to note that although the factors G and F enter the above equation in the same way, they are fundamentally different: G reflects the impact of statistical fluctuations in the detection process for a single

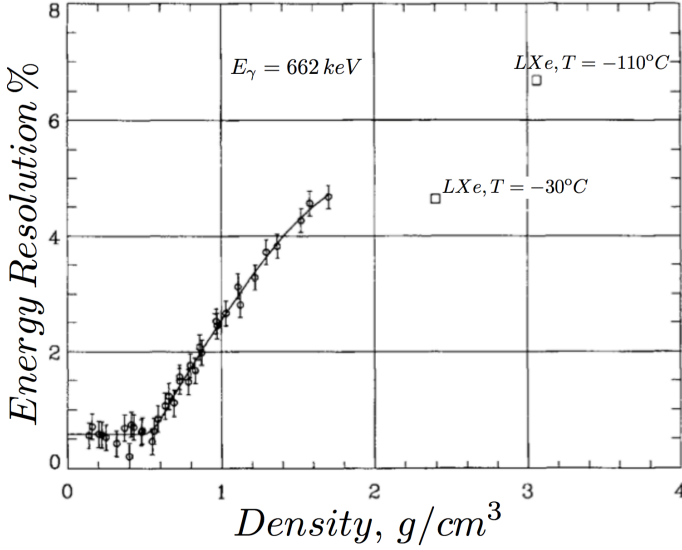


Figure 3.2: Density dependence of the energy resolution (% FWHM) measured in xenon using the ionization signal generated by 662-keV gamma rays from ^{137}Cs . Reproduced from Bolotnikov and Ramsey (1997) [123].

electron, while F reflects a constraint on fluctuations in energy partitioning for a fixed total energy [103]. All experimental approaches for detecting electroluminescence tend to have the smallest G as possible, trying to reach as close as possible the Fano limit. In the case, where $F = G = 0.15$, the obtained energy resolution at $Q_{\beta\beta}$ value in a HPXe detector would be:

$$\delta E/E = 0.42\% \text{ FWHM} \quad (3.22)$$

This value is in agreement with the one obtained in [124], where a HPXe TPC was used to measure the energy resolution of a 122 keV γ -ray source. An energy resolution of 2.2 % FWHM was obtained at this energy, so if extrapolating as $E^{-1/2}$, the energy resolution at $Q_{\beta\beta}$ value of ^{136}Xe would be

$$\delta E/E = 0.44\% \text{ FWHM} \quad (3.23)$$

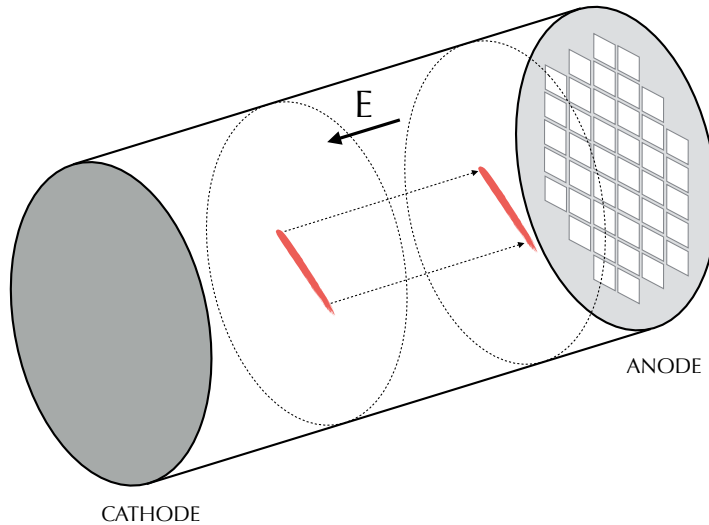


Figure 3.3: Working principle of a TPC [125]: the ionization electrons produced along the path of a charged particle (represented by the red trace) are drifted under the influence of an external electric field towards an amplification and readout plane that registers the signal amplitudes and transverse positions. The longitudinal coordinate is obtained from the arrival time of the signals.

3.2 The SOFT Concept

The working principle of TPCs is illustrated in Figure 3.3. A uniform electric field is established along the symmetry axis of a cylindrical chamber filled with a gaseous detection medium. The ionization electrons produced along the path of a charged particle traversing the cylinder are drifted under the influence of the field towards an amplification and readout plane with 2D spatial segmentation. This plane registers the amplitudes and transverse positions of the ionization signals. The longitudinal coordinate is obtained from the arrival time of the signals. The TPC, therefore, provides a full three-dimensional measurement of the trajectory and energy deposition pattern (dE/dx) of a charged particle.

Double beta decay experiments, as described in Section § 2.3,

need extremely good energy resolution as the only available protection against $2\nu\beta\beta$ background; as well as good tracking capabilities, which helps on improve topological discrimination of signal and backgrounds. In order to fulfill these requirements, NEXT detectors use the SOFT concept [103] that performs energy and tracking measurements in different planes specially designed to achieve the best performance in both tasks (See Figure 3.4).

According to Section § 3.1, signal amplification by electroluminescence is the appropriate option to reach optimal energy resolution in gaseous xenon. This is implemented with an additional electric field region after the drift volume with intensity between the excitation and ionization thresholds of ^{136}Xe .

The electroluminescence generated in that gap by the ionization electrons can be detected by a plane of photosensors located in the cathode plane chosen specially for energy measurement. PMTs have low noise and high gain thus providing a very good resolution, and can cover large areas at a reasonable cost, which makes them one of the best options. Conversely PMTs contain excessive levels of radioactive contaminants, so detector designs must contain the minimum number of PMTs necessary to obtain a robust measurement of the optical signals.

The topological reconstruction requires a dense array of small photosensors (SiPMs) to provide the transverse coordinates of the signals. The array is located in the anode plane, behind the EL region. Cathode PMTs, able to detect the faint signal coming from the primary scintillation light of xenon, provide the *start-of-event* trigger to reconstruct the absolute position of signals along the longitudinal coordinate. In this way, the combination of SiPMs and PMTs signals a full and precise 3D reconstruction of signal is achieved. To improve the resolution of the whole procedure, the internal walls of the active volume are covered with a reflector, increasing the light collection efficiency.

3.3 Detectors

The NEXT experiment will search for the neutrinoless double beta decay of ^{136}Xe using a pressurized xenon gas time projection chamber that implements the (asymmetric) SOFT detector concept described

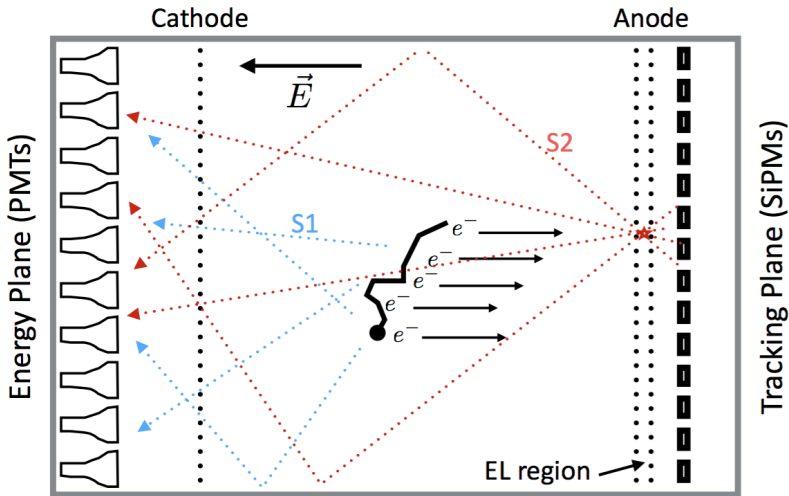


Figure 3.4: The SOFT concept [103]. EL light generated at the EL region is recorded in the photosensor plane right behind it and used for tracking. It is also recorded in the photosensor plane behind the transparent cathode and used for a precise energy measurement. The cathode is also used to detect primary scintillation light and provide t_0 information.

in the previous section. The experiment is a collaboration involving about 60 physicists and engineers from 13 different research institutes and universities in Spain, Portugal, USA, Colombia, Israel and Russia.

The first phase of the project (2009–2014) has been largely devoted to R&D with two small-size prototypes, NEXT-DEMO and NEXT-DBDM, built with the double aim of demonstrating the detector concept and gaining technical expertise to facilitate the design, construction and operation of a larger system. Both prototypes and their main results are described in § 3.3.1.

Currently, the collaboration is operating NEXT-NEW, a medium-size prototype placed underground and run under low background conditions. It has been conceived as a demonstrator of all the technological solutions adopted for higher-volume detectors, so it can be seen as a general assay. It has the physics goal of measuring the ^{136}Xe

$2\nu\beta\beta$ decay half-life. The detector is described in § 3.3.2.

The following phase of the project is the NEXT-100 detector. It is currently under construction and will incorporate all the knowledge gained constructing and operating NEXT-NEW, demonstrating the scalability of the technology. It is expected to start operations along 2019. It will contain around 100 kg of gaseous Xenon at 15 bar with the physics goal of detecting ^{136}Xe $0\nu\beta\beta$ decays. The detector is described in § 3.3.3 and is the object of study of this thesis.

3.3.1 R&D Prototypes

NEXT-DEMO

The NEXT-DEMO detector was designed as a proof-of-concept prototype of the NEXT technology, approximately 4.5 times smaller than NEXT-100. It was neither radiopure nor shielded against natural radioactivity, and it was installed in a clean-room at the *Instituto de Física Corpuscular* (IFIC), in Valencia, Spain.

The detector consists of a stainless steel vessel 60 cm long and 30 cm in diameter that can withstand pressure up to 15 bar. It contains a 300 mm long *drift volume* and a 5 mm long *EL gap* delimited by three stainless steel wire grids (*cathode*, *gate* and *anode*). The anode is set at ground potential, while the gate is at a negative voltage such that an electric field above the excitation threshold of xenon ($0.86 \text{ kV cm}^{-1} \text{ bar}^{-1}$) is created in the EL gap. A moderate, uniform electric field (0.5 kV cm^{-1} , typically) is established in the drift region by supplying a large negative voltage to the cathode, then grading it using a series of metallic rings that enclose the volume and are connected electrically via $0.5\text{-G}\Omega$ resistors. Inside the electric-field rings, six reflecting panels made of polytetrafluoroethylene (PTFE) are mounted forming an hexagonal tube. The panels were coated with tetraphenyl butadiene (TPB), which shifts the VUV light emitted by xenon to blue light, so as to improve the light collection efficiency of the detector. A cutaway drawing of NEXT-DEMO detector is shown in Figure 3.5.

The tracking plane is placed 5–10 mm away from the anode. It consists of 256 Hamamatsu S10362-11-050P SiPMs (1 mm^2 active area) regularly positioned at a pitch of 1 cm and distributed between four boards, each with 64 sensors arranged as an 8×8 matrix. Since the

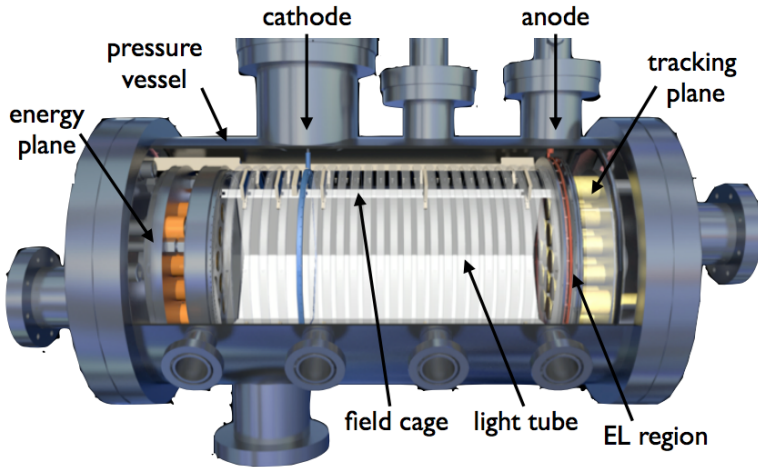


Figure 3.5: Cross-section drawing of the NEXT-DEMO prototype with major parts labelled (top), and image of the field cage standing on the lab (bottom).

SiPMs are not directly sensitive at the emission wavelength of xenon, the boards were coated with TPB.

The energy plane is equipped with 19 Hamamatsu R7378A photomultiplier tubes [126]. These are 1-inch, pressure-resistant (up to 20 bar) PMTs with acceptable quantum efficiency ($\sim 15\%$) in the VUV region and higher efficiency at the TPB emission wavelengths ($\sim 25\%$). The resulting photocathode coverage of the energy plane is 39%. The gain of the PMTs is adjusted to about 5×10^6 to place the mean amplitude of a single photoelectron pulse well above the electronic noise.

Natural xenon circulates in a closed loop through the vessel and a system of purifying filters that remove the electronegative impurities from the gas before and during operation; and signal processing, digitization and read-out are performed using an electronics chain based on the *Scalable Readout System* developed by the RD51 Collaboration [127]. Further details of the detector can be found in several dedicated publications [115, 128–131] by the collaboration.

The response of NEXT-DEMO was studied using a $1\text{-}\mu\text{Ci}$ ^{22}Na calibration source placed at a lateral port. Sodium-22 is a long-lived β^+ radioactive isotope, and the annihilation of the positron emitted in its decay—which rarely leaves the source—results in two back-to-back 511-keV gammas. The coincident detection of the forward gamma in the TPC and of the backward gamma in an external NaI scintillator coupled to a photomultiplier was used to trigger the detector readout. This arrangement optimized the acquisition of useful calibration data.

The latest results obtained [132], once all corrections were applied, show an energy resolution for the K_α peak of $(5.691 \pm 0.003)\%$ FWHM, and $(1.62 \pm 0.01)\%$ FWHM for the ^{22}Na photopeak. Extrapolating these two values to the Q value of ^{136}Xe assuming an $E^{-1/2}$ dependence results in a predicted energy resolution of 0.63% FWHM and 0.74% FWHM, respectively.

An event topology reconstruction was also performed in NEXT-DEMO. Single electrons resulting from the interactions of ^{22}Na 1275 keV gammas and electron-positron pairs produced by conversions of gammas from the ^{208}Tl decay chain were used to represent the background and the signal in a double beta decay. These data were used to develop algorithms for the reconstruction of tracks and the identification of the energy deposited at the end-points, providing an extra background rejection factor of $24.3 \pm 1.4\%$, while maintaining

an efficiency of $66.7 \pm 1.0\%$ for signal events [133].

NEXT-DBDM

The NEXT-DBDM prototype was designed with the goal of demonstrating near-intrinsic energy resolution in high-pressure xenon gas. It has been built and operated at the Lawrence Berkeley National Laboratory (USA).

The detector consists of a stainless steel cylindrical pressure vessel (20 cm diameter, 33.5 cm length), housing the TPC and one plane instrumented with a PMT array. It is connected to a gas system allowing for full system pump-down and constant recirculation of the xenon gas during operation through a hot getter to remove electronegative impurities (O_2 , H_2O , N_2 , etc.). A cutaway drawing of the DBDM prototype is shown in Figure 3.6. The TPC consists of a hexagonal field cage made of teflon panels supported by thin plastic frames. The internal faces of the panels house copper strips connected through 100-M Ω resistors to grade the potential and produce a uniform electric field. The TPC holds a drift region of length 8 cm and an amplification region 5 mm long, implemented with grids of stainless-steel wire mesh, 88% transparent.

The measurement plane is located at the end opposite the amplification region (13.5 cm away) facing the active region. It is instrumented with an array of 19 1-inch diameter Hamamatsu 7378A [126] photomultiplier tubes (the same model as those used in NEXT-DEMO) arranged in a hexagonal pattern.

The energy resolution achievable with the TPC was studied using gamma rays of 662 keV from a ^{137}Cs radioactive source. After fiducial selection based on EL light registered on the PMT plane, and electron attachment correction; energy resolutions of 1% FWHM for 662-keV gamma rays, and 5% FWHM for 30-keV fluorescence xenon X-rays were obtained at 10 and 15 bar respectively. These results extrapolate to a 0.5% FWHM resolution at 2458 keV ($Q_{\beta\beta}$ for ^{136}Xe $0\nu\beta\beta$ decays), very close to the Fano limit (see 3.18) of xenon gas.

A more detailed description of the detector and its results can be found in a dedicated paper [134].

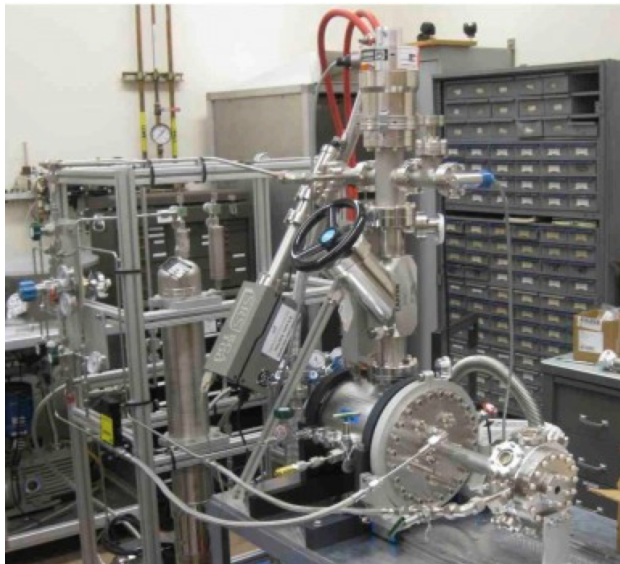
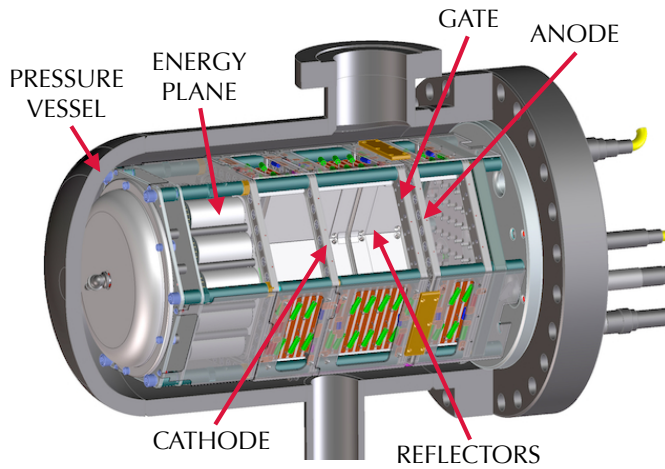


Figure 3.6: Cutaway drawing of the NEXT-DBDM detector with major parts labelled (top), and image of the complete setting of NEXT-DBDM in operation mode (bottom).

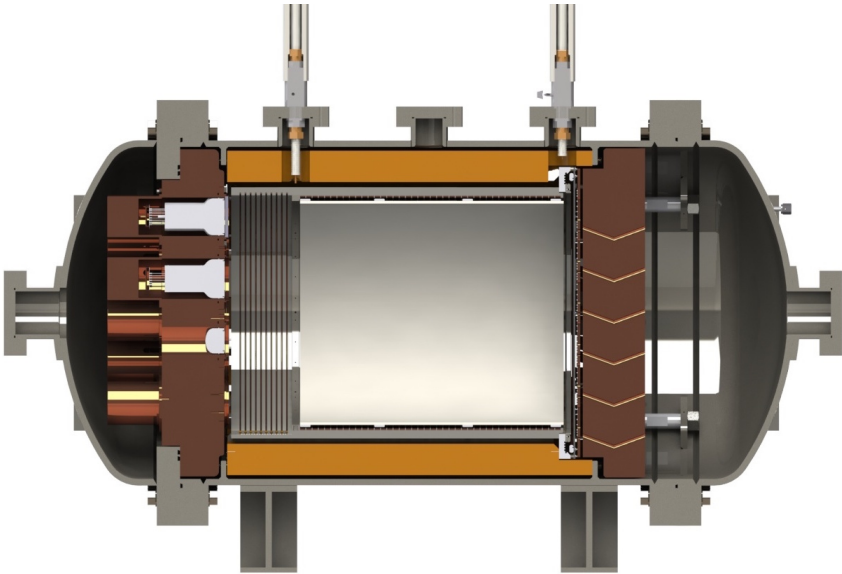


Figure 3.7: Cross-section drawing of the NEW detector.

3.3.2 NEXT NEW

The NEXT-White² (NEW) detector, currently in operation at the Laboratorio Subterráneo de Canfranc (LSC), is a 1:2 scaled-down version of NEXT-100, made with low-background conditions. The design of NEW follows closely that of NEXT-100, implementing the same technical solutions and using the same materials and photosensors (See Figure 3.7). In this way, NEW serves as a large demonstrator of the NEXT technology, and its construction and operation represent a huge step forward, and have provided valuable information for the future construction, operation and calibration of NEXT-100.

In addition to the goal of the R&D and expertise gained in high-pressure xenon detectors, NEXT-NEW has several physics objectives:

- The DEMO and DBDM prototypes are too small to contain tracks of the energies of interest for $0\nu\beta\beta$ searches in ^{136}Xe . Therefore, NEW data will be extremely useful for the optimization of reconstruction and pattern-recognition algorithms at those energies.

²Named after the pass away of our collaborator, the late Prof. James T. White.

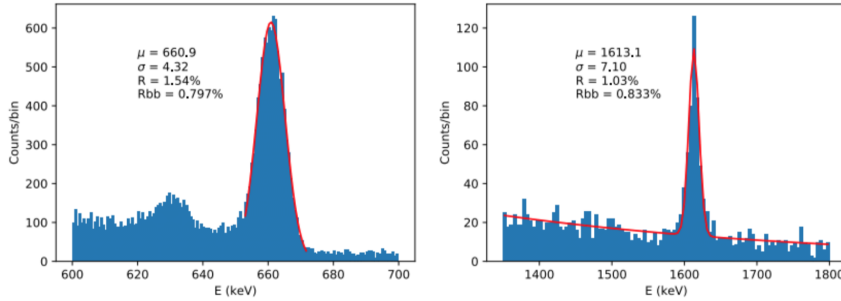


Figure 3.8: NEXT-NEW data fit to a Gaussian of the 662 keV photo-peak from ^{137}Cs de-excitation (left), and the fit to a Gaussian + exponential of the double escape peak from ^{208}Tl decay (right).

In particular, NEW will allow for the accurate characterization of the characteristic 2-electron tracks of our signal.

- It allows to check the validity of the background model estimated using detector simulations and data from material screening. As NEW deploys the same technology and materials chosen for NEXT-100, a validation of its background model will also directly imply the validation of that of NEXT-100.
- Finally, it may be possible to measure the half-life of the $2\nu\beta\beta$ decay mode of ^{136}Xe .

Recent NEXT-NEW data have reported an extrapolated energy resolution of approximately 0.8% FWHM at $Q_{\beta\beta}$ when measuring energy depositions of 662 keV (from de-excitation gammas of ^{137}Cs), and 1593 keV (from the double escape peak of the 2615 keV gamma from ^{208}Tl decay), as depicted in figure 3.8. Moreover a resolution of 0.5% for point like events from krypton has been also reached [135], and the collaboration expects to acquire the needed know-how to reproduce this energy resolution for longer events such as $\beta\beta$ -decays.

As previously mentioned, NEW shares most of the building technology with NEXT-100, so NEW detector design will be described in depth. It is worth noting that although some parts of the detector must be scaled-up in their NEXT-100 versions, some of them will be reused in their current state.

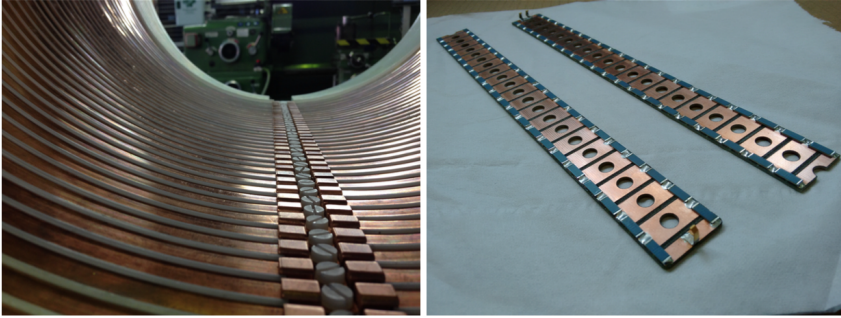


Figure 3.9: Detailed view of field cage copper rings (left) and resistor chain (right).

Electroluminescent TPC

One of the key technological challenges to be solved in NEXT detectors is the large sizes of the field cages. While in NEXT-DEMO the TPC was 16 cm in width and 40 cm long, the size of NEXT-100 will be 1 meter in width and 1.2 meter long. In this sense, building an intermediate field cage to test different technological approaches appeared very reasonable.

Finally, the main body of the NEW field cage is an open-ended cylinder of 49 cm external diameter, made of high-density polyethylene (HDPE) that provides electrical insulation from the vessel and structural support to other components. Three regions are defined inside the field cage: the buffer, the drift and the EL regions.

The buffer is 11.2 cm long and extends from the PMTs to the cathode. Its aim is to downgrade uniformly the high voltage (up to 50 kV) of the cathode to zero, in order to protect the PMTs.

The drift region extends from the cathode to the gate and is 52.7 cm long and represents the active volume of the detector. The cathode and the gate consist of stainless-steel wire meshes of 1 cm pitch, providing a 98.5% and 84% open area mesh respectively. The HDPE shell is lined with ultra pure copper [136] strips inter-connected with low background 10 GOhm resistors (see Figure 3.9) to degrade the high voltage, thus providing an homogeneous and uniform moderate electric field (300-600 V/cm). A teflon cylinder coated with tetraphenyl

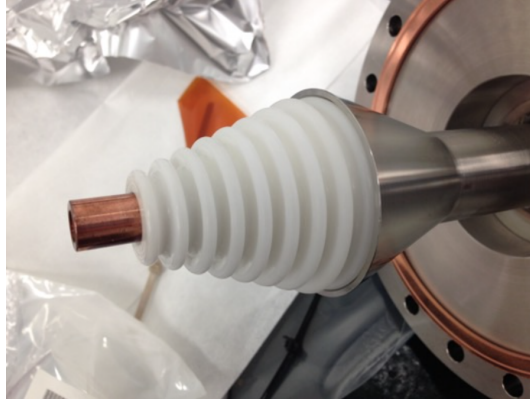


Figure 3.10: Detailed view of NEW high voltage feedthrough.

butadiene (TPB) lines the inside face of the field cage body along the drift length to increase the light collection efficiency.

The EL region extends from the gate to the anode, and was designed to hold up to 20 kV. The anode is a fused-silica rigid plate (52 cm diameter) coated with indium tin oxide (ITO) to make its surface conductive. It is also coated with the wave length shifter (WLS) TPB to convert the VUV light to blue light, a wavelength to which the fused silica has better transparency, and which matches the optimum response of the SiPMs.

One of the main design challenges has been the feedthroughs aimed to provide up to 50 kV between cathode and gate, passing through the pressurized vessel without creating leaks. They consist of an inner conductive rod surrounded by a custom made HDPE insulator manufactured by external companies according to NEXT specifications (see Figure 3.10).

NEXT-100 is expected to follow the same technological design to implement its corresponding field cage.

Energy Plane

The collaboration demonstrated with its two small prototypes, in the R&D phase [132, 134], that an extraordinary energy resolution was achievable with electroluminescent TPCs read out by PMTs. NEW followed the same technological approach and selected Hamamatsu's

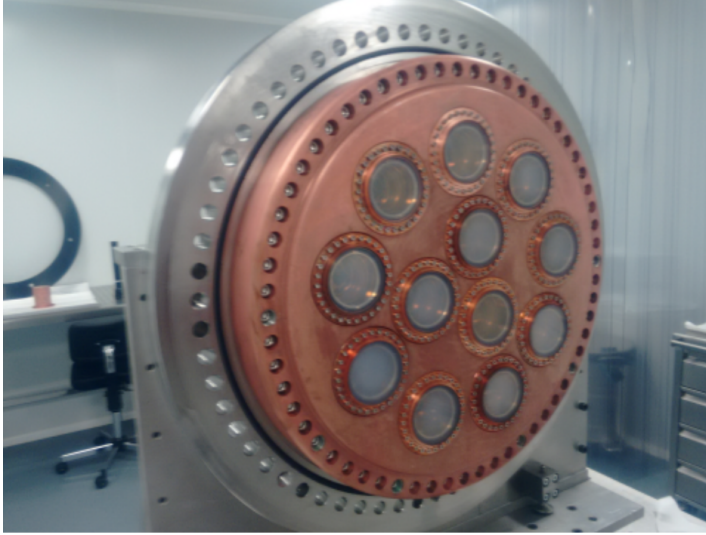


Figure 3.11: NEW energy plane consisting of 12 PMTs coupled to sapphire windows, arranged in two concentric rings.

3-inch R11410-10 PMTs [137] to perform the calorimetry readout, and NEXT-100 detector will use them as well.

In NEW, 12 PMTs are arranged in two rings, 3 PMTs in the inner and 9 in the outer, leading to a 35% photocathode coverage (see Figure 3.11). The PMTs plane is placed ~ 13 cm behind the cathode mesh to give enough space to downgrade the electric field and protect it from the high voltage.

As PMTs cannot withstand pressures above 6 atmospheres, they need to be separated from the high pressure xenon. This is done with sapphire windows that are coupled to the PMT windows with optical gel (NyoGel OCK-451) to match their refraction indexes. The sapphire windows are coated with TPB to match the maximum quantum efficiency of PMTs and to avoid the poor transparency of sapphire to VUV light.

The electronic bases of the PMTs (Kapton circuit boards) are pinned behind the PMT with heat dissipators connected to the copper shield. Shielded twisted pair cables are used to supply the high voltage needed and to extract the signal.

Tracking Plane

One of the flagships of NEXT detectors is the extra handle for background rejection provided by topological reconstruction. To be able to perform a reasonably good reconstruction, a high granularity of sensors is needed. NEXT-DEMO demonstrated [131] the reliability of multi-pixel photon counters (MPPCs) to achieve this goal. The number of devices employed is a compromise; it must provide a detailed reconstruction of events with the minimum number of devices to reduce backgrounds (no shielding exists between the tracking plane and the active volume) and costs.

SensL MicroFC-10035-SMT-GP SiPMs [138], with an active area of $1 \times 1 \text{ mm}^2$, are used in NEW thanks to their high efficiency to the re-emission wavelength of TPB ($\sim 50\%$), low dark count rate and especially their high radiopurity (thanks to their main component: silicon, and low mass). Considering that charge diffusion in pure xenon with electric fields around 0.5 kV/cm is about $1 \text{ cm}/\sqrt{\text{m}}$, a final pitch of 1 cm was selected as the ideal one [139].

SiPMs are arranged in 8×8 sets mounted on specially designed dice boards (DBs) made of radiopure Kapton. Although Geiger mode operation of SiPMs requires a unique bias voltage this is not viable due to the total number of detectors needed (1792 for NEW and 7200 for NEXT-100). So due to practical reasons, the 64 SiPMs grouped in the same DB share the same bias voltage, therefore all of them must be specially selected to have similar gains and reduce their gain dispersion. This selection is made after an automatized characterization of individual SiPMs as described in [140]. The DBs also incorporate a blue LED for calibration purposes and a temperature sensor. To increase the light collected by PMTs in the energy plane, a reflective teflon mask is fitted on top of the DBs reflecting the photons that do not reach SiPMs (see Figure 3.12).

The Kapton dice boards (KDB) are planar flexible circuits with many advantages. They allow for an automatic oven soldering of SiPMs on the pads, making the process feasible for many devices; they need a negligible amount of adhesive for their manufacturing, consequently reducing their background contribution [141]; and finally they can incorporate a flexible large tail that allows for the displacement of SiPM connectors behind the copper plate [142] thus shielding their

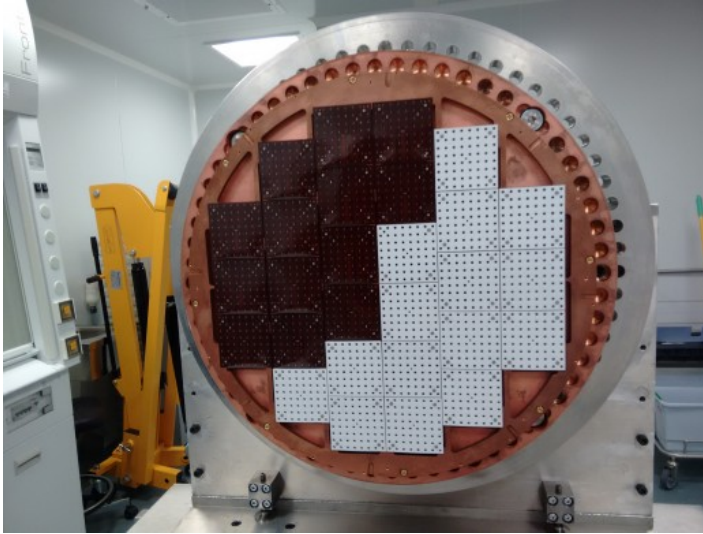


Figure 3.12: NEW tracking plane made of 28 custom designed dice boards, with 64 ($1 \times 1 \text{ mm}^2$ SensL) SiPMs each, forming a dense array of 1 cm pitch for topological reconstruction. Right half of boards covered with reflective teflon masks, and left half of boards without.

background contribution.

Programmable, multichannel SiPM power supplies were designed and produced in-house and reached a voltage stability better than 2 mV, representing a gain stability of 0.5 %. They incorporate a temperature auto-compensation voltage loop and an Ethernet interface for remote controlling [143].

Vessel

The NEW pressure vessel (NPV) is made of Ti-stainless steel alloy, and its dimensions lie between NEXT-DEMO and NEXT-100. It consists of three different parts: a main cylindrical vessel and two symmetric torispherical endcaps (see Figure 3.13). The cylindrical body has an internal radius of 64 cm and is 950 cm long and 2.4 cm thick. The endcaps, 1.26 cm thick and 30 cm long, are coupled to the central body with an O-ring junction for tightness. The vessel was built by a specialized company based in Madrid and it has the American Society

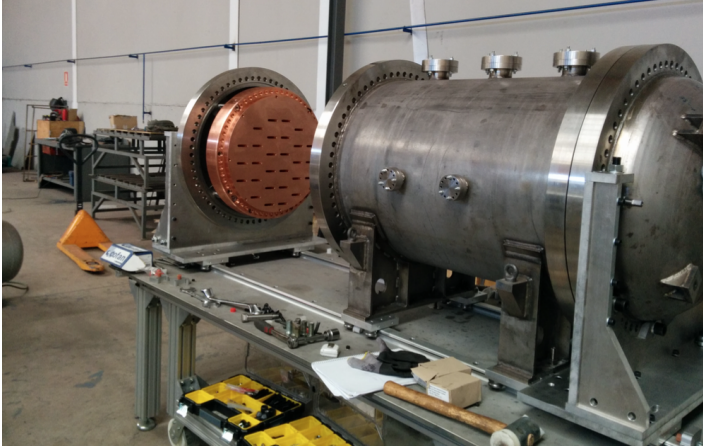


Figure 3.13: NEW vessel during its first assembly in its operational horizontal position. The tracking plane endcap is opened, showing the tracking plane copper shielding.

of Mechanical Engineers (ASME) certification. The whole system can hold up to 20 bar.

The NPV includes several nozzles for different purposes: to host the two high-voltage feedthroughs, gas recirculation, and calibration.

NEXT-100 vessel will use the same technological approach as NEW, and will be made of the same materials.

Inner Copper Shielding

A vessel of such size implies a large amount of background generated inside. To mitigate this, an inner shielding made of ultra-pure copper has been installed. This inner copper shielding (ICS), as in the vessel, consists of three different sections. The central part, positioned between the vessel and the field cage, consists of copper bars 6 cm thick. The energy plane endcap is shielded with the carrier plate of the PMTs being 12 cm thick, and the holes corresponding to PMTs are compensated by small caps 6 cm thick placed behind the PMT bodies. In a similar way, the tracking plane endcap is shielded by the support plate of the dice boards. It is also 12 cm thick and contains rectangular holes to allow the KDB tails to pass through (see Figure 3.14).



Figure 3.14: Detailed view of copper bars shielding the vessel body, with the energy plane viewed from the anode.

NEXT-100 ICS will use the same technological approach and materials than NEW.

Shielding

Similar to other detectors searching for rare physics, NEXT detectors need to be shielded against natural radioactive background coming from the rocky walls of the laboratory. A typical solution in these cases is the use of lead due to its high stopping power thanks to its density. The NEXT collaboration decided to build a shielding structure able to hold NEW and NEXT-100 indistinctly, and the LSC bought ancient roman lead (activity lower than 0.4 mBq/Kg) from the OPERA detector [144] to build it.

The shielding consists of a lead castle 195 cm in width, 265 cm high and 293 cm in length, with a wall thickness of 20 cm. It is made of staggered lead bricks ($200 \times 100 \times 50 \text{ mm}^3$) held by a stainless steel frame. The total weight is ~ 65 tonnes. The lead castle is made of two halves mounted on a system of wheels that move on rails with the help of an electric engine. The movable castle has an open and a closed position. The former is used for the installation and service of

the pressure vessel; the latter position is used in normal operation (see Figure 3.15).

An elevated working platform has been built around the castle prior to the installation of NEXT-100. It is designed to withstand a uniform load of 1500 kg/m^2 . It is anchored to the hall ground and walls. It allows direct access to the detector, and it is where peripheral components such as the electronics racks and gas system are placed.

Due to the mild seismic activity of the part of the Pyrenees where the LSC is located, a comprehensive seismic study has been conducted as part of the project risk analysis. As a result, an anti-seismic structure holding the vessel within the shielding castle has been built. This structure is anchored through a dynamic sink directly to the ground, and it is independent of the working platform to allow seismic displacements in case of an earthquake.

Gas System

The main goal of the gas system is to be able to purify the xenon gas, eliminating electronegative impurities (mainly O_2 and CO_2) present in the gas. Ionization electrons attach to these impurities, producing negative ions, and therefore reducing the electron collection efficiency of the detector. The purification is performed by recirculating the xenon through different external filters specially designed for these purposes. An additional molecular pump is employed to maintain the vacuum continually in the volume behind the energy plane.

The gas system has three different operational phases:

- Depressurization of the detector: First of all, before filling with xenon, the system must be brought to a vacuum level of 10^{-5} bar to eliminate all impurities the detector could contain. This is done with three turbo-molecular pumps. To improve the process, detector components not sensitive to heat are warmed to aid in the removal of any water vapor attached to their surfaces. The whole process is monitored with two Residual Gas Analyzers (RGAs) that measure the levels of impurities via mass spectrometry.
- Pressurization and recirculation: After reaching the desired level of vacuum, the vessel is filled with gas directly from the bottles.

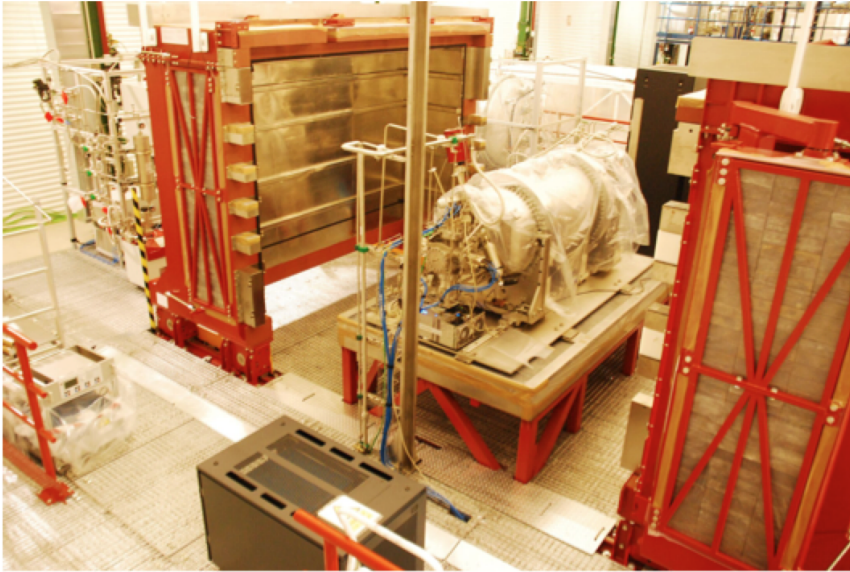


Figure 3.15: Top: Detailed view of NEXT shielding structure in its open position, with NEW vessel placed on the anti-seismic platform. Bottom: View of the shielding structure in its closed position during installation.

To ensure proper operation, before filling with enriched xenon, the whole process is checked with a less costly gas, such as argon. Once the detector is filled with xenon, the gas circulation is initiated.

The most vulnerable component of the gas system is the recirculation compressor, which must have sufficient redundancy to minimize the probability of failure and leakage. The compressor chosen by the Collaboration moves the gas through the system via a triple stainless steel diaphragm with sniffer ports to monitor for leakage between each of the diaphragms.

The gas moves through the re-circulation loop for continuous purification via cold and hot getters. The cold getter (Micro-Torr MC4500-902FV) removes water and oxygen that, especially during the first days of operation, could still be present in the gas [115]. The hot getter removes nitrogen and methane. The system has two cold getters mounted in parallel for backup purposes, and after them one serial-mounted hot getter.

- **Recovery:** Two different types of scenarios exist in which all the xenon in the gas system may be evacuated: controlled evacuations and emergency recoveries. The former is done via cryo-pumping. There is a recovery bottle that can be immersed in liquid nitrogen causing a drop of the temperature, thus creating a pressure gradient, and a slow recovery of all the gas in the system. In addition, an automatic recovery system is needed to evacuate the chamber in case of an emergency, such as an over-pressure that could potentially cause an explosion or an under-pressure indicating a leak in the system. In this case a KARTEN valve directly connecting the vessel to an expansion tank is open to quickly reduce the gas pressure in the system.

The entire system is continuously monitored by a complex LabView-based software developed by the collaboration.

With some scale factors and some minor improvements related with safety, the whole gas system will be reused by NEXT-100 as it is.

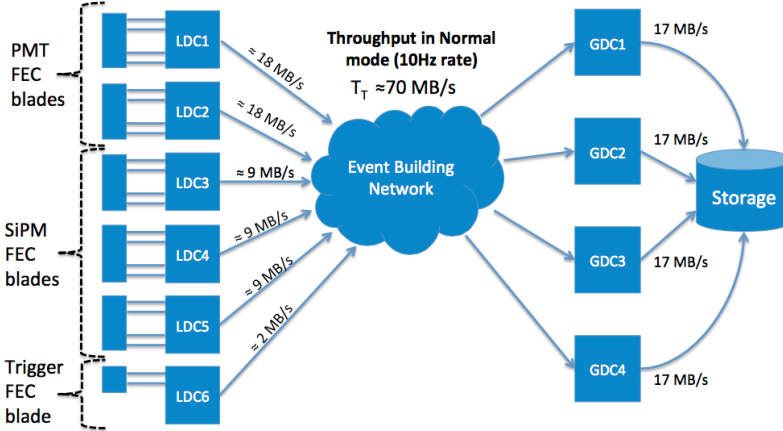


Figure 3.16: NEXT DAQ system with expected throughputs.

Data Acquisition

NEW data acquisition system (DAQ) follows a modular architecture known as the Scalable Readout System (SRS), developed within CERN endorsed by NEXT Collaboration [145] under the auspices of the RD51 Collaboration [127, 146].

At the top of the hierarchy, a PC farm running the DAQ software, DATE, receives event data from the DAQ modules via Gigabit Ethernet optical links. The DATE PCs (Local Data Concentrators, LDCs) assemble incoming fragments into sub-events, which are sent to one or more additional PCs (Global Data Concentrators, GDC). The GDCs build complete events and store them to disk for offline analysis.

The DAQ modules used are Front-End Concentrator (FEC) cards, which serve as the generic interface between the DAQ system and application-specific front-end modules. The FEC module can interface different kinds of front-end electronics by using the appropriate plug-in card. Three different FEC plug-in cards are used in NEW: energy plane (EP) readout digitization, trigger generation, and tracking plane (TP) readout digitization. A more detailed description of the whole electronics system can be found in [147].

Additionally, there is a slow control system in charge of reading

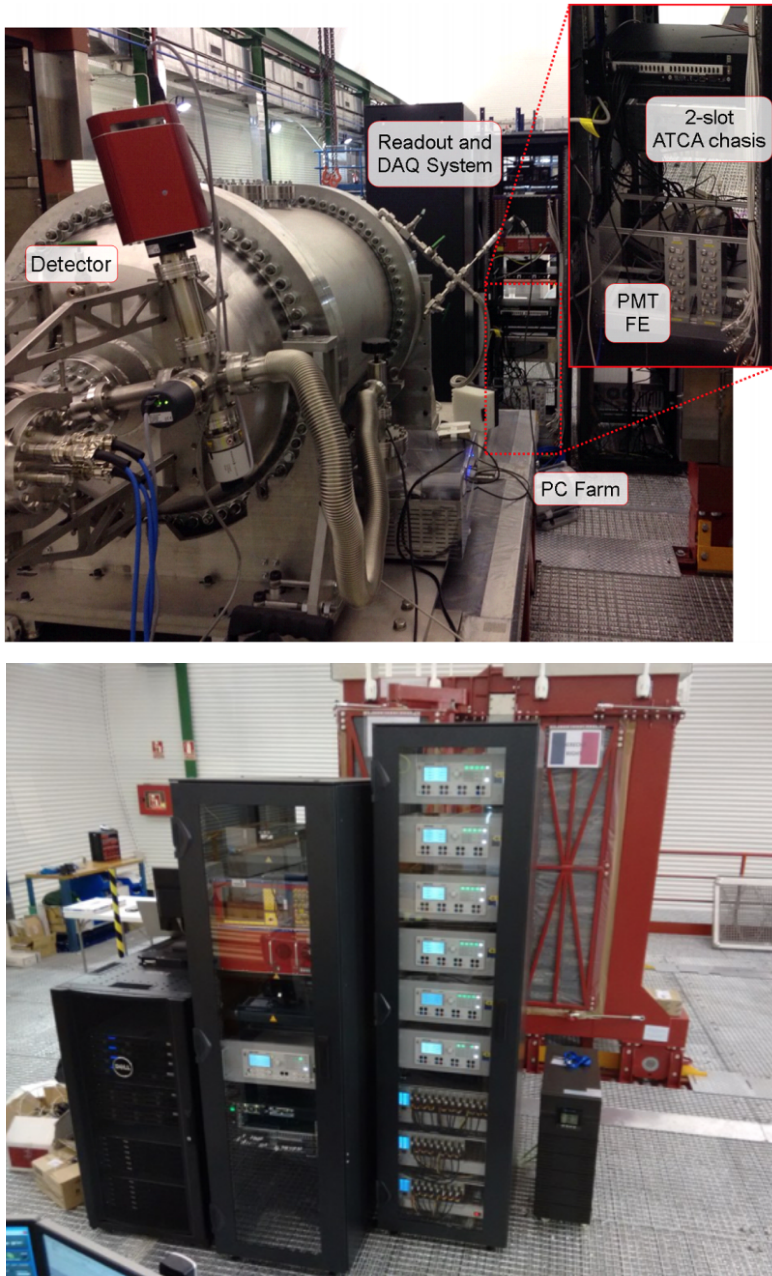


Figure 3.17: NEW electronic racks and the Slow Control PC during installation.

two temperature sensors for the EP front-end boxes (used to detect overheating due to a malfunction or fire), one vessel pressure sensor and a PMT vacuum side pressure sensor. A schematic drawing of all the electronics with expected throughputs can be seen in Figure 3.16.

During operation, all the electronics (front-ends, power supplies, slow controls, etc.) stand close to the vessel but outside the shielding castle to reduce the signal transfer losses (see Figure 3.17); and all of them are connected to the LSC main power line via UPS units for enhanced safety and protection.

NEXT-100 will follow the same technological approach for data acquisition, triggering and slow control as in NEW, with a scale-up of all the systems.

3.3.3 NEXT-100

The NEXT experiment was formally proposed to the *Laboratorio Subterráneo de Canfranc* (LSC) in 2009 in a *Letter of Intent* [148] that outlined the physics case and basic design concepts of an EL TPC for $0\nu\beta\beta$ -decay searches with a source mass of the order of 100 kg of ^{136}Xe . The detector design was narrowed down in the NEXT-100 *Conceptual Design Report* [149] published in 2011, and fixed a year later in the *Technical Design Report* (TDR) [102].

As we have already mentioned in section § 3.3.2, the NEXT-100 detector shares most of its construction technology with NEW, some of the systems will be reused as they are, and some of them require scaling up. The following is a summary of the NEXT-100 detector referenced to NEW. See Figure 3.18 for a detailed drawing.

The NEXT-100 field cage is a larger version of that installed in NEW. The main body is an HDPE cylinder of 148 cm length, 107.5 cm inner diameter and 2.5 cm wall thickness that provides structural stiffness and electric insulation; with copper rings for electric field shaping embedded in its inner face. The TPC anode is a fused-silica window 1 cm thick coated with ITO and TPB. The two other electrodes of the TPC, EL gate and cathode are built with highly-transparent stainless steel wire mesh, and they are positioned 0.5 cm and 106.5 cm away from the anode, respectively.

The energy plane of NEXT-100 will be composed of 60 Hamamatsu R11410-10 photomultiplier tubes (the same model as those used in

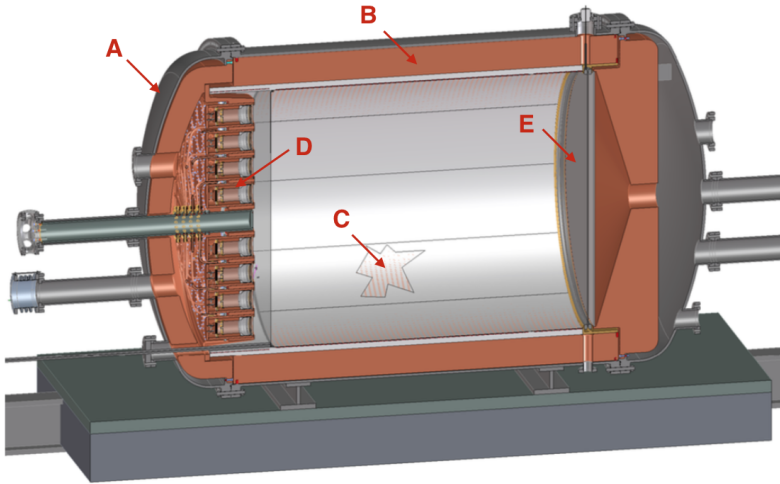


Figure 3.18: Cross-section drawing of NEXT-100 detector. A: stainless-steel pressure vessel, B: inner copper shielding, C: electric-field cage, D: energy plane, E: tracking plane.

NEW) located behind the cathode of the TPC and covering approximately 37% of its area. As they do not withstand high pressure, they must be sealed into individual pressure-resistant, vacuum-tight copper enclosures coupled to sapphire windows. PMT and enclosure windows are optically coupled using an optical gel with a refractive index between those of fused silica and sapphire. All the copper enclosures are mounted into a common carrier plate made of radio-pure copper.

The NEXT-100 tracking plane will consist of a matrix of silicon photomultipliers (SiPMs) placed at a pitch of 1 cm located behind the fused-silica window that closes the EL gap. The SiPM chosen is the Hamamatsu model S10362-11-050P as they are very cost-effective and their radioactivity can be very low. The SiPMs will be mounted on 8×8 flexible circuit boards made of Kapton. Like in NEW, the boards will have a long tail following a zigzagging path through the support copper plate to avoid a straight path for external gammas, and allowing to place SiPM connectors behind the plate. All the front-end electronics will be outside the chamber. In total, the NEXT-100 tracking plane will be composed of 7168 SiPMs distributed between 112 boards.

The pressure vessel of NEXT-100, shown in Figure 3.19 has already been manufactured. It consists of a cylindrical central section of 160 cm length, 136 cm inner diameter and 1 cm wall thickness, and two identical torispherical heads of 35 cm height, 136 cm inner diameter and 1 cm wall thickness. It has been fabricated with stainless steel Type 316Ti due to its low levels of natural radioactive contaminants.

NEXT-100 ICS will follow the same design than NEW, and it will incorporate some improvements such as 12 cm thickness central barrel, zigzagging piggytails for SiPMs connectors, and a copper endcap for PMTs instead of hats. The ICS will provide an attenuation of three orders of magnitude for γ radioactivity from the vessel.

Finally, the NEW shielding lead castle as it is, the gas system with minor improvements for safety reasons, and a scaled up version of NEW electronics system will be reused by the NEXT-100 detector.

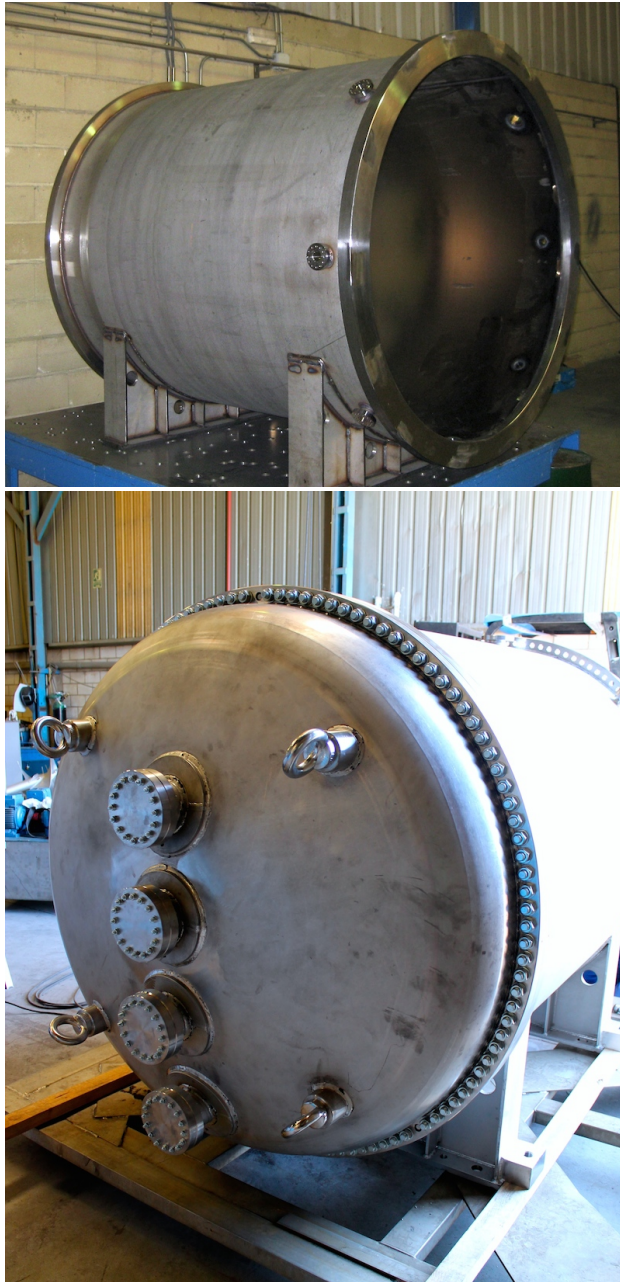


Figure 3.19: The NEXT-100 pressure vessel during the final stages of fabrication.

NEXT $0\nu\beta\beta$ Backgrounds

4

As we have seen in Section § 2.3, building detectors capable of identifying efficiently and unambiguously the rare $\beta\beta$ decays represent a considerable experimental challenge, and a low background rate is of the uppermost importance.

NEXT-100 is devoted to the search of ^{136}Xe $0\nu\beta\beta$ decays. These events basically consist of two electrons originated in a common vertex, with a total energy deposition equal to ^{136}Xe $Q_{\beta\beta}$ (2458 keV). Electrons below the so-called *critical energy* (about 12 MeV in gaseous xenon [43]) lose their energy via ionization with a more or less constant dE/dx until they become non-relativistic. At about that time, their effective energy deposition rate rises (see Figure 4.1), mostly due to the occurrence of strong multiple scattering, and the particles lose the remainder of their energy in a relatively short distance, generating a high deposition area, named as *blob* in NEXT slang. In summary, $\beta\beta$ decay events are reconstructed as single tracks featuring blobs at both extremes (see Figure 4.2).

Every physical process that can lead to a signal similar to this one is considered a potential background source. In principle, charged particles (muons, betas, etc.) entering the detector can be eliminated with essentially perfect efficiency defining a small veto region (of a few centimeters) around the boundaries of the active volume. Therefore only confined tracks generated by external neutral particles, such as high-energy gamma rays, or by internal contamination in the xenon gas could mimic our signal. Most of them are single electrons, thus having only one end-of-track blob and therefore, they will be reconstructed with a topology clearly different than that of signal events, as depicted in Figure 4.2.

A list of background sources that were considered on NEXT back-

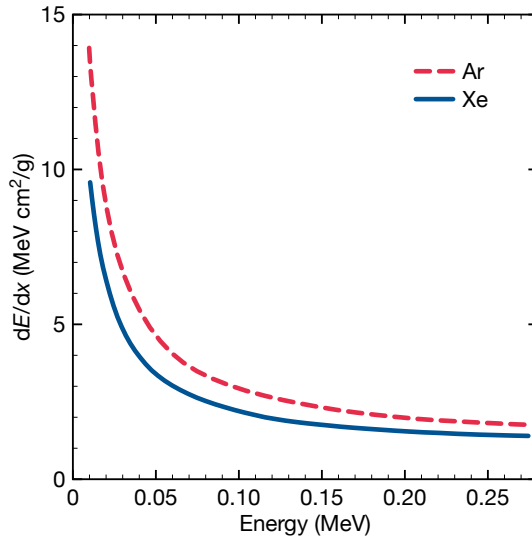


Figure 4.1: Energy loss for electrons in argon and xenon as a function of energy. Note the steep increase in dE/dx below 50 keV that results in the end-of-track blobs. Redrawn from Thomas et al. (1988) [150].

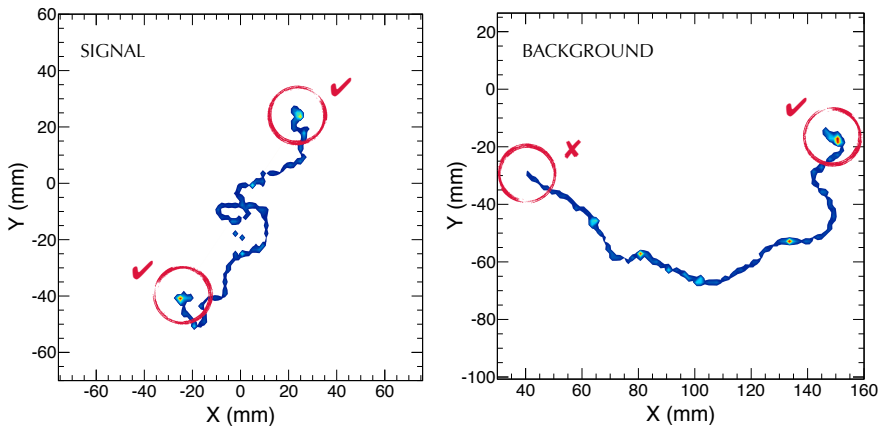


Figure 4.2: Monte Carlo simulation of signal ($0\nu\beta\beta$ decay of ^{136}Xe) and background (single electron of energy equal to the Q value of ^{136}Xe) events in gaseous xenon at 15 bar. The ionization tracks left by signal events feature large energy deposits, or *blobs*, at both ends.

Table 4.1: List of background sources considered during the development of NEXT background model and whether they were included in the sensitivity calculations.

Background Source	Status
Long Lived radionuclides in detector materials	Inc. in model
Flux of gammas from lab rocks	Negligible
Airborne Radon in LSC Hall A	Negligible
^{214}Bi from Radon decay in xenon gas	Negligible
^{214}Bi from Radon decay in TPC Cathode	Inc. in model
Underground cosmogenic muons	Inc. in model
Underground cosmogenic activation in xenon	Inc. in model
Underground cosmogenic activation in other detector materials	Negligible
Flux of neutrons from lab rocks	Inc. in model
^{136}Xe $2\nu\beta\beta$ decay	Inc. in model
ν_e elastic scattering	Negligible
Neutrino capture on ^{136}Xe	Negligible
Activation products from (α,n) reactions	Negligible

ground model is provided in Table 4.1, and they are discussed in detail in the remainder of this chapter. Measured activities of relevant sources are given also in this chapter, while the description of how these backgrounds have been simulated is done in Section § 5.4, and their final contribution to the global background budget is evaluated in Section § 6.3.

4.1 Natural Decay Series

The natural radioactivity of detector components is usually the main background in $0\nu\beta\beta$ -decay experiments. Even though the half-lives of the natural decay chains are comparable to the age of the universe, they are very short compared to the half-life sensitivity of the new-generation experiments. Consequently, even traces of these nuclides can become a significant background.

Particularly pernicious are ^{208}Tl and ^{214}Bi , decay products from the Thorium and Uranium decay series respectively (see Figures 4.3 and 4.4) due to the high-energy gammas emitted in their decays. From the Uranium chain, the daughter isotope of ^{214}Bi , ^{214}Po , emits a number of de-excitation gammas with energies around and above the ^{136}Xe $Q_{\beta\beta}$ [151]. Most of these gamma lines have very low intensity, and hence their contribution to the background rate is negligible. The gamma of 2447 keV (1.57% intensity [151]), however, is very close to $Q_{\beta\beta}$, and its photoelectric peak overlaps the signal peak even for energy resolutions as good as 0.5% FWHM [152]. From the Thorium chain, the decay product of ^{208}Tl , ^{208}Pb , emits a de-excitation gamma of 2615 keV with an intensity of 99.75% [151]. Electron tracks from its photopeak can lose energy via bremsstrahlung and fall into the *region of interest* (ROI). Additionally, even though the Compton edge of the 2.6 MeV gamma is at 2382 keV, well below $Q_{\beta\beta}$, the Compton-scattered gamma can generate other electron tracks close enough to the initial Compton electron so that they are reconstructed as a single track with energy around $Q_{\beta\beta}$.

Lower-energy gammas from long-lived radionuclides like ^{60}Co and ^{40}K are expected to dominate at energies below 1.5 MeV, well below ^{136}Xe $Q_{\beta\beta}$ (2458 keV). Although they do not contribute to the $0\nu\beta\beta$ background, they are very significant for $2\nu\beta\beta$ measurements, so they are systematically tracked as part of NEXT screening program.

^{208}Tl and ^{214}Bi are present at some level in all materials. Therefore, all $0\nu\beta\beta$ -decay experiments must follow an extensive selection campaign looking for extremely radiopure materials and characterizing their activities. Many of the activities have been determined by gamma-ray spectroscopy using the ultra-low background high purity Germanium (HPGE) detectors of the Radiopurity Service of the LSC [136]. Despite their high sensitivity, a few of the screened materials reached the HPGE detectors limits, being only possible to set upper limits to their activities. Another techniques like Glow Discharge Mass Spectrometry (GDMS) and Inductively Coupled Plasma Mass Spectrometry (ICPMS), have been used to improve limits of materials that could be destroyed. Limits quoted in literature from other experiments have been used for materials like quartz, too expensive to be destroyed and allow the measurement; or copper, whose activity

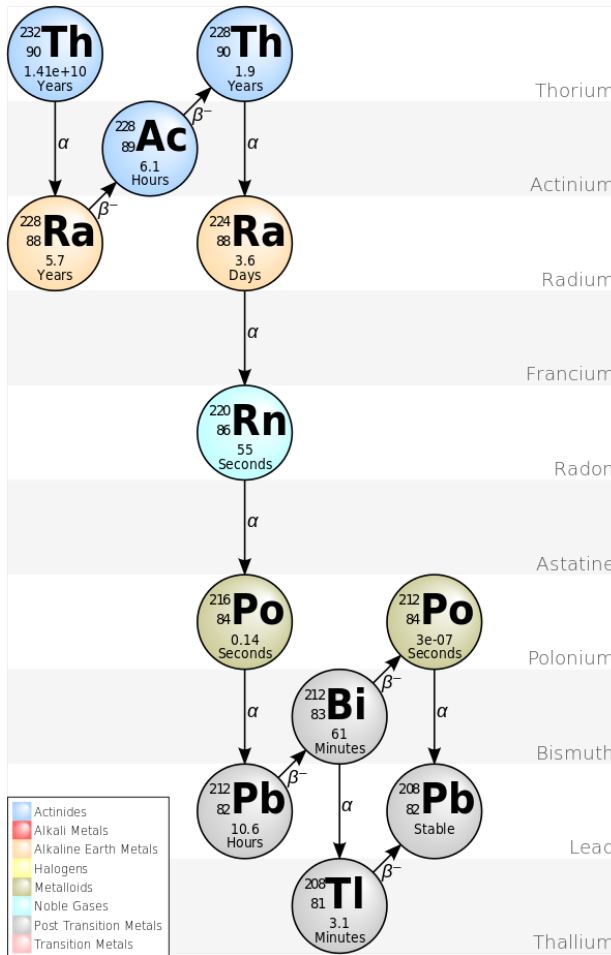


Figure 4.3: Thorium decay series, from ^{232}Th to ^{208}Pb [153].

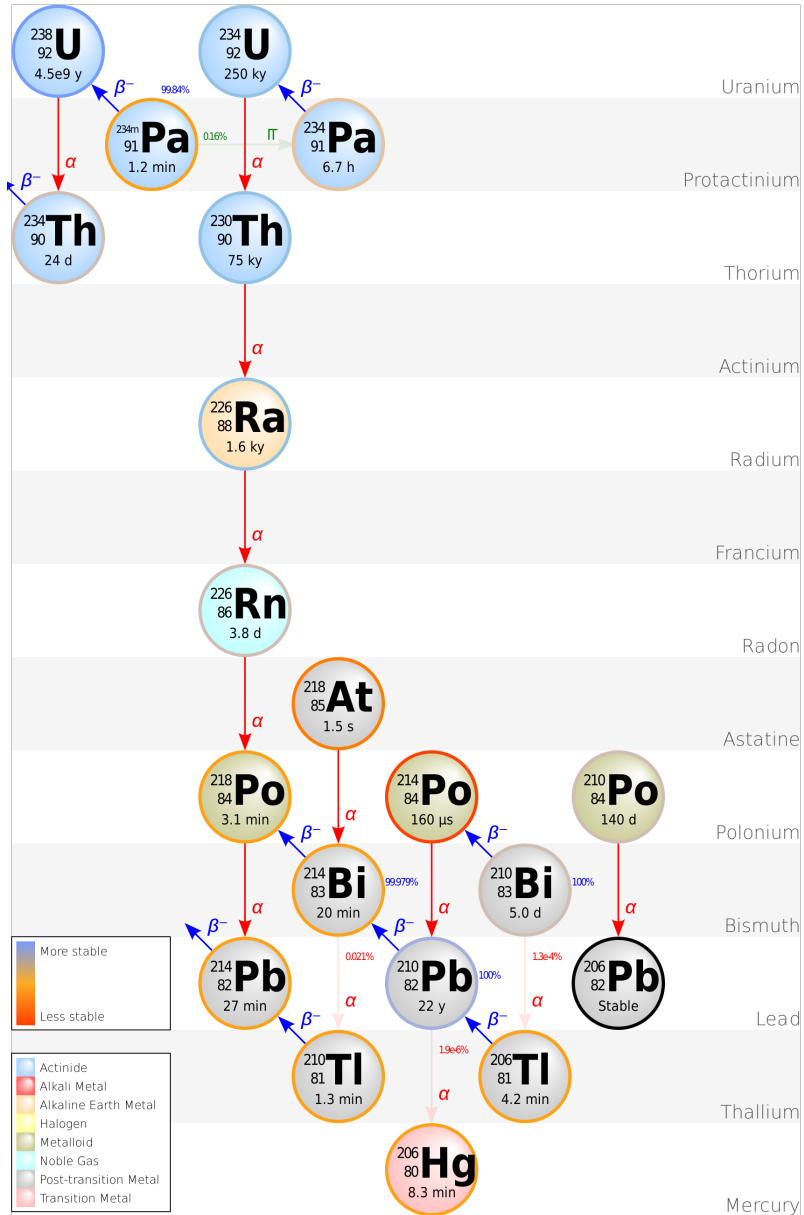


Figure 4.4: Uranium decay series, from ^{238}U to ^{206}Pb [153].

is below our detector limits, and the best achievable electroformed copper activity provided by Majorana experiment [83] has been used. However, converting the concentrations of nuclides at the head of the decay chains determined by these methods into background rates requires assumptions regarding the chain equilibrium. Assuming secular equilibrium is realized, these techniques can only estimate, rather than rigorously predict, the expected background rates.

The campaigns are still ongoing in a continuous screening and selection process of new components and materials suitable to be used to improve the total background budget of the detector. Procedures and activities have been published in different papers [136, 141, 154–158] during past years, as proof of the effort made by the collaboration on this issue.

Some points arisen along screening campaigns deserve specific comments:

- PMTs are expected to be one of the biggest contributors to the background budget of NEXT, so all of them, instead of a sample, need to be evaluated. The strategy followed to do the measurements in a reasonable time, consisted of taking measurements of three PMTs at a time to identify non tolerable levels of backgrounds in any unit (see Figure 4.5). Finally a joint analysis of all PMTs was performed. The results were published in [158], and they were in good agreement with similar studies from other experiments [93, 159, 160].
- SiPMs analysis revealed an unacceptable high activity of firstly selected Hamamatsu MPPCs, mainly coming from the high number of sensors needed, and from their proximity to the active volume. Finally more radiopure SiPMs from SensL were selected, and now the leading source of backgrounds from the tracking plane are the Dice Boards. Results have been published in [141].
- The anti-rust paint used in the steel structure supporting the lead castle shielding was revealed as too radioactive. So, although current measurements in NEW are occurring with this paint, it will be removed for the NEXT-100 operation.

The NEXT material screening data are recorded and stored in an online database. The data catalog systematically keeps track of these

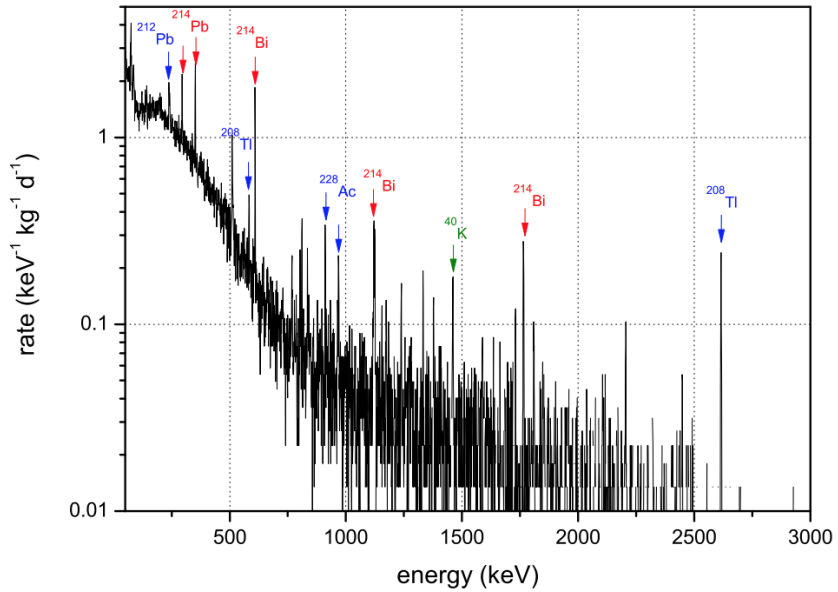


Figure 4.5: Top: Pictures from the LSC Radiopurity Service of the setup for material screening: Hamamatsu PMTs R11410-10 (left), and SensL SiPMs $6 \times 6 \text{ mm}^2$ (right). Bottom: Recorded spectra of a complete screened material by the HPGe Oroel.

measurements and their uncertainties to enable the computation of the total background rate. The more relevant activity numbers (90% CL) for NEXT-100 elements are summarized in Table 4.2 grouped in main detector systems. The given values are a combination of the measured activity for each one of their components times the amount of them present in the element. For instance, the ^{214}Bi activity assumed for the PMT bases is calculated by multiplying the activity screened for each one of the base components (capacitors, resistors, pins, etc.) by the number of PMTs in the detector (60), giving a total activity of 35.1 mBq. Notice that these values are total elements activities, and that they will suffer a huge attenuation from detector shieldings and the analysis process, before becoming real backgrounds. The uncertainties of measured activities are well below the presence of many limits so they are not presented.

Finally, it is worth to note that underground laboratory rock walls are another intense source of high-energy gammas due to the presence of different radioactive contaminants in their composition. These gammas could interact in the detector, producing background, but they can be suppressed by placing the detector in a shielding system typically made of dense and radiopure material as lead, copper and even water (see Figure 4.6). The total gamma flux in Hall A at LSC is $1.06 \pm 0.24 \text{ cm}^{-2} \text{ s}^{-1}$, with contributions from ^{40}K ($0.52 \pm 0.23 \text{ cm}^{-2} \text{ s}^{-1}$), ^{238}U ($0.35 \pm 0.03 \text{ cm}^{-2} \text{ s}^{-1}$) and ^{232}Th ($0.19 \pm 0.04 \text{ cm}^{-2} \text{ s}^{-1}$) [161], and the NEXT lead shield (see Section § 3.3.2), will attenuate this flux by more than 4 orders of magnitude, making its contribution to the final background negligible.

4.2 Radon

Radon, an intermediate decay product of the Uranium and Thorium series, is also a potential source of background for NEXT. It is one of the densest substances in gaseous state under normal conditions, and it is also the only gas in the atmosphere with radioactive isotopes. While the average rate of production of ^{220}Rn (from the Thorium decay series) is about the same as ^{222}Rn (from the Uranium decay series), the longer half-life of the latter (3.8 days versus 55 seconds) makes it much more abundant. The relevant part of the ^{222}Rn decay serie is depicted

Table 4.2: NEXT-100 radioactive budget from the natural contamination of ^{208}Tl and ^{214}Bi in the different materials and components (mBq). In bold, activity grouped into detector subsystems. Note some activities not coming from activity measurements but from upper limits.

VOLUME	^{208}Tl	^{214}Bi	Total
Dice Boards	1.26	8.10	9.36
DB Plugs	214	685	899
TRACKING PLANE	215.26	693.1	908.36
PMTs	11.4	21.0	32.4
PMT Bases	9.48	35.1	44.6
Enclos. Windows	< 1.19	< 5.34	< 6.53
ENERGY PLANE	22.1	61.4	83.5
Field Cage Barrel	< 1.06	< 8.59	< 9.65
Anode Quartz	0.233	1.44	1.67
FIELD CAGE	< 1.29	< 10.03	< 11.32
Inner Cu Shield	< 12.5	24.9	< 37.43
Tracking Support	< 0.24	0.48	< 0.71
Carrier Plate	< 0.77	1.54	< 2.30
COPPER SHIELD	< 13.5	26.94	< 40.44
VESSEL	< 197	< 603	< 800
SHIELDING CASTLE	530	5460	5990

in Figure 4.7.

Two basic mechanisms can lead radon to become a background. Airborne radon from outside the pressure vessel (basically the laboratory and the volume inside the Lead castle), and infiltrated radon into the Active region produced by the emanation of detector and gas system components. Although the signature of this background source is ultimately the same as the one described in section § 4.1, we distinguish the two categories since some radon contamination can be suppressed via active filtration systems depending on its origin.

The activity of airborne ^{222}Rn at the Laboratorio Subterráneo de

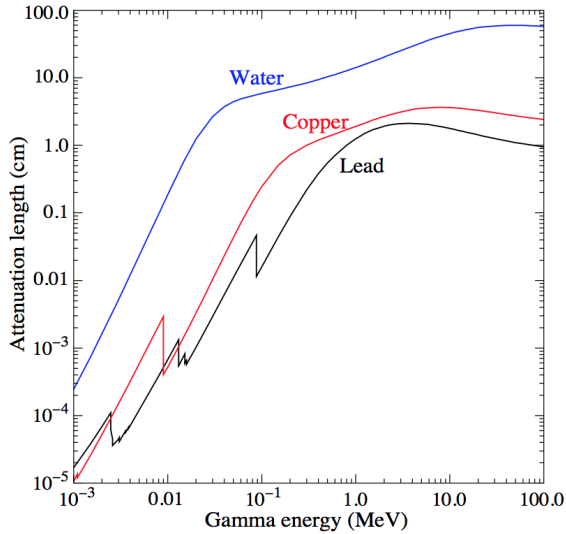


Figure 4.6: γ ray attenuation lengths in some common shielding materials [43].

Canfranc (Hall A) has been measured to be 66 Bq/m^3 [162], what would represent an extremely high source of background for NEXT. To overcome this issue two options were considered, flushing continuously the internal volume of the lead castle shield with a clean and dense gas that displace the radon contaminated air (nitrogen for instance), or installing a mitigation system at the lab, such as NEMO-3 [163] and DarkSide [164] experiments. Finally, LSC purchased a radon abatement system by ATEKO. It was installed in Hall A in December 2015 (see Figure 4.8). It is capable of reducing ^{222}Rn content to 1 mBq/m^3 , reducing the initial activity in around 3 orders of magnitude, thus making the contribution of airborne radon backgrounds to the whole budget, negligible. Figure 4.9 illustrates the airborne ^{222}Rn suppression in terms of its contribution to the total $2\nu\beta\beta$ signal expected in NEXT-NEW in a wide energy spectrum.

Radon can also emanate from detector material and components and from the gas system itself, reaching the active volume and being impossible to be shielded. The α decays of radon (either ^{220}Rn or ^{222}Rn)

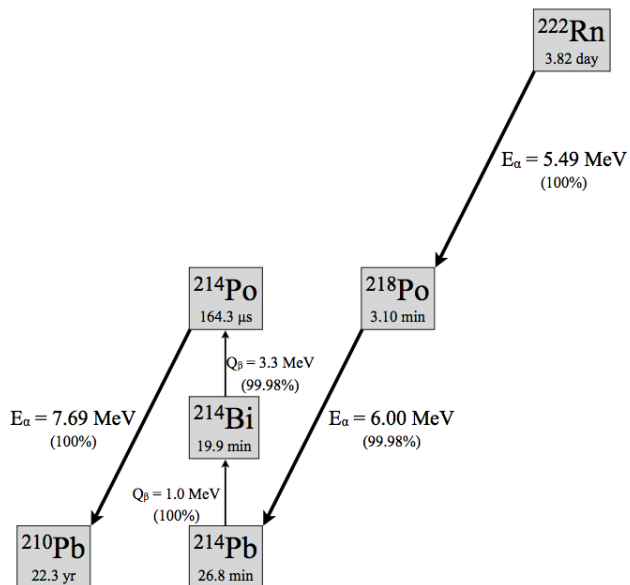


Figure 4.7: ^{222}Rn decay serie relevant for activity estimation.



Figure 4.8: Radon Abatement system by ATEKO installed in LSC Hall A.

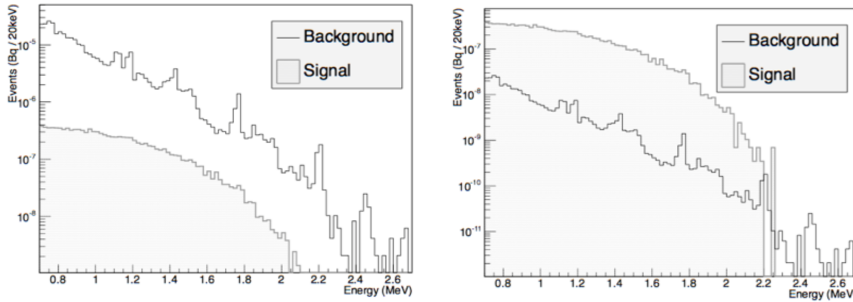


Figure 4.9: Expected $2\nu\beta\beta$ signal and airborne ^{222}Rn in NEXT-NEW with (right) and without (left) ATEKO abatement system [165].

in the bulk xenon do not represent a background: they have energies much higher than $Q_{\beta\beta}$ (see Figure 4.7), and their very short tracks are easily identified [115, 129] with 100% efficiency. In addition, a small fraction (0.2%) of the ^{214}Bi beta decays occurring in the xenon bulk will produce an electron track with energy around $Q_{\beta\beta}$. Eventually, the disintegration of ^{214}Bi is followed shortly after by the α decay of ^{214}Po ($T_{1/2} = 164 \mu\text{s}$ [151]) (so-called Bi-Po coincidence). Its detection can be used to identify and suppress with high efficiency these background events, making negligible their contribution.

These alphas are useful, however, to monitor the activity of radon in the xenon gas [46, 115], and has been recently used to measure the ^{222}Rn activity in NEXT-NEW [166]. The total measured ^{222}Rn activity in the fiducial volume is $1.81 \pm 0.17 \text{ mBq}$ which corresponds to an activity per unit volume of $36.4 \pm 3.5 \text{ mBq/m}^3$.

The way to extrapolate NEXT-NEW values to NEXT-100 depends on the main source of the emanated radon. In the design of NEXT-100 we have tried to avoid or minimize the use of materials and components known to emanate radon in high rates, such as plastics, cables or certain seals. Nevertheless, estimating a priori the radon emanation rate and consequent activity is very difficult, so two different extrapolation approaches are considered.

The pessimistic extrapolation assumes that ^{222}Rn emanation is dominated by the degassing of detector components, and scales with the detector surface area. The NEXT-NEW measured ^{222}Rn activity

per unit of surface is 2.78 ± 0.27 mBq/m², what would extrapolate to a NEXT-100 total activity of 18.34 ± 1.76 mBq. In the other hand, the optimistic extrapolation assumes that ²²²Rn emanation is dominated by gas system and not by detector components. Considering that the gas system will be the same for NEXT-NEW and NEXT-100, the NEXT-100 total activity would be: 2.97 ± 0.29 mBq, corresponding to a value per unit of volume of 2.31 ± 0.22 mBq/m³.

The progeny of radon is positively charged and will drift toward the TPC cathode. Therefore, a majority of the subsequent ²¹⁴Bi beta decays will occur on the cathode rather than in the active volume [46]. This assumption has been completely confirmed by the last alpha data measured in NEXT-NEW [166], finding a ratio of ²¹⁴Po to ²²²Rn in the fiducial volume of 0.051 ± 0.011 %, what in practice means that $\sim 100\%$ of ²¹⁴Bi decay from the cathode plane.

So finally we can conclude that all radon contributions to NEXT-100 background budget are negligible except the one coming from cathode ²¹⁴Bi decays. These cathode events are equivalent to other background sources close to the active volume: if the β particle enters the active volume, the event can then be vetoed; otherwise, the de-excitation gamma rays interacting in the xenon can generate background tracks able to mimic the signal.

To evaluate this contribution, given that all branching ratios from ²²²Rn to ²¹⁴Bi are nearly 100% (see Figure 4.7), a cathode originated ²¹⁴Bi activity from 2.97 mBq to 18.34 mBq for the optimistic and pessimistic scenarios respectively, must be considered. Results are presented in Section 6.3, and in case of being too high, a radon trap based on molecular sieves [167], or traps based on designs followed by other experiments like XENON100 [168], should be implemented in NEXT.

4.3 Muons and Neutrons

Finally, backgrounds with origin in the radiation from the atmosphere and outer space must be considered. These cosmic muons and neutrons are mitigated by placing the detector in underground facilities that reduce the flux in Earth's surface by several orders of magnitude (see Figure 4.10). Several facilities are currently available to host physics experiments around the world [60]. Figure 4.11 arranges them

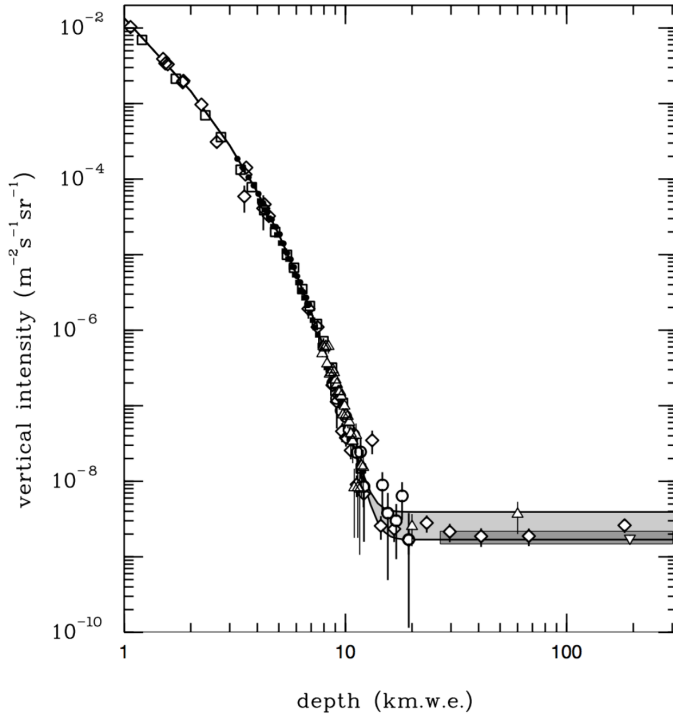


Figure 4.10: Vertical muon intensity vs depth (1 km.w.e. = 105 g cm^{-2} of standard rock). The experimental data are from: \diamond : the compilations of Crouch [169], \square : Baksan [170], \circ : LVD [171], \bullet : MACRO [172], \blacksquare : Frejus [173], and \triangle : SNO [174]. The shaded area at large depths represents neutrino-induced muons of energy above 2 GeV (around $2 \times 10^{-9} \text{ m}^{-2} \text{ s}^{-1} \text{ sr}^{-1}$) [43].

according to their depth and corresponding cosmic ray muon flux.

Muons

Muons are the most numerous (75 %) charged particles at sea level. Most muons are produced high in the atmosphere (typically 15 km) and lose about 2 GeV by ionization before reaching the ground with a $\cos^2(\theta)$ shape and an average energy of 4 GeV. Moreover, their intensity falls off rapidly with depth as seen in Figure 4.10. The LSC (850 m

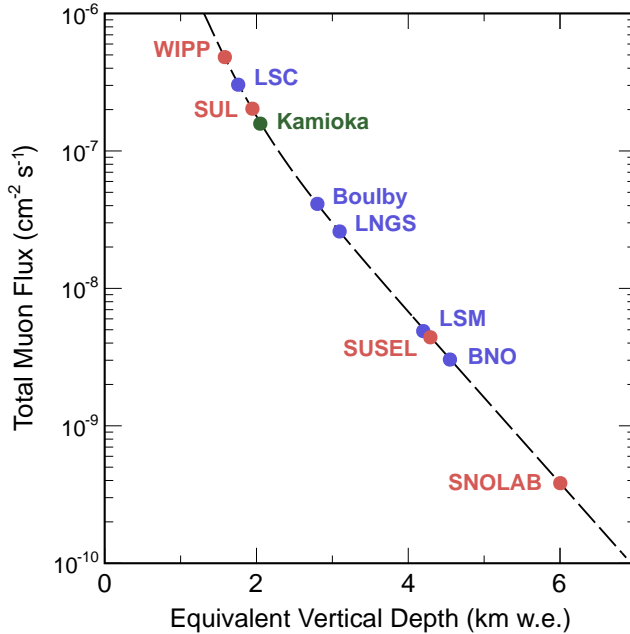


Figure 4.11: Total muon flux measured at various underground sites currently available to host physics experiments [60, 175]. An empirical parameterization [175] is shown as a dashed line. Facilities shown in red, blue and green are located, respectively, in North America, Europe and Asia. The full names and host countries of the facilities shown in the figure, from top to bottom, are the following: Waste Isolation Pilot Plant (WIPP), USA; Laboratorio Subterráneo de Canfranc (LSC), Spain; Soudan Underground Laboratory (SUL), USA; Kamioka Observatory (Kamioka), Japan; Boulby Palmer Laboratory (Boulby), United Kingdom; Laboratorio Nazionale del Gran Sasso (LNGS), Italy; Laboratoire Souterrain de Modane (LSM), France; Sanford Underground Science and Engineering Laboratory (SUSEL), USA; Baksan Neutrino Observatory (BNO), Russia; and Sudbury Neutrino Observatory Laboratory (SNOLAB), Canada.

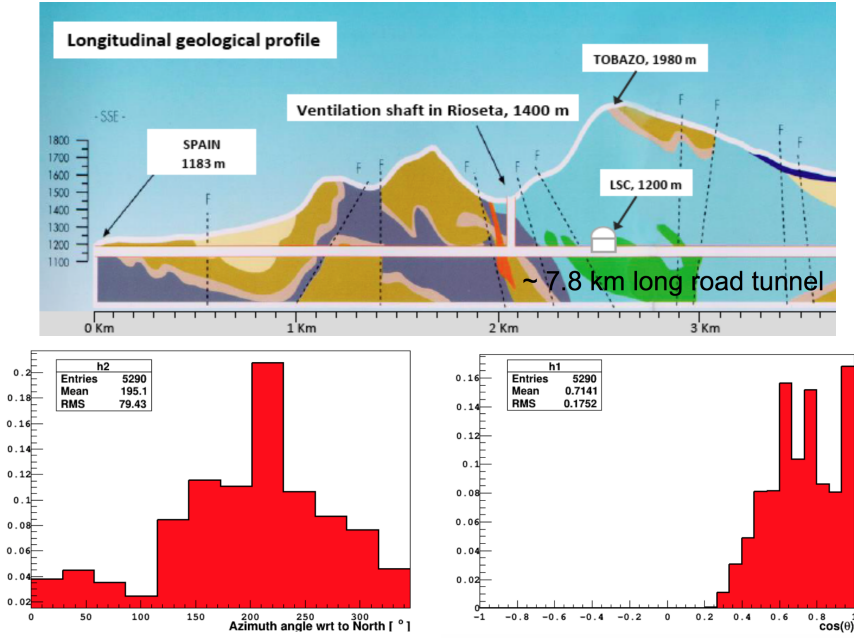


Figure 4.12: Top: Geological profile surrounding LSC. Bottom: Measured angular distribution: azimuth (Left) and elevation (Right) of cosmogenic muons [176].

under the Tobazo mountain ~ 2450 m.w.e. [162]) has measured a muon flux of $3 \times 10^{-6} \text{ cm}^{-2}\text{s}^{-1}$ [176] with an angular distribution that follows the geological shape surrounding the lab (See Figure 4.12).

The expected average energy of muons at LSC is analytically computed with the formula given in [175]:

$$\langle E_\mu \rangle = \frac{\epsilon_\mu(1 - e^{-bh})}{\gamma_\mu - 2}. \quad (4.1)$$

where h is the laboratory depth in km.w.e (2,450 for LSC Hall A), and the parameters ϵ_μ , b and γ_μ have been studied by several authors [177, 178] for standard rock ($A = 22$, $Z = 11$, $\rho = 2.65 \text{ g cm}^{-2}$). Uncertainties in these parameters are due to uncertainties in the muon energy spectrum in the atmosphere, details of muon energy loss in the media, and the local rock density and composition. We have used two different sets

of parameters provided by Lipari et al. [177] ($b = 0.383/\text{km.w.e.}$, $\gamma_\mu = 3.7$ and $\epsilon_\mu = 618 \text{ GeV}$) and Groom et al. [178] ($b = 0.4/\text{km.w.e.}$, $\gamma_\mu = 3.77$ and $\epsilon_\mu = 693 \text{ GeV}$), getting an average muon energy between 221 and 245 GeV.

Cosmogenic muons may produce fast neutrons and unstable nuclides in underground detectors through several mechanisms, including muon spallation (virtual photon nuclear disintegration), muon elastic scattering on neutrons, photonuclear reactions from electromagnetic showers, nuclear capture of stopped muons, and secondary neutron reactions from previous processes [179].

In principle, muons crossing the detector can be easily identified by their straight extended track with constant energy deposition in the active volume [130]. Moreover, active muon tagging systems allow to veto secondary background with sufficiently short half-lives with reasonable detector dead time, as done by EXO-200 [179]. On the other hand, secondary neutron interactions, specifically neutron capture, are of particular interest to low-background studies, as they may lead to activation of unstable nuclides with long half-lives, thus making unfeasible being vetoed by any dead-time. Most of these nuclides and their daughters are irrelevant as they are not capable of producing events near the $2\nu\beta\beta$ $Q_{\beta\beta}$. Simulations revealed that only ^{137}Xe , which β decays ranges up to a Q-value of 4173 keV, represent a noticeable background, and it is therefore the only cosmogenic radionuclide included in the background model.

Cosmogenic activation of detector components when being managed at the surface (specially those with intermediate-Z materials such as Cu and Fe) represents also an issue. To minimize the accumulation of long-lived activity, a proper management of parts and materials above ground during manufacturing and detector assembly is a must. To get it, some experiments such as MAJORANA [83] are even electro-forming copper underground, and some detector parts are being stored underground for long periods before being used.

Neutrons

The neutron background is a limiting factor in many rare event experiments because of the large penetrability of neutrons and the possibility of inducing background signals, specially in the direct search of WIMP

dark matter, as neutrons interact with the detector in the same way WIMPs do. In $\beta\beta$ decay searches they are also relevant as neutron captures can lead to the activation of different radionuclides present on different parts of the detector, or release protons and alphas that finally can generate energetic gammas able to mimic our signal.

Although the use of underground laboratories reduce the neutron background (in part muon induced) by several orders of magnitude with respect to sea level ($\phi_{sea} \approx 10^{-2} \text{ cm}^{-2} \text{ s}^{-1}$), lab rocks may represent an intense source of neutrons depending of their composition. These neutrons are produced in the spontaneous fission of ^{nat}U (mainly ^{238}U) and Th; and via alpha particles produced from the decay of intermediate nuclei in the natural decay chains, reacting with light nuclei in the rocks and producing neutrons via (α, n) reactions [180]. These neutrons are specially problematic as they are not in time coincidence with any muon, so they can not be vetoed by a dead-time.

Given its importance, the neutron field has been measured in different energy ranges in the majority of underground laboratories. In the case of the LSC, during the preparation of the IGEX-DM experiment the neutron background was investigated [181] at the old LAB2500. A value of $\phi_{LAB2500} = 3.82 \pm 0.44 \times 10^{-6} \text{ cm}^{-2} \text{ s}^{-1}$ was estimated, due essentially to radioactivity-related neutrons coming from the rock. The muon-induced contribution obtained was found to contribute only to the level of $10^{-9} \text{ cm}^{-2} \text{ s}^{-1}$, almost three orders of magnitude lower than the neutron flux due to the rock radioactivity. The most updated results on neutron flux at LSC Hall A [182], was made with an experimental setup consisting of six large ^3He proportional tubes embedded in high-density polyethylene block of different thickness, positioned in the middle of Hall A. They obtained a total flux of $\phi_{HallA} = 1.38 \pm 0.14 \times 10^{-5} \text{ cm}^{-2} \text{ s}^{-1}$ [183], following an energy distribution from the thermal peak ($1.00 \times 10^{-10} - 5.00 \times 10^{-7} \text{ MeV}$) up to 100 MeV depicted in Figure 4.13, and listed in Table 4.3 (without the normalization of the energy bin width). The results presented correspond to the average of the 4 different analysis methods followed in [182] (BAYES, CHIMEM, GRAVEL and MAXED), showing all of them very similar total flux and energy distribution (maximum difference between the four methods is 9%).

Table 4.3: Measured neutron flux in LSC Hall A for logarithmically distributed energy bins starting from the thermal peak up to 100 MeV.

Lower Energy (MeV)	Upper Energy (MeV)	$\phi(cm^{-2}s^{-1})$
1.00×10^{-10}	5.00×10^{-7}	9.17×10^{-7}
5.00×10^{-7}	1.69×10^{-6}	9.28×10^{-7}
1.69×10^{-6}	5.74×10^{-6}	1.30×10^{-6}
5.74×10^{-6}	1.95×10^{-5}	1.49×10^{-6}
195×10^{-5}	6.60×10^{-5}	1.10×10^{-6}
6.60×10^{-5}	2.24×10^{-4}	8.05×10^{-7}
2.24×10^{-4}	7.58×10^{-4}	6.22×10^{-7}
7.58×10^{-4}	2.57×10^{-3}	5.11×10^{-7}
2.57×10^{-3}	8.71×10^{-3}	4.86×10^{-7}
8.71×10^{-3}	2.95×10^{-2}	4.51×10^{-7}
2.95×10^{-2}	0.10	5.08×10^{-7}
0.10	0.16	3.62×10^{-7}
0.16	0.25	1.05×10^{-6}
0.25	0.40	4.91×10^{-7}
0.40	0.63	4.81×10^{-7}
0.63	1.00	6.21×10^{-7}
1.00	1.58	8.04×10^{-7}
1.58	2.51	5.17×10^{-7}
2.51	3.98	3.09×10^{-7}
3.98	6.31	2.18×10^{-7}
6.31	10.0	1.40×10^{-7}
10.0	20.0	1.46×10^{-7}
20.0	50.0	2.56×10^{-7}
50.0	100.0	6.17×10^{-8}

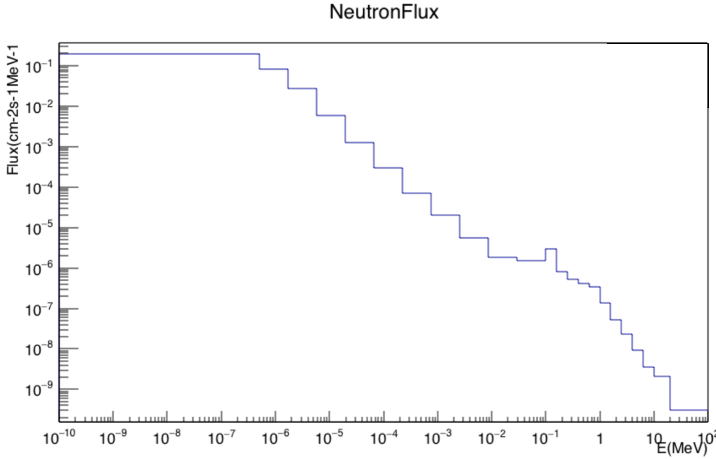


Figure 4.13: Measured neutron flux at LSC Hall A [182].

4.4 Negligible Backgrounds

As $0\nu\beta\beta$ decay experiments become more sensitive, and intrinsic radioactivity in detector materials is reduced, previously minor contributions to the background must be understood and must be subject of future studies. In this section several background sources with negligible contributions to date are presented.

$2\nu\beta\beta$

The $2\nu\beta\beta$ decay of ^{136}Xe (see Figure 2.3 - left), follows an energy spectrum depicted in Figure 2.2. Considering the finite energy resolution of any detector, the tail of the energy spectrum of the $2\nu\beta\beta$ will mix with the gaussian corresponding to $0\nu\beta\beta$ energy measure. Figure 4.14 represent the energy spectra of both decay modes in case of real detectors with different energy resolutions.

Considering that $2\nu\beta\beta$ decays will exactly have the same topology than $0\nu\beta\beta$ ones, it is worth to notice that energy resolution is the only protection against this background. Recent data from NEXT-NEW indicate that being conservative, an energy resolution of 0.7% FWHM at $Q_{\beta\beta}$ will be reached in NEXT operation, which will imply a negligible $2\nu\beta\beta$ background level.

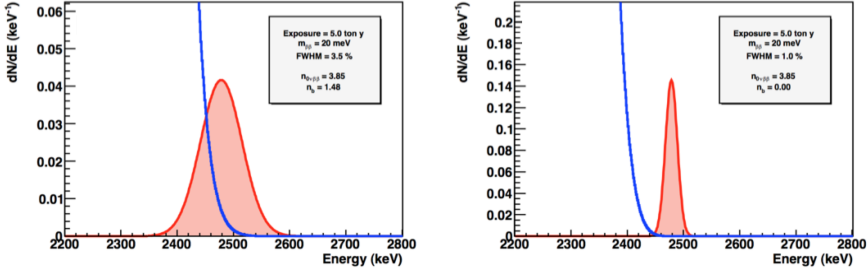


Figure 4.14: Energy spectra of $\beta\beta$ decay modes for an experiment with energy resolution of 3.5% (left) and 1% (right) FWHM at $Q_{\beta\beta}$, assuming $m_{\beta\beta} = 20$ meV and $T_{1/2}^{2\nu} = 2.165 \times 10^{21}$ years [46].

Solar Neutrino Interactions

Interactions of solar neutrinos in the detector are a potential source of background for $0\nu\beta\beta$ experiments that can't be vetoed anyway, as discussed in [77].

Electron-neutrino elastic scattering ($\nu_e + e^- \rightarrow \nu_e + e^-$) in the detector volume results in the emission of energetic electrons that can mimic the signature of a $0\nu\beta\beta$ event. From the studies carried out by other experiments [184], and the expected topology of potential backgrounds, values of the order of 10^{-7} cts $\text{keV}^{-1} \text{kg}^{-1} \text{yr}^{-1}$ is expected, therefore this contribution must be considered negligible.

From other side, the neutrino capture process via the charged-current reaction $\nu_e + {}^{136}\text{Xe} \rightarrow e^- + {}^{136}\text{Cs}$ also contributes to background, due to the combination of the e^- with a de-excitation gamma from ${}^{136}\text{Cs}$, and the decay of ${}^{136}\text{Cs}$ to ${}^{136}\text{Ba}$ with a half-life of 13.16 days and $Q = 2548.2$ eV. The contribution of this process to background in other experiments with worse energy resolution than NEXT, is estimated to be in the order of 10^{-7} cts $\text{keV}^{-1} \text{kg}^{-1} \text{yr}^{-1}$ [77], what implies that this background is negligible for NEXT.

Alpha captures

This is a second-order source of background. The decay chain of ${}^{222}\text{Rn}$ contains ${}^{210}\text{Po}$ that decays to ${}^{206}\text{Pb}$ emitting an α with a half-life of 138 days (see figure 4.4). This α can create background through (α, n)

reactions with low- Z detector materials such as F, C, O, Al, and Si contained in the sapphire and quartz present in NEXT-100 detector. The emitted neutrons could eventually activate ^{136}Xe producing ^{137}Xe whose β -decay (with Q -value of 4173 keV) could finally mimic the signal.

Estimates made by other experiments [77] allow to claim that under the assumption that proper surface treatment and handling will be performed during construction, this background will be several orders of magnitude below the expected total background of NEXT detectors.

Detector Simulation

5

Detector simulation is an essential tool in the design process of any detector that also allows to study its performance. It provides design guides, it allows to estimate acceptable levels of radioactive impurities in all detector materials and components, and finally it releases signal efficiency and rejection factors for any potential background source. These last factors together with background activity measurements are essential to assess the complete background model of any experiment.

NEXT simulation tool is called NEXUS (acronym of *NEXT Utility for Simulation* [59]). It is based on the Geant4 toolkit (see § 5.1), the standard simulation code in particle physics, and it is the first link in the software framework of the NEXT experiment. The output of NEXUS is expressed in exactly the same format that the output of NEXT data acquisition system (DAQ) once reconstructed, which allows to run exactly the same analysis algorithms to both of them.

On this chapter the basic structure of NEXUS § 5.1, and the three different modes of run § 5.2 are described. The validation efforts made to assure the quality of the simulation results are also described in § 5.3. Finally, some specific issues of NEXT-100 simulation § 5.4 will be given.

5.1 Geant4 and Nexus

Geant4 [185–187] is a software toolkit for the simulation of the passage of particles through matter using Monte Carlo methods managed by the International Geant4 Collaboration. It is written in C++ and designed with an emphasis on modularity and expandability that allows the users to load and use only the components needed. All aspects of the simulation process are considered in the toolkit: description and

navigation of detector geometries, models for the interaction of particles with matter, particle tracking, detector response, visualization and user interface. It also provides a large set of utilities including a set of physics units and constants, particle management compliant with the Particle Data Group, interfaces to event generators and object persistency solutions.

Geant4 divides a detector simulation into several basic components that the user must define; namely:

- *Detector geometry*: the physical layout of the simulated system made of a number of volumes, including a description (microscopic and macroscopic) of the materials used in its construction.
- *Physics list*: a collection of physics processes and their associated particles to be considered in the simulation. Geant4 provides seven major categories of processes: electromagnetic, hadronic, transportation, decay, optical, photolepton-hadron and parameterization.
- *Event generation*: the initial conditions of each primary event to be simulated; that is, the number and type of particles in the event, their position within the detector geometry and their initial three-momentum.
- *User actions*: operations that retrieve data of interest to the user about the trajectory and interactions of particles as they propagate through the detector. This information is available at several processing stages during the simulation.

NEXUS is a Geant-based computer program that comprises a collection of such components. The user selects via a macro file the components of each of the above categories that wants to load at runtime. These components may have their own macro commands that let the user further refine the configuration of the simulation. The output information from the simulation is saved to disk in the form of high-level data objects —such as particles, tracks or detector hits— described in an internal library of the Collaboration called GATE, based on ROOT [188,189], a physics standard scientific software framework. Such a design, illustrated in Figure 5.1, allows the simulation of many

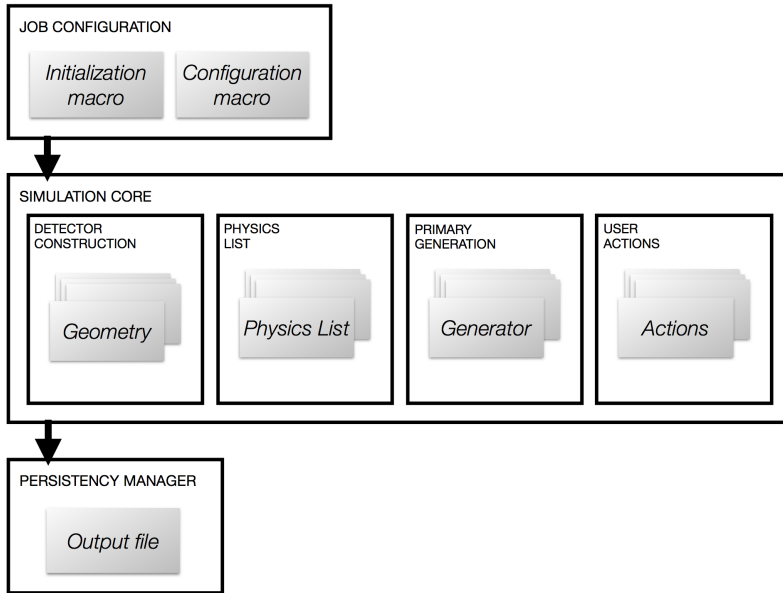


Figure 5.1: Basic structure of the NEXUS detector simulation program from [59].

different systems to be performed with the same program, and have been used inside the collaboration to simulate all the detectors developed.

The basic simulation unit in Geant4 is the *event*, consisting of a set of *primary particles* that interact with the detector materials producing an associated *detector response*. The data flow during the simulation of an event in NEXUS is outlined in Figure 5.2. A *generator* produces *primary particles* with a given momentum and position within the detector. The events can be filtered at generation time so that only those with a certain property (e.g. energy above a certain threshold) are kept. During this step, the run number for the simulated dataset and event numbers for each event are established. Event numbers are consecutive in a single run, but events may be omitted because of filtering. Run numbers for simulated datasets derive from the job options used to generate the sample and mimic real run numbers

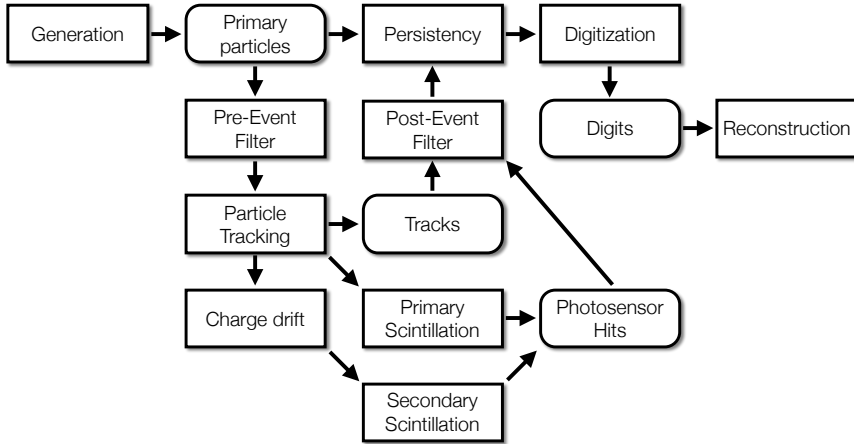


Figure 5.2: From [59]: event data flow in NEXUS from generation (top left) to reconstruction (top right). Algorithms are placed in square-cornered boxes and persistent data objects are placed in rounded boxes.

used during data taking. A record of the particles produced by the generator is stored in the simulation output file.

All primary particles are propagated through the detector geometry by Geant4 down to zero range, and in their interactions with the detector materials further particles may be generated. The trajectories and associated energy deposits of charged particles in the active volume of the detector are recorded as *track hits* and written to the output file. The number of photons converted in a given photosensor is stored as time histograms called *photosensor hits*. Its sampling time (bin width) can be configured by the user. The genealogy of each simulated particle and the history of their interactions are also stored in the output file. The digitization constructs *digits*, i.e. data structures equivalent to those generated by the NEXT DAQ, using the photosensor hits. Detector noise is added at this stage. Finally, a post-event filtering step decides whether to store an event depending on the results of the simulation. A record of the number of filtered events is stored in the output file together with other basic statistics of the run.

5.2 Simulation Modes

The *full simulation* of a $0\nu\beta\beta$ signal event with all the physical processes involved requires of huge computing effort. From the description in § 3.1, we know that a single $0\nu\beta\beta$ decay implies the generation and propagation of $\sim 62.7 \times 10^3$ primary scintillation gammas (from eq. 3.8), the generation and drift of $\sim 112 \times 10^3$ ionization electrons (from eq. 3.6), and the propagation through the EL-gap and processing of $\sim 10^7$ electroluminescence photons per ionization electron. All this translates into a CPU-time of several hours per signal event, which in practice limits the utility of the simulation.

To address this problem a new mode of simulation run was developed: the *parameterized simulation*. In this mode, the electroluminescence photons are not tracked individually, and its detection probability is replaced by a looked up in a table indexed by its $x - y$ production location in the amplification plane. This table is produced in an independent Monte Carlo run in which a large number of photons is generated per point on a grid dividing the EL plane, and the detection probability for each photosensor recorded based on the number of photons collected. The parameterized simulation of a single $0\nu\beta\beta$ decay takes around few hundredths of a second of CPU-time, improving the time needed by the full simulation in 5 orders of magnitude. This mode is currently being used to make all the studies of energy and spatial resolutions, calibration, etc. of NEXT-NEW detector, and it is expected to be used also in NEXT-100.

However the aim of this thesis relies on the evaluation of the expected background ratio of the whole detector for different configurations, and this volume of calculation is not affordable even with the parameterized simulation. So, with the goal of being able to carry out these studies, we developed a *fast-simulation* mode. In this simplified mode, neither the primary scintillation nor the ionization charge collection and amplification are simulated. Monte Carlo hits are stored in the output file, and they will suffer a *pseudo-reconstruction* in analysis time (see description in Section § 6.1.1), to model the full simulation chain as close as possible.

The fast simulation mode has enabled to run a complete set of backgrounds for the whole detector in few months, making feasible the assessment of the background model; but several levels of simplifi-

cation in the simulation have had to be assumed. These assumptions have to be somehow validated to give credibility to the results of these studies, and all the validation effort is explained in the next section § 5.3.

5.3 Validation

All the results given in this thesis are based on *fast-simulation* mode data, so in order to be confident on them, a lot of effort has been put to validate this simulation mode. In this section the comparisons between parameterized mode with data, and with the full mode are presented. There is an extra comparison between parameterized and fast simulations that, as far as it is based on results obtained from the classical analysis, will be presented as an output of the analysis in § 6.2.

5.3.1 Data vs Parameterized Simulation

The first validation effort was done with data from the NEXT-DEMO detector, being part of the first studies of the topological signature in high pressure xenon gas electronuminescent TPCs [133].

The analysis was performed using data from two different calibration sources to study the topology of background-like and signal-like events in NEXT-DEMO. Background-like events were studied using a ^{22}Na calibration source. The de-excitation of the first excited state of the ^{22}Na daughter isotope ^{22}Ne , produces a gamma with an energy of 1.275 MeV. These gammas can produce a photo-electron which leaves a track in NEXT-DEMO of approximately 7 cm length (at 10 bar pressure). On the other hand, signal-like events were obtained using a ^{228}Th source. The ^{228}Th decay chain includes ^{208}Tl , the daughter of which, ^{208}Pb , is created in an excited state which de-excites emitting a 2.615 MeV gamma. This gamma can produce an electron-positron pair with a signature which mimics, except for the total energy, the topology of a $0\nu\beta\beta$ event. The positron produces a blob equivalent in energy to that of the electron, and, when it annihilates, emits two back-to-back 511 keV gammas. Due to the size and the pressure of NEXT-DEMO, there is a high probability for both gammas to escape the active volume. In this case, the energy deposited in the chamber is

1.593 MeV and the track left by the electron-positron pair is around 6 cm long. Although the energy of these signal-like events is higher than that of background-like events, the track is slightly shorter on average because both the electron and the positron, individually, have a lower energy than the photo-electron of the ^{22}Na decay. These two sources produce tracks of comparable size and energy hence providing two data sets with good characteristics for topological studies and validations.

The ^{22}Na and ^{208}Tl data were taken under the following detector conditions: 10 bar pressure, 667 V cm^{-1} drift field and $2.4\text{ kV cm}^{-1}\text{ bar}^{-1}$ EL field. The sources were placed outside the lateral port positioned midway between cathode and anode. The simulation was run in parameterized mode with light tables generated for the same detector conditions. Main comparison results are depicted in figures 5.3 and 5.4 showing very good agreement between topological features of simulations and data.

5.3.2 *Full vs Parameterized Simulations*

As discussed above, full simulation of a single event takes a few hours to run, what makes unfeasible any statistical study based on this mode of simulation. Parameterized simulation reduces the CPU times from hours to hundredths of second per event, but to trust on their results, some statistical comparisons must be made first. In this section the generation of the Look Up Tables (LUTs) for scintillation and electroluminescence signals, how they are used in the simulation, and their validation are presented.

Scintillation Parameterization

Parameterization of scintillation signal is made for the energy plane of NEXT detectors through the following steps:

- The Active volume is virtually divided into a cubic grid over-covering it (1 cm pith for NEXT-NEW, and 2 cm for NEXT-100).
- 10^6 photons of 7.21 eV (corresponding to the average ^{136}Xe scintillation wave-length of 172.05 nm) are isotropically emitted per grid point.

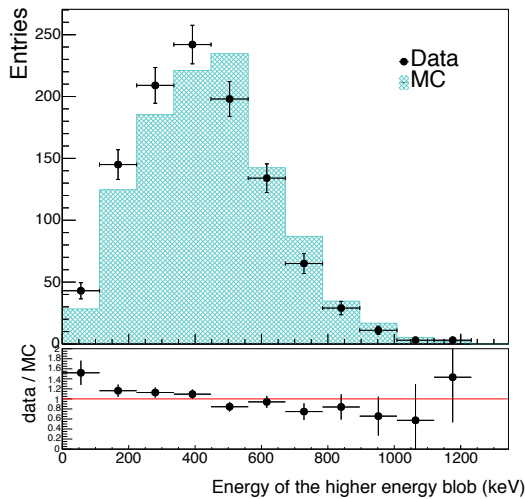
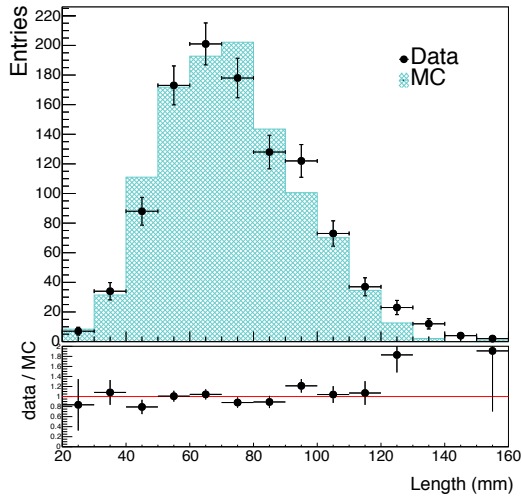


Figure 5.3: From [133]: comparison between data and Monte Carlo parameterized simulations, for the reconstructed length of the tracks (top) and the reconstructed energy inside the blob candidate with higher energy (bottom). ^{22}Na samples are used. Bins 12 and 13 in the bottom plot are not shown due to lack of MC statistics.

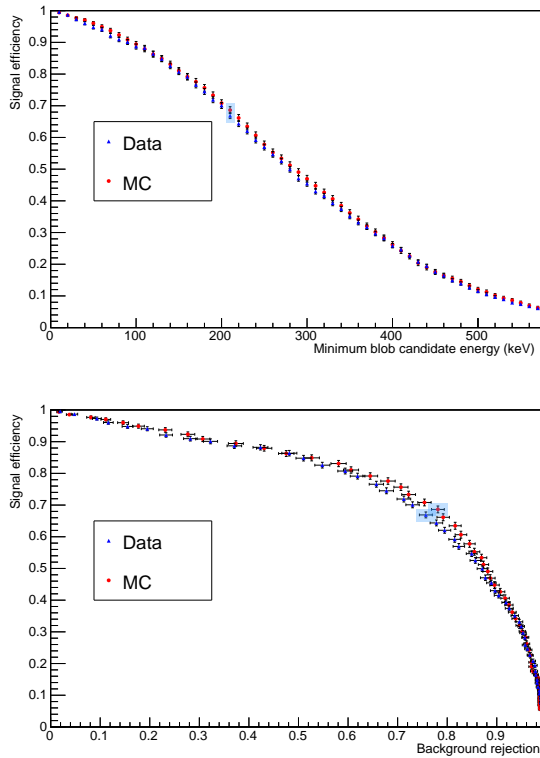


Figure 5.4: From [133]: (Top) Signal efficiency as a function of the required minimum energy of the lower energy blob candidate. Both data and Monte Carlo parameterized simulation are shown and the values corresponding to the cut used in this analysis are highlighted. (Bottom) Signal efficiency as a function of background rejection varying the required minimum energy of the lower energy blob candidate.

- The probability of reaching any PMT (P_i) is computed as the number of photons reaching the PMT ($N_{detected}$) divided by the number of photons emitted (N_{shot}): $P_i = N_{detected} / N_{shot}$
- Previous probabilities present certain symmetries in terms of relative PMT positions expressed in cylindrical coordinates (rad, φ) respect to the (x,y) of the grid point, and the distance to the energy plane (the z coordinate). These symmetries are parameterized using the next function:

$$f(r, z) = \sum_{i=0}^2 \left(\sum_{j=0}^4 a_{ij} \cdot z^j \right) r^i \quad (5.1)$$

where z is the distance of the grid point to the energy plane (modeled by a 4th degree polynomial), and r is the transverse distance between the (x,y) position of the grid point and the PMT position (modeled by a 2nd degree polynomial). The relative angle between the (x,y) position of the grid point and the PMT (φ) is also discretized in nine different sectors with same probability pattern, so finally we have a set of formulas (5.1), one per φ sector.

Parameterized simulations of scintillation light follow the next procedure: the number of emitted photons (N_{shot}) for each point along the simulated track is calculated taking a sample from a gaussian distribution with mean (E_{dep} / W_{sci} , see § 3.1). The number of detected photons ($N_{detected}$) for each PMT is calculated as the summation of all the detected photons coming from every point of the simulated track. The individual number of photons coming from a single point, is calculated taking a sample from a poisson distribution with mean equal to ($N_{shot} * P_i$) being P_i the detection probability of photon emitted from that particular point by that particular PMT, given by the formula (5.1) corresponding to the appropriate φ sector.

The results of NEXT-NEW parameterized simulations in terms of total number of scintillation photons are presented in Figure 5.5 showing negligible differences. On the top, the total number of scintillation photons detected by the whole energy plane, accurately reproducing the peak around 50 photons, and the long tail corresponding to events located in front of any PMT. On the bottom, the number of photons

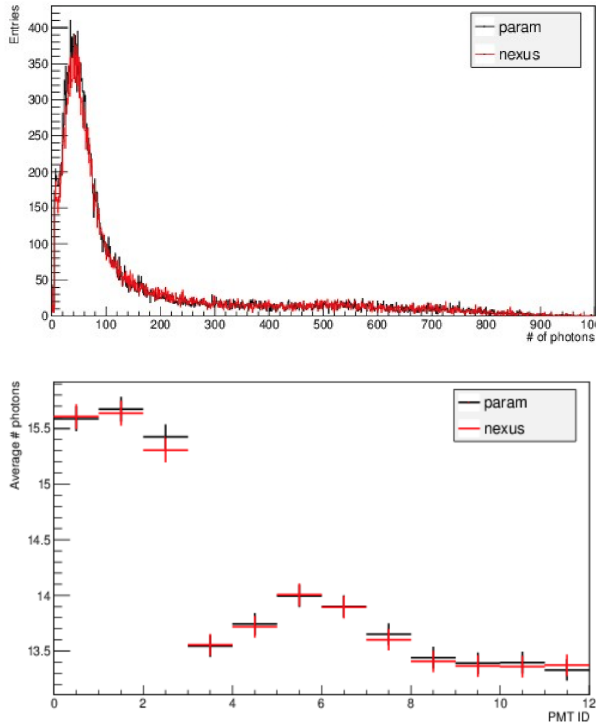


Figure 5.5: Comparison between the full and parameterized simulation modes of NEXT-NEW, in terms of the number of scintillation photons detected by the whole energy plane (top), and per PMT (bottom).

detected by each of the 12 PMTs, with the three of them placed in the internal ring detecting significantly more photons than those placed in the outer one.

Electroluminescence Parameterization

Parameterization of electroluminescence signal (so-called S_2) is made for the energy and tracking planes of NEXT detectors, following the next steps:

- The EL-mesh is virtually divided into a square grid of 1 mm pitch over-covering it.

- 10^3 electrons are placed at the beginning of the EL-region passing through the EL-gap and yielding a large number of photons ($\sim 10^4$ per electron).
- The probability of reaching any PMT (P_i) is computed as in the case of the scintillation light, as $P_i = N_{detected} / N_{shot}$, but in this case, due to the high dispersion in photon arrival times, the probability is computed per time bin. Given the barely-uniform spatial distribution of electroluminescence light in the energy plane, these probabilities are parameterized only using the absolute transverse distance of the emission point to the center of the chamber per PMT.
- In the tracking plane, only those SiPM within a radius of 2 cm for each x-y point are considered to calculate the detection probability (computed in the same way than those for PMTs), as the light roughly decreases two orders of magnitude for further sensors. The parameterization of these probabilities is made per time bin, with a polynomial using the relative transverse distance between the emission point and the SiPM.

Parameterized simulations of electroluminescence light follow the next procedure:

- Every ionization hit from the simulation is translated to a number of electrons taking a sample from a poisson distribution with mean (E_{dep} / W_i , see Section § 3.1). The drift to the EL-mesh of every ionization electron is automatically done, translating the (X,Y) coordinates to the EL-mesh applying a blur effect according to the transverse diffusion in gas xenon, and the arrival time being computed according to the Z coordinate and longitudinal diffusion.
- The time binned detection probabilities for every PMT and relevant SiPM are retrieved and used to calculate the number of detected photons per time bin and sensor coming from every ionization electron, chosen to be a poisson distributed variable with mean the number of photons emitted times the corresponding detection probability.

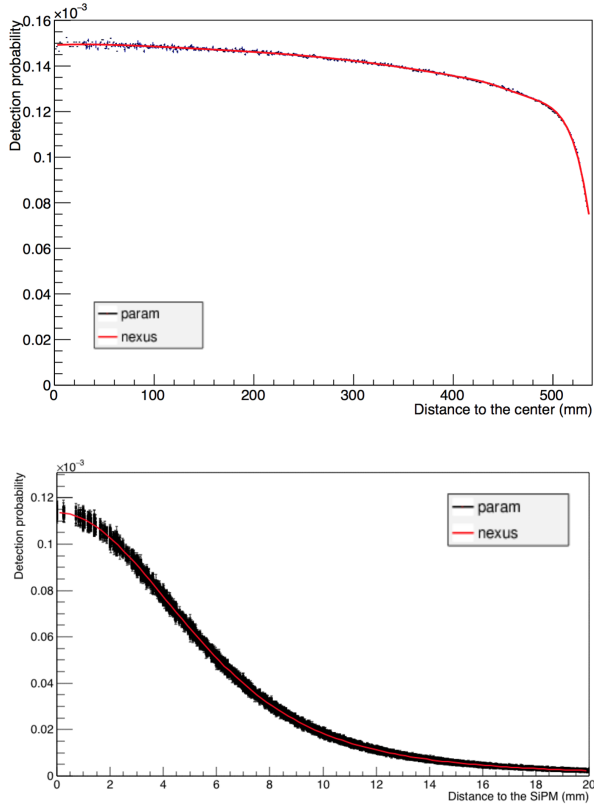


Figure 5.6: Comparison between the full and parameterized simulation modes of NEXT-100, in terms of detection probability of electroluminescence light in the energy plane as a function of the absolute distance to the center (top), and in the energy plane as a function of the absolute distance from the electron to the sensor (bottom).

- The sum of all the photon distributions from all the ionization electrons calculated before, provides the time distribution of detected electroluminescence photons per sensor.

This procedure has been validated for NEXT detectors, finding very good agreement between full and parameterized simulations, as depicted in figure 5.6.

5.4 NEXT-100 Simulation

The study of detectors with Monte Carlo type simulations implies a faithful modeling of the detector geometry with all the properties of the materials used, the use of models of all the physics processes taking place in the detector, to be able to generate all signals and backgrounds in the way they happen in real life, and finally store all the information needed to perform all the studies. As commented above, all NEXT detectors have been simulated using NEXUS, and in this section, simulation of NEXT-100 specific issues are presented.

Geometry

NEXT-100 geometry simulation includes the external shielding and all detector components that are relevant for background simulations. Since an approximate geometry is used for the shape, several checks have been made to verify that the mass of materials and placements of components are accurately reproduced. Special care has been put in optical properties of material involved in light transportation, as the detector uses photosensor readout.

The building up of the whole geometry is done in code modules that recreate each component, following the *matrioska* concept in which bigger systems contain smaller subsystems to compose the complete detector, as depicted in Figure 5.7.

A schematic view of NEXT-100 subsystems are presented in Figure 5.8.

Event Generators

Event generation in NEXUS is done in two steps. One has to specify, first, the position from where the initial particles must be generated, and, second, the kind of particles and their momenta. Vertex generators for every relevant part of the detector have been developed, and when any of these parts has been too complicated (i.e. the vessel), the vertex is computed in two steps, the first to decide in which subpart to shoot according to their relative masses and activities, and the latter to randomly generate the vertex inside the subpart. All the vertex generators developed for NEXT-100 geometry are listed in Table 5.1

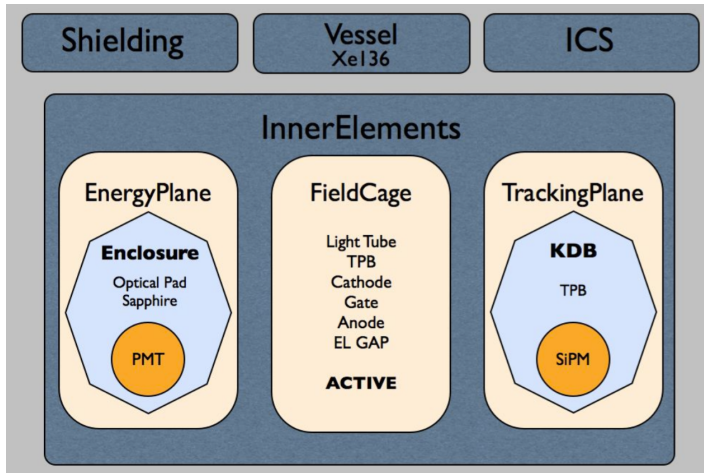


Figure 5.7: From [165]: hierarchical arrangement of NEXT-100 geometry in NEXUS.

together with all the detector components that make use of them, and the type of signals generated from them.

Different approaches to generate initial particles and their momentum have been used depending on the type of the signals. The most basic one is the *single-particle* generator, that can produce particles — selected by their Geant4 name or PDG identifier — with a configurable position and momentum. This generator was used for the generation of cosmogenic muons and neutrons. Neutrons have their origin in the laboratory walls, so a virtual surface (thin layer surrounding the lead castle) was defined to generate the vertex from it. Neutrons were isotropically shot and the energy was set following the measured neutron flux at LSC Hall A depicted in Figure 4.13. Cosmogenic muons were shot from a virtual surface (thin layer on the top of the shielding castle over-covering it) at fixed energies. The measured muon angular distribution depicted in Figure 4.12 was somehow simplified, and finally distributions shown in Figure 5.9 were followed. It was also considered the proportion of ($\mu^+/\mu^- = 1.3$) to select the charge of initial particles.

A variation of the single-particle generator is employed for the production of radioisotopes in the simulation of calibration sources or the

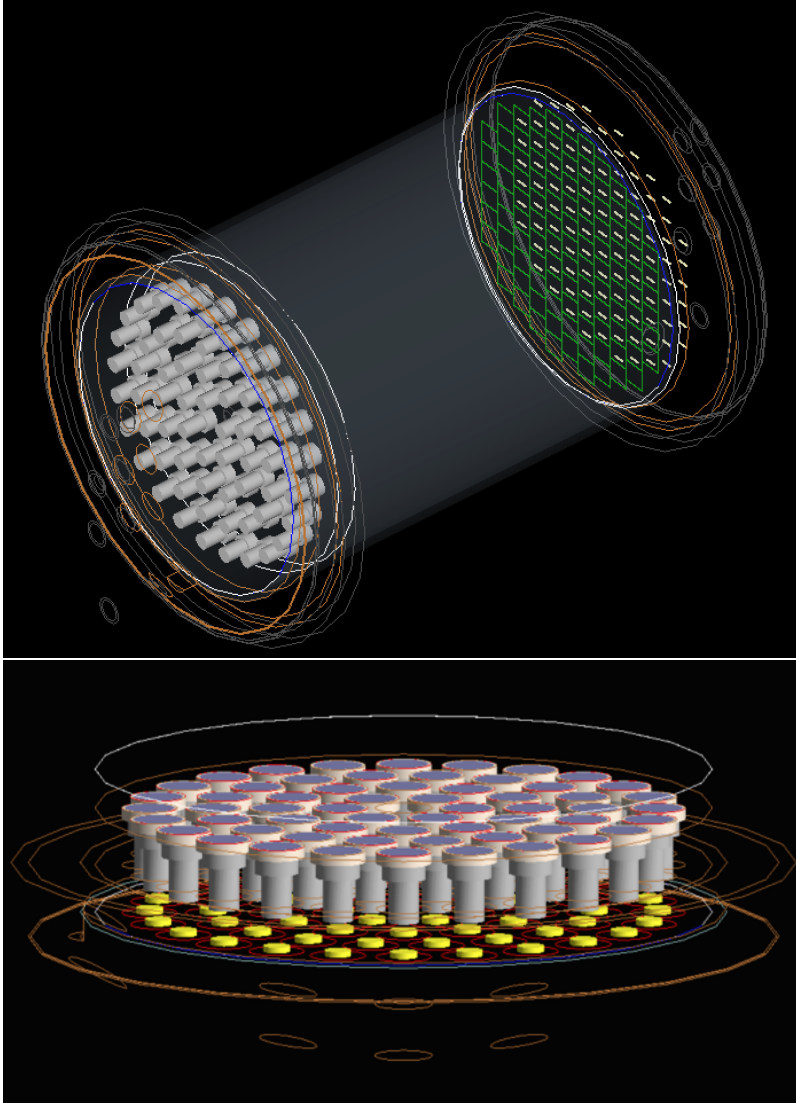


Figure 5.8: Schematic view of NEXT-100 geometry simulation. Top: On the left the energy plane with a schematic view of PMTs in grey. On the right the tracking plane with DiceBoards in green. The ICS is shown with orange borders, containing wholes in the tracking plane to allow cables to pass through. The vessel including its manifolds are shown with grey borders. The field cage barrel is shown in transparent grey. Bottom: Detailed view of the energy plane with PMTs (bodies in dark grey, windows in light grey and bases in yellow).

Table 5.1: List of vertex generators developed in NEXT-100 simulation, with the list of detector component that make use of them and the type of signals that make use of them.

Vertex Generator	Detector Components	Backgr. Types
ACTIVE-Gen	ACTIVE	$\beta\beta$ decays
FIELD CAGE-Gen	FIELD CAGE	^{208}Tl , ^{214}Bi
DICE-Gen	DICE BOARDS, SiPMs ANODE PLATE, GATE Mesh	^{208}Tl , ^{214}Bi
TRK-SUPPORT-Gen	TRACKING SUPPORT	^{208}Tl , ^{214}Bi
CARRIER-Gen	CARRIER PLATE	^{208}Tl , ^{214}Bi
ENC-WIN-Gen	ENCLOSURE WINDOW CATHODE Mesh	^{208}Tl , ^{214}Bi ^{214}Bi from ^{222}Rn
PMT-Gen	PMTs, PMT Bases	^{208}Tl , ^{214}Bi
ICS-Gen	INNER COPPER SHIELDING	^{208}Tl , ^{214}Bi
VESSEL-Gen	VESSEL, DICE-BOARD Plugs	^{208}Tl , ^{214}Bi
AIR-Gen	Air inside SHIELDING	^{222}Rn
SH-STRUCT-Gen	SHIELDING STRUCT	^{208}Tl , ^{214}Bi
SHIELDING-Gen	LEAD CASTLE	^{208}Tl , ^{214}Bi
NEUTRON-Gen	Virtual Surface surrounding the Castle	Neutrons
MUON-Gen	Virtual Surface top of the Castle	Muons

natural radioactivity (^{208}Tl , ^{214}Bi and ^{137}Xe) of detector components. Geant4 uses data retrieved from the ENSDF [190] to simulate the decay of radioactive nuclei by α , β^\pm and γ emission and by electron capture. The thorium and uranium series can be simulated down to the stable isotopes that end the decay chains. If the user is only interested in certain isotopes of the series, the simulation can be interrupted once the decay chain reaches a specified point, saving computation time on simulated events that would ultimately be discarded in the analysis. Present background studies stopped ^{208}Tl decay chain in ^{208}Pb and ^{214}Bi decay chain in ^{210}Pb .

The DECAY0 Monte Carlo event generator [191], a separate Fortran program written by V. I. Tretyak and collaborators, is used for the

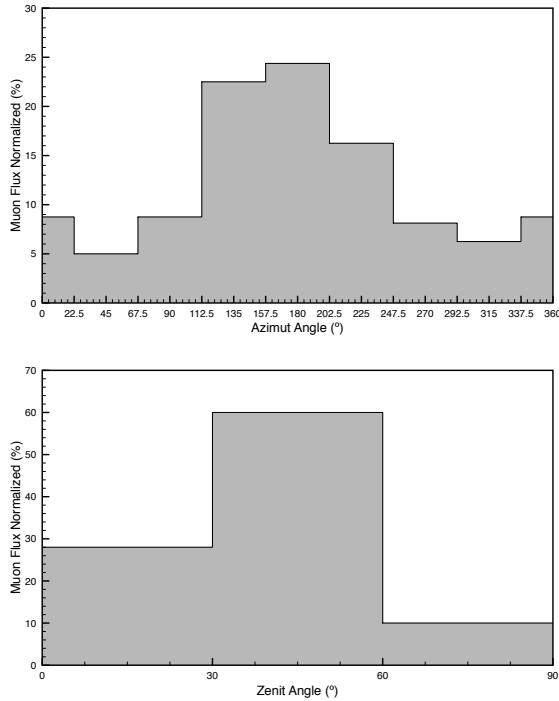


Figure 5.9: Muons angular distribution implemented in NEXUS (Azimut (top) and Zenit (down)).

production of $\beta\beta$ -decay events. DECAY0 can simulate 14 different $\beta\beta$ decay modes—including $2\nu\beta\beta$ decay and $0\nu\beta\beta$ decay mediated by the exchange of light Majorana neutrinos—for 21 candidate isotopes. The program outputs text files with the initial time, energy and angular distribution of the particles emitted in the decays, which is used by NEXUS to set the initial events.

Physics

By default, NEXUS loads the *low-energy* physics list provided by Geant4 [192] that makes use of the Penelope models [193] and the Lawrence Livermore National Laboratory data libraries [194] for an accurate description of the electromagnetic interactions of charged particles and γ -rays with matter from down to 10 eV up to approximately

100 GeV.

Some of the physics processes require a production threshold below which the energy loss is assumed continuous and no secondary particle is generated. Geant4 defines such a threshold as a range cut-off, which is internally converted to an energy for individual materials. In NEXUS, the range is set to 750 μm for γ particles, electrons and positrons, corresponding to an energy threshold of 2 keV for gammas, and 30 keV for electrons and positrons.

NEXUS simulation of neutrons and muons also needed the use of GEANT4 *EmExtraPhysics* to assign photo-nuclear reactions to γ s, electro-nuclear reactions to electrons and positrons, and muon-nuclear reactions to μ^+ and μ^- ; GEANT4 *IonPhysics* to be able to handle ions, and GEANT4 *StoppingPhysics* to activate muon and pion captures. Moreover, for a high precision simulation of neutrons behavior at low energies, the QGSP-BERT-HP physics list was also used.

In addition to previous models, NEXUS employs for the *full* and *parameterized* simulation modes, the Geant4 optical physics list, which contains models describing the production and propagation of optical photons. Moreover, as Geant4 does not include code for simulating the drift and amplification of ionization charges our own models have been developed for them.

Classical Analysis 6

The aim of this chapter is to present the final sensitivity of NEXT-100 to the effective Majorana neutrino mass ($m_{\beta\beta}$) based on signal efficiency and the sum of all the relevant background contributions. These contributions are computed by multiplying the background activity by some estimated rejection factor for every background type and origin. These factors are calculated based on a classical analysis deeply described in Section § 6.1. The first result is the validation of the fast simulation mode, presented in § 6.2 and carried out by comparing the intermediate and final results of the analysis when applied to fast and parameterized simulations. Following, the complete NEXT-100 background model is presented in § 6.3, ending with the expected total background rate. To finalize, signal efficiency and total background rate is translated to NEXT-100 sensitivity in terms of $T_{1/2}^{0\nu}$ and $m_{\beta\beta}$ in § 6.4.

6.1 Analysis Description

The classical analysis consists on a set of reconstruction algorithms, analysis algorithms, and filters, applied to simulations on an event-by-event basis. The number of MC events generated was chosen to keep the statistical uncertainty within 10% for all significant background contributors. The largest sets of MC simulated events were of 10^9 ^{208}Tl and 10^9 ^{214}Bi decay events from every component of the detector. The only way to afford the simulation of such quantity of events in a reasonable period of time was to run dedicated *fast-mode* simulations, which on the other hand implies the need to make a dedicated comparison between analysis run over fast and parameterized simulations (described in Section § 6.2) to validate the approximation.

The collection of algorithms implementing the *pseudo-reconstruction* and classical analysis are grouped in FANAL (from Fast Analysis) as a complete analysis package over NEXUS simulation files on an event-by-event basis. These algorithms are written in C++ and Python depending on their external dependences. A collaboration developed analysis framework called CENTELLA is used to handle the logistics of the analysis. The framework reads simulated events from NEXUS input files and pass them through all the algorithm chain in sequential mode. In each step, the events get extra information acquired along the analysis process, or they are discarded if they do not meet the requirements imposed. Finally, the framework accounts for global and partial number of read and written events in each algorithm, and it writes all the events that successfully passed all the cuts in some new output files.

As explained above the number of events to be simulated is huge and therefore, also the number of events to be analyzed. To speed up the analysis process, only those events whose total energy deposited in the active volume is higher than 2.3 MeV are stored at the simulation stage (handled by NEXUS), since events with lower energies would never be able to mimic a signal at $Q_{\beta\beta}$ (2458 keV).

After that, NEXT-100 MC events with $E_{\text{dep}} > 2.3$ MeV, are passed trough FANAL algorithms to compute their selection efficiencies or rejection factors that will be used to estimate the sensitivity of our detector. The whole set of algorithms will perform a *pseudo-reconstruction* that will turn simulated data into data closer to reality; followed by a fiducial cut, topology reconstruction and selection, and an energy ROI (Region Of Interest) cut, that finally will conclude if the event analyzed is compatible with our $0\nu\beta\beta$ signal. A detailed description of these steps is found in the following sections.

6.1.1 Energy and Position Smearing

Monte Carlo truth information is smeared by the detector spatial and energy resolutions to provide *pseudo-reconstructed* events as similar as possible to real detector data.

As the detector reads the energy as a global value, the same approach is followed in the energy smearing. The nominal energy resolution expected by NEXT-100 is 0.7% FWHM at $Q_{\beta\beta}$. This resolution is

translated to the corresponding sigma for the MC deposited energy of the event being evaluated at each moment. The reconstructed event energy is calculated gaussianly smearing the truth energy with the computed sigma. This smearing corresponds to an energy correction factor that once calculated, is applied to the energy of all the MC hits of the event. Right after the energy smearing application, a tighter energy cut between 2.4 and 2.5 MeV is applied to get rid of irrelevant events. Note that previous soft cut on energy of 2.3 MeV made in simulation time does not introduce any border effect in the new interval.

The position smearing is done by dividing the active volume of the detector into a regular 3D grid of small cuboids known as *voxels*. The smeared energy from every hit falling inside each one of the voxels is accumulated and associated to the center of it. Voxels dimension, which are configurable, are typically proportional to the spatial resolution of the detector, and for this classical analysis they have been set to have a dimension of (10 x 10 x5) mm, according to the transversal ($\sim 8.5 \text{ mm}/\sqrt{m}$) and longitudinal diffusion ($\sim 4 - 5 \text{ mm}/\sqrt{m}$) for high pressure xenon measured in NEXT-DEMO [131].

In addition to spatial discretization, voxels positions are shifted in z-coordinate to account with differences in the time they take place in the detector. In other words, not all the decay products of e.g. ^{214}Bi decays are generated at the same time, and therefore their energy depositions will be seen at different moments in the detector. The first deposition sets the time origin of the event, and delayed depositions are shifted in z, a distance equal to the time difference respect the origin multiplied by the drift velocity. These voxels, with discretized and shifted position and smeared energy, play the role of energy depositions as if they were measured by the real detector, and pass through the same analysis algorithms chain than them.

Based on these voxels, a fiducial filter is implemented to get rid of most of the backgrounds coming from outside the active volume. It filters every event with at least one voxel inside a veto region, defined as a 2 cm thick slice around the active volume, with an energy higher than a certain threshold. This energy threshold has been set to a conservative value of 10 keV according to the minimum energy able to be detected. This filter discards all charged particles getting into the veto region, the ones entering the detector and those which may have left the active volume depositing part of their energy in passive

materials; and represent a very good deal between background and signal rejection, as will be depicted in § 6.3. Moreover, the veto region defined by this filter accomplish a second objective, it discards the boundaries of the active region where the inhomogeneity of the electric field could affect the quality of the track reconstruction.

6.1.2 Topology

Once an event has been *pseudo-reconstructed* by smearing its energy and position, and it has deposited an energy close enough to $Q_{\beta\beta}$, confined in the fiducial region of the detector; it is time to study the topology of the event. The expected topology of a $\beta\beta$ decay is a single continuous energy deposition called *track*, as the two initial electrons of the decay share the same initial vertex and will be reconstructed together. Around both extremes, the track has high density deposited energy areas named as *blobs*, corresponding to the Bragg peaks of the initial electrons. Unlike $\beta\beta$ topology, backgrounds with origin in different particles will be reconstructed with more than one track, and those coming from a single particle will have a single track but with just one blob in the extreme corresponding to the end of the particle, featuring a topology clearly different from that of the signal (see Figure 4.2).

As a first requirement, a connectivity criterium between the collection of voxels generated in previous step must be defined to group them into tracks. This collection can be regarded as a *graph*, defined as a set of nodes and links that connect them. A graph of n nodes is characterized by its distance matrix, a square ($n \times n$) matrix that contains the geometric distance between the center of any pair of connected nodes (that is to say, if they share a face, an edge or a corner). Next, the "Breadth First Search" (BFS) algorithm [195] is used to group the voxels into tracks and to find their end-points and length. The BFS algorithm is a graph search algorithm which finds the minimum path between two connected nodes, starting from one node and exploring all its neighbours first, then the second level neighbours and so on, until it reaches the second node. The BFS algorithm divides the whole collection of voxels into connected sets or tracks, and finds the end-points of every track, defined as the pair of voxels with largest distance between them, where the distance of two voxels is the short-

est path that connects them. The distance between the end-points is the length of the track. Current BFS algorithm has been implemented as a set of C++ algorithms grouped into a library named PAOLINA, callable from any of the C++ CENTELLA algorithms, and discussed thoroughly in [133].

It is worth to note here that, apart from the BFS algorithm implemented in PAOLINA and used in this study, there are other approaches inside the collaboration to deal with topology reconstruction. One of the most recent ones is the "Maximum Likelihood Expectation Maximization" (ML-EM), which given a statistical model that describes the forward problem and any outcome, it provides the model parameters maximizing the likelihood and the most probable source of the outcome. A bi-dimensional version of the ML-EM method in which the photosensor signals integrated over time are used to reconstruct a transverse projection of the event, has been implemented as a standalone library called RESET [196, 197]; but the high computing time needed by this algorithm makes it unfeasible to be used in the study.

Once reconstructed tracks are created, those whose energy are below a threshold that would make them invisible to the detector are discarded. After this energy cut, we take advantage of the different number of tracks that signal and backgrounds present. Approximately 70 % of the signal events satisfy the single-track condition, whereas only 10% of ^{208}Tl and ^{214}Bi events do so. Taking into account that, according to Eq. (6.13), the maximization of the ratio ε/\sqrt{b} —where ε and b are, respectively, the acceptances of signal and background—optimizes the experimental sensitivity to $m_{\beta\beta}$. It would only be worth accepting events with more than one track if the fraction of background events passing the cut were such that

$$b' \leq (\varepsilon'/\varepsilon)^2 b, \quad (6.1)$$

where the unprimed and primed quantities are, respectively, the default acceptance (that is, track multiplicity equal to 1) and the alternative (i.e. higher track multiplicities) selection cuts. For the values shown in Figure 6.1 ($\varepsilon = 0.71$, $\varepsilon' = 0.89$, $b = 0.11$), we would only improve for $b' \leq 0.17$. However, the fraction of background events with one or two reconstructed tracks is almost 40%.

The second selection criterium based on topology exploits the characteristic energy-deposition pattern of $0\nu\beta\beta$ -decay tracks (see Fig. 4.2)

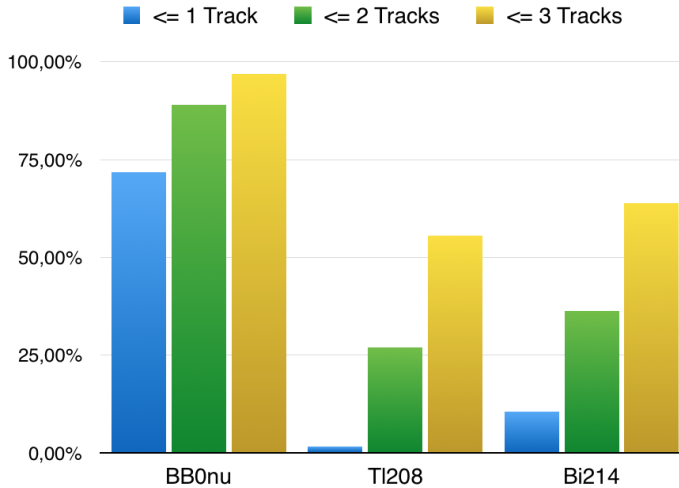


Figure 6.1: Cumulative fraction of events as a function of the track multiplicity (i.e. number of reconstructed tracks per event) for $0\nu\beta\beta$, and ^{208}Tl and ^{214}Bi from the field cage.

featuring blobs at both ends. The blob energy is defined as the total energy contained in all the voxels whose distance *along the track* (distance calculated walking through connected voxels, given by the BFS algorithm) to the extreme of the track is smaller than a given radius. The optimum radius value is the one that provides the best discrimination between the energy of a real blob, and the energy corresponding to the initial vertex of a particle. This study was conducted for $0\nu\beta\beta$, ^{208}Tl and ^{214}Bi based on a blind study where the blob candidate with the lowest energy was selected as the one corresponding to the start of the particle. The results are depicted in Figure 6.2 and they show that radii smaller than 15 mm present a wide range of blob energies for signal events, and that bigger radii are needed to get clear discrimination between signal and background blob energies. Finally an optimum radius size of 18 mm was set.

Figure 6.3 shows the distributions of signal and background events in terms of the energies of the end-of-track blobs. The populations of signal and background are clearly separated. Additionally, the

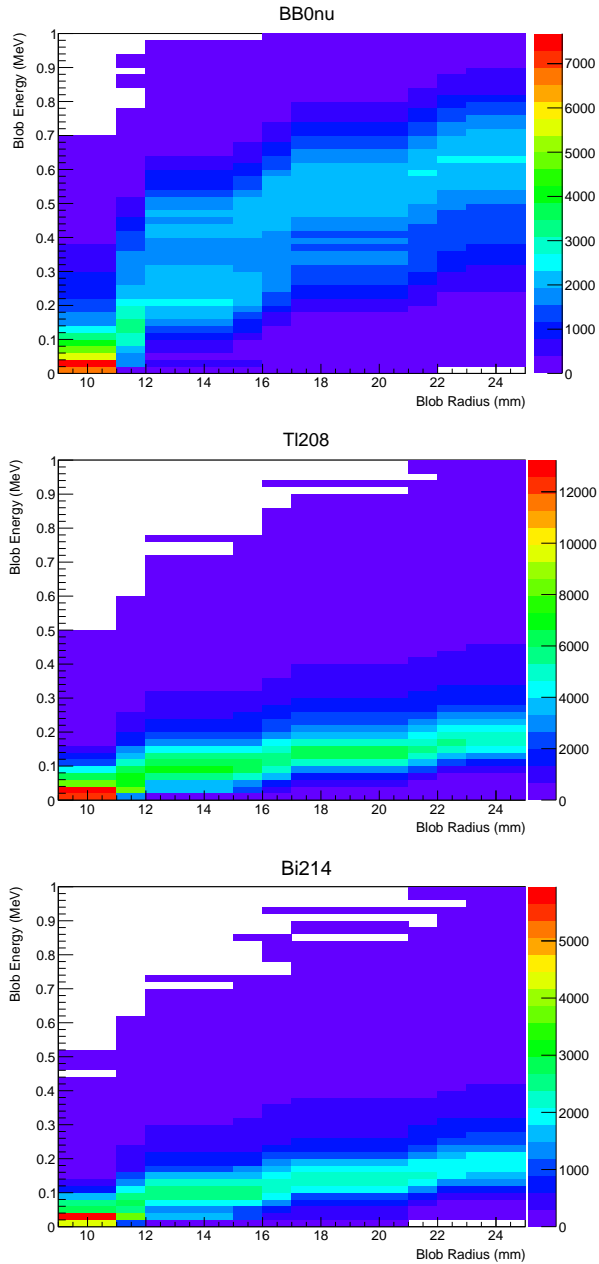


Figure 6.2: Lowest energy blob of $0\nu\beta\beta$ (top panel), ^{208}Tl (centre) and ^{214}Bi (bottom) events in terms of the radius [mm].

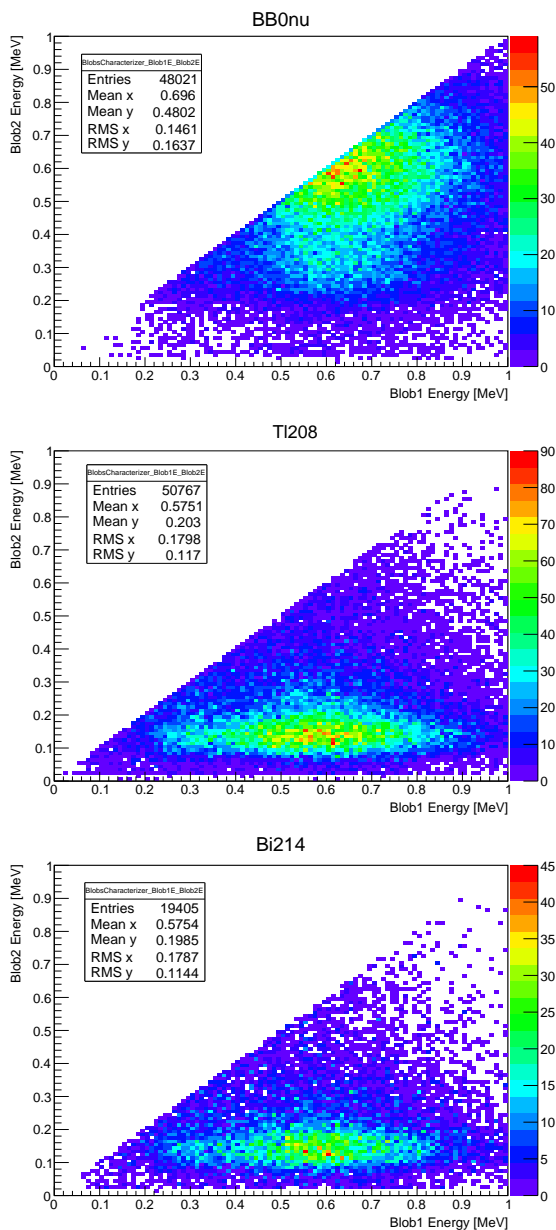


Figure 6.3: Distribution of $0\nu\beta\beta$ (top panel), ^{208}Tl (centre) and ^{214}Bi (bottom) events in terms of the energies of the end-of-track blob candidates. The blob labelled as '1' corresponds to the more energetic one, whereas 'blob 2' corresponds to the less energetic of the two.

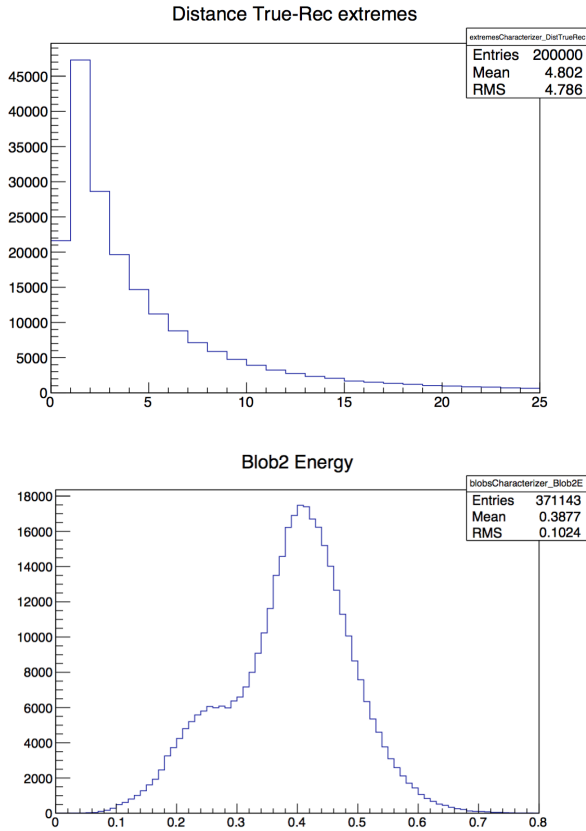


Figure 6.4: Top: Distance (mm) between real and reconstructed extremes for single-track signal events. Badly-reconstructed extremes imply lower energies around them, with a direct impact on the shape of the reconstructed energy (MeV) of Blob2 as illustrated on the bottom figure.

distributions of ^{208}Tl and ^{214}Bi are very similar, indicating that they correspond to the same type of events (single-electron tracks with energy around $Q_{\beta\beta}$). The signal distribution presents a dense populated area between 0.2 and 0.3 MeV for Blob2 energy corresponding to events with convoluted topology, whose tracks has been reconstructed with one of their extremes miss-placed, so assigning to the corresponding blob an energy well below the expected (see Figure 6.4). From the plots, a simple and reasonably clean selection cut could be established with a threshold around 0.35 MeV on the energy of the less energetic blob. However, according to the Neyman-Pearson lemma [198], the most efficient selection criterium is based on the likelihood ratio test statistic:

$$\mathcal{L} = \frac{P(E_1, E_2 | 0\nu\beta\beta)}{P(^{208}\text{Tl}) \cdot P(E_1, E_2 | ^{208}\text{Tl}) + P(^{214}\text{Bi}) \cdot P(E_1, E_2 | ^{214}\text{Bi})}, \quad (6.2)$$

where $P(E_1, E_2 | H)$ is the probability for an event with blob energies E_1 and E_2 to be signal ($H \equiv 0\nu\beta\beta$) or background ($H \equiv ^{208}\text{Tl}$ or $H \equiv ^{214}\text{Bi}$), and $P(^{208}\text{Tl})$ and $P(^{214}\text{Bi})$ are the *a priori* probabilities for a background event to be either ^{208}Tl or ^{214}Bi . In other words, $P(E_1, E_2 | H)$ is the probability given in Figure 6.3, and $P(^{208}\text{Tl})$ and $P(^{214}\text{Bi})$ are the relative initial abundances of each background source. Once the likelihood ratio (or the natural logarithm of the likelihood function, the so-called log-likelihood, which is, in general, more convenient to work with) is computed for all values of E_1 and E_2 (see Figure 6.5), the selection threshold value (\mathcal{L}) that maximizes the figure of merit ε/\sqrt{b} is chosen.

6.1.3 ROI

The last analysis step is to identify the optimal Region Of Interest (ROI) that maximizes the figure of merit ε/\sqrt{b} , and to apply the corresponding cut. The process is based on the PDF distributions of signal and backgrounds (Figure 6.6 - Top and Center), and goes through the entire range of possibilities (Figure 6.6 - Bottom). Although a wide range features very similar figure of merits, the final ROI selected was: 2448 – 2477 keV.

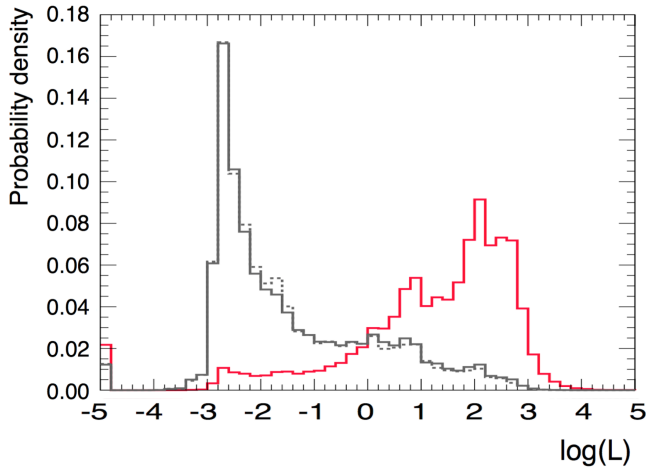


Figure 6.5: Likelihood-ratio distributions for signal (red, solid histogram) and background (^{208}Tl : grey, solid histogram; ^{214}Bi : grey, dotted histogram) for the Blobs energy cut.

6.1.4 Summary

As a summary of the classical analysis process, it can be concluded that $0\nu\beta\beta$ decays leave a clear trace in NEXT-100 described as a single track, with blobs at its both extremes, and of an anergy close enough to $^{136}\text{Xe } Q_{\beta\beta}$. While a high percentage of signal events will pass all the filters, backgrounds will not do it. The classical analysis ends with an acceptance factor per type of event and source after passing through all the algorithms chain explained above, that can be summarized as follows:

1. Pseudo-reconstruction of simulated data according to energy and spatial resolutions of the detector.
2. Soft energy cut to speed-up the analysis process.
3. Fiducial cut to get rid of backgrounds from external charged particles.
4. Topology cut 1: based on track multiplicity to avoid backgrounds generated from several particles at the same time.

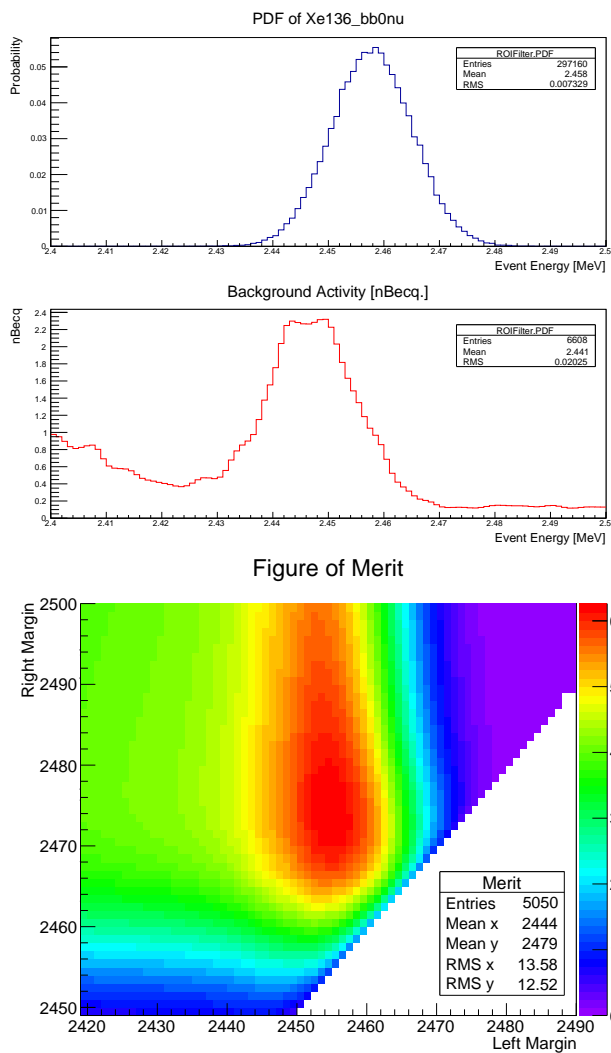


Figure 6.6: PDF distribution for signal (top) and the combination of ^{208}Tl and ^{214}Bi (center) proportional to their abundances. Bottom: Figure of merit for a wide range of energy limits used to set the optimum ROI.

5. Topology cut 2: based on blobs to avoid backgrounds from single electrons.
6. ROI cut

The acceptance values for all relevant backgrounds of NEXT-100 is found in Section § 6.3, and they will be the base, together with background activities, to the assessment of NEXT-100 background model.

6.2 Parameterized and Fast Modes comparison

As discussed in Chapter § 5, there are three different modes to simulate NEXT detectors. Present study relies on NEXT-100 *fast-mode* simulations, and although several validation tests have been done to be confident on the data got (see Section § 5.3), an extra test remains to be done. Current section is devoted to the comparison of the whole algorithm chain applied to simulations run in parameterized and fast modes.

Current comparison was run using the same set of calibration parameterized-mode data of NEXT-NEW at 15 bar. The fast-simulation based analysis made use of MC-hits only, and performed the *pseudo-reconstruction* described in section § 6.1.1, while the parameterized-mode simulation data was introduced into the algorithms chain right after the *pseudo-reconstruction*, so all the selection criteria could be compared one to one.

As a first step, the comparison allowed to appropriately tune certain thresholds used in the analysis to fit fast to parameterized data. Specifically, the *voxel energy threshold* was set to 1.5 keV, and the *track energy threshold* was set to 3.0 keV.

The first check was the energy resolution got when using the parameterized simulation data ('parameterized scenario') and the fast simulation data plus *pseudo-reconstruction* ('fast scenario') getting the same mean energy, and an energy resolution very similar, although a little bit better for the parameterized scenario (Fast: 0.49 % vs Param: 0.47 % FWHM at $Q_{\beta\beta}$, see Figure 6.7).

Finally, once the fast analysis was fine-tuned, $2\nu\beta\beta$, ^{208}Tl and ^{214}Bi data were passed through the total set of classical cuts. Main results of

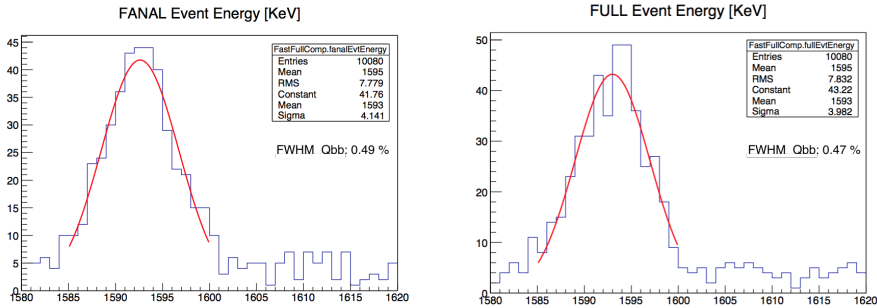


Figure 6.7: Energy resolution for krypton (^{83}Kr) MC data for the fast (left) and parameterized (right) simulation modes.

Table 6.1: Comparison of classical cuts efficiencies of fast and parameterized scenarios.

Classical Cut	Fast Scenario			Param. Scenario		
	$2\nu\beta\beta$	^{214}Bi	^{208}Tl	$2\nu\beta\beta$	^{214}Bi	^{208}Tl
Fiducial	68,7%	52,1%	57,8%	70,4%	53,8%	59,6%
Topol. (1 track)	27,9%	26,0%	9,4%	26,0%	20,5%	8,3%
Topol. (2 blobs)	85,7%	33,5%	33,3%	83,7%	39,0%	39,9%
ROI	85,6%	67,1%	67,1%	85,1%	68,6%	68,6%
Total	14,0%	3,0%	1,2%	13,0%	3,0%	1,4%

the comparison are found in Table 6.1. It is worth to note that global efficiencies for signal and backgrounds are very similar, although a deeper look reveals that the parameterized and fast scenarios behave slightly different in terms of topology. The parameterized scenario reconstructs tracks inaccurately disconnecting real single tracks, what makes the topology cut harder than its fast version, although newer version of the BFS algorithm are expected to improve on this. In the other hand the blobs cut has a clear better behavior in the fast scenario that somehow compensates previous discrepancy, giving very similar global results, what allows to rely on the results of present study.

6.3 NEXT-100 Background Model

To assess the NEXT-100 background model, all the relevant backgrounds enumerated in Chapter § 4 have been evaluated: backgrounds coming from natural decay chains of ^{232}Th and ^{238}U , background coming from radon contamination, which ultimately translates into an extra ^{214}Bi activity from the cathode, neutrons coming from laboratory walls and cosmogenic muons. All of them have been assessed by multiplying the measured activity of detector materials and components by the global rejection factor calculated with the classical analysis. The addition of all of them compose the overall background model expected for NEXT-100 detector.

6.3.1 Natural Decay Chains

The assessment of ^{232}Th and ^{238}U decay chains is done via the study of ^{208}Tl and ^{214}Bi as the only radionuclides of the corresponding chains with sufficiently energetic gammas to mimic the signal. The activity of all the detector materials and components is described on Section § 4.1, and the rejection factors to apply have been computed separately for both radionuclides, for all relevant detector systems.

A summary of the classical cuts efficiencies for signal and backgrounds are presented in Table 6.2 taking into consideration the contribution on the most relevant parts of the detector. The natural radioactive backgrounds, ^{208}Tl and ^{214}Bi , are suppressed by more than 6 orders of magnitude (global rejection factor), while the expected signal efficiency is 32%.

Final contributions of each detector subsystem to the overall background rate of NEXT-100 is shown in Table 6.3, and a graphical representation of them, grouped into big detector systems, is depicted in Figure 6.8. The photosensors and their associated electronics are the dominant source of background in NEXT-100, being the total expected background from ^{232}Th and ^{238}U of 4.09×10^{-4} cts $\text{keV}^{-1} \text{kg}^{-1} \text{yr}^{-1}$. Notice, however, that our knowledge is, in any case, quite uncertain, given that for most background sources only upper activity limits have been measured ($\sim 30\%$ of total background) and therefore the final background contribution could be sensibly lower.

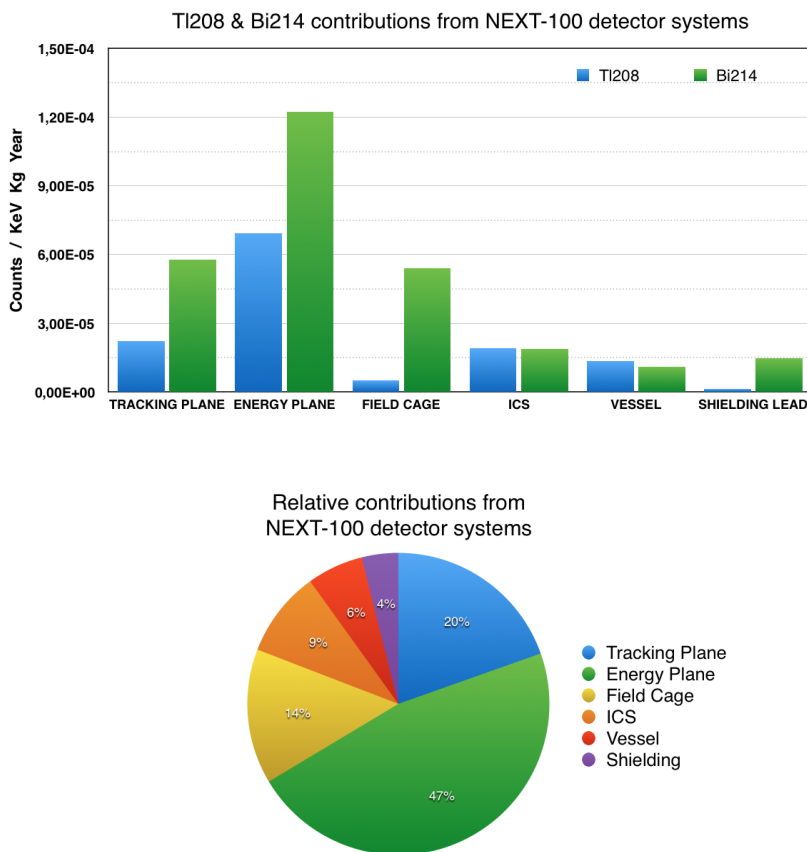


Figure 6.8: ^{208}Tl and ^{214}Bi contributions of NEXT-100 detector systems (top), and their relative weight (bottom). Total Value: 4.09×10^{-4} cts $\text{keV}^{-1} \text{kg}^{-1} \text{yr}^{-1}$.

Table 6.2: Efficiencies of classical selection criteria for $0\nu\beta\beta$ -decay events, and ^{208}Tl and ^{214}Bi average values from the dominant sources of background.

Selection criteria	$0\nu\beta\beta$ (%)	^{208}Tl	^{214}Bi
Fiducial	0.68	7.72×10^{-3}	9.78×10^{-5}
$E \in [2.4, 2.5]$ MeV	0.98	1.27×10^{-1}	7.24×10^{-1}
Topology (1 Track)	0.72	2.37×10^{-2}	1.11×10^{-1}
Topology (2 Blobs)	0.74	1.14×10^{-1}	1.01×10^{-1}
Energy ROI	0.91	1.44×10^{-1}	4.45×10^{-1}
<i>Total</i>	0.32	3.80×10^{-7}	3.52×10^{-7}

6.3.2 Radon

As explained in Section § 4.2, radon can contribute to NEXT backgrounds through different mechanisms, although it is expected that only ^{214}Bi activity from cathode, from the decay of ^{222}Rn in the active region, have a relevant role in global background rate. The expected increase of ^{214}Bi activity in cathode has been extrapolated to NEXT-100 from NEXT-NEW measured values under two different scenarios depending on the main origin source of ^{222}Rn , ranging from 2.97 ± 0.29 in case of radon coming from the gas system, to 18.34 ± 1.76 mBq in case of coming from the degassing of detector materials.

The applicable rejection factor is calculated in the same way than any ^{214}Bi contamination, and a dedicated simulation from the cathode and the corresponding analysis process was run to evaluate it. The efficiencies of single classical cuts are enumerated in table 6.4, and as a summary, a total computed factor is 2.02×10^{-7} , leading to a total activity from $7.18 (\pm 0.69) \times 10^{-6}$ to $4.44 (\pm 0.43) \times 10^{-5}$ cts $\text{keV}^{-1} \text{kg}^{-1} \text{yr}^{-1}$ for the two different scenarios. Even in the pessimistic scenario, the radon-induced background is expected to be one order of magnitude smaller than the one induced by ^{208}Tl and ^{214}Bi decays from detector components evaluated in previous section. Therefore, we can conclude that radon-induced backgrounds are not expected to be a problem for NEXT-100 physics program, and that the installation of an active

Table 6.3: Final contribution of NEXT-100 detector subsystems to overall background model, coming from the natural contamination of ^{232}Th and ^{238}U in the different materials and components. Note some activities coming from upper limits measurements.

VOLUME	^{208}Tl		^{214}Bi		Total	
	mBq	%	mBq	%	mBq	%
Dice Boards (DB)	6.29×10^{-7}	5.77	3.79×10^{-6}	16.24	4.42×10^{-6}	12.91
DB Plugs	1.23×10^{-6}	11.27	1.06×10^{-6}	4.53	2.29×10^{-6}	6.68
TRACKING PLANE	1.86×10^{-6}	17.03	4.85×10^{-6}	20.77	6.71×10^{-6}	19.59
PMTs	2.90×10^{-6}	26.56	3.07×10^{-6}	13.14	5.96×10^{-6}	17.41
PMT Bases	2.41×10^{-6}	22.09	5.12×10^{-6}	21.96	7.53×10^{-6}	22.00
Encls. Windows	$< 4.95 \times 10^{-7}$	4.54	$< 2.04 \times 10^{-6}$	8.74	$< 2.53 \times 10^{-6}$	7.40
ENERGY PLANE	5.80×10^{-6}	53.18	1.02×10^{-5}	43.84	1.60×10^{-5}	46.81
Field Cage	$< 3.00 \times 10^{-7}$	2.75	$< 3.86 \times 10^{-6}$	16.53	$< 4.16 \times 10^{-6}$	12.14
Anode Quartz	1.16×10^{-7}	1.07	6.74×10^{-7}	2.89	7.90×10^{-7}	2.31
FIELD CAGE	$< 4.16 \times 10^{-7}$	3.82	$< 4.53 \times 10^{-6}$	19.42	$< 4.95 \times 10^{-6}$	14.45
Inner Cu Shield	$< 1.35 \times 10^{-6}$	12.38	1.31×10^{-6}	5.61	$< 2.66 \times 10^{-6}$	7.76
Tracking Support	$< 1.06 \times 10^{-7}$	0.97	1.50×10^{-7}	0.64	$< 2.55 \times 10^{-7}$	0.75
Carrier Plate	$< 1.35 \times 10^{-7}$	1.24	1.09×10^{-7}	0.47	$< 2.44 \times 10^{-7}$	0.71
COPPER SHIELD	$< 1.59 \times 10^{-6}$	14.59	1.57×10^{-6}	6.72	$< 3.16 \times 10^{-6}$	8.22
VESSEL	$< 1.13 \times 10^{-6}$	10.37	$< 9.31 \times 10^{-7}$	3.99	$< 2.06 \times 10^{-6}$	6.02
SHIELDING CASTLE	1.10×10^{-7}	1.01	1.23×10^{-6}	5.26	1.34×10^{-6}	3.91
TOTAL [mBq]	$< 1.09 \times 10^{-5}$		$< 2.33 \times 10^{-5}$		$< 3.42 \times 10^{-5}$	
TOTAL [cts $\text{keV}^{-1} \text{kg}^{-1} \text{yr}^{-1}$]	$< 1.30 \times 10^{-4}$		$< 2.79 \times 10^{-4}$		$< 4.09 \times 10^{-4}$	

Table 6.4: Classical cuts efficiencies for ^{214}Bi decays from the cathode, with origin on active volume ^{222}Rn . Partial values in %, and total acceptance.

Classical Cut	Efficiency (%)
$E \in [2.4 - 2.5] \text{ MeV}$	0.14
Fiducial	2.84
Topology (1 Track)	11.42
Topology (2 blobs)	10.07
Energy ROI	44.49
Total	2.02×10^{-7}

filtration system to mitigate internal radon (a radon trap) does not appear necessary.

6.3.3 Muons and Neutrons

The final contributions of muons and neutrons to the NEXT background rate consists of events taking place at different times. The earliest ones are associated to fast electromagnetic interactions and happen in the first 5 milliseconds, while the delayed ones are associated to the decay of radionuclides activated by neutron captures (see Figure 6.9). Both contributions must be carefully evaluated, and if any of them could represent a significant background, be vetoed.

Backgrounds coming from electromagnetic interactions, either coming from muons or neutrons, have been evaluated through the same procedure than others, passing the simulated data through all the *pseudo-reconstruction* and analysis algorithms. In the other hand, potential radionuclides in detector materials whose decays were able to mimic the $\beta\beta$ signal must be identified first. Simulations revealed that only ^{137}Xe , which β decays to ^{137}Cs with a Q-value of 4173 keV and a half-life of ~ 3.8 minutes, represents a noticeable background for NEXT-100. ^{137}Xe contribution is evaluated in two steps, first the probability of activation is computed for both muons and neutrons, and latter the probability of its decay to mimic a $0\nu\beta\beta$ signal.

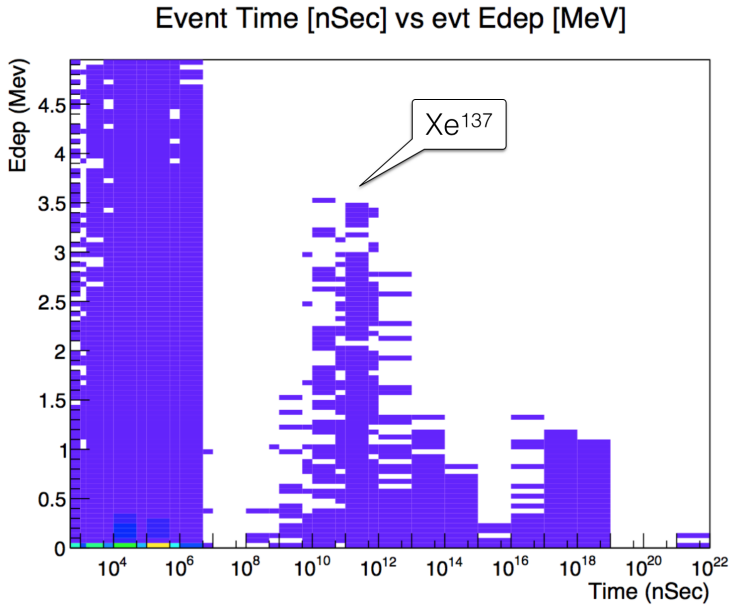


Figure 6.9: Energy deposition of neutron backgrounds along the time. Depositions with problematic energy (> 2.4 MeV) are grouped in two moments: first 5 milliseconds populated with the so-called electromagnetic interactions, and depositions around 10^{11} nano-seconds corresponding to ^{137}Xe beta decays.

Muons

To assess muons contribution, they have been simulated from a virtual surface on top of the lead castle over-covering it to avoid dead-angles, following a simplified version of the angular distribution measured in LSC Hall A (see Figure 5.9), and with the right charge ratio of $\mu^+ / \mu^- = 1.3$. Although the expected average muon energy ranges from 221 to 245 GeV, the angular distribution suggests differences of more than double in the amount of rock traversed by muons before reaching the lab with direct impact in the real energy of muons, so we decided to simulate two fixed energies: 200 and 500 GeV trying to cover the whole range of possibilities. These huge energies made the simulations really hard to manage in terms of computing time and files size. The measured flux of $3 \times 10^{-6} \text{ cm}^{-2} \text{ s}^{-1}$ [176] has been considered for

Table 6.5: Summary of muon contributions to NEXT-100 background rate via electromagnetic interactions and ^{137}Xe activations.

Muon Energy (GeV)	200	500
EM. Accep. Factor	4.33×10^{-7}	7.90×10^{-7}
EM. Contribution (cts $\text{keV}^{-1} \text{kg}^{-1} \text{yr}^{-1}$)	7.08×10^{-5}	1.29×10^{-4}
^{137}Xe activation prob.	4.69×10^{-4}	1.00×10^{-3}
^{137}Xe Accep. Factor	7.74×10^{-8}	1.65×10^{-7}
^{137}Xe Contribution (cts $\text{keV}^{-1} \text{kg}^{-1} \text{yr}^{-1}$)	1.27×10^{-5}	2.70×10^{-5}

present study. A summary of the results is shown in Table 6.5.

Assuming a real muon energy close to 200 GeV, the analysis reveals that the electromagnetic contribution: 7.08×10^{-5} cts $\text{keV}^{-1} \text{kg}^{-1} \text{yr}^{-1}$ would represent an increase of $\sim 15\%$ over the total expected background from ^{208}Tl and ^{214}Bi , and it could be even worse in case of more energetic muons. As muons can not be vetoed anyway, a tagging system must be implemented to get rid of their electromagnetic contribution mainly coming from neutron captures and muon *bremsstrahlung*. These systems are very common in underground experiments (e.g. EXO [179]), and basically consist on scintillator panels surrounding the whole detector able to tag muons very efficiently. By applying a reasonable dead time after each muon detection, in which any signal registered in the detector is discarded, the totality of the electromagnetic background is discarded. Unfortunately the long half-life of ^{137}Xe (~ 3.8 min) makes unfeasible to avoid these backgrounds with this same method.

Summing up, assuming the implementation of a muon tagging system of $\sim 100\%$ efficiency, and a 5 ms dead time per muon, a percentage lower than 0.007% of detector dead time would hence allow to get rid of muon contributions via electromagnetic interactions, but not of the contribution via ^{137}Xe activations. This way, the total 200 GeV muon contribution would be of **1.27×10^{-5}** cts $\text{keV}^{-1} \text{kg}^{-1} \text{yr}^{-1}$, representing just a $\sim 3\%$ background increase respect to ^{208}Tl and

^{214}Bi contributions, that could be considered as negligible.

Neutrons

A dedicated simulation of neutrons was run to assess their contribution to NEXT-100 background rate. They were isotropically generated from a virtual thin layer surrounding NEXT-100 detector (outside the lead castle), following the measured energy spectrum [182] depicted in Figure 4.13, the activity considered on present study comes from the measured flux in LSC Hall A: $\phi_{HallA} = 1.38 \pm 0.14 \times 10^{-5} \text{ cm}^{-2} \text{ s}^{-1}$ [182]. A summary of relevant results is shown in Table 6.6. Muons with energies below 100 keV do not appear in the table as the probability of reaching the active volume is so low that their contributions are negligible.

Simulations have revealed an unacceptable high rate of background coming from neutrons, either by electromagnetic interactions or ^{137}Xe activations. To address it, a new layer of shielding capable of attenuating the neutron flux is needed in NEXT. Neutrons from natural radioactivity have relatively low energies and can be effectively suppressed by a neutron shield. Typically, shields made of plastic or water doped with a substance having a high thermal neutron capture cross section are used. Ideally, such a neutron shield should be as close to the detector as possible to be effective for tertiary neutrons.

NEXT proposes a layer of 20 cm boron doped (5%) polyethylene slabs (commercially available) placed around the lead castle. This setup allows to shield neutron flux from lab rocks by at least 3 orders of magnitude [199] as depicted in Figure 6.10, and the inner lead shield would shield the secondary gamma flux generated in plastic. This veto reduces neutrons background from both, the electromagnetic interactions and the ^{137}Xe activations making therefore, its final contribution to NEXT-100 background rate negligible.

Finally, we would like to point a physical process that will allow to measure the real neutron rate in the active volume. Hydrogen present in the field-cage (made of HPDE), captures very efficiently incoming neutrons, leading to a deuteron and a de-excitation gamma of 2224.566 keV. Very often, this gamma enters the active volume and decays via pair-production. The e^+e^- pair features a clear single track with two blobs at their extremes of 1202 keV (see Figure 6.11) that it

Table 6.6: Summary of neutron contributions to NEXT-100 background rate via electromagnetic interactions and ^{137}Xe activations.

Neutron Energy (MeV)	0.10 - 0.16	0.16 - 0.25	0.25 - 0.40	0.40 - 0.63	0.63 - 1.00	1.00 - 1.58	1.58 - 2.51
EM. Accep. Factor	8.52×10^{-9}	2.54×10^{-8}	4.68×10^{-8}	5.34×10^{-8}	5.50×10^{-8}	5.24×10^{-8}	4.19×10^{-8}
EM. Contribution (cts $\text{keV}^{-1} \text{kg}^{-1} \text{yr}^{-1}$)	1.03×10^{-5}	8.83×10^{-5}	7.64×10^{-5}	8.53×10^{-5}	1.14×10^{-4}	1.40×10^{-4}	7.22×10^{-5}
^{137}Xe activation prob.	7.80×10^{-6}	3.06×10^{-5}	4.92×10^{-5}	6.23×10^{-5}	6.53×10^{-5}	6.57×10^{-5}	6.89×10^{-5}
^{137}Xe Accep. Factor	1.29×10^{-9}	5.05×10^{-9}	8.12×10^{-9}	1.03×10^{-8}	1.08×10^{-8}	1.08×10^{-8}	1.14×10^{-8}
^{137}Xe Contribution (cts $\text{keV}^{-1} \text{kg}^{-1} \text{yr}^{-1}$)	1.55×10^{-6}	1.76×10^{-5}	1.33×10^{-5}	1.64×10^{-5}	2.23×10^{-5}	2.90×10^{-5}	1.96×10^{-5}
Neutron Energy (MeV)	2.51 - 3.98	3.98 - 6.31	6.31 - 10.0	10.0 - 20.0	20.0 - 50.0	50.0 - 100.0	Total
EM. Accep. Factor	5.28×10^{-8}	5.54×10^{-8}	5.89×10^{-8}	1.15×10^{-7}	2.27×10^{-7}	4.45×10^{-7}	
EM. Contribution (cts $\text{keV}^{-1} \text{kg}^{-1} \text{yr}^{-1}$)	5.43×10^{-5}	4.01×10^{-5}	2.75×10^{-5}	5.59×10^{-5}	1.94×10^{-4}	9.14×10^{-5}	1.05×10^{-3}
^{137}Xe activation prob.	7.32×10^{-5}	6.75×10^{-5}	8.47×10^{-5}	1.47×10^{-4}	3.09×10^{-4}	6.28×10^{-4}	
^{137}Xe Accep. Factor	1.21×10^{-8}	1.11×10^{-8}	1.40×10^{-8}	2.42×10^{-8}	5.09×10^{-8}	1.04×10^{-7}	
^{137}Xe Contribution (cts $\text{keV}^{-1} \text{kg}^{-1} \text{yr}^{-1}$)	1.24×10^{-5}	8.07×10^{-6}	6.52×10^{-6}	1.17×10^{-5}	4.33×10^{-5}	2.13×10^{-5}	2.23×10^{-4}

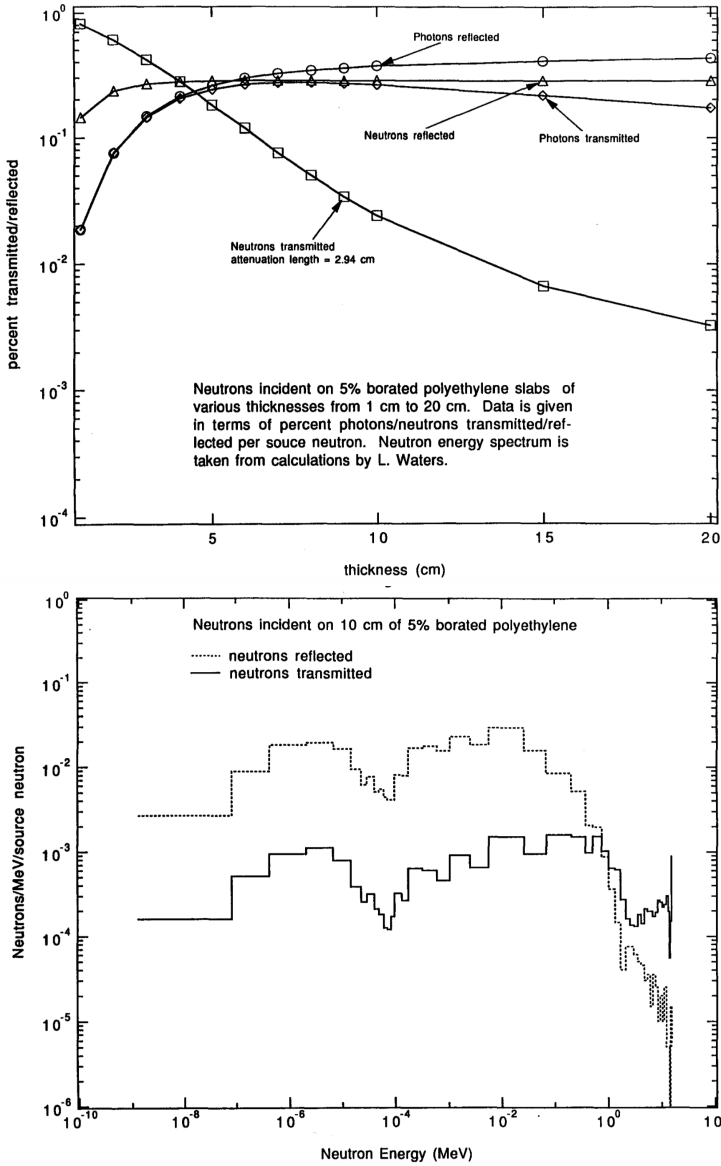


Figure 6.10: Top: Percent of neutrons transmitted and reflected from boron doped (5%) polyethylene slabs as a function of thickness, calculated with respect to the number of incident neutrons, and integrated over all energies. Bottom: Energy spectra for both transmitted and reflected neutrons for a boron doped (5%) polyethylene slab 10 cm thick [199].

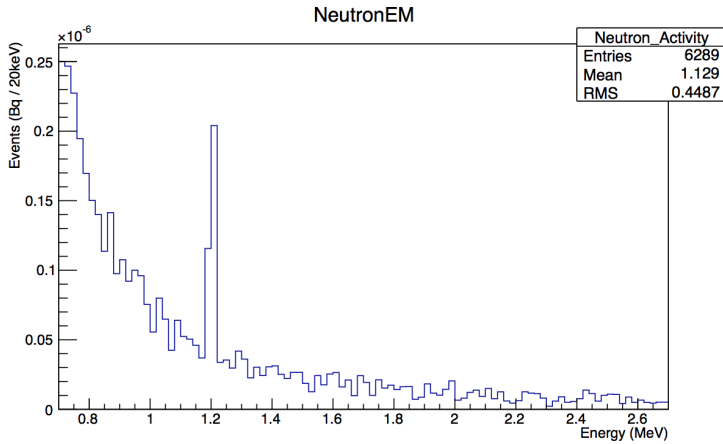


Figure 6.11: Clear signal of 1202 keV from the pair-production of the gamma generated in the de-excitation of deuteron, created by neutron captures by hydrogen molecules present in the field cage.

is expected to be clearly identified in current NEXT-NEW experiment and therefore, also in NEXT-100.

^{137}Xe

As commented above, neutrons and muons can contribute to NEXT-100 background rate via fast electromagnetic interactions, and via ^{137}Xe activations. The assessment of the latter has been done in two different steps. The first step evaluated the activation probability by either muons and neutrons, re-using the simulations done for the electromagnetic interactions. Simulations also revealed an homogeneous distribution of activations within the active volume. The second step consisted on the simulation of ^{137}Xe decays homogeneously distributed in the active volume to evaluate their probability to feature a $\beta\beta$ -like signal, by passing simulated data through all the classical cuts. Partial efficiencies for every cut are enumerated in Table 6.7, while the total contribution of muons and neutrons to NEXT-100 background rate from ^{137}Xe activations are found in Table 6.5 and Table 6.6 respectively. The energy distribution of ^{137}Xe decays is basically flat for energies of our interest, as depicted in Figure 6.12.

Table 6.7: Classical cuts efficiencies for ^{137}Xe decays in the active volume. Partial values in %, and total acceptance.

Classical Cut	Cut %
$E \in [2.4 - 2.5]$ MeV	2.7
Fiducial	82.9
Topology (1 Track)	54.8
Topology (2 blobs)	6.4
Energy ROI	21.3
Total	1.65×10^{-4}

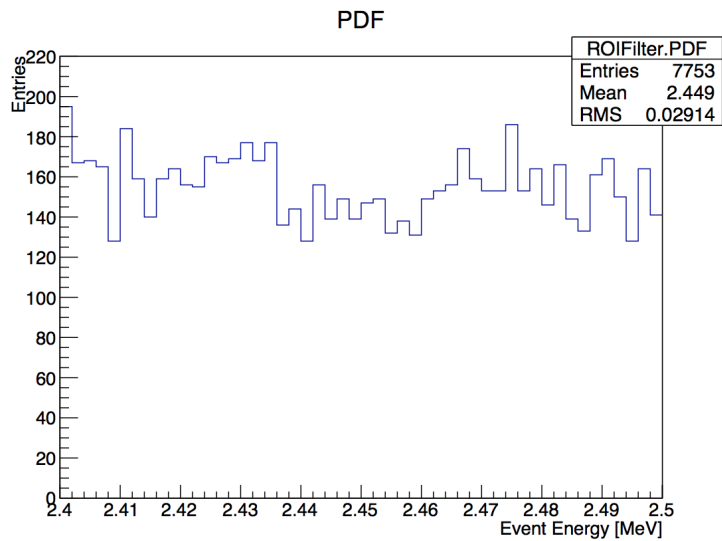


Figure 6.12: ^{137}Xe decay energy distribution.

6.3.4 Summary

In this section, we have evaluated all the contributions to NEXT-100 background model relevant for the search of $0\nu\beta\beta$ decays, together with the assessment of different mitigation possibilities. Below a brief description of all of them can be found. The total expected background of NEXT-100 standard is: $< 4.22 \times 10^{-4} \text{ cts keV}^{-1} \text{ kg}^{-1} \text{ yr}^{-1}$.

- *Natural decay chains* of ^{232}Th and ^{238}U present in detector material and components are the most relevant contribution to NEXT-100 background rate. Radionuclides ^{208}Tl and ^{214}Bi from both decay chains respectively contribute with a total activity of $4.09 \times 10^{-4} \text{ cts keV}^{-1} \text{ kg}^{-1} \text{ yr}^{-1}$, mainly coming from the photosensors. It is important to notice here that 30% of this activity has been assessed considering upper activity limits and not real measurements, so the final contribution could be significantly lower.
- ^{222}Rn *progeny* can contribute through several mechanisms to NEXT-100 background, but only its presence in the active volume represents a significative contribution. This radon activity has a direct translation to a ^{214}Bi activity from cathode contributing from 7.18×10^{-6} to $4.44 \times 10^{-5} \text{ cts keV}^{-1} \text{ kg}^{-1} \text{ yr}^{-1}$ depending on its main origin, the gas system components or the degassing of detector materials. Although it is expected to be a minor contribution, in case of becoming more relevant than expected for NEXT-100, the installation of a radon trap in the gas system would reduce its contribution in severals order of magnitude, making it **negligible**.
- *Cosmogenic muons* can contribute via fast electromagnetic interactions and ^{137}Xe activations. Their expected energy in LSC is around 220 GeV what makes unfeasible a possible veto. A tagging system able to detect their pass trough the detector allows the suppression of the electromagnetic contribution in exchange of a detector dead time lower than 0.007%. This way, the total muon contribution comes from ^{137}Xe and represents $1.27 \times 10^{-5} \text{ cts keV}^{-1} \text{ kg}^{-1} \text{ yr}^{-1}$.

- *Neutrons from lab walls*, as muons, can contribute via fast electromagnetic interactions and ^{137}Xe activations. Both contributions would represent an unacceptable high background rate of 1.27×10^{-3} cts $\text{keV}^{-1} \text{kg}^{-1} \text{yr}^{-1}$, what forces NEXT to implement a new level of shielding. Boron doped (5%) polyethylene slabs 20 cm thick, allow to reduce neutron total contribution by three orders of magnitude turning it **negligible**.

6.4 NEXT-100 Sensitivity

In this section we finalize the NEXT-100 classical analysis by giving the numbers of its sensitivity in terms of ^{136}Xe $0\nu\beta\beta$ half-lives and Majorana neutrino mass, $m_{\beta\beta}$, for different scenarios; making use of the background rate evaluated in section § 6.3. First, an introduction to the method followed to assess these sensitivities [200] is briefly described.

6.4.1 Sensitivity Procedure

As explained in Section § 2.2, the lifetime for the $0\nu\beta\beta$ process, if mediated by light Majorana neutrino exchange, is given by (2.4). Although with high uncertainty mainly coming from the $M^{0\nu}$ estimate, the effective neutrino Majorana mass, $m_{\beta\beta}$, can be inferred from a non-zero $0\nu\beta\beta$ -rate measurement and, conversely, a null observation can be interpreted in terms of an upper bound on $m_{\beta\beta}$.

First of all, let us figure out the number of $0\nu\beta\beta$ decays expected in a detector. The radioactive decay law gives the evolution of the number of atoms susceptible of decay with time:

$$N(t) = N_0 \cdot 2^{-t/T_{1/2}^{0\nu}} \quad (6.3)$$

where N_0 is the initial number of atoms, and $T_{1/2}^{0\nu}$ is the half-life of the process. If we assume now that $t \ll T_{1/2}^{0\nu}$ ($\Rightarrow 2^{-t/T_{1/2}^{0\nu}} \approx (1 - \log 2 \cdot \frac{t}{T_{1/2}^{0\nu}})$), and express N_0 in terms of the isotope mass, the number of expected $0\nu\beta\beta$ -decays can be expressed as:

$$0\nu\beta\beta \text{ decays} = \log 2 \frac{\varepsilon \cdot M \cdot N_A}{W} \frac{t}{T_{1/2}^{0\nu}} \quad (6.4)$$

where M is the mass of the $\beta\beta$ -emitting isotope, W is its molar mass, N_A is the Avogadro constant and ε is the detection efficiency. However, due to the stochastic nature of radioactivity, the experiment may actually yield a different result. Taking in consideration the few number of decays expected, the probability follows a Poisson distribution

$$\text{Prob}(n; \mu) = \frac{\mu^n}{n!} e^{-\mu} \quad (6.5)$$

where μ is the expected number of $0\nu\beta\beta$ -decays given by (6.4), and n is the observed number of events.

A standard way to report this type of results, proposed by Jerzy Neyman in 1937 [201], is to give a *confidence interval*, calculated from the observations (n), within which there is a given probability that the parameter μ falls:

$$P(\mu_{low}(n) \leq \mu \leq \mu_{up}(n)) = \gamma, \quad (6.6)$$

where γ , usually expressed as a percentage, is the *confidence level* (CL) of the interval, and μ_{low} and μ_{up} , known as the *confidence limits*, are commonly selected to yield equal tail probabilities, resulting in the so-called *central confidence interval*. In the case of no signal detection, the confidence interval only provides the upper limit that, given a desired CL and setting ($n = 0$) in (6.5) we get:

$$\mu_{up} = -\log(1 - CL). \quad (6.7)$$

Therefore, an ideal experiment that observes no events after a given exposure, rather than saying that nothing was found, would report an upper limit (at a given confidence level) on the expected number of events (i.e. $N = \mu_{up} = 2.3$ at 90% CL).

In the more realistic case of an experiment with background (b), the expected number of total events must be rewritten in the form:

$$\text{Po}(n; \mu + b) = \frac{(\mu + b)^n}{n!} e^{-(\mu + b)}, \quad (6.8)$$

where μ is the unknown mean signal expectation, b is the known mean background expectation, and n is the total number of detected events (signal + background). If we try to follow the classical Neyman

construction of confidence limits in this case, negative limits of μ_{low} and even for μ_{up} are obtained when the number of detected events is small compared to the expected number of background events. To face this problem, the *de facto* standard frequentist approach to compute confidence intervals proposed by Feldman-Cousins [202] has been used. This new method uses an ordering principle based on likelihood ratios that prevents of unphysical results for upper confidence limits for null results, and two-sided confidence limits for non-null results.

Given an experiment searching for new phenomena in the absence of true signal, the detection of n events of background would lead to an upper confidence limit. The *sensitivity* of such an experiment, is defined as the average upper confidence limit one would get from a large ensemble of experiments with the same expected background and no signal. Accordingly, the sensitivity of a double beta decay experiment to $m_{\beta\beta}$ can be expressed combining Equations (2.4) and (6.4) as

$$\mathcal{S}(m_{\beta\beta}) = \mathcal{A} \sqrt{\frac{\bar{N}}{\varepsilon Mt}}, \quad (6.9)$$

where

$$\mathcal{A} \equiv \left(\frac{W}{\log 2 N_A} \frac{m_e^2}{G^{0\nu} |M^{0\nu}|^2} \right)^{1/2} \quad (6.10)$$

is a constant that depends only on the considered $\beta\beta$ isotope and \bar{N} is the average upper limit on the expected number of events in the absence of signal.

In the ideal case of a background-free experiment, the experiment with no true signal would always detect $n=0$ events with no fluctuations, and hence, the average upper limit would be given by (6.7) and consequently the sensitivity is only a function of the exposure in the form $(Mt)^{-1/2}$. In the more-realistic case with an expected background level (b), the average upper limit is:

$$\bar{N}(b) = \sum_{n=0}^{\infty} \text{Po}(n;b) \mathcal{U}(n;b), \quad (6.11)$$

where $\mathcal{U}(n;b)$ is a function that returns the Feldman-Cousins upper limit for a given observation n and a known background level b .

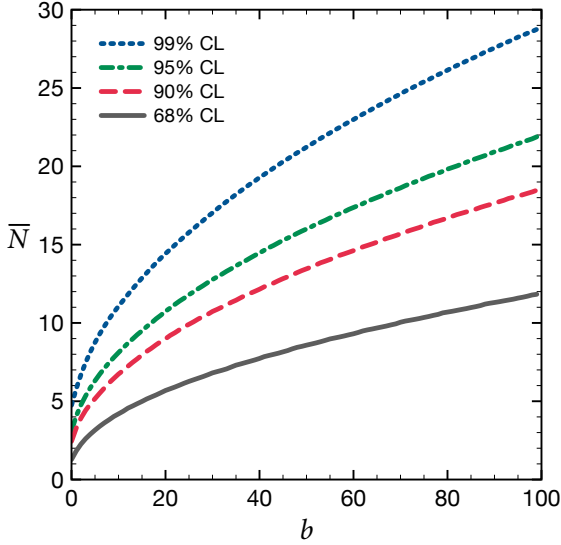


Figure 6.13: Average upper limit on the expected number of events observed by a large ensemble of experiments with the expected background and no true signal as a function of the expected background for the case of a measurement of a Poisson variable.

Figure 6.13 shows the value of \bar{N} as a function of b for 4 different confidence levels. In the case of large background, these curves are approximately given by

$$\bar{N}(b) \simeq k \sqrt{b}. \quad (6.12)$$

If we express the number of backgrounds (b) in terms of the typical background rate (B) managed by $\beta\beta$ -decay experiments expressed in (cts keV $^{-1}$ kg $^{-1}$ yr $^{-1}$), and substitute it in (6.9) we finally get the sensitivity expression used in present study:

$$\mathcal{S}(m_{\beta\beta}) = \mathcal{A} \sqrt{k} \sqrt{1/\varepsilon} \left(\frac{B \Delta E}{M t} \right)^{1/4} \quad (6.13)$$

It is worth to note here, that the presence of background in $\beta\beta$ decay experiments reduces dramatically the sensitivity, improving only as $(Mt)^{-1/4}$ instead of the $(Mt)^{-1/2}$ expected in the background-free case.

6.4.2 Sensitivity Results

The sensitivity of NEXT-100 to neutrinoless double beta decays has been calculated with the procedure described in previous section, based on Feldman-Cousins confidence intervals at 90% CL, applied to the background rate obtained with the classical analysis (Section § 6.3.4). Sensitivity numbers are given for both, $^{136}\text{Xe } 0\nu\beta\beta T_{1/2}^{0\nu}$, and $m_{\beta\beta}$, related between them by equation (2.4). Figure 6.14 illustrate the sensitivity of NEXT-100 *Standard* version. It is worth to note here that after 3 \sim 5 years of data taking (270 \sim 450 kg \cdot yr of exposure), the margin of improvement slows down significantly, close to the $(Mt)^{-1/4}$ ratio expected in the presence of large background. Reached sensitivity values at 90% CL after 5 (10) years of data taking are: 9.85×10^{25} (1.56×10^{26}) years, corresponding to an upper limit on the Majorana neutrino mass of 57-161 (**45-127**) meV, depending on the NME method used.

The main conclusion at this point is that NEXT-100 standard version would reach a sensitivity in terms of $T_{1/2}^{0\nu}$ in the order of 10^{26} years after 5 years of data taking, which is similar to the best published limit to date provided by KamLAND-Zen collaboration [1]. On the contrary, even with the most optimistic NME value of the literature, more than 7 years of data taking would be needed to reach the upper limit of the $m_{\beta\beta}$ band allowed by the inverted hierarchy. In this sense, next chapter § 7 is devoted to evaluate different techniques directly applicable to NEXT-100 detector to improve the sensitivity, leading to the so-called *High Definition* version of NEXT detector.

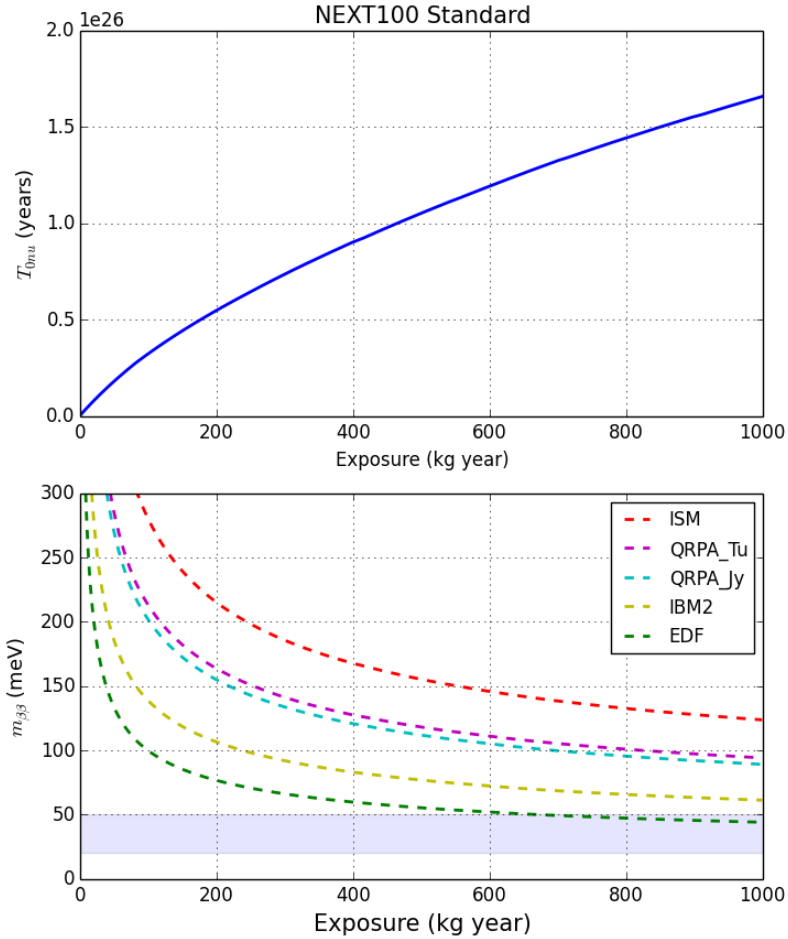


Figure 6.14: Sensitivity (at 90% CL) of NEXT-100 *Standard* version to $0\nu\beta\beta$ -decay. Top figures correspond to $T_{1/2}^{0\nu}$ sensitivity, and bottom to $m_{\beta\beta}$ sensitivity for all the available ^{136}Xe NME estimates listed in Table 3.1: ISM (red), QRPA-Tu (magenta), QRPA-Jy (cyan), IBM2 (yellow) and EDF (green). Light blue horizontal band corresponds to the range of neutrino Majorana masses, $m_{\beta\beta}$, for the inverted hierarchy.

NEXT High Definition

Chapter § 6 has revealed that *NEXT-100 Standard* version, although presents a competitive sensitivity with respect to similar experiments, will not be able to cover the inverted hierarchy range of $m_{\beta\beta}$ masses. Present chapter is devoted to explore and assess different strategies directly applicable to our detector, based on the know-how acquired by the collaboration in recent years, leading to a detector with improved sensitivity called *NEXT-100 High Definition*.

These techniques are focused on improving the physical response of the detector such as the spatial and energetic resolutions, and on the improvement of the topological signature analysis using novel techniques. The following sections will describe each one of these techniques, and at the end of the chapter the new sensitivity results of *NEXT-100 High Definition* will be given.

7.1 High Spatial Resolution

One of the most important handles of gaseous xenon TPCs to get rid of backgrounds is the possibility to exploit the different topological signatures presented by signal and backgrounds (see Figure 4.2). Event discrimination based on topology is directly related with the quality of the image of the event registered by detector photosensors. The diffusion suffered by electrons along the drift length until reaching the anode blurs the image, limiting the definition of the image and hiding the finest details of event tracks especially for large drift distances, and therefore, reducing the discrimination effectiveness.

The large electron diffusion ($\sim 10 \text{ mm}/\sqrt{m}$ transverse and $\sim 4 - 5 \text{ mm}/\sqrt{m}$ longitudinal at the values of pressure and reduced electric field that will be used in NEXT100) is determined by the inef-

ficient electron energy loss in elastic collisions with the xenon atoms, in particular in the range of reduced electric fields of few tens of V/cm/bar used in the drift region. Simulations performed inside the collaboration [203] have shown how the addition of minimum concentrations of CO₂, CH₄ and CF₄ sensibly reduces the transverse and longitudinal diffusions as depicted in figure 7.1, and have been confirmed by recent measurements of xenon-CO₂ mixtures [204]. Concentrations below the percent level of CO₂ and CF₄ may be enough for reducing the diffusion and reach a transverse and longitudinal diffusions around 2 mm/ \sqrt{m} (for a drift field of 30V/cm/bar and at 10 bar pressure), down to the order of the error introduced by the instrumentation. This low diffusion allows to see the finest details of event topology what in practice means an improvement on the ability to discriminate signal out of background events.

The counterpart of gas mixing is the reduction of xenon EL yield that could lead to a degradation of the energy resolution. Chosen gases are highly transparent to xenon scintillation light, what in practice means that the sub-percent levels of additives required for the diffusion improvement are compatible with the high energy resolutions requested in the experiment. For instance, CO₂ concentrations $\sim 0.05\%$ providing an overall electron diffusion around 2.5 mm/ \sqrt{m} allows a tolerable EL yield. These last numbers together with the easy handling (non-flammable) and low cost, make CO₂ the a-priori most interesting option. It is worth to notice here more recent approaches in gas mixing pointing that the addition of Helium at 10-15% could represent a significative decrease in electron diffusion while maintaining the EL yield unaffected [205].

Figures 7.2 and 7.3 illustrate the effect of the different diffusion (or definition) scenarios, standard and HD, for two different events of ¹³⁶Xe $0\nu\beta\beta$, and ²⁰⁸Tl respectively. From the images it is obvious that although in many cases, like the signal event depicted in figure 7.2, the standard diffusion is enough to extract the relevant information from the event topology, the High Definition allows a better identification of tracks, their extremes, and a more precise account of blob energies (see figure 7.3).

The improvement in topology discrimination has been carefully assessed. As a first step, simulated data was *pseudo-reconstructed* using voxels of (2,2,2) mm according to the diffusion values expected for the

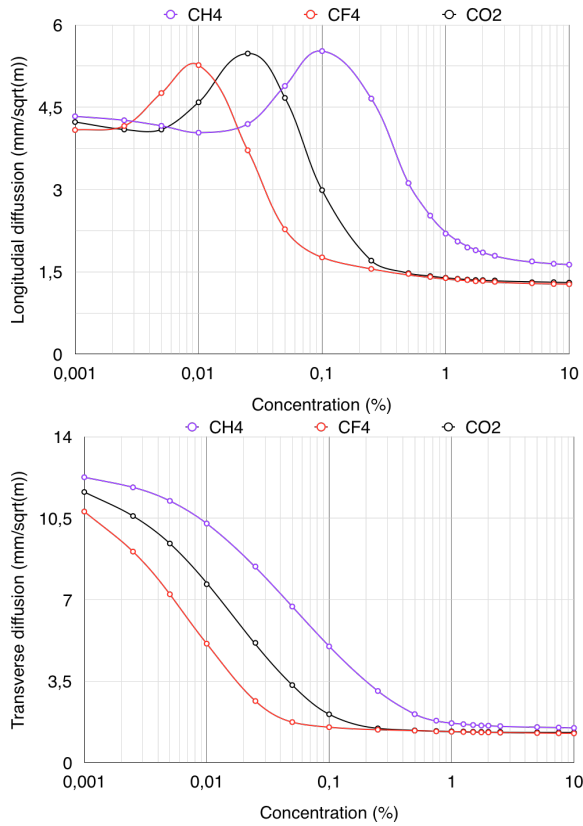


Figure 7.1: From [203], longitudinal (top) and transverse (bottom) diffusion of electrons in gas for different concentrations of CO_2 , CH_4 and CF_4 for a drift field of $30\text{V}/\text{cm}/\text{bar}$ and at 10 bar pressure.

high definition version; and the selection algorithms of the analysis related with topology were fine tuned to the new scenario. A summary of the new rejection factors are listed in Table 7.1. The improvement (around factor 3 in background rejection) mainly comes from the track multiplicity because now, algorithms are able to see the extra tracks, much more abundant in background events, more efficiently; and from a better selection of blobs at the end of tracks.

These improvements on rejection factors associated to the topological signature have a direct impact on the total background budget expected in the detector that will be presented in Section § 7.4 together

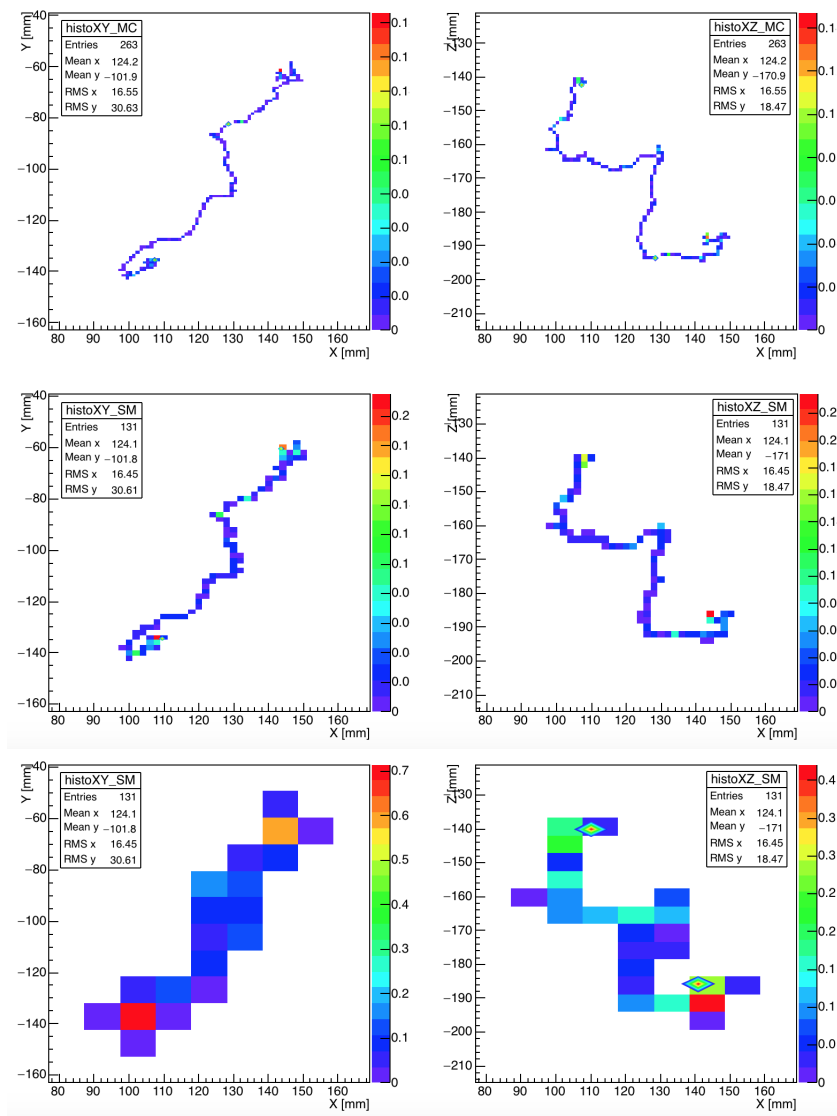


Figure 7.2: Effect of diffusion in a ^{136}Xe $0\nu\beta\beta$ event. Top: True event, Center: High Definition and Bottom: Standard Definition. Left images correspond to XY and right to XZ projections.

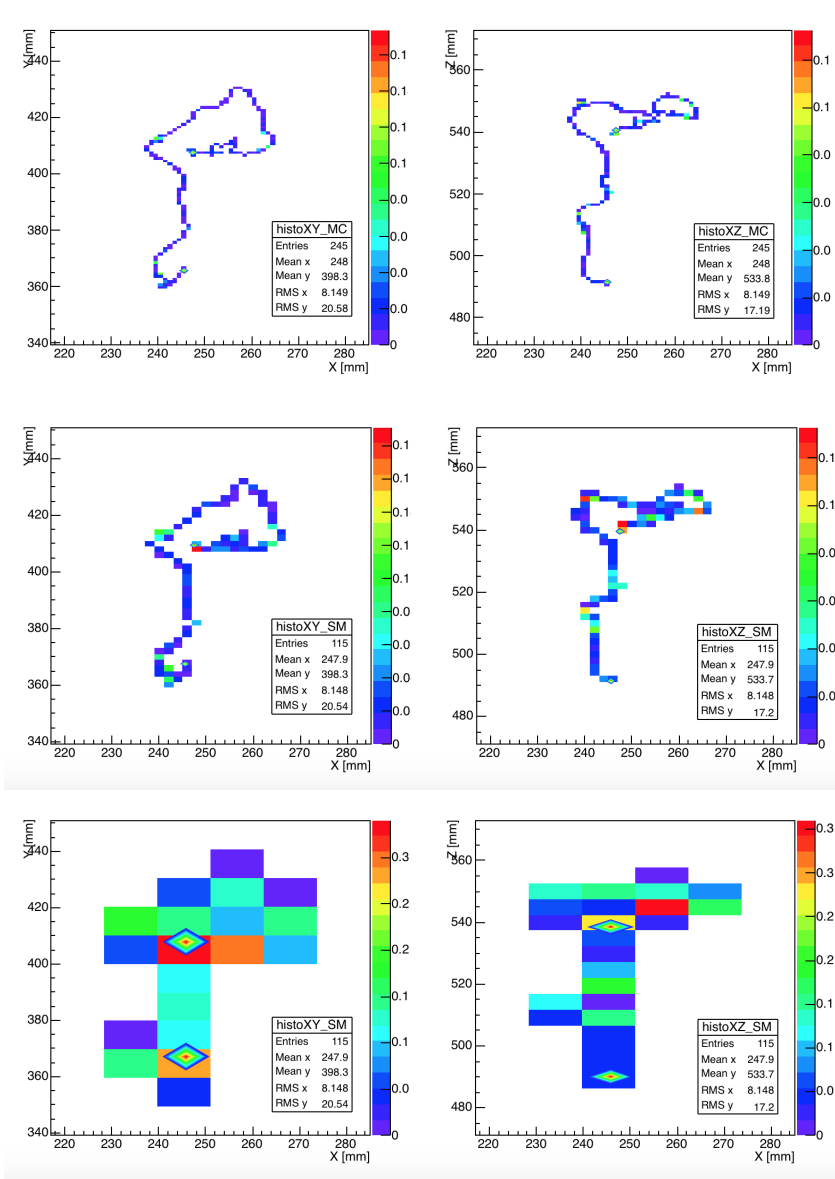


Figure 7.3: Effect of diffusion in a ^{208}Tl event. Top: True event, Center: High Spatial Definition and Bottom: Standard Spatial Definition. Left images correspond to XY and right to XZ projections.

Table 7.1: Efficiencies of selection criteria for NEXT-100 High Spatial Resolution for $0\nu\beta\beta$ -decay events, ^{208}Tl and ^{214}Bi average values from the dominant sources of background, and ^{137}Xe in Active volume.

Selection criteria	$0\nu\beta\beta$	^{208}Tl	^{214}Bi	^{137}Xe
Fiducial	0.68	7.72×10^{-3}	9.78×10^{-5}	8.35×10^{-1}
$E \in [2.4, 2.5]$ MeV	0.98	1.27×10^{-1}	7.24×10^{-1}	2.69×10^{-2}
Topology (1 Track)	0.56	1.04×10^{-2}	4.84×10^{-2}	3.86×10^{-1}
Topology (2 Blobs)	0.84	8.84×10^{-2}	7.83×10^{-2}	5.18×10^{-2}
Energy ROI	0.91	1.36×10^{-1}	4.49×10^{-1}	2.05×10^{-1}
<i>Total</i>	0.28	1.42×10^{-7}	1.39×10^{-7}	9.19×10^{-5}

with the impact of the extra handles that compose the *high definition* version of NEXT-100.

7.2 Deep Neural Networks

Previous analysis follow the classic approach of data analysis based on sequential algorithms to be applied in order to take advantage of known different physical characteristics of signal and background such as geometrical distribution, topological signature or deposited energy. In this section a novel approach based on the use of “Deep Neural Networks” (DNNs) is presented and assessed.

The use of artificial neural networks to solve complex problems has been explored since the 1940s, but only in recent years, with the dramatic increase in computing power, the use of computationally intense neural networks with many inner layers has become feasible. These neural nets that are many layers deep, are capable of handling large amounts of data exhibiting a vast array of features such as image [206] and speech [207] recognition. It has also found recent applications in physics, including event classification in high-energy and neutrino physics experiments [208–210].

7.2.1 *Deep Learning*

Neural networks consist of layers of neurons which compute an output value based on one or several input values. The output is a function of the weighted sum of the inputs x_i plus a bias variable b , i.e. $f(\sum_i w_i x_i + b)$, where f is called the activation function and w_i are the weights of the neuron, one for each input. The idea is that with several layers of many neurons connected together, the values of the final (“output”) layer of neurons will correspond to the solution of some problem given the values input to the initial layer (called the “input” layer). The weights and biases of all neurons in the network together determine the final output value, and so the network must be trained (the weights and biases must be adjusted) so that the network solves the correct problem. This is done by using a training dataset, and for each training event, presenting input data to the network, examining its resulting output, and adjusting the weights and biases of the network in a manner that minimizes the discrepancy between the output of the final layer a and the expected output y . This adjustment procedure is done by computing a cost function which depends on the actual and expected outputs and quantifies the discrepancy between them, computing the gradients of the cost function with respect to the weights and biases in all neurons, and changing the weights and biases in a manner that minimizes the cost function. After many training iterations, the weights and biases in the network will ideally have converged to values that not only yield the expected output when the network is presented with an event from the training dataset, but also yield the expected output when presented with similar events not used in training. The technical details behind the mathematical implementation of such a scheme are discussed at length in [211].

Recently, multi-layer convolutional neural networks (CNNs) have been identified as a powerful technique for image recognition problems. These neural networks consist of convolutional layers of n columns of m neurons - layers of neurons that share a common set of $m \times n$ weights and a bias. The set of weights + biases is called a filter or kernel, and this filter is combined in a multiplicative sum (a convolution) with an $m \times n$ subset of input neurons to give an output value. The filter is moved along the image, each time covering a different $m \times n$ subset of input neurons, and the set of output values corre-

sponding to a single filter is called a feature map. With this strategy, further convolutional layers can be used to analyze the higher-level features encoded in the feature maps output from previous layers. Often to reduce the amount of computation and neurons present in deeper layers, max-pooling operations are performed, in which the neuron with maximum output value in an $m \times n$ window (or “pool”) is selected, and all others in the pool are discarded. Such an operation performed on a layer of neurons leads to a new layer of reduced size. A deep CNN may be constructed from a series of several such convolutional operations and max-pooling operations, along with more conventional fully-connected layers, in which all neurons output from the previous layer are connected to the input of each neuron in the fully-connected layer (see figure 7.4 for a general schematic).

7.2.2 DNNs and NEXT-100

The first incursion of NEXT collaboration into DNNs has the main goal to identify if DNNs can learn to classify events as signal or background better than conventional analysis methods.

In this initial study, GoogLeNet [206], a sophisticated 22-layers-deep convolutional neural network designed for image recognition was used. Although it is designed to handle full-color 2D images, it was chosen as its implementation was readily available in the Caffe [213] deep learning framework along with an easy interface to input several DNN models. Each event was input to the net as an image consisting of three color (RGB) channels, one for each of three projections of the 3D voxelized track, $(R, G, B) \rightarrow (xy, yz, xz)$, being the intensity of each pixel directly proportional to the deposited energy.

As a first comparison, it was decided to compare the background acceptance obtained when fixing the same signal acceptance yielded by classical analysis. The network was trained with more than 400K events (50% signal and 50% background) that had been subject to the same voxelization procedure and single-track cut used on the classical analysis, therefore only assessing the discrimination based on blobs. The standard ($10 \times 10 \times 5$ mm) and the high ($2 \times 2 \times 2$ mm) definition scenarios were studied, and results are listed in Table 7.2. They clearly show an improvement on background rejection, which is much better

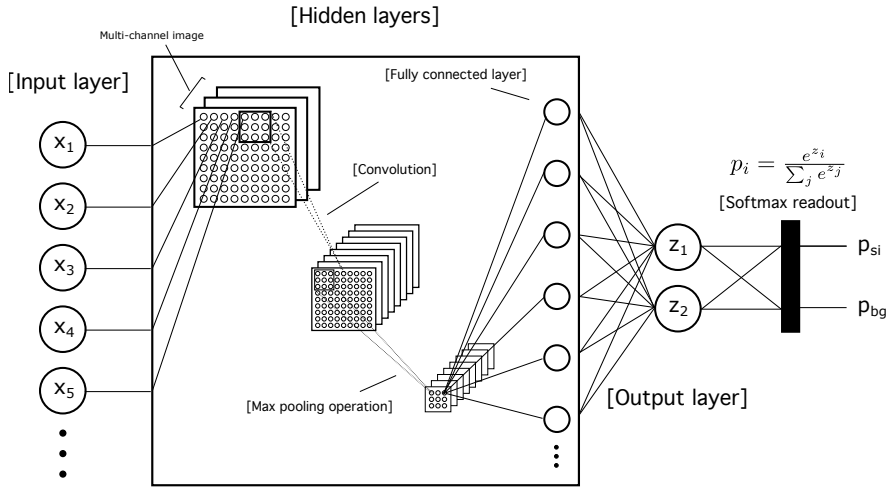


Figure 7.4: From [212], schematic of a deep convolutional neural network for 2-category classification. The input layer consists of the pixel intensities of an image. The hidden layers consist of several different operations performed on the input neurons - this example shows a 3×3 convolution followed by a 3×3 max-pooling operation, with the resulting neurons input to a fully-connected layer which feeds the two neurons in the output layer. The activation function of the two neurons in the final layer is such that the two outputs are exponentiated and normalized. The values in such a layer, called a “softmax” readout layer, can then be interpreted as probabilities of classification as signal or background.

for the high definition scenario as it preserves the finest details of topological signatures.

As a second step, the whole range of signal efficiencies was studied. The output layer of the DNN gives a probability that a given event is signal and a probability that it is background, and these probabilities add to 1. By varying the probability threshold for determining whether an event is classified as signal or background the whole range of signal efficiencies and the corresponding background acceptances can be analyzed. From the expression of the sensitivity for $0\nu\beta\beta$ -decay experiments (6.13), we define a figure of merit $F = s/\sqrt{b}$, where s and b are the fractions of signal and background events accepted, so that

Table 7.2: From [212], comparison of conventional and DNN-based analyses. The comparison shows, for a given percentage of signal events correctly classified, the number of background (^{214}Bi from the field-cage) events accepted (mistakenly classified as signal).

Analysis	Definition	Signal (%)	Bkgnd. (%)
Classic	Std. ($10 \times 10 \times 5$)	76.6	11.0
DNN	Std. ($10 \times 10 \times 5$)	76.6	9.4
Classic	High ($2 \times 2 \times 2$)	86.2	7.6
DNN	High ($2 \times 2 \times 2$)	86.2	4.7

the higher F the greater the sensitivity. The plot of signal efficiency vs. background rejection together with the corresponding figure of merit is depicted on figure 7.5. The optimal figures of merit are found to be 66.7% signal vs 6.6% background acceptances for the case of standard definition, and **69.0% vs 2.5%** for the case of high definition. A deeper description of the procedure followed and the results obtained, together with an evaluation of the analysis process with DNNs can be found in [212]. The translation of these improvements in terms of background level and detector sensitivity is presented in Section § 7.4.

It is worth to notice here that although results shown below already show a remarkable improvement compared to classic analysis, there is still a lot of room for improvement. As aforementioned, GoogLeNet is a CNN designed to handle full-color 2D images, and it is expected that CNNs able to handle 3D images yield better results. Moreover, in present study CNNs have been applied to substitute the classic blob-cut, but they could be also aimed to be in charge of the complete discrimination based on the full topological signature and energy of events or even more, be in charge of the whole analysis beginning with the response of the photosensors.

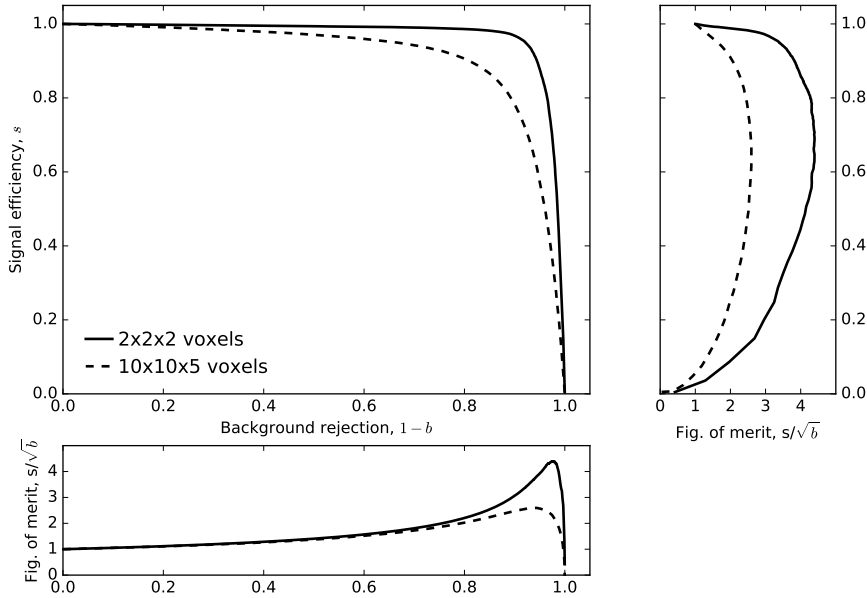


Figure 7.5: From [212], signal efficiency vs. background rejection for DNN analysis of single-track NEXT-100 Monte Carlo events for standard ($10 \times 10 \times 5$ mm) and high ($2 \times 2 \times 2$ mm) definitions. The figure of merit F is also shown as a function of background rejection.

7.3 High Energy Resolution

The nominal energy resolution expected in NEXT-100 detector is 0.7%, but the last energy resolution achieved with NEXT-NEW when reconstructing point-like events from krypton is a much better figure of 0.5% [135]. A great effort is being made by the collaboration to improve the spatial corrections that in practice would lead to reconstruct signal longer tracks with this high energetic resolution.

The high energy resolution allows to reduce the Region Of Interest (ROI) of our experiment which has a direct impact on the amount of background at the same time that signal efficiency remains unaffected or even slightly improves. Keeping in mind the spectra of significative backgrounds (Figure 6.6 (top) for ^{208}Tl and ^{214}Bi , and Figure 6.12 for ^{137}Xe), the reduction of ^{208}Tl and ^{137}Xe backgrounds is directly proportional to the ROI size reduction, while the reduction of ^{214}Bi

is even more dramatic as the peaks of the xenon signal (2457.83 keV) and bismuth (2447 keV) become sharper and the intersection of both gaussians decreases significantly. In particular the new ROI represents more than 20% reduction in ^{208}Tl and ^{137}Xe and more than 40% in ^{214}Bi that is reflected together with the rest of the *High Definition* improvements in Table 7.3.

7.4 NEXT100-HD Sensitivity

The global improvement in background rejections coming from the aforementioned extra handles lead to a dramatic reduction of the radioactive budget of NEXT-100. Contributions from the relevant components identified in Section § 6.3.4 have been re-evaluated and the corresponding numbers are listed in Table 7.3, yielding a total activity of 6.82×10^{-5} cts keV $^{-1}$ kg $^{-1}$ yr $^{-1}$ with a signal efficiency of **29.3%**. The corresponding sensitivity at 90% CL for both $T_{1/2}^{0\nu}$ and $m_{\beta\beta}$ are depicted in figure 7.6 and some concrete values are listed in Table 7.4, while a comparison between the *Standard* and *High Definition* versions of NEXT-100 in terms of $T_{1/2}^{0\nu}$ is depicted in figure 7.7. Reached sensitivity values at 90% CL after 5 (10) years of data taking are: 1.48×10^{26} (**2.65×10^{26}**) **years**, corresponding to an upper limit on the Majorana neutrino mass of 47-131 (**35-98**) **meV**, depending on the NME method used.

At this point it is important to highlight that NEXT-100 *High Definition* expects ~ 0.12 counts/year what in practice means a "quasi-background free" experiment. Under these circumstances the figure of merit $F = s/\sqrt{b}$ is not followed, and the signal efficiency becomes much more important. Consequently the previous results have been computed with the improvement factors from DNN analysis listed in Table 7.2 instead of those maximizing F .

As expected in background-free experiments, the sensitivity of NEXT-100 *High Definition* to ^{137}Xe $T_{1/2}^{0\nu}$ improves linearly with the exposure as depicted in Figure 7.6. In light of these results we conclude that NEXT-100 detector concept in its *High Definition* version can be directly extrapolated to the tonne scale looking to cover the entire Inverted Hierarchy of neutrino masses. This extrapolation of the NEXT detector will be the main subject of next Chapter § 8.

Table 7.3: NEXT-100 High-Definition background contributions from significant sources (cts keV⁻¹ kg⁻¹ yr⁻¹).

Bkgnd. Source	²⁰⁸ Tl	²¹⁴ Bi	¹³⁷ Xe
Tracking Plane	3.82×10^{-6}	8.33×10^{-6}	
Energy Plane	1.12×10^{-5}	1.86×10^{-5}	
Field Cage	$< 9.98 \times 10^{-7}$	$< 7.51 \times 10^{-6}$	
ICS	$< 2.44 \times 10^{-6}$	$< 2.64 \times 10^{-6}$	
Vessel	$< 2.37 \times 10^{-6}$	$< 1.62 \times 10^{-6}$	
Shielding Lead	2.22×10^{-7}	2.13×10^{-6}	
Cosmogenic Muons			6.34×10^{-6}
Total	$< 2.10 \times 10^{-5}$	$< 4.08 \times 10^{-5}$	6.34×10^{-6}

Table 7.4: Sensitivity values at 90% CL of NEXT-100 *Standard* and *High Definition* versions. $T_{1/2}^{0\nu}$ sensitivity is expressed in years, and $m_{\beta\beta}$ sensitivity in meV. The $m_{\beta\beta}$ range corresponds to the largest (EDF) and smallest (ISM) ¹³⁶Xe NME estimates listed in Table 3.1.

Years	NEXT100 - Std.		NEXT100 - HD.	
	$T_{1/2}^{0\nu}$	$m_{\beta\beta}$	$T_{1/2}^{0\nu}$	$m_{\beta\beta}$
1	2.99×10^{25}	104 - 291	3.26×10^{25}	99 - 279
3	6.87×10^{25}	69 - 192	9.30×10^{25}	59 - 165
5	9.85×10^{25}	57 - 161	1.48×10^{26}	47 - 131
10	1.56×10^{26}	45 - 127	2.65×10^{26}	35 - 98

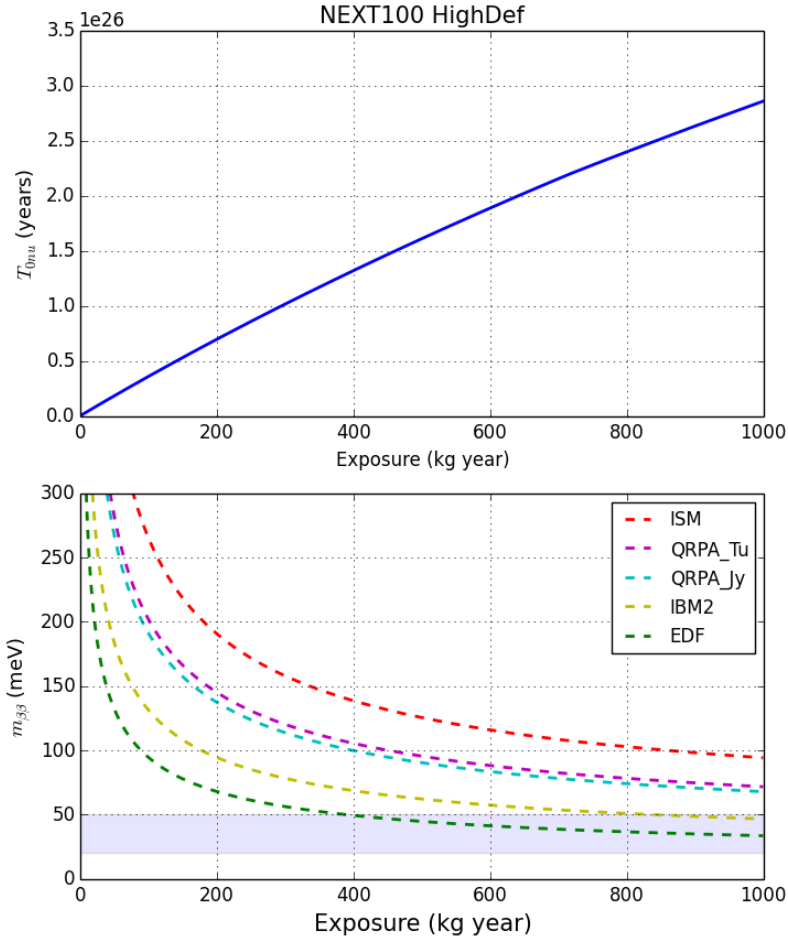


Figure 7.6: Sensitivity (at 90% CL) of NEXT-100 *High Definition* version to $0\nu\beta\beta$ -decay. Top figures correspond to $T_{1/2}^{0\nu}$ sensitivity, and bottom to $m_{\beta\beta}$ sensitivity for all the available ^{136}Xe NME estimates listed in Table 3.1: ISM (red), QRPA-Tu (magenta), QRPA-Jy (cyan), IBM2 (yellow) and EDF (green). Light blue horizontal band corresponds to the range of neutrino Majorana masses, $m_{\beta\beta}$, for the inverted hierarchy.

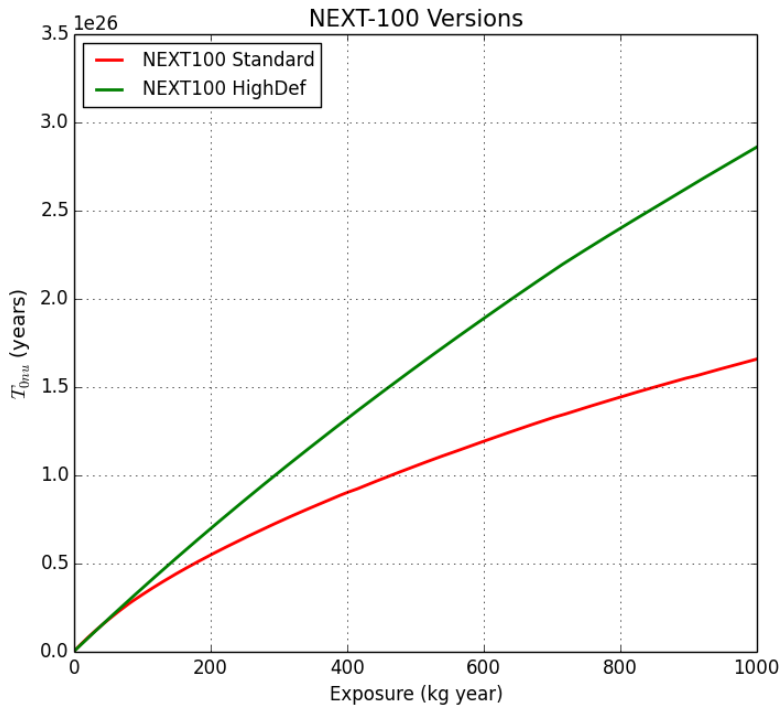


Figure 7.7: Comparison of sensitivity (at 90% CL) to $0\nu\beta\beta$ -decay of NEXT-100 *Standard* and *High Definition* versions.

Towards The Inverted Hierarchy

8

Chapter § 7 has revealed that NEXT-100 *High Definition* is, in practice, a background-free detector. Moreover, the technical approaches followed in its design allow a simple extrapolation to a detector of bigger size. In fact, the increase of isotope mass would take profit of the low background level reached by NEXT technology to fully cover the Inverted Hierarchy of neutrino masses.

In the first Section § 8.1 a simple extrapolation of NEXT-100 design to accommodate 1000 Kg of xenon gas, called *NEXT-Ton*, is presented together with the assessment of the background rate and sensitivity expected. The second section will be devoted to present and evaluate the efforts of NEXT-collaboration in the search for the "saint grail" of $\beta\beta$ -decay experiments based on xenon, the so-called *barium tagging*.

8.1 NEXT-Ton

NEXT-Ton detector is a direct extrapolation of NEXT-100 detector design, able to accommodate 1000 kg of high pressure xenon gas (HPGXe). Apart from the re-scaling of the detector, certain assumptions have been reasonably taken to improve the detector performance such as detector component upgrades. The analysis has been carried out as described in Chapter § 7 although as aforementioned, there is plenty of room for improvement specially on DNN analysis.

Following, the main key points of NEXT-Ton detector design are listed:

- The *Shielding Castle* is replaced by a water tank able to shield incoming gammas and neutrons from outside the detector.

- The pressure *Vessel* shares the same cylindrical design with NEXT-100, and it has been scaled up to be able to contain the 1000 Kg of HPGXe. The new vessel is 2 cm thick, 324 cm long and has an internal diameter of 162 cm.
- The *Inner Copper Shielding* (ICS) has been scaled up in the same way than the vessel. New dimensions are: 12 cm thick, 300 cm long and an internal radius of 150 cm.
- The *Energy Plane* concept changes looking for more radiopure approaches. The PMTs used to read the scintillation would be replaced by a SiPM array of $5 \times 5 \text{ mm}^2$. From one side, this change would imply a dramatic reduction on the radioactive budget as the PMTs energy plane of NEXT-100 represents almost 50% of the total background. From other side, the new photo-sensors allow a higher coverage of the plane and a more regular light pattern, which in practice implies an improvement in the energy resolution and in the minimum visible energy. Moreover, this new SiPM array could be placed if necessary in the anode, sharing the plane with the small SiPM array devoted to tracking, and leaving the cathode for other uses (see next Section § 8.2).
- The *Tracking Plane* is just an extension of the NEXT-100 one adding extra Dice Boards (DBs). New DBs would be manufactured in fiberglass which is much more radiopure than current kapton.
- The *Field Cage* is scaled up to the bigger version needed based on the knowledge acquired in NEXT-100 construction.

With the new detector design, the copper from the inner shielding represents almost all the detector backgrounds coming from natural decay chains. The new energy and tracking planes are expected to be extremely radiopure and their final contributions negligible; while the vessel activity, in case of needed, can be vetoed with a thicker ICS without increasing the copper contribution as it would be self-shielded. This way, the only relevant background sources will be the ^{208}Tl and ^{214}Bi contributions from the ICS and the ^{137}Xe de-excitations coming from cosmogenic muons. The extrapolation of the activities has been

made considering that a bigger size detector represents an increase in material masses, a higher probability of interaction of gammas and neutrons in the active volume, and an improvement of events fiduciality.

The total background expected in *NEXT-Ton* detector is 2.59×10^{-6} cts keV⁻¹ kg⁻¹ yr⁻¹ (38% from ICS and 62% from ¹³⁷Xe activated by muons), while the signal efficiency would be 27%. This extremely low background rate represents less than 1 count of background after 5 years of data taking, which allows a quasi-linear improvement of $T_{1/2}^{0\nu}$ sensitivity with the exposure. It is worth to notice here that ¹³⁷Xe contribution represents more than 60% of the background, that in case of need, could be significantly reduced by placing the detector in an underground lab deeper than the LSC (see figure 4.11).

The corresponding sensitivities at 90% CL for both $T_{1/2}^{0\nu}$ and $m_{\beta\beta}$ are depicted in figure 8.1 and specifically, after 5 (10) years of data taking are: 1.47×10^{27} (**2.80×10^{27}**) years, corresponding to an upper limit on the Majorana neutrino mass of 15-42 (**11-30**) meV, depending on the NME method used.

We have also contemplated a *pessimistic* scenario where the background expected from ²⁰⁸Tl and ²¹⁴Bi from detector materials and components is an order of magnitude higher than the aforementioned expected activity from the ICS. This activity would imply a minor reduction in sensitivity (as depicted in figure 8.5) thanks to the low level of backgrounds expected, reaching a sensitivity of 1.27×10^{27} (2.17×10^{27}) years at 90% CL after 5 (10) years of data taking.

So in light of these results, it must be concluded that the scale-up of NEXT technology to the tonne scale would **totally cover** the inverted hierarchy of Majorana neutrino masses in a reasonable period of time of data taking, so it must be pursued by the Collaboration by all possible means.

8.2 Barium Tagging

A unique possibility offered by xenon-based experiments is that all backgrounds except the $2\nu\beta\beta$ decay mode could be effectively removed by identification of the daughter barium ion released by any $\beta\beta$ -decay, what together with a sufficient energy resolution (better

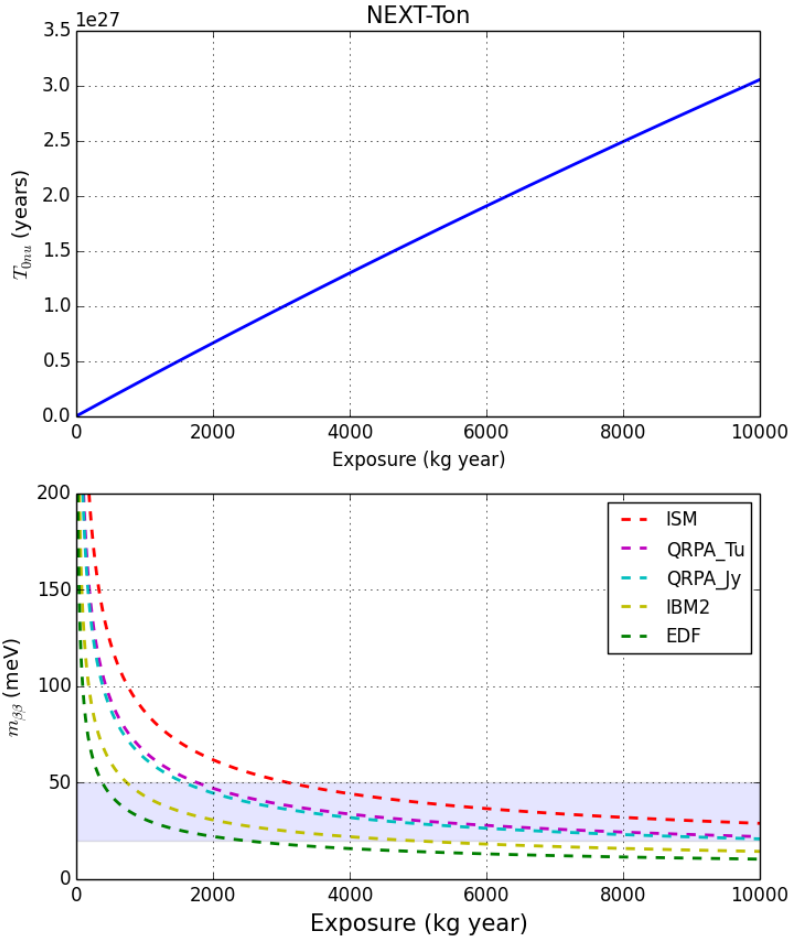


Figure 8.1: Sensitivity (at 90% CL) of NEXT-Ton to $0\nu\beta\beta$ -decay. Top figures correspond to $T_{1/2}^{0\nu}$ sensitivity, and bottom to $m_{\beta\beta}$ sensitivity for all the available ^{136}Xe NME estimates listed in Table 3.1: ISM (red), QRPA-Tu (magenta), QRPA-Jy (cyan), IBM2 (yellow) and EDF (green). Light blue horizontal band corresponds to the range of neutrino Majorana masses, $m_{\beta\beta}$, for the inverted hierarchy.

than $\sim 2\%$ at $Q_{\beta\beta}$), would imply in practice a background-free experiment. The so-called “*barium tagging*” has been a subject of R&D for at least 20 years [214–216], but at the time being, a convincing method of barium ion extraction and identification remains elusive.

The NEXT collaboration is carrying out a R&D program to employ “single molecule fluorescence imaging” (SMFI) techniques to detect the barium daughter ion in high pressure xenon gas [217]. SMFI is a technique invented by physicists and developed by bio-chemists that enables single-molecule sensitive, super-resolution microscopy. It employs non-fluorescent in isolation molecules, which become fluorescent upon chelation with a suitable ion. A small optically thin region containing these molecules is interrogated repeatedly with typically blue or near-UV photons that excite them, getting a strong fluorescence response from those chelated.

The difficult process of realizing SMFI-based barium tagging can be broadly broken into four steps of increasing difficulty: 1) identify molecules which provide a strong fluorescent response to Ba^{++} ions; 2) develop a scanning system which can be used to tag barium ions remotely inside a large detector; 3) establish whether the chelation and fluorescence behavior is maintained in a HPGXe environment; 4) optimize the detection technique to the single molecule regime. A deep description of the challenge is described in [218].

In the case of NEXT-100, the Ba^{++} ion released is very unlikely to recombine with nearby free electrons so it will be the dominant ion yielded and thus, it eventually drift to the sensor plane. In [218] the use of fluorophores such as Fluo-3 and Fluo-4 (see figure 8.2), whose value for Ca^{++} measurements has already been proved [219], are explored as potential fluorescent molecules. Figure 8.3 shows a very promising CCD-camera scan of a fluorophores surface during and after a single Ba^{++} ion detection.

The success on Ba^{++} detection would imply that none of the relevant background sources identified on previous versions of NEXT detectors would represent a real background, and that ^{136}Xe $2\nu\beta\beta$ -decays would be the only event type able to mimic our signal. Considering a ^{136}Xe $T_{1/2}^{2\nu} = 2.165 \times 10^{21}$ years [46] and assuming a global rejection factor of $\sim 10^{-10}$ (computed with the classic method), the expected background rate would be $\sim 5 \times 10^{-9}$ cts keV $^{-1}$ kg $^{-1}$ yr $^{-1}$.

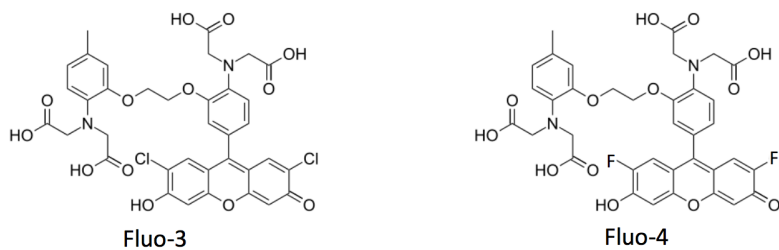


Figure 8.2: From [218], structure of Fluo-3 and Fluo-4 molecules under study as fluorescence molecules for barium-tagging.

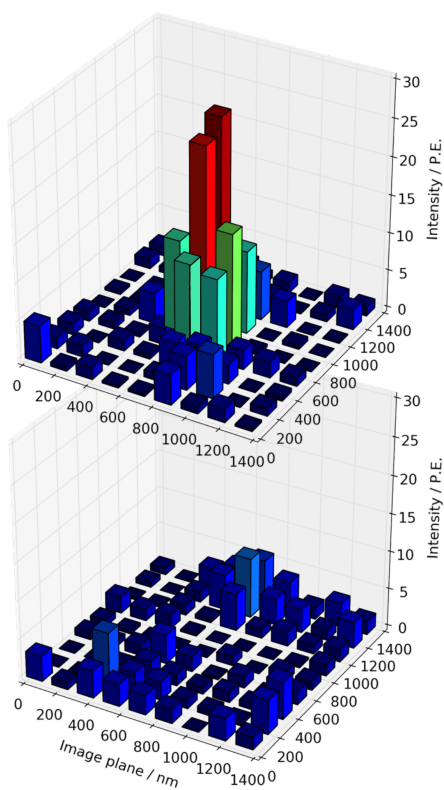


Figure 8.3: From [217], CCD-camera scan of a fluorophore surface during (top) and after (bottom) a single Ba^{++} ion detection.

This background rate yields to less than 2×10^{-4} counts after 10 years of data taking, what in practice means a background-free experiment.

Assuming an efficiency close to 100% of the barium tagging process, the analysis cuts looking for the differences in topology of signal and background events could be by-passed. It would lead to no increase on $2\nu\beta\beta$ background rate and at the same time, a significant increase in signal efficiency, passing from 27% to 56%, what represents a dramatic improvement on sensitivity as depicted in figure 8.4. According to section § 6.4.1, the sensitivity of current detector could be computed with the formula (6.7) for ideal background-free experiments, although the same formula used for previous versions (6.13) has been finally used for the comparison. The corresponding sensitivities at 90% CL for both $T_{1/2}^{0\nu}$ and $m_{\beta\beta}$ after 5 (10) years of data taking are: 3.21×10^{27} (**6.41×10^{27}**) years, corresponding to an upper limit on the Majorana neutrino mass of 10-28 (**7-20**) meV, depending on the NME method used. Figure 8.5 illustrates the improvement in sensitivity when applying the barium tagging to NEXT-Ton, and some concise values are listed in Table 8.1.

Although section § 8.1 has concluded that NEXT-Ton would be able to cover the inverted hierarchy of neutrino masses, the barium tagging would allow to reach this goal in a much shorter time period of few years. Even more, if neutrino masses would follow the normal ordering instead of the inverted, Majorana neutrino absolute mass would be in the order of 1 meV, which at the end converts barium tagging in "a must" of any experiment aimed to look for $^{136}\text{Xe } 0\nu\beta\beta$ decays.

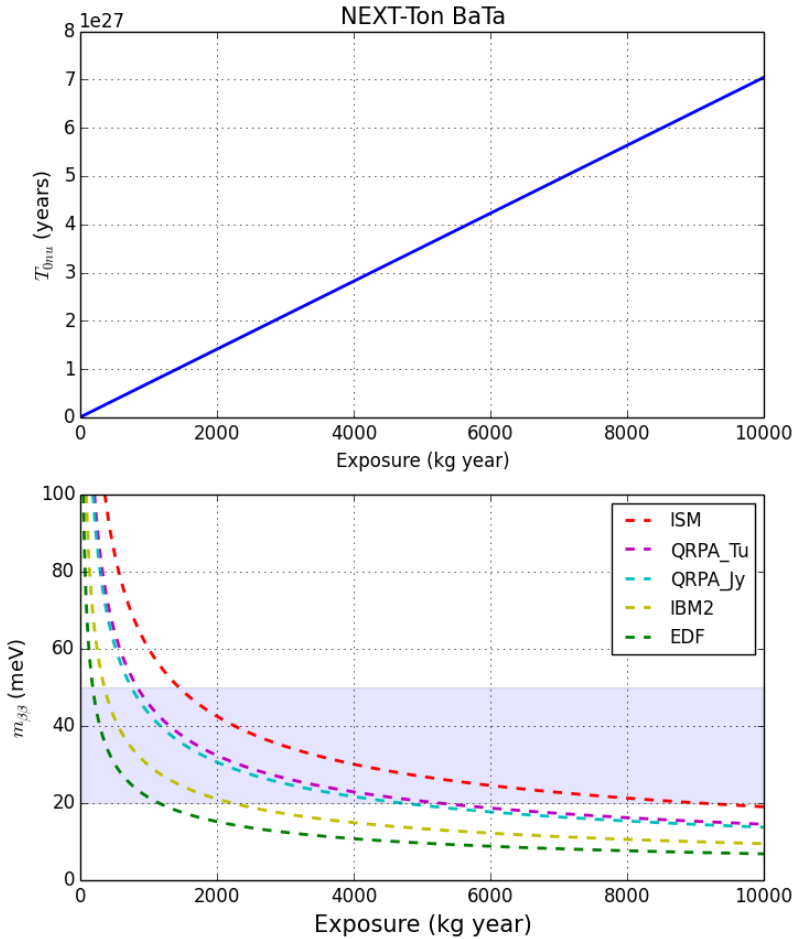


Figure 8.4: Sensitivity (at 90% CL) of *NEXT-Ton Ba-Ta* to $0\nu\beta\beta$ -decay. Top figures correspond to $T_{1/2}^{0\nu}$ sensitivity, and bottom to $m_{\beta\beta}$ sensitivity for all the available ^{136}Xe NME estimates listed in Table 3.1: ISM (red), QRPA-Tu (magenta), QRPA-Jy (cyan), IBM2 (yellow) and EDF (green). Light blue horizontal band corresponds to the range of neutrino Majorana masses, $m_{\beta\beta}$, for the inverted hierarchy.

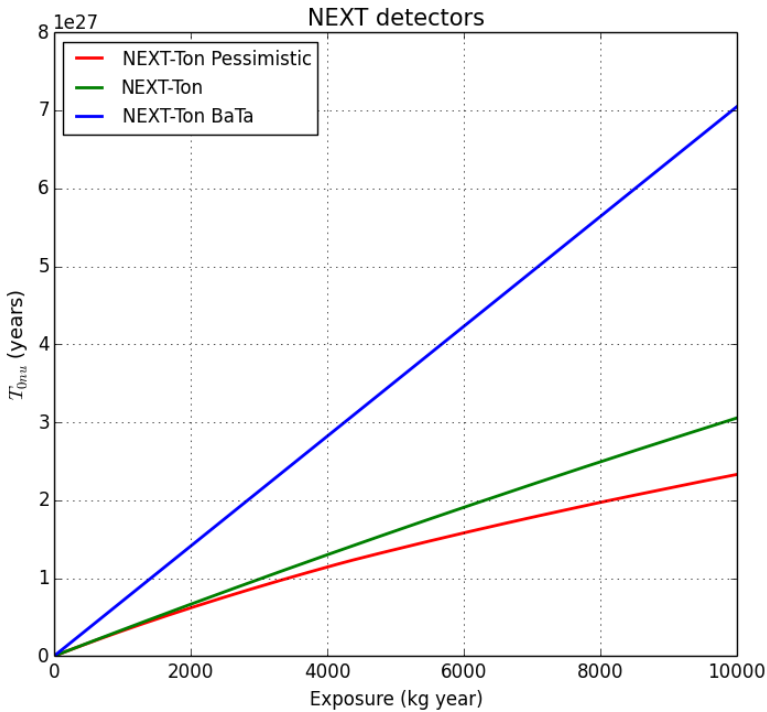


Figure 8.5: Comparison of sensitivity (at 90% CL) to $0\nu\beta\beta$ -decay of NEXT-Ton with and without *Barium Tagging*. The pessimistic scenario in which background from natural decay chains is one order of magnitude higher than expected (*NEXT-Ton Pessimistic*) has been added to the comparison.

Table 8.1: Sensitivity values at 90% CL of NEXT-Ton with and without *Barium Tagging*. $T_{1/2}^{0\nu}$ sensitivity is expressed in years, and $m_{\beta\beta}$ sensitivity in meV. The $m_{\beta\beta}$ range corresponds to the largest (EDF) and smallest (ISM) ^{136}Xe NME estimates listed in Table 3.1.

Years	NEXT-Ton		NEXT-Ton + BaTa	
	$T_{1/2}^{0\nu}$	$m_{\beta\beta}$	$T_{1/2}^{0\nu}$	$m_{\beta\beta}$
1	3.06×10^{26}	32 - 91	6.41×10^{26}	22 - 63
3	8.99×10^{26}	19 - 53	1.92×10^{27}	13 - 36
5	1.47×10^{27}	15 - 42	3.21×10^{27}	10 - 28
10	2.80×10^{27}	11 - 30	6.41×10^{27}	7 - 20

Bibliography

- [1] KamLAND-Zen, A. Gando et al., *Search for Majorana Neutrinos near the Inverted Mass Hierarchy Region with KamLAND-Zen*, Phys. Rev. Lett. **117** (2016), no. 8, 082503, [arXiv:1605.02889]. [Addendum: Phys. Rev. Lett.117,no.10,109903(2016)].
- [2] W. Pauli, *Dear radioactive ladies and gentlemen*, Phys. Today **31N9** (1978) 27.
- [3] C. D. Ellis and W. A. Wooster, *The average energy of disintegration of radium e*, Proceedings of the Royal Society of London A: Mathematical, Physical and Engineering Sciences **117** (1927), no. 776, 109–123, [<http://rspa.royalsocietypublishing.org/content/117/776/109.full.pdf>].
- [4] E. Fermi, *An attempt of a theory of beta radiation. 1.*, Z. Phys. **88** (1934) 161–177.
- [5] E. Majorana, *Theory of the symmetry of electrons and positrons*, Nuovo Cim. **14** (1937) 171–184.
- [6] H. Bethe and R. Peierls, *The 'neutrino'*, Nature **133** (1934) 532.
- [7] B. Pontecorvo, *Inverse beta process*, Camb. Monogr. Part. Phys. Nucl. Phys. Cosmol. **1** (1991) 25–31.
- [8] F. Reines, C. L. Cowan, F. B. Harrison, A. D. McGuire, and H. W. Kruse, *Detection of the free anti-neutrino*, Phys. Rev. **117** (1960) 159–173.

- [9] B. Cleveland, T. Daily, R. Davis Jr., J. R. Distel, K. Lande, C. K. Lee, P. S. Wildenhain, and J. Ullman, *Measurement of the solar electron neutrino flux with the Homestake chlorine detector*, *Astrophys. J.* **496** (1998) 505–526.
- [10] G. Danby, J. M. Gaillard, K. A. Goulianos, L. M. Lederman, N. B. Mistry, M. Schwartz, and J. Steinberger, *Observation of High-Energy Neutrino Reactions and the Existence of Two Kinds of Neutrinos*, *Phys. Rev. Lett.* **9** (1962) 36–44.
- [11] DONUT, J. Sielaff, *Observation of tau neutrino charged current interactions*, in *36th Rencontres de Moriond on Electroweak Interactions and Unified Theories Les Arcs, France, March 10-17, 2001*, 2001, hep-ex/0105042.
- [12] S. M. Bilenky, *Neutrino. History of a unique particle*, *Eur. Phys. J.* **H38** (2013) 345–404, [arXiv:1210.3065].
- [13] Wikipedia, *Standard model — wikipedia, the free encyclopedia*, 2014. http://en.wikipedia.org/w/index.php?title=Standard_Model&oldid=592640485.
- [14] Kamiokande-II, K. S. Hirata et al., *Observation of B-8 Solar Neutrinos in the Kamiokande-II Detector*, *Phys. Rev. Lett.* **63** (1989) 16.
- [15] GALLEX, P. Anselmann et al., *GALLEX results from the first 30 solar neutrino runs*, *Phys. Lett.* **B327** (1994) 377–385.
- [16] SAGE, D. Abdurashitov et al., *Results from SAGE*, *Phys. Lett.* **B328** (1994) 234–248.
- [17] B. Pontecorvo, *Inverse beta processes and nonconservation of lepton charge*, *Sov. Phys. JETP* **7** (1958) 172–173. [*Zh. Eksp. Teor. Fiz.*34,247(1957)].
- [18] Super-Kamiokande, R. Wendell et al., *Atmospheric neutrino oscillation analysis with sub-leading effects in Super-Kamiokande I, II, and III*, *Phys. Rev.* **D81** (2010) 092004, [arXiv:1002.3471].

- [19] SNO, Q. R. Ahmad et al., *Direct evidence for neutrino flavor transformation from neutral current interactions in the Sudbury Neutrino Observatory*, Phys. Rev. Lett. **89** (2002) 011301, [nucl-ex/0204008].
- [20] KamLAND, S. Abe et al., *Precision Measurement of Neutrino Oscillation Parameters with KamLAND*, Phys. Rev. Lett. **100** (2008) 221803, [arXiv:0801.4589].
- [21] I. Esteban, M. C. Gonzalez-Garcia, M. Maltoni, I. Martinez-Soler, and T. Schwetz, *Updated fit to three neutrino mixing: exploring the accelerator-reactor complementarity*, JHEP **01** (2017) 087, [arXiv:1611.01514].
- [22] C. Weinheimer and K. Zuber, *Neutrino Masses*, Annalen Phys. **525** (2013), no. 8-9, 565–575, [arXiv:1307.3518].
- [23] V. Lobashev, V. Aseev, A. Belesev, A. Berlev, E. Geraskin, et al., *Direct search for mass of neutrino and anomaly in the tritium beta-spectrum*, Nucl. Phys. Proc. Suppl. **87** (2000) 275–277.
- [24] C. Kraus, B. Bornschein, L. Bornschein, J. Bonn, B. Flatt, et al., *Final results from phase II of the Mainz neutrino mass search in tritium beta decay*, Eur. Phys. J. **C40** (2005) 447–468, [hep-ex/0412056].
- [25] Particle Data Group, K. Olive et al., *Review of Particle Physics*, Phys. Rev. **C38** (2014) 090001.
- [26] KATRIN Collaboration, A. Osipowicz et al., *KATRIN: A Next generation tritium beta decay experiment with sub-eV sensitivity for the electron neutrino mass. Letter of intent*, 2001, hep-ex/0109033.
- [27] J. Lesgourgues and S. Pastor, *Massive neutrinos and cosmology*, Phys. Rept. **429** (2006) 307–379, [astro-ph/0603494].
- [28] WMAP Collaboration, C. Bennett et al., *The Microwave Anisotropy Probe (MAP) mission*, Astrophys. J. **583** (2003) 1–23, [astro-ph/0301158].
- [29] O. Lahav and A. R. Liddle, *The Cosmological Parameters 2014*, 2014, arXiv:1401.1389.

- [30] Planck, P. A. R. Ade et al., *Planck 2015 results. XIII. Cosmological parameters*, *Astron. Astrophys.* **594** (2016) A13, [arXiv:1502.01589].
- [31] R. Emami, T. Broadhurst, P. Jimeno, G. Smoot, R. Angulo, J. Lim, M. C. Chu, and R. Lazkoz, *Evidence of Neutrino Enhanced Clustering in a Complete Sample of Sloan Survey Clusters, Implying $\Sigma m_\nu = 0.11 \pm 0.03 eV$* , 2017, arXiv:1711.05210.
- [32] C. Giunti and C. W. Kim, *Fundamentals of Neutrino Physics and Astrophysics*. OXFORD University Press, 2007.
- [33] P. Hernandez, *Neutrino physics*, 2010, arXiv:1010.4131.
- [34] P. Minkowski, *$\mu \rightarrow e\gamma$ at a rate of one out of 109 muon decays?*, *Physics Letters B* **67** (1977), no. 4, 421 – 428.
- [35] T. Yanagida, *Horizontal Symmetry and Masses of Neutrinos*, *Prog.Theor.Phys.* **64** (1980) 1103.
- [36] M. Gell-Mann, P. Ramond, and R. Slansky, *Complex Spinors and Unified Theories*, *Conf.Proc.* **C790927** (1979) 315–321, [arXiv:1306.4669].
- [37] R. Mohapatra and G. Senjanović, *Neutrino mass and spontaneous parity nonconservation*, *Phys. Rev. Lett.* **44** (Apr, 1980) 912–915.
- [38] G. F. Smoot and K. Davidson, *Wrinkles in time*. Avon Books, 1996.
- [39] J. H. Christenson, J. W. Cronin, V. L. Fitch, and R. Turlay, *Evidence for the 2π Decay of the K_2^0 Meson*, *Phys. Rev. Lett.* **13** (1964) 138–140.
- [40] M. Fukugita and T. Yanagida, *Baryogenesis without Grand Unification*, *Phys. Lett. B* **174** (1986) 45.
- [41] S. Davidson, E. Nardi, and Y. Nir, *Leptogenesis*, *Phys. Rept.* **466** (2008) 105–177, [arXiv:0802.2962].
- [42] S. R. Elliott, A. A. Hahn, and M. K. Moe, *Direct evidence for two-neutrino double beta decay in ^{82}Se* , *Phys. Rev. Lett.* **59** (1987) 2020–2023.

- [43] Particle Data Group, C. Patrignani et al., *Review of Particle Physics*, Chin. Phys. **C40** (2016), no. 10, 100001.
- [44] NEMO-3, R. Arnold et al., *Measurement of the double-beta decay half-life and search for the neutrinoless double-beta decay of ^{48}Ca with the NEMO-3 detector*, Phys. Rev. **D93** (2016), no. 11, 112008, [arXiv:1604.01710].
- [45] CUORE, C. Alduino et al., *Measurement of the two-neutrino double-beta decay half-life of ^{130}Te with the CUORE-0 experiment*, Eur. Phys. J. **C77** (2017), no. 1, 13, [arXiv:1609.01666].
- [46] EXO Collaboration, J. B. Albert et al., *An improved measurement of the $2\nu\beta\beta$ half-life of Xe-136 with EXO-200*, Phys. Rev. C **89** (2014) 015502, [arXiv:1306.6106].
- [47] W. H. Furry, *On transition probabilities in double beta disintegration*, Phys. Rev. **56** (1939) 1184–1193.
- [48] M. Doi, T. Kotani, and E. Takasugi, *Double beta decay and Majorana neutrino*, Prog. Theor. Phys. Suppl. **83** (1985) 1.
- [49] J. Kotila and F. Iachello, *Phase space factors for double- β decay*, Phys. Rev. C **85** (2012) 034316, [arXiv:1209.5722].
- [50] M. Mirea, T. Pahomi, and S. Stoica, *Values of the phase space factors involved in double beta decay*, Rom. Rep. Phys. **67** (2015), no. 3, 872.
- [51] J. Menéndez, A. Poves, E. Caurier, and F. Nowacki, *Disassembling the nuclear matrix elements of the neutrinoless $\beta\beta$ decay*, Nucl. Phys. A **818** (2009) 139–151, [arXiv:0801.3760].
- [52] F. Šimkovic, V. Rodin, A. Faessler, and P. Vogel, *$0\nu\beta\beta$ and $2\nu\beta\beta$ nuclear matrix elements, quasiparticle random-phase approximation, and isospin symmetry restoration*, Phys. Rev. **C87** (2013), no. 4, 045501, [arXiv:1302.1509].
- [53] J. Hyvärinen and J. Suhonen, *Nuclear matrix elements for $0\nu\beta\beta$ decays with light or heavy Majorana-neutrino exchange*, Phys. Rev. **C91** (2015), no. 2, 024613.

- [54] J. Barea, J. Kotila, and F. Iachello, *$0\nu\beta\beta$ and $2\nu\beta\beta$ nuclear matrix elements in the interacting boson model with isospin restoration*, Phys. Rev. **C91** (2015), no. 3, 034304, [arXiv:1506.08530].
- [55] N. Vaquero López, T. R. Rodríguez, and J. L. Egido, *Shape and pairing fluctuations effects on neutrinoless double beta decay nuclear matrix elements*, Phys. Rev. Lett. **111** (2013) 142501, [arXiv:1401.0650].
- [56] L. S. Song, J. M. Yao, P. Ring, and J. Meng, *Nuclear matrix element of neutrinoless double- β decay: Relativity and short-range correlations*, Phys. Rev. **C95** (2017), no. 2, 024305, [arXiv:1702.02448].
- [57] EXO Collaboration, J. B. Albert et al., *Search for Majorana neutrinos with the first two years of EXO-200 data*, Nature **510** (2014) 229–234, [arXiv:1402.6956].
- [58] KamLAND-Zen Collaboration, K. Asakura et al., *Results from KamLAND-Zen*, 2014, arXiv:1409.0077.
- [59] J. Martín-Albo, *The NEXT experiment for neutrinoless double beta decay searches*. PhD thesis, Valencia U., IFIC, 2015.
- [60] A. Bettini, *Underground laboratories*, Nucl. Instrum. Meth. A **626-627** (2011) S64–S68.
- [61] M. K. Moe, *New approach to the detection of neutrinoless double beta decay*, Phys. Rev. C **44** (1991) 931–934.
- [62] S. D. Biller, *Probing Majorana neutrinos in the regime of the normal mass hierarchy*, Phys. Rev. **D87** (2013), no. 7, 071301, [arXiv:1306.5654].
- [63] A. V. Tikhomirov, *Centrifugal enrichment of stable isotopes and modern physical experiments*, Czech. J. Phys. **50** (2000) 577–580.
- [64] A. Giuliani and A. Poves, *Neutrinoless double-beta decay*, Adv. High Energy Phys. **2012** (2012) 857016.

- [65] A. S. Barabash, *Brief review of double beta decay experiments*, in *Proceedings, 2nd International Conference on Particle Physics and Astrophysics (ICPPA 2016): Moscow, Russia, October 10-14, 2016*, 2017, arXiv:1702.06340.
- [66] CUORE Collaboration, D. Artusa et al., *Searching for neutrinoless double-beta decay of ^{130}Te with CUORE*, 2014, arXiv:1402.6072.
- [67] C. Arnaboldi et al., *A calorimetric search on double beta decay of Te-130* , Phys. Lett. B **557** (2003) 167–175, [hep-ex/0211071].
- [68] E. Andreotti et al., *^{130}Te neutrinoless double-beta decay with CUORICINO*, Astropart. Phys. **34** (2011) 822–831, [arXiv:1012.3266].
- [69] CUORE, K. Alfonso et al., *Search for Neutrinoless Double-Beta Decay of ^{130}Te with CUORE-0*, Phys. Rev. Lett. **115** (2015), no. 10, 102502, [arXiv:1504.02454].
- [70] J. Ouellet, *The Coldest Cubic Meter in the Known Universe*, 2014, arXiv:1410.1560.
- [71] CUORE, C. Alduino et al., *Cuore Sensitivity to $0\nu\beta\beta$ Decay*, Eur. Phys. J. **C77** (2017), no. 8, 532, [arXiv:1705.10816].
- [72] CUORE, C. Alduino et al., *The projected background for the CUORE experiment*, Submitted to: Eur. Phys. J. C (2017) [arXiv:1704.08970].
- [73] J. N. Marx and D. R. Nygren, *The Time Projection Chamber*, Phys. Today **31N10** (1978) 46.
- [74] EXO Collaboration, M. Auger et al., *The EXO-200 detector, part I: Detector design and construction*, JINST **7** (2012) P05010, [arXiv:1202.2192].
- [75] EXO-200, N. Ackerman et al., *Observation of Two-Neutrino Double-Beta Decay in ^{136}Xe with EXO-200*, Phys. Rev. Lett. **107** (2011) 212501, [arXiv:1108.4193].
- [76] EXO-200, J. B. Albert et al., *Searches for Double Beta Decay of ^{134}Xe with EXO-200*, 2017, arXiv:1704.05042.

- [77] nEXO, J. B. Albert et al., *Sensitivity and Discovery Potential of nEXO to Neutrinoless Double Beta Decay*, 2017, arXiv:1710.05075.
- [78] GERDA Collaboration, K. H. Ackermann et al., *The GERDA experiment for the search of $0\nu\beta\beta$ decay in ^{76}Ge* , Eur. Phys. J. C **73** (2013) 2330, [arXiv:1212.4067].
- [79] GERDA Collaboration, C. Macolino, *Search for neutrinoless double beta decay with the GERDA experiment*, Nuovo Cim. C **36** (2013), no. 6, 13–20.
- [80] GERDA, M. Agostini et al., *Results on Neutrinoless Double- β Decay of ^{76}Ge from Phase I of the GERDA Experiment*, Phys. Rev. Lett. **111** (2013), no. 12, 122503, [arXiv:1307.4720].
- [81] M. Agostini et al., *Background free search for neutrinoless double beta decay with GERDA Phase II*, 2017, arXiv:1703.00570. [Nature544,47(2017)].
- [82] Majorana, N. Abgrall et al., *The Majorana Demonstrator Neutrinoless Double-Beta Decay Experiment*, Adv. High Energy Phys. **2014** (2014) 365432, [arXiv:1308.1633].
- [83] N. Abgrall et al., *The Majorana Demonstrator radioassay program*, Nucl. Instrum. Meth. A **828** (2016) 22–36, [arXiv:1601.03779].
- [84] KamLAND Collaboration, S. Abe et al., *Production of radioactive isotopes through cosmic muon spallation in KamLAND*, Phys. Rev. C **81** (2010) 025807, [arXiv:0907.0066].
- [85] R. S. Raghavan, *New approach to the search for neutrinoless double beta decay*, Phys. Rev. Lett. **72** (1994) 1411–1414.
- [86] KamLAND-Zen Collaboration, A. Gando et al., *Measurement of the double- β decay half-life of ^{136}Xe with the KamLAND-Zen experiment*, Phys. Rev. C **85** (2012) 045504, [arXiv:1201.4664].
- [87] SNO Collaboration, J. Boger et al., *The Sudbury neutrino observatory*, Nucl. Instrum. Meth. A **449** (2000) 172–207, [nucl-ex/9910016].

- [88] SNO+ Collaboration, S. Biller, *SNO+ with tellurium*, 2014, arXiv:1405.3401.
- [89] SNO+, E. Caden, *Status of the SNO+ Experiment*, in *15th International Conference on Topics in Astroparticle and Underground Physics (TAUP 2017) Sudbury, Ontario, Canada, July 24-28, 2017*, 2017, arXiv:1711.11094.
- [90] NEMO, SuperNEMO, L. Vala, *Results of NEMO 3 and status of SuperNEMO*, Nucl. Phys. Proc. Suppl. **188** (2009) 62–64, [arXiv:0901.0473].
- [91] NEMO, R. Arnold et al., *First results of the search of neutrinoless double beta decay with the NEMO 3 detector*, Phys. Rev. Lett. **95** (2005) 182302, [hep-ex/0507083].
- [92] P. P. Povinec, *Background constrains of the supernemo experiment for neutrinoless double beta-decay searches*, Nuclear Instruments and Methods in Physics Research Section A: Accelerators, Spectrometers, Detectors and Associated Equipment **845** (2017) 398 – 403. Proceedings of the Vienna Conference on Instrumentation 2016.
- [93] PandaX, X. Cao et al., *PandaX: A Liquid Xenon Dark Matter Experiment at CJPL*, Sci. China Phys. Mech. Astron. **57** (2014) 1476–1494, [arXiv:1405.2882].
- [94] K. Nakamura et al., *AXEL—a high pressure xenon gas TPC for neutrinoless double beta decay search*, Nucl. Instrum. Meth. **A845** (2017) 394–397.
- [95] A. Bettini, *The Canfranc Underground Laboratory (LSC)*, Eur. Phys. J. Plus **127** (2012) 112.
- [96] E. Bellotti, O. Cremonesi, E. Fiorini, et al., *The Milano experiment on double beta decay of Xe-136*, J. Phys. G **17** (1991) S231–S241.
- [97] J. C. Vuilleumier et al., *Search for neutrinoless double beta decay in Xe-136 with a time projection chamber*, Phys. Rev. D **48** (1993) 1009–1020.

- [98] R. Luescher et al., *Search for $\beta\beta$ decay in Xe-136: New results from the Gotthard experiment*, Phys. Lett. B **434** (1998) 407–414.
- [99] C. Jacobaeus, T. Francke, B. Lund-Jensen, J. Ostling, P. Pavlopoulos, et al., *A High position resolution X-ray detector: An 'Edge on' illuminated capillary plate combined with a gas amplification structure*, IEEE Trans. Nucl. Sci. **53** (2006) 554–561, [physics/0411082].
- [100] LUX Collaboration, D. Akerib et al., *The Large Underground Xenon (LUX) Experiment*, Nucl. Instrum. Meth. **A704** (2013) 111–126, [arXiv:1211.3788].
- [101] T. Ohashi, K. Ebisawa, Y. Fukazawa, K. Hiyoshi, M. Horii, et al., *The Gas Imaging Spectrometer on Board ASCA*, Publ. Astron. Soc. Jap. **48** (1996) 157–170.
- [102] NEXT Collaboration, V. Alvarez et al., *NEXT-100 Technical Design Report (TDR): Executive Summary*, JINST **7** (2012) T06001, [arXiv:1202.0721].
- [103] D. Nygren, *High-pressure xenon gas electroluminescent TPC for 0- ν $\beta\beta$ -decay search*, Nucl. Instrum. Meth. A **603** (2009) 337–348.
- [104] M. Wang, G. Audi, F. G. Kondev, M. Maccormick, and X. Xu, *The 2012 Atomic Mass Evaluation and Future*, JPS Conf. Proc. **6** (2015) 010001.
- [105] M. Redshaw, E. Wingfield, J. McDaniel, and E. G. Myers, *Mass and double- β -decay Q value of Xe-136*, Phys. Rev. Lett. **98** (2007) 053003.
- [106] P. M. McCowan and R. C. Barber, *Q value for the double-beta decay of Xe-136*, Phys. Rev. C **82** (2010) 024603.
- [107] R. L. Platzman, *Total ionization in gases by high-energy particles: An appraisal of our understanding*, Int. J. Appl. Radiat. Isot. **10** (1961) 116–127.
- [108] C. A. B. Oliveira, M. Sorel, J. Martín-Albo, et al., *Energy Resolution studies for NEXT*, JINST **6** (2011) P05007, [arXiv:1105.2954].

- [109] T. Takahashi, S. Konno, T. Hamada, M. Miyajima, S. Kubota, A. Nakamoto, A. Hitachi, E. Shibamura, and T. Doke, *Average energy expended per ion pair in liquid xenon*, Phys. Rev. **A12** (1975) 1771–1775.
- [110] A. J. P. L. Policarpo, *Light production and gaseous detectors*, Phys. Scripta **23** (1981) 539–549.
- [111] E. Aprile, A. E. Bolotnikov, A. I. Bolozdynya, and T. Doke, *Noble gas detectors*. Wiley-VCH Verlag GmbH & Co. KGaA, Weinheim (Germany), 2006.
- [112] A. Parsons et al., *High pressure gas scintillation drift chambers with wave shifter fiber readout*, IEEE Trans. Nucl. Sci. **37** (1990) 541–546.
- [113] S. J. C. do Carmo, F. I. G. M. Borges, F. P. Santos, T. H. V. T. Dias, and C. A. N. Conde, *Absolute primary scintillation yield of gaseous xenon under low drift electric fields for 5.9 keV X-rays*, JINST **3** (2008) P07004.
- [114] L. M. P. Fernandes et al., *Primary and secondary scintillation measurements in a xenon Gas Proportional Scintillation Counter*, JINST **5** (2010) P09006, [arXiv:1009.2719].
- [115] NEXT, L. Serra et al., *An improved measurement of electron-ion recombination in high-pressure xenon gas*, JINST **10** (2015), no. 03, P03025, [arXiv:1412.3573].
- [116] C. Monteiro et al., *Secondary scintillation yield in pure xenon*, JINST **2** (2007) P05001.
- [117] C. M. B. Monteiro et al., *Secondary scintillation yield in pure xenon*, JINST **2** (2007) P05001, [physics/0702142].
- [118] U. Fano, *Ionization yield of radiations. (II) The fluctuations of the number of ions*, Phys. Rev. **72** (1947) 26–29.
- [119] A. J. P. L. Policarpo, M. A. F. Alves, M. Salete, S. C. P. Leite, and M. C. M. dos Santos, *Detection of soft x-rays with a xenon proportional scintillation counter*, Nucl. Instrum. Meth. **118** (1974) 221–226.

- [120] H. Sipilä, *Energy resolution of the proportional counter*, Nucl. Instrum. Meth. A **133** (1976) 251.
- [121] D. F. Anderson, T. T. Hamilton, W. H.-M. Ku, and R. Novick, *A large area, gas scintillation proportional counter*, Nucl. Instrum. Meth. **163** (1979) 125–134.
- [122] EXO Collaboration, E. Conti et al., *Correlated fluctuations between luminescence and ionization in liquid xenon*, Phys. Rev. B **68** (2003) 054201, [hep-ex/0303008].
- [123] A. Bolotnikov and B. Ramsey, *The spectroscopic properties of high-pressure xenon*, Nucl. Instrum. Meth. A **396** (1997) 360–370.
- [124] A. Bolozdynya, V. Egorov, A. Koutchenkov, G. Safronov, G. Smirnov, S. Medved, and V. Morgunov, *A high pressure xenon self-triggered scintillation drift chamber with 3d sensitivity in the range of 20–140 keV deposited energy*, Nuclear Instruments and Methods in Physics Research Section A: Accelerators, Spectrometers, Detectors and Associated Equipment **385** (1997), no. 2, 225 – 238.
- [125] D. R. Nygren, *A time projection chamber*. PEP-198, 1975.
- [126] Hamamatsu Photonics, *Photomultiplier tube R7378A*. Datasheet, 2004.
- [127] J. Toledo, H. Muller, R. Esteve, J. M. Monzo, A. Tarazona, and S. Martoiu, *The Front-End Concentrator card for the RD51 Scalable Readout System*, JINST **6** (2011) C11028.
- [128] NEXT Collaboration, V. Álvarez et al., *Initial results of NEXT-DEMO, a large-scale prototype of the NEXT-100 experiment*, JINST **8** (2013) P04002, [arXiv:1211.4838].
- [129] NEXT Collaboration, V. Álvarez et al., *Ionization and scintillation response of high-pressure xenon gas to alpha particles*, JINST **8** (2013) P05025, [arXiv:1211.4508].
- [130] NEXT Collaboration, V. Álvarez et al., *Operation and first results of the NEXT-DEMO prototype using a silicon photomultiplier tracking array*, JINST **8** (2013) P09011, [arXiv:1306.0471].

- [131] NEXT Collaboration, D. Lorca et al., *Characterisation of NEXT-DEMO using xenon K_{α} X-rays*, JINST **9** (2014) P10007, [arXiv:1407.3966].
- [132] NEXT, L. Serra, D. Lorca, J. Martin-Albo, M. Sorel, and J. J. Gomez-Cadenas, *Latest results of NEXT-DEMO, the prototype of the NEXT 100 double beta decay experiment*, in *Proceedings, 37th International Conference on High Energy Physics (ICHEP 2014): Valencia, Spain, July 2-9, 2014*, 2014, arXiv:1410.6700.
- [133] NEXT, P. Ferrario et al., *First proof of topological signature in the high pressure xenon gas TPC with electroluminescence amplification for the NEXT experiment*, JHEP **01** (2016) 104, [arXiv:1507.05902].
- [134] NEXT Collaboration, V. Alvarez et al., *Near-Intrinsic Energy Resolution for 30 to 662 keV Gamma Rays in a High Pressure Xenon Electroluminescent TPC*, Nucl. Instrum. Meth. **A708** (2013) 101–114, [arXiv:1211.4474].
- [135] NEXT, G. Martínez-Lema et al., *Calibration of the NEXT-White detector using ^{83m}Kr decays*, 2018, arXiv:1804.01780.
- [136] V. Alvarez et al., *Radiopurity control in the NEXT-100 double beta decay experiment: procedures and initial measurements*, JINST **8** (2013) T01002, [arXiv:1211.3961].
- [137] K. Lung et al., *Characterization of the Hamamatsu R11410-10 3-Inch Photomultiplier Tube for Liquid Xenon Dark Matter Direct Detection Experiments*, Nucl. Instrum. Meth. **A696** (2012) 32–39, [arXiv:1202.2628].
- [138] SensL MicroFC-10035-SMT-GP. <http://bit.ly/1tn1yjh>.
- [139] NEXT, V. Alvarez et al., *NEXT-100 Technical Design Report (TDR): Executive Summary*, JINST **7** (2012) T06001, [arXiv:1202.0721].
- [140] J. Rodriguez, M. Querol, J. Diaz, J. J. Gomez-Cadenas, D. Lorca, V. Alvarez, A. Martinez, and A. Gil, *Mass production automated test system for the NEXT SiPM tracking plane*, in *Proceedings, 2012 IEEE Nuclear Science Symposium and Medical Imaging Conference*

- (NSS/MIC 2012): *Anaheim, California, USA, October 29–November 3, 2012*, pp. 1106–1108, 2012.
- [141] NEXT, S. Cebrián et al., *Radiopurity assessment of the tracking readout for the NEXT double beta decay experiment*, JINST **10** (2015), no. 05, P05006, [arXiv:1411.1433].
- [142] J. Rodríguez, J. Toledo, R. Esteve, D. Lorca, and F. Monrabal, *The front-end electronics for the 1.8-kchannel SiPM tracking plane in the NEW detector*, JINST **10** (2015), no. 01, C01025.
- [143] M. Querol, J. Rodríguez, J. Toledo, R. Esteve, V. Álvarez, and V. Herrero, *A programmable, multichannel power supply for SiPMs with temperature compensation loop and Ethernet interface*, JINST **11** (2016), no. 12, C12035.
- [144] OPERA, M. Guler et al., *OPERA: An appearance experiment to search for $\nu/\mu \leftrightarrow \nu/\tau$ oscillations in the CNGS beam. Experimental proposal*, 2000.
- [145] S. Martoiu, H. Muller, A. Tarazona, and J. Toledo, *Development of the scalable readout system for micro-pattern gas detectors and other applications*, JINST **8** (2013) C03015.
- [146] RD51, M. Chefdeville, *RD51, a world-wide collaboration for the development of micro pattern gaseous detectors*, J. Phys. Conf. Ser. **309** (2011) 012017.
- [147] R. Esteve, J. Toledo, J. Rodríguez, M. Querol, and V. Álvarez, *Readout and data acquisition in the next-new detector based on srs-atca*, Journal of Instrumentation **11** (2016), no. 01, C01008.
- [148] NEXT Collaboration, F. Grañena et al., *NEXT, a HPGXe TPC for neutrinoless double beta decay searches (Letter of Intent)*, 2009, arXiv:0907.4054.
- [149] NEXT Collaboration, V. Álvarez et al., *The NEXT-100 experiment for neutrinoless double beta decay searches (Conceptual Design Report)*, 2011, arXiv:1106.3630.
- [150] J. Thomas, D. A. Imel, and S. Biller, *Statistics of charge collection in liquid argon and liquid xenon*, Phys. Rev. A **38** (1988) 5793.

- [151] National Nuclear Data Center, *Nudat database, version 2.7*. Available online at <http://www.nndc.bnl.gov/nudat2/>.
- [152] NEXT, J. Martín-Albo et al., *Sensitivity of NEXT-100 to Neutrinoless Double Beta Decay*, JHEP **05** (2016) 159, [arXiv:1511.09246].
- [153] Wikipedia, *Natural decay chain — wikipedia, the free encyclopedia*. https://en.wikipedia.org/wiki/Decay_chain.
- [154] V. Álvarez et al., *Radiopurity control in the NEXT-100 double beta decay experiment*, AIP Conf. Proc. **1549** (2013) 46–49.
- [155] P. J. Pérez, *The NEXT-100 experiment for Neutrino-less Double Beta decay: Main features, Results from Prototypes and Radiopurity issues..*, PoS **EPS-HEP2013** (2013) 528.
- [156] NEXT, T. Dafni et al., *Results of the material screening program of the NEXT experiment*, Nucl. Part. Phys. Proc. **273-275** (2016) 2666–2668, [arXiv:1411.1222].
- [157] S. Cebrián et al., *Radon and material radiopurity assessment for the NEXT double beta decay experiment*, AIP Conf. Proc. **1672** (2015) 060002, [arXiv:1505.07052].
- [158] NEXT, S. Cebrián et al., *Radiopurity assessment of the energy readout for the NEXT double beta decay experiment*, JINST **12** (2017), no. 08, T08003, [arXiv:1706.06012].
- [159] E. Aprile et al., *Material screening and selection for XENON100*, Astropart. Phys. **35** (2011) 43–49, [arXiv:1103.5831].
- [160] D. S. Akerib et al., *An Ultra-Low Background PMT for Liquid Xenon Detectors*, Nucl. Instrum. Meth. **A703** (2013) 1–6, [arXiv:1205.2272].
- [161] I. Bandac, *Gamma flux at the LSC*. Private communication, 2013.
- [162] I. Bandac, S. Borjabad, A. Ianni, R. Nuñez-Lagos, C. Pérez, S. Rodríguez, and J. A. Villar, *Ultra-low background and environmental measurements at Laboratorio Subterráneo de Canfranc (LSC)*, Appl. Radiat. Isot. **126** (2017) 127–129.

- [163] NEMO Collaboration, A. Nachab, *Radon reduction and radon monitoring in the NEMO experiment*, AIP Conf. Proc. **897** (2007) 35–38.
- [164] DarkSide Collaboration, M. Bossa, *DarkSide-50, a background free experiment for dark matter searches*, JINST **9** (2014) C01034.
- [165] M. Nebot Guinot, *Calibration and background model of the NEW detector at the LSC*. PhD thesis, Valencia U., IFIC, 2017.
- [166] NEXT, P. Novella et al., *Measurement of radon-induced backgrounds in the NEXT double beta decay experiment*, 2018, arXiv:1804.00471.
- [167] A. C. Ezeribe, W. Lynch, R. R. M. Gregorio, J. Mckeand, A. Scarff, and N. J. C. Spooner, *Demonstration of radon removal from SF₆ using molecular sieves*, JINST **12** (2017), no. 09, P09025, [arXiv:1707.07772].
- [168] XENON100, E. Aprile et al., *Online²²² Rn removal by cryogenic distillation in the XENON100 experiment*, Eur. Phys. J. **C77** (2017), no. 6, 358, [arXiv:1702.06942].
- [169] M. Crouch, *An improved world survey expression for cosmic ray vertical intensity vs. depth in standard rock*, 1987.
- [170] Yu. M. Andreev, V. I. Gurentsov, I. M. Kogai, and A. E. Chudakov, *Intensity and angular distribution of cosmic ray muons according to data of the Baksan scintillation telescope*, Bull. Russ. Acad. Sci. Phys. **53N2** (1989) 125–128. [Izv. Ross. Akad. Nauk Ser. Fiz.53,332(1989)].
- [171] LVD, M. Aglietta et al., *Neutrino induced and atmospheric single muon fluxes measured over five decades of intensity by LVD at Gran Sasso Laboratory*, Astropart. Phys. **3** (1995) 311–320.
- [172] MACRO, M. Ambrosio et al., *Vertical muon intensity measured with MACRO at the Gran Sasso Laboratory*, Phys. Rev. **D52** (1995) 3793–3802.
- [173] FREJUS, C. Berger et al., *Experimental Study of Muon Bundles Observed in the Frejus Detector*, Phys. Rev. **D40** (1989) 2163.

- [174] Y. Tserkovnyak, R. J. Komar, C. W. Nally, and C. E. Waltham, *A three-dimensional calculation of atmospheric neutrino fluxes*, in *27th International Cosmic Ray Conference (ICRC 2001) Hamburg, Germany, August 7-15, 2001*, pp. 7–15, 2001.
- [175] D. Mei and A. Hime, *Muon-induced background study for underground laboratories*, *Phys. Rev. D* **73** (2006) 053004, [astro-ph/0512125].
- [176] A. Ianni, *Canfranc underground laboratory*. Private communication from workshop, 2016.
- [177] P. Lipari and T. Stanev, *Propagation of multi - TeV muons*, *Phys. Rev. D* **44** (1991) 3543–3554.
- [178] D. E. Groom, N. V. Mokhov, and S. I. Striganov, *Muon stopping power and range tables 10-MeV to 100-TeV*, *Atom. Data Nucl. Data Tabl.* **78** (2001) 183–356.
- [179] EXO-200, J. B. Albert et al., *Cosmogenic Backgrounds to $0\nu\beta\beta$ in EXO-200*, *JCAP* **1604** (2016), no. 04, 029, [arXiv:1512.06835].
- [180] H. Wulandari, J. Jochum, W. Rau, and F. von Feilitzsch, *Neutron flux underground revisited*, *Astropart. Phys.* **22** (2004) 313–322, [hep-ex/0312050].
- [181] J. M. Carmona et al., *Neutron background at the Canfranc Underground Laboratory and its contribution to the IGEX-DM dark matter experiment*, *Astropart. Phys.* **21** (2004) 523–533, [hep-ex/0403009].
- [182] D. Jordan et al., *Measurement of the neutron background at the Canfranc Underground Laboratory LSC*, *Astropart. Phys.* **42** (2013) 1–6.
- [183] J. Taín, *Private communication*.
- [184] N. F. de Barros and K. Zuber, *Solar neutrino-electron scattering as background limitation for double beta decay*, *J. Phys.* **G38** (2011) 105201, [arXiv:1103.5757].

- [185] Geant4 Collaboration, S. Agostinelli et al., *Geant4: A simulation toolkit*, Nucl. Instrum. Meth. A **506** (2003) 250–303. Software available online at <http://geant4.cern.ch/>.
- [186] J. Allison et al., *Geant4 developments and applications*, IEEE Trans. Nucl. Sci. **53** (2006) 270.
- [187] J. Allison et al., *Recent developments in GEANT4*, Nucl. Instrum. Meth. **A835** (2016) 186–225.
- [188] R. Brun and F. Rademakers, *ROOT: An object oriented data analysis framework*, Nucl. Instrum. Meth. A **A389** (1997) 81–86. See also <http://root.cern.ch/>.
- [189] R. Brun, P. Canal, and F. Rademakers, *Design, development and evolution of the ROOT system*, PoS **ACAT2010** (2010) 002.
- [190] National Nuclear Data Center, *Evaluated Nuclear Structure Data File (ENSDF)*. Available online at <http://www.nndc.bnl.gov/ensdf/>.
- [191] O. A. Ponkratenko, V. I. Tretyak, and Y. G. Zdesenko, *The event generator DECAY4 for simulation of double beta processes and decay of radioactive nuclei*, Phys. Atom. Nucl. **63** (2000) 1282–1287, [[nuc1-ex/0104018](http://arxiv.org/abs/nuc1-ex/0104018)].
- [192] J. Apostolakis, S. Giani, M. G. Pia, L. Urban, M. Maire, and P. Nieminen, *GEANT4 low-energy electromagnetic models for electrons and photons*, 1999.
- [193] F. Salvat, *The penelope code system. Specific features and recent improvements*, Annals Nucl. Energy **82** (2015) 98–109.
- [194] D. E. Cullen et al., *Photon and electron interaction evaluated data libraries*. Available online at <http://www-nds.iaea.org/epdl97/>.
- [195] T. H. Cormen, C. E. Leiserson, R. L. Rivest, and C. Stein, *Introduction to algorithms*, pp. 531–539. The MIT Press, 3rd ed., 2009.

- [196] NEXT, A. Simón, P. Ferrario, and A. Izmaylov, *Event reconstruction in NEXT using the ML-EM algorithm*, Nucl. Part. Phys. Proc. **273-275** (2016) 2624–2626.
- [197] NEXT, A. Simón et al., *Application and performance of an ML-EM algorithm in NEXT*, JINST **12** (2017), no. 08, P08009, [arXiv:1705.10270].
- [198] J. Neyman and E. S. Pearson, *On the problem of the most efficient tests of statistical hypotheses*, Phil. Trans. R. Soc. Lond. A **231** (1933) 289–337.
- [199] C. R. Wuest, *TART Calculations of Neutron Attenuation and Neutron-induced Photons on 5% and 20% Borated Polyethylene Slabs*, 1992.
- [200] J. J. Gómez-Cadenas, J. Martín-Albo, M. Sorel, et al., *Sense and sensitivity of double beta decay experiments*, JCAP **1106** (2011) 007, [arXiv:1010.5112].
- [201] J. Neyman, *Outline of a theory of statistical estimation based on the classical theory of probability*, Phil. Trans. R. Soc. A **236** (1937) 333–380.
- [202] G. J. Feldman and R. D. Cousins, *A Unified approach to the classical statistical analysis of small signals*, Phys. Rev. D **57** (1998) 3873–3889, [physics/9711021].
- [203] C. D. R. Azevedo, L. M. P. Fernandes, E. D. C. Freitas, D. Gonzalez-Diaz, F. Monrabal, C. M. B. Monteiro, J. M. F. dos Santos, J. F. C. A. Veloso, and J. J. Gomez-Cadenas, *An homeopathic cure to pure Xenon large diffusion*, JINST **11** (2016), no. 02, C02007, [arXiv:1511.07189].
- [204] NEXT, C. A. O. Henriques et al., *Secondary scintillation yield of xenon with sub-percent levels of CO₂ additive for rare-event detection*, Phys. Lett. **B773** (2017) 663–671, [arXiv:1704.01623].
- [205] R. Felkai, F. Monrabal, D. Gonzalez-Díaz, M. Sorel, N. López-March, and J. J. Gómez-Cadenas, *Helium-Xenon mixtures to improve topological signature in high pressure gas Xenon TPCs*, 2017, arXiv:1710.05600.

- [206] C. Szegedy, W. Liu, Y. Jia, P. Sermanet, S. E. Reed, D. Anguelov, D. Erhan, V. Vanhoucke, and A. Rabinovich, *Going deeper with convolutions*, CoRR **abs/1409.4842** (2014) [arXiv:1409.4842].
- [207] G. Hinton, L. Deng, D. Yu, G. E. Dahl, A. r. Mohamed, N. Jaitly, A. Senior, V. Vanhoucke, P. Nguyen, T. N. Sainath, and B. Kingsbury, *Deep neural networks for acoustic modeling in speech recognition: The shared views of four research groups*, IEEE Signal Processing Magazine **29** (Nov, 2012) 82–97.
- [208] A. Aurisano, A. Radovic, D. Rocco, A. Himmel, M. D. Messier, E. Niner, G. Pawloski, F. Psihas, A. Sousa, and P. Vahle, *A Convolutional Neural Network Neutrino Event Classifier*, JINST **11** (2016), no. 09, P09001, [arXiv:1604.01444].
- [209] P. Baldi, P. Sadowski, and D. Whiteson, *Searching for Exotic Particles in High-Energy Physics with Deep Learning*, Nature Commun. **5** (2014) 4308, [arXiv:1402.4735].
- [210] L. de Oliveira, M. Kagan, L. Mackey, B. Nachman, and A. Schwartzman, *Jet-images — deep learning edition*, JHEP **07** (2016) 069, [arXiv:1511.05190].
- [211] M. A. Nielsen, *Neural networks and deep learning*, 2016.
- [212] NEXT, J. Renner et al., *Background rejection in NEXT using deep neural networks*, JINST **12** (2017), no. 01, T01004, [arXiv:1609.06202].
- [213] Y. Jia, E. Shelhamer, J. Donahue, S. Karayev, J. Long, R. B. Girshick, S. Guadarrama, and T. Darrell, *Caffe: Convolutional architecture for fast feature embedding*, CoRR **abs/1408.5093** (2014) [arXiv:1408.5093].
- [214] B. Mong et al., *Spectroscopy of Ba and Ba⁺ deposits in solid xenon for barium tagging in nEXO*, Phys. Rev. **A91** (2015), no. 2, 022505, [arXiv:1410.2624].
- [215] D. Sinclair et al., *Prospects for Barium Tagging in Gaseous Xenon*, J. Phys. Conf. Ser. **309** (2011) 012005.

- [216] T. Brunner et al., *An RF-only ion-funnel for extraction from high-pressure gases*, *Int. J. Mass Spectrometry* **379** (2015) 110, [arXiv:1412.1144].
- [217] A. D. McDonald et al., *Demonstration of Single Barium Ion Sensitivity for Neutrinoless Double Beta Decay using Single Molecule Fluorescence Imaging*, Submitted to: *Phys. Rev. Lett.* (2017) [arXiv:1711.04782].
- [218] B. J. P. Jones, A. D. McDonald, and D. R. Nygren, *Single Molecule Fluorescence Imaging as a Technique for Barium Tagging in Neutrinoless Double Beta Decay*, *JINST* **11** (2016), no. 12, P12011, [arXiv:1609.04019].
- [219] D. Thomas, S. Tovey, T. Collins, M. Bootman, M. Berridge, and P. Lipp, *A comparison of fluorescent ca^{2+} indicator properties and their use in measuring elementary and global ca^{2+} signals*, *Cell calcium* **28** (October, 2000) 213—223.

